Atomistic Molecular Dynamics Studies of Grain Boundary Structure and Deformation Response in Metallic Nanostructures

Laura Anne Patrick Smith

Dissertation submitted to the Faculty of the

Virginia Polytechnic Institute and State University

in partial fulfillment of the requirements for the degree of

Doctor of Philosophy

in

Materials Science and Engineering

Diana Farkas, Chair

David Clark

William Reynolds

Celine Hin

March 24, 2014

Blacksburg, VA

Keywords: grain boundaries, molecular dynamics, nanocrystalline, molecular dynamics simulation, LAMMPS, mechanical response, strain rate, plastic strain, interatomic potentials

Atomistic Molecular Dynamics Studies of Grain Boundary Structure and Deformation Response in Metallic Nanostructures

Laura Anne Patrick Smith

Abstract

The research reported in this dissertation focuses on the response of grain boundaries in polycrystalline metallic nanostructures to applied strain using molecular dynamics simulations and empirical interatomic force laws. The specific goals of the work include establishing how local grain boundary structure affects deformation behavior through the quantitative estimation of various plasticity mechanisms, such as dislocation emission and grain boundary sliding. The effects of strain rate and temperature on the plastic deformation process were also investigated. To achieve this, molecular dynamics simulations were performed on both thin-film and quasi-2D virtual samples constructed using a Voronoi tessellation technique. The samples were subjected to virtual mechanical testing using uniaxial strain at strain rates ranging from $10^5 s^{-1}$ to $10^9 s^{-1}$. Seven different interatomic embedded atom method potentials were used in this work. The model potentials describe different metals with fcc or bcc crystal structures. The model was validated against experimental results from studying the tensile deformation of irradiated austenitic stainless steels performed by collaborators at the University of Michigan. The results from the model validation include a novel technique for detecting strain localization through adherence of gold nanoparticles to the surface of an experimental sample prior to deformation. Similar trends with respect to intergranular crack initiation were observed between the model and the experiments.

Simulations of deformation in the virtual samples revealed for the first time that equilibrium grain boundary structures can be non-planar for model potentials representing fcc materials with

low stacking fault energy. Non-planar grain boundary features promote dislocation as deformation mechanisms, and hinder grain boundary sliding. This dissertation also reports the effects of temperature and strain rate on deformation behavior and correlates specific deformation mechanisms that originate from grain boundaries with controlling material properties, deformation temperature and strain rate.

Dedication

I would like to thank several members of the Materials Science and Engineering department for their invaluable assistance and support in completing this degree. LeeAnn Ellis, Amy Hill, Cindy Perdue, and Kim Grandstaff in particular. I would also like to thank David Clark, Diana Farkas, Bill Reynolds, Jon Zimmerman, and Celine Hin for their guidance and advice. All of you have been so supportive and encouraging throughout the ridiculous number of things that happened while I studied.

I would also like to thank my family for being so patient and loving while I worked through this. I could not have done it without your help, particularly Jeremiah for stepping into my life midway through this degree and helping me so much with Lois. I am so blessed.

And I would like to express my love and appreciation for Jeffrey Patrick. I would not have gone back to school without his support and encouragement, and I could not have continued without the love and assistance from his family. Beverly, Jerry, Deby, Philip, Brady, and Kayla, I will love you forever.

Attribution

The collaborators in this work and co-authors of the resulting publications are:

Mike McMurtrey *– Ph.D. student at University of Michigan. Project: Irradiation assisted stress corrosion cracking refers to intergranular stress corrosion cracking that is accelerated under the action of irradiation in light water reactor core components.*

Lucas Hale *- Ph.D. Materials Science University of Minnesota. Currently Postdoctoral Researcher Lawrence Livermore National Laboratories. Studies atomic-scale modeling and simulation of the mechanical behavior of materials.*

Jonathan Zimmerman *- Ph.D. Mechanical Engineering · Stanford University. Principal Member of Technical Staff at Sandia National Laboratories. Research engineer with a specialty of atomic-scale modeling and simulation of the mechanical behavior of materials, and of coupling atomic-scale and continuum models of material behavior.*

Niklas Floyd *– M.S. Materials Science & Engineering, Virginia Tech, 2010. Reactor Inspector, U.S. Nuclear Regulatory Commission. Project: large scale atomistic study of tensile deformation in a virtual FCC polycrystalline sample with columnar grain structure and a [110] texture.*

Joshua Kacher *– Ph.D. Student at University of Illinois at Urbana-Champaign. Projects: In situ TEM studies of grain growth rate in nanograin PLD nickel and in situ TEM studies of dislocation-grain boundary interactions under strain at elevated temperatures.*

Bai Cui *– Ph.D. Imperial College London, London, UK (2011).Research Associate, Department of Materials Science and Engineering, University of Illinois at Urbana-Champaign.*

Diana Farkas *- Ph.D. University of Delaware, 1980. Professor, MSE Virginia Tech, Program Director, Metals and Metallic Nanostructures, NSF Division of Materials Research. Dissertation advisor and committee chair.*

Gary Was *- Sc.D. (NE), Massachusetts Institute of Technology, 1980. Chair, Department of Nuclear Engineering and Radiological Sciences, University of Michigan, 1994 - 1999. Professor, Department of Nuclear Engineering and Radiological Sciences, University of Michigan*

Ian Robertson - D.Phil. in metallurgy from Oxford University, England, 1982. 2014 ASM Edward DeMille Campbell Memorial Lecturer. Dean, College of Engineering, Univ. of Wisconsin.

The specific contributions from my collaborators are as follows:

Chapter 4: Mr. McMurtrey and Dr. Was contributed:

Figures 1, 2, 3, 4, 6, 7, 8, 9, 13, 14, 18(a)

Tables 1, 2

Sections 1, 2, 3, 5.1.1, 5.2.1, 6, 7

Chapter 5: Mr. McMurtrey and Dr. Was contributed:

Figures 1, 2, 3(a), experimental parts of 5, experimental parts of 6, 7, 8, 9, 13, 14

Table 1

Sections 1, 2, 3, Experiment-related parts of 4, 5, 6

Chapter 8: Dr. Hale and Dr. Zimmerman contributed:

Figures 3 (a) and (b), the dislocation and twinning type and slip plane analysis, and the general fault energy curves.

Chapter 9: Niklas Floyd contributed

Figures 5, 6(a) and the data for 6(b)

Chapter 10: Mr. Kacher, Dr. Cui, and Dr. Robertson

Figures 1, 2, 3, 4, 5

Section 2

Contents

List of Figures

Chapter 3

Chapter 4

Chapter 7

Chapter 8

Chapter 10

List of Tables

1 Introduction

Improved structural materials resistant to various environments are key in many applications. One example is in the area of nuclear energy. The world-wide demand for energy is continually increasing. Of the existing technologies for providing electricity generation, one technology in particular stands out as having the capability of meeting the demand for power. Nuclear power plants are a viable, sustainable method of providing base-load power generation. In the United States, there are currently 100 operating nuclear reactors providing a significant portion of the power required [1]. The initial operating licenses issued to each plant were valid for 40 years. As the plants age, renewal licenses for some of the oldest reactors have been issued for an additional 20 years of operation. Recently, the Nuclear Regulatory Commission has begun researching whether extending operating licenses beyond 60 years is feasible given the expected material degradation over the life of the reactor [2].

A leading cause of material degradation is its service environment. The environment inside a nuclear reactor pressure vessel includes high pressures, high temperatures, and radiation. Due to this extreme, corrosive environment, austenitic stainless steel alloys are used to line the pressure vessels. This austenitic stainless steel is subject to both embrittlement and intergranular stress corrosion cracking [3]. Left undetected, cracks may lead to failure of the pressure vessel. In order to prevent cracks from developing unnoticed, it is necessary to study the causes of intergranular stress corrosion cracking in austenitic stainless steel, including the factors that contribute to intergranular crack nucleation. It is therefore very important to be able to develop new structural materials for these applications. This development requires an understanding of the basic atomic level processes that control mechanical and environmental response.

Atomistic computer simulation has been used extensively to study mechanical properties of crystalline materials and interfaces [4] that are governed by the microstructure at the atomic scale [5-8]. Progress in simulation techniques and advances in computer hardware have been particularly important in materials with grain sizes under 100 nm, where the length scales that are possible through simulations can reach those of experimental methods [9-13].

Even though there is still a large gap between the time scales that can be achieved by atomistic methods and those available to experiments [14], atomistic modeling can play a critical role in advancing the understanding of microstructure evolution and mechanical properties, particularly if simulation results are combined with recent advances in the experimental characterization tools [15]. The combination of simulation and experiment can provide new insight into critical phenomena at the atomistic level that can aid in the design and development of new structural materials [16].

Realistic simulation of mechanical behavior in metallic materials typically requires the generation of representative polycrystalline microstructures in the form of a grain boundary network. Simulations at the atomistic level require increasingly larger numbers of atoms. These simulations are now possible, due to the advancement of available computational power.

1.1 Motivation: Materials used in nuclear reactor pressure vessels

Nuclear reactor pressure vessels are made out of carbon steel due to its desirable strength and low cost. A major drawback to carbon steel is its susceptibility to corrosion by boric acid, which is added to the water inside the reactor to help control the nuclear reaction. In order to prevent this corrosion from occurring, a layer of corrosion-resistant austenitic stainless steel is used to create a barrier between the borated water and the carbon steel. Over time, due to the high

neutron flux, the hot borated water, and high pressures, the stainless steel becomes embrittled and may develop intergranular stress corrosion cracking. These cracks originate in grain boundaries, the interfacial regions found between the grains that make up the steel, for reasons that are not yet fully understood. Under the right conditions these cracks may propagate along the grain boundary network, ultimately growing large enough to cause failure of the material. The specific conditions under which intergranular cracks nucleate and grow are subjects of intense research. Some key factors that promote the nucleation of intergranular stress corrosion cracking include the yield stress, the stacking fault energy, and dislocation emission, absorption, and pileups at grain boundaries as noted in Chopra and Rao [17]. In this context, the relationships between stacking fault energy, yield strength, and dislocation activity at grain boundaries is clearly of interest. One method by which these relationships may be probed is to investigate materials with a high grain boundary density. Nanocrystalline materials present this opportunity, since with a decreasing grain size, the volume fraction of grain boundary interface increases. This increased number of grain boundary interfaces presents a clear way to investigate the relationships between stacking fault energy, yield strength, and dislocation activity at grain boundaries. With the increase in the grain boundary interfacial area, an increase in the variety of grain boundary structures is available for study. We can then work to pinpoint the effects of parameters such as the stacking fault energy, yield strength, and dislocation emission and interaction with the grain boundary. In addition, nanocrystalline materials have been shown to have unique resistance to radiation effects [18].

It is important to study the factors that cause intergranular crack initiation, including how local grain boundary structure affects deformation, what governs local grain boundary structure, how quantitative measures of deformation mechanisms change as a function of strain rate, and what

specific atomistic parameters govern overall material deformation. In addition, it is critical to understand how deformation is affected at elevated temperature.

1.2 Research goals

This research seeks to use molecular dynamics computer simulations to probe the interrelated factors leading to crack nucleation and growth in complex grain boundary networks.

The work proposed here involves a basic study of the structure of grain boundary networks and their mechanical response in materials at a molecular atomistic level. This project requires descriptions of the interactions between the various atoms that are based on both experimental data as well as first principle quantum mechanical calculations. Once this description is obtained the equilibrium atomic configuration around any defect or interface can be calculated through energy minimization schemes or molecular dynamics techniques. The detailed information on the atomistic configuration of the defective region is then linked to the properties in the material that are controlled by such defects. In recent years the increased speed of available computing facilities has allowed us to undertake large scale massive simulations. It is now possible to conduct simulations involving millions of atoms and study the structures of defective solids and their relation with material properties. Furthermore, the new computer architectures and increasing speeds allow the study of defects that are realistic and three dimensional in nature. These large scale simulations pose new challenges in the ways in which the results can be visualized and analyzed. Despite recent progress, we are still limited to grain sizes in the nanometer range and deformation rates that are much faster than experiment. The realistic simulations in this dissertation are relevant to the properties of nanocrystalline materials.

Nanocrystalline materials are used due to their high grain boundary to bulk ratios, allowing this research to focus on the role of grain boundaries in deformation and crack initiation.

The overall goal of this work is to use large-scale simulations to further the understanding of how grain boundary networks control mechanical response in metallic materials. The specific goals of the work include

- Determine two key effects of the stable stacking fault energy:
    - The effect of the stable stacking fault energy on relaxed grain boundary structure
    - The quantitative estimation of local grain boundary structures on deformation through:
        - Grain boundary sliding.
        - Dislocation emission, absorption, and slip transfer behavior.
        - Quantitative estimates of dislocation emission and grain boundary sliding as functions of:
            - stacking fault energy.
            - strain rate.
            - temperature.

1.3 Dissertation organization

This dissertation is organized into three main sections and a conclusion. The first section is comprised of chapters 1 through 3. It includes the Introduction (Chapter 1), the background information and literature review (Chapter 2), and the methods and techniques used in this research program (Chapter 3). The second section consists of Chapters 4 and 5, which detail the model validation process, through comparisons of simulation and experiments. These two

chapters have been published in Materials Science and Engineering: A [19] (chapter 4) and in the International Journal of Plasticity [20] (chapter 5). In the third section, Chapters 6 through 10, the main simulation results of the research are presented. Three of these chapters have been published at this time: Chapters 6 and 7 in Philosophical Magazine A [21] [22], and Chapter 8 in Modelling and Simulation in Materials Science Engineering [23]. Chapters 9 and 10 will be submitted for publication shortly. Finally, the major conclusions from this work are detailed in the conclusions (Chapter 11).

1.4 Research overview

There are several steps necessary in order to successfully complete the investigation of the factors that contribute to intergranular crack initiation and deformation in nanocrystalline materials. The initial step is to validate the model against experimental results in similar materials:

- Compare intergranular crack initiation trends in Ni and in Fe-13Cr-15Ni austenitic stainless steel, with an emphasis on the angle of the crack grain boundary with respect to the tension axis and slip transfer in both cracked and uncracked boundaries. (Chapter 4)
- Compare areas of local strain in excess of the homogenous strain imposed on the sample to ensure the simulations accurately represent local deformation in experimental samples. (Chapter 5)

Once the model is validated, the research can address issues that are not necessarily accessible to current experimental techniques. The work proceeds in several distinct steps, as follows:

- Determine the relationship between the grain boundary angle with respect to the tensile axis and its effect on both deformation and crack initiation. (Chapter 6)
- Determine how stable stacking fault energies affect the relaxed grain boundary structures and how that in turn affects deformation through investigation of materials with two very different stacking fault energies. (Chapter 7)
- Determine deformation mechanisms in bcc tantalum as a function of strain rate. Determine the dominant deformation mechanisms as a function of strain rate, and at what strain rate strain rate effects become pronounced. (Chapter 8)
- Determine what interatomic parameter is the governing parameter for specific deformation mechanisms, grain boundary energetics, and the yield and flow stress shown in the stress-strain diagram. (Chapter 9)
- Quantitatively assess the differences in dislocation emission, grain boundary sliding, strain rate sensitivity, and activation energies due to elevated temperature. (Chapter 10)

References

[1] U. S. N. R. Commission, "Information Digest, 2013–2014 (NUREG-1350, Volume 25) Section 3," U. S. N. R. Commission, Ed., ed, 2013.

[2] N. E. Institute. (2014, March 24). *Subsequent License Renewal: Creating the Foundation for Nuclear Plant Operation Beyond 60 Years* Available: http://www.nei.org/Master-Document-Folder/Backgrounders/White-Papers/Subsequent-License-Renewal

[3] U. S. N. R. Commission, "Irradiation-Assisted Stress Corrosion Cracking Behavior of Austenitic Stainless Steels Applicable to LWR Core Internals (NUREG/CR-6892, ANL-04/10)," U. S. N. R. Commission, Ed., ed, 2006.

[4] Y. Mishin, M. Asta, and J. Li, "Atomistic modeling of interfaces and their impact on microstructure and properties," *Acta Materialia,* vol. 58, pp. 1117-1151, Feb 2010.

[5] M. W. Finnis, "Concepts for simulating and understanding materials at the atomic scale,"

Mrs Bulletin, vol. 37, pp. 477-484, May 2012.

[6] S. M. Foiles and M. I. Baskes, "Contributions of the embedded-atom method to materials science and engineering," *Mrs Bulletin,* vol. 37, pp. 485-491, May 2012.

[7] F. F. Abraham, R. Walkup, H. J. Gao, M. Duchaineau, T. D. De la Rubia, and M. Seager, "Simulating materials failure by using up to one billion atoms and the world's fastest computer: Work-hardening," *Proceedings of the National Academy of Sciences of the United States of America,* vol. 99, pp. 5783-5787, Apr 30 2002.

[8] S. M. Foiles, "Embedded-atom and related methods for modeling metallic systems," *Mrs Bulletin,* vol. 21, pp. 24-28, Feb 1996.

[9] H. Huang and H. Van Swygenhoven, "Atomistic Simulations of Mechanics of Nanostructures," *Mrs Bulletin,* vol. 34, pp. 160-162, Mar 2009.

[10] N. Li, J. Wang, X. Zhang, and A. Misra, "In-situ TEM Study of Dislocation-Twin Boundaries Interaction in Nanotwinned Cu Films," *Jom,* vol. 63, pp. 62-U62, Sep 2011.

[11] J. R. Greer, D. Jang, and X. W. Gu, "Exploring Deformation Mechanisms in Nanostructured Materials," *Jom,* vol. 64, pp. 1241-1252, Oct 2012.

[12] S. J. Fensin, C. Brandl, E. K. Cerreta, G. T. Gray, T. C. Germann, and S. M. Valone, "Nanoscale Plasticity at Grain Boundaries in Face-centered Cubic Copper Under Shock Loading," *Jom,* vol. 65, pp. 410-418, Mar 2013.

[13] J. Lao, M. N. Tam, D. Pinisetty, and N. Gupta, "Molecular Dynamics Simulation of FCC Metallic Nanowires: A Review," *Jom,* vol. 65, pp. 175-184, Feb 2013.

[14] C. Brandl, P. M. Derlet, and H. Van Swygenhoven, "Strain rates in molecular dynamics simulations of nanocrystalline metals," *Philosophical Magazine,* vol. 89, pp. 3465-3475, 2009 2009.

[15] I. M. Robertson, C. A. Schuh, J. S. Vetrano, N. D. Browning, D. P. Field, D. J. Jensen*, et al.*, "Towards an integrated materials characterization toolbox," *Journal of Materials Research,* vol. 26, pp. 1341-1383, Jun 2011.

[16] T. M. Pollock and R. LeSar, "The feedback loop between theory, simulation and experiment for plasticity and property modeling," *Current Opinion in Solid State & Materials Science,* vol. 17, pp. 10-18, Feb 2013.

[17] O. K. Chopra and A. S. Rao, "A review of irradiation effects on LWR core internal materials - IASCC susceptibility and crack growth rates of austenitic stainless steels,"

Journal of Nuclear Materials, vol. 409, pp. 235-256, Feb 2011.

[18] Y.-Q. Chang, Q. Guo, J. Zhang, L. Chen, Y. Long, and F.-R. Wan, "Irradiation effects on nanocrystalline materials," *Frontiers of Materials Science,* vol. 7, pp. 143-155, 2013/06/01 2013.

[19] M. D. McMurtrey, G. S. Was, L. Patrick, and D. Farkas, "Relationship between localized strain and irradiation assisted stress corrosion cracking in an austenitic alloy," *Materials Science and Engineering a-Structural Materials Properties Microstructure and Processing,* vol. 528, pp. 3730-3740, Apr 2011.

[20] M. D. McMurtrey, G. S. Was, B. Cui, I. Robertson, L. Smith, and D. Farkas, "Strain localization at dislocation channel–grain boundary intersections in irradiated stainless steel," *International Journal of Plasticity,* vol. 56, pp. 219-231, 5// 2014.

[21] D. Farkas and L. Patrick, "Tensile deformation of fcc Ni as described by an EAM potential," *Philosophical Magazine,* vol. 89, pp. 3435-3450, 2009 2009.

[22] L. Smith and D. Farkas, "Non-planar grain boundary structures in fcc metals and their role in nano-scale deformation mechanisms," *Philosophical Magazine,* vol. 94, pp. 152-173, Jan 2014.

[23] L. Smith, J. A. Zimmerman, L. M. Hale, and D. Farkas, "Molecular dynamics study of deformation and fracture in a tantalum nano-crystalline thin film.," *MSMSE,* vol. Accepted, 2014.

2 Background and Literature Review

Intergranular stress corrosion cracking (IGSCC) is a persistent problem in aging nuclear power plants. These are cracks that develop in grain boundaries and grow along the grain boundary, weakening the material and potentially leading to failure. An example of the consequences of IGSCC can be found in the history of the Davis-Besse nuclear power plant. On March 5, 2002, a hole the size of a football was found in the carbon steel reactor vessel head at Davis-Besse nuclear power plant located in northwest Ohio [1]. Root cause analysis showed that an IGSCC – type crack developed in a control rod drive nozzle in the reactor head. This crack allowed borated water, water that has had boric acid added to it in order to assist in controlling the nuclear reaction, to seep through the protective layer of Alloy 600. This borated water then began corroding the carbon steel from which the reactor head is made. Fortunately, the crack and corrosion were discovered before a catastrophic failure occurred. This event shows the impact and potential catastrophic consequences of IGSCC in nuclear reactors and the importance of understanding the factors that contribute to the formation and propagation of these cracks. Since IGSCC happens in grain boundaries, it is vitally important to understand the role of grain boundaries in deformation and how they contribute to mechanical behavior.

2.1 Deformation mechanisms in grain boundaries

Grain boundaries are clearly a key factor in both IGSCC and the overall deformation of the material. Grain boundaries act as both sources of dislocations and contribute to the strength of a material by acting as a barrier to dislocation movement. Inhibiting the motion of dislocations through grains blocks the onset of plasticity, raising the yield and flow stress of the material and thus the strength. Dislocations pile up at grain boundaries when transferring across the boundary

is impeded. This is known as grain-boundary strengthening. Logically, if grain boundaries contribute to the strength of the material, then it stands to reason that more grain boundaries in a material equates to higher strength. One way to increase the number of grain boundaries is to reduce the grain size, increasing the volume fraction of material devoted to grain boundaries in a polycrystalline material. Two researchers, working independently, separately identified the strengthening effect of reducing the grain size [2, 3]. The resulting theory, called the Hall-Petch effect, is a theory that seeks to explain why the strength of a material increases as grain size decreases and is described through the following relation:

$$\sigma_y = \sigma_0 + kd^{-1/2} \qquad 2.1$$

Where σ_y is the yield stress, σ_0 is a material constant, k is a strengthening coefficient, and d is the grain size. In theory, this indicates that a material with infinitely small grains would have infinite strength. This is impossible, however, since grain sizes at the extreme small end have no long-range order and are effectively amorphous. Amorphous materials have no long-range order and lack the organization to support dislocations. Materials with grain sizes in the nanometer range are possible, and show interesting and desirable properties [4]. Deformation in nanomaterials with grain sizes less than about 100 nm is restricted to grain boundary mediated deformation. At this grain size, Frank-Read sources are prevented from operating, and thus the only source for dislocations is the grain boundary itself. The study of deformation in nanomaterials allows the researcher to focus only on factors that affect grain boundary deformation.

The grain boundary network acts as a source of dislocations when the sample is loaded [38]. Tschopp and co-workers [70-72] studied the evolution of grain boundaries in copper bicrystals under uniaxial tension. Spearot and co-workers that reported that areas of larger free volume in the grain boundary, such as the “E” structural units can constitute favored sites for dislocation

nucleation [73]. These findings also point out the importance of excess free volume in the grain boundary as a critical parameter related to dislocation emission. Kinoshita and co-workers [74] reported that extrinsic grain boundary dislocations are often present in the grain and that the force required to emit these dislocations is highly dependent on detailed atomic level changes in the dislocation cores. These lead to a strong dependence on local grain boundary structure and have a significant effect on the emission process. McPhie and co-workers [75] showed that dislocation nucleation is much more likely to occur at defect sites within a grain boundary, stressing the importance of the local structure of the grain boundary as well as the relaxation state of the boundary.

2.2 Deformation in nanomaterials

Deformation in nanocrystalline materials is significantly different than deformation in macroscale materials. With grains that average less than 100nm in diameter, the operation of conventional dislocation sources, such as Frank-Reed sources, are inhibited [5]. This leaves two main mechanisms for deformation: grain boundary sliding and dislocation emission from the grain boundaries. Grain boundary sliding as a deformation mechanism becomes significant when dislocation emission and pileup at grain boundaries is limited by the grain size [6].. The critical grain size at which this occurs varies, but is generally thought to be in the 20-40 nm range [5]. In addition to grain boundary sliding, motion of the grain boundary normal to the grain boundary plane has also been observed. Grain boundary sliding and coupled migration have been studied by multiple researchers, including Cahn et al. [7, 8], Farkas et al. [9, 10], and Velasco et al. [11]. Dislocation emission as a deformation mechanism at the nanoscale has been investigated through molecular dynamics in previous studies. Yamakov et al. used molecular dynamics to study

dislocation emission and twin formation in aluminum nanocrystals [12]. de Koenig et al. [13] showed that local grain boundary structure affects the nature of the dislocation interaction, including slip transfer. Tschopp et al. [14, 15] also studied the effect of local structure on grain boundary emission, including how structural units in the boundary can dissociate into partial dislocations which then emit into the grain. Vo et al. [16] showed that the competition between dislocation emission and grain boundary sliding at the nanoscale is dependent on grain size and strain rate.

It has been well established that grain boundary sliding and dislocation emission are significant deformation mechanisms at the nanoscale, but the relationship between these deformation mechanisms and the specific atomistic parameters that control remains a topic of investigation. Experimental research performed by An et al. [17] used high pressure torsion to investigate the effect of stacking fault energy on deformation in nanocrystalline Cu and Cu-Al alloys. It was found that stacking fault energy affected the uniformity of microstructure, with materials that have high or low stacking fault energies having more microstructural uniformity than materials with moderate stacking fault energies. Molecular dynamics simulations were used by Jin et al. [18, 19] to study dislocation transmission across twin boundaries in Al, Cu, and Ni. Jin was able to relate the resistance to slip transfer to a resistance parameter R that was dependent upon the stable and unstable stacking fault energy. Deng et al. [20] expanded on this work with Au, Ag, Al, Cu, Pd, and Ni nanowires. Deng was able to show that the unstable stacking fault energy was directly proportional to the yield stress and to the stress at which leading partial dislocations emit from interfaces. Simulations by Asaro et al. [21] in Cu, Al, and Ni showed that the ratio of the stable and unstable stacking fault energies significantly affects the emission of a trailing partial dislocation from grain boundaries, which in turn affects the equilibrium partial separation

distance. Stable and unstable stacking fault energies are clearly critical in the deformation of nanocrystalline fcc materials, though work to determine how the stable and unstable stacking fault energy correlates to both grain boundary structures and subsequent deformation has yet to be performed. Changes in grain boundary structures due to deformation through both grain boundary sliding and dislocation emission may also contribute to intergranular crack nucleation, another known deformation mechanism at the nanoscale.

Intergranular crack nucleation and growth has been observed in nanocrystalline materials. Experimental work by Liu et al. [22] in Au thin films with average grain sizes of about 8nm showed that cracks develop and propagate along the grain boundary network. Atomistic simulations of both fcc and bcc materials show that cracks in nanocrystalline materials nucleate through a nanovoid formation and coalescence process [23-30]. Nanovoids, once nucleated, grow through a process of dislocation emission from the nanovoid surface [31-37]. Eventually the nanovoids will attain sufficient size to breach the top and bottom surfaces of the sample, forming a crack. The newly formed crack can then propagate along the grain boundary network, significantly weakening the material and contributing to plastic strain. Dislocation emission, grain boundary sliding, and intergranular crack initiation all contribute to plastic deformation in the nanoscale and are the subject of the research presented in this work.

The research presented in this work uses molecular dynamics simulations to study the behavior of grain boundaries to applied strain, including factors that favor crack initiation, dislocation emission and grain boundary sliding. In particular, this work seeks to more firmly establish the relationship between specific deformation mechanisms that originate in the grain boundary and either the stable or unstable stacking fault energy.

2.3 Model materials investigated

In order to gain insight into basic mechanisms model materials are chosen, to represent a range of metals. In this work, four model fcc materials and one bcc model material are investigated. The fcc materials of interest are copper, aluminum, nickel, and palladium. The work was also expanded to include bcc tantalum in order to explore deformation in nanocrystalline bcc materials. These specific metals were chosen due to the availability of accurate interatomic potentials with differing stable and unstable stacking fault energies, cohesive energies, and elastic constants. When choosing model materials potentials one should consider their accuracy or ability to reproduce properties of interest as closely as possible, their transferability, meaning that they can be used to study a variety of properties for which it was not fit and their computational speed, since faster calculations enable the study of more realistic structures. The choice of the interatomic potential also depends on the area of intended application. The model potentials used here were developed to represent aluminum, copper, nickel, palladium, and tantalum. We emphasize, that we work with model materials and therefore we have chosen two different potentials representing Al and two representing Ni. See section 3.3 for a detailed discussion of the interatomic potentials chosen to perform these simulations.

In order to investigate the effects of stable and unstable stacking fault energy on deformation, materials with a wide range of energies are needed. The materials chosen for this work are aluminum, copper, nickel, palladium, and tantalum. Experimental values for each material are shown in Table 1 and compared with the austenitic stainless steel used in chapters 4 and 5. The materials chosen have a range of yield strengths, stacking fault energies, and elastic moduli. The yield strength is the stress at which plastic deformation begins, the stacking fault energy is a measure of the excess energy in the material due to stacking irregularities in fcc materials, and

the elastic modulus is a measure of the resistance of the material to elastic deformation under applied stress or strain. By comparing the yield strengths, stacking fault energies, and elastic moduli of the studied materials to those of the austenitic stainless steel, we can choose materials that have a higher and lower yield strength, stacking fault energies, and elastic modulus. This allows us to more easily isolate the effects of these parameters on deformation and intergranular crack nucleation.

In this work, we use empirical models for each material. The models are fit to experimental data like that listed in Table 1, including the lattice parameter, the cohesive energy, and the stable stacking fault energy. Refer to section 3.3 for the specific values used in each potential.

Table 1: Experimental material properties for the materials studied in this work

Metal	Crystal structure (fcc/bcc)	Lattice Parameter (nm)	γ_{SF} (mJ/m^2)	σ_y (MPa)	E (GPa)
Fe-Cr-Ni Stainless Steels	Fcc	0.3589 [38]	10 – 100 [38]	136-220 [39]	-
Aluminum	Fcc	0.4050 [39]	135 [40] 160-200 [41] 200 [42]	40-50 [39]	62 [39]
Copper	Fcc	0.3615 [39]	55[42] 70 [43] 80 [40]	209 [39]	128 [39]
Nickel	Fcc	0.3518 [39]	132 [44] 225 [42] 240 [40]	317 [39]	207 [39]
Palladium	Fcc	0.3890 [39]	180 [45]	200 [46]	21 [46]
Tantalum	bcc	0.3302 [39]	-	250 [39]	186 [39]

References

[1] U. S. N. R. Commission, "Fact Sheet on Improvements Resulting From Davis-Besse Incident," ed. Washington DC, 2009.

[2] N. J. Petch, "The cleavage strength of polycrystals," *J. Iron Steel Inst. Lond.,* vol. 173, pp. 25-28, 1953.

[3] E. O. Hall, "The Deformation and Ageing of Mild Steel: III Discussion of Results," *Proceedings of the Physical Society. Section B,* vol. 64, p. 747, 1951.

[4] M. A. Meyers, A. Mishra, and D. J. Benson, "Mechanical properties of nanocrystalline materials," *Progress in Materials Science,* vol. 51, pp. 427-556, May 2006.

[5] H. Van Swygenhoven and J. R. Weertman, "Deformation in nanocrystalline metals," *Materials Today,* vol. 9, pp. 24-31, 5// 2006.

[6] Y. Z. Tang, E. M. Bringa, and M. A. Meyers, "Inverse Hall-Petch relationship in nanocrystalline tantalum," *Materials Science and Engineering a-Structural Materials Properties Microstructure and Processing,* vol. 580, pp. 414-426, Sep 2013.

[7] J. W. Cahn and Y. Mishin, "Recrystallization initiated by low-temperature grain boundary motion coupled to stress," *International Journal of Materials Research,* vol. 100, pp. 510-515, Apr 2009.

[8] J. W. Cahn, Y. Mishin, and A. Suzuki, "Coupling grain boundary motion to shear deformation," *Acta Materialia,* vol. 54, pp. 4953-4975, Nov 2006.

[9] D. Farkas, A. Froseth, and H. Van Swygenhoven, "Grain boundary migration during room temperature deformation of nanocrystalline Ni," *Scripta Materialia,* vol. 55, pp. 695-698, 2006.

[10] D. Farkas, S. Mohanty, and J. Monk, "Strain-driven grain boundary motion in nanocrystalline materials," *Materials Science and Engineering a-Structural Materials Properties Microstructure and Processing,* vol. 493, pp. 33-40, Oct 15 2008.

[11] M. Velasco, H. Van Swygenhoven, and C. Brandl, "Coupled grain boundary motion in a nanocrystalline grain boundary network," *Scripta Materialia,* vol. 65, pp. 151-154, Jul 2011.

[12] V. Yamakov, D. Wolf, S. R. Phillpot, A. K. Mukherjee, and H. Gleiter, "Dislocation processes in the deformation of nanocrystalline aluminium by molecular-dynamics simulation," *Nature Materials,* vol. 1, pp. 45-48, Sep 2002.

[13] M. de Koning, R. J. Kurtz, V. V. Bulatov, C. H. Henager, R. G. Hoagland, W. Cai*, et al.*, "Modeling of dislocation-grain boundary interactions in FCC metals," in *Workshop on Modeling and Experimental Validation*, Les Diableret, Switzerland, 2002, pp. 281-289.

[14] M. A. Tschopp, G. J. Tucker, and D. L. McDowell, "Structure and free volume of < 110 > symmetric tilt grain boundaries with the E structural unit," *Acta Materialia,* vol. 55, pp. 3959-3969, Jun 2007.

[15] G. J. Tucker, M. A. Tschopp, and D. L. McDowell, "Evolution of structure and free volume in symmetric tilt grain boundaries during dislocation nucleation," *Acta Materialia,* vol. 58, pp. 6464-6473, Nov 2010.

[16] N. Q. Vo, R. S. Averback, P. Bellon, S. Odunuga, and A. Caro, "Quantitative description of plastic deformation in nanocrystalline Cu: Dislocation glide versus grain boundary sliding," *Physical Review B,* vol. 77, Apr 2008.

[17] X. H. An, Q. Y. Lin, S. D. Wu, Z. F. Zhang, R. B. Figueiredo, N. Gao*, et al.*, "Significance of stacking fault energy on microstructural evolution in Cu and Cu-Al alloys processed by high-pressure torsion," *Philosophical Magazine,* vol. 91, pp. 3307-3326, 2011 2011.

[18] Z. H. Jin, P. Gumbsch, K. Albe, E. Ma, K. Lu, H. Gleiter*, et al.*, "Interactions between non-screw lattice dislocations and coherent twin boundaries in face-centered cubic metals," *Acta Materialia,* vol. 56, pp. 1126-1135, Mar 2008.

[19] Z. H. Jin, P. Gumbsch, E. Ma, K. Albe, K. Lu, H. Hahn*, et al.*, "The interaction mechanism of screw dislocations with coherent twin boundaries in different face-centred cubic metals," *Scripta Materialia,* vol. 54, pp. 1163-1168, Mar 2006.

[20] C. Deng and F. Sansoz, "Fundamental differences in the plasticity of periodically twinned nanowires in Au, Ag, Al, Cu, Pb and Ni," *Acta Materialia,* vol. 57, pp. 6090-6101, Dec 2009.

[21] R. J. Asaro and S. Suresh, "Mechanistic models for the activation volume and rate sensitivity in metals with nanocrystalline grains and nano-scale twins," *Acta Materialia,* vol. 53, pp. 3369-3382, Jul 2005.

[22] J. B. Liu, A. M. Nie, C. Z. Dong, P. Wang, H. T. Wang, M. S. Fu*, et al.*, "Grain boundary structure dependent fracture in nanocrystalline Au films," *Materials Letters,* vol. 65, pp. 2769-2771, Sep 2011.

[23] D. Farkas, H. Van Swygenhoven, and P. M. Derlet, "Intergranular fracture in nanocrystalline metals," *Physical Review B,* vol. 66, p. 4, Aug 2002.

[24] S. L. Frederiksen, K. W. Jacobsen, and J. Schiotz, "Simulations of intergranular fracture

in nanocrystalline molybdenum," *Acta Materialia,* vol. 52, pp. 5019-5029, Oct 2004.

[25] A. J. Cao and Y. G. Wei, "Atomistic simulations of crack nucleation and intergranular fracture in bulk nanocrystalline nickel," *Physical Review B,* vol. 76, p. 5, Jul 2007.

[26] B. Wu and Y. G. Wei, "A Computational Model for Intergranular Fracture in Nanocrystalline and Ultra-Fine Polycrystalline Metals," in *Ductility of Bulk Nanostructured Materials*. vol. 633-634, Y. Zhao and X. Liao, Eds., ed Stafa-Zurich: Trans Tech Publications Ltd, 2010, pp. 39-53.

[27] A. J. Cao, "Molecular dynamics simulations of nanocrystalline nickel and copper revealing different failure model of fcc metals," in *Ductility of Bulk Nanostructured Materials*. vol. 633-634, Y. Zhao and X. Liao, Eds., ed Stafa-Zurich: Trans Tech Publications Ltd, 2010, pp. 31-37.

[28] Y. Cheng, Z. H. Jin, Y. W. Zhang, and H. Gao, "On intrinsic brittleness and ductility of intergranular fracture along symmetrical tilt grain boundaries in copper," *Acta Materialia,* vol. 58, pp. 2293-2299, Apr 2010.

[29] D. V. Bachurin and P. Gumbsch, "Accommodation processes during deformation of nanocrystalline palladium," *Acta Materialia,* vol. 58, pp. 5491-5501, Sep 2010.

[30] Y. F. Zhang, P. C. Millett, M. Tonks, and B. Biner, "Deformation-twin-induced grain boundary failure," *Scripta Materialia,* vol. 66, pp. 117-120, Jan 2012.

[31] D. C. Ahn, P. Sofronis, M. Kumar, J. Belak, and R. Minich, "Void growth by dislocation-loop emission," *Journal of Applied Physics,* vol. 101, Mar 2007.

[32] E. M. Bringa, S. Traiviratana, and M. A. Meyers, "Void initiation in fcc metals: Effect of loading orientation and nanocrystalline effects," *Acta Materialia,* vol. 58, pp. 4458-4477, Aug 2010.

[33] M. A. Meyers, S. Traiviratana, V. A. Lubarda, D. J. Benson, and E. M. Bringa, "The role of dislocations in the growth of nanosized voids in ductile failure of metals," *Jom,* vol. 61, pp. 35-41, Feb 2009.

[34] R. E. Rudd, "Void growth in bcc metals simulated with molecular dynamics using the Finnis-Sinclair potential," *Philosophical Magazine,* vol. 89, pp. 3133-3161, 2009 2009.

[35] Y. Z. Tang, E. M. Bringa, and M. A. Meyers, "Ductile tensile failure in metals through initiation and growth of nanosized voids," *Acta Materialia,* vol. 60, pp. 4856-4865, Jul 2012.

[36] Y. Z. Tang, E. M. Bringa, B. A. Remington, and M. A. Meyers, "Growth and collapse of nanovoids in tantalum monocrystals," *Acta Materialia,* vol. 59, pp. 1354-1372, Feb 2011.

[37] S. Traiviratana, E. M. Bringa, D. J. Benson, and M. A. Meyers, "Void growth in metals: Atomistic calculations," *Acta Materialia,* vol. 56, pp. 3874-3886, Sep 2008.

[38] R. E. Schramm and R. P. Reed, "Stacking fault energies of seven commercial austenitic stainless steels," *Metallurgical Transactions A,* vol. 6, pp. 1345-1351, 1975/07/01 1975.

[39] A. International, *Properties and Selection: Nonferrous Alloys and Special-Purpose Materials*: ASM International, 2002.

[40] B. E. P. Beeston, I. L. Dillamore, and R. E. Smallman, "The stacking-fault energy of some nickel-cobalt alloys," *Metal Science,* vol. 2, pp. 12-14, 1968.

[41] L. E. Murr, *Interfacial phenomena in metals and alloys*: Addison-Wesley Pub. Co, 1975.

[42] P. C. J. Gallagher, "The influence of alloying, temperature, and related effects on the stacking fault energy," *Metallurgical Transactions,* vol. 1, pp. 2429-2461, 1970/09/01 1970.

[43] J. A. Venables, "The electron microscopy of deformation twinning," *Journal of Physics and Chemistry of Solids,* vol. 25, pp. 685-692, 7// 1964.

[44] P. Humble, M. H. Loretto, and L. M. Clarebrough, "The nature of defects in quenched nickel," *Philosophical Magazine,* vol. 15, pp. 297-303, 1967/02/01 1967.

[45] J. P. Hirth and J. Lothe, *Theory of Dislocations*: Krieger Publishing Company, 1982.

[46] Matbase. (2014, 03). *Palladium Material Properties*. Available: http://www.matbase.com/material-categories/metals/non-ferrous-metals/other-non-ferrous-metals/material-properties-of-palladium.html#properties

3 Simulation Tools

Computer simulations offer an attractive method of investigating the atomistic mechanisms involved in deformation of nanocrystalline materials that are not possible with experimental techniques. The choice of simulation technique depends on several factors, including the scale of the sample being simulated and the specific information desired. There are several simulation techniques available, including *ab initio*, molecular dynamics, and continuum-level simulations. The smallest scale simulation technique is *ab initio* simulations, where the number of atoms is limited to about 100, but extremely detailed information about the quantum states of each electron associated with the individual atoms is factored in to the calculations. This gives extremely accurate results, but at the expense of the number of atoms available to the calculation. Molecular dynamics simulations allow for a much larger sample, with greater than a million atoms included in the simulation. In molecular dynamics, the specific quantum information for each atom is lost, but the number of atoms considered is greatly increased. In addition to simulation techniques that consider individual atoms, there are continuum-level simulations, using finite element analysis techniques to consider sample sizes that approach experimental scales. The cost for such an increase in sample size is the atomistic-level information available to both molecular dynamics and ab initio techniques. In this work, molecular dynamics was chosen as the simulation technique due to the sample sizes of about a million atoms and the availability of accurate potentials.

3.1 Sample Generation

The virtual samples used in this work were created using a Voronoi construction technique. Two types of samples with columnar grains were generated: a fully periodic quasi-2D sample, and

thin-film samples with free surfaces in the positive and negative z directions. These samples are discussed in more detail in the following sections.

3.1.1 Periodic quasi-2D samples

The quasi-2D samples were created with periodic boundary conditions in all directions. With periodic conditions, a large system can be simulated by modeling a small part of the overall sample and tiling images of the sample. These samples have 9 grains of 40nm average diameter and 719 598 atoms. The periodicity along the z axis is the lattice periodicity in the [1 1 0] direction common to all grains. The grain boundaries in these samples are of pure tilt character around the [1 1 0] axis with random misorientation angles as well as random orientations of the grain boundary planes. The quasi-2D samples used with the fcc potentials in this work have been adjusted to be proportional to the lattice parameter of the simulated metal. Apart from the simulation box size, the samples are exactly the same. This allows differences in relaxed grain boundary structure and deformation behavior to be isolated to differences in the interatomic potential used. Note that the 40nm grain size precludes Frank-Read sources from operating, and restricts dislocation-mediated deformation to only straight-line dislocations. The dislocation core is parallel to the periodicity in the z direction and thus is normal to the [1 1 0] texture of the sample.

3.1.2 Thin-film samples

Two sets of thin-film samples were generated using a Voronoi process similar to that used to create the quasi-2D sample. The first set of samples was created to simulate bcc tantalum. Two samples with different sizes were created: one very small, with only three grains, and one an

order of magnitude larger. The first has three grains with random grain orientations, about 500K atoms, and a thickness of 7nm. This extremely small sample was created specifically to facilitate simulations at a strain rate of $10^5 s^{-1}$. A sample one order of magnitude larger, with the same 7 nm thickness was created in order to ensure that deformation processes observed in the first sample were not size dependent. This sample contained 30 grains and about 5M atoms. Both samples were used in simulations with strain rates from $10^6 s^{-1}$ to $10^9 s^{-1}$ with a goal of identifying the effect of strain rate on deformation.

The second set of thin-film samples was created from orientation imaging microscopy (OIM) scans of the experimental samples used in chapters 4 and 5. OIM uses scanning electron microscopy (SEM) technology to determine the grain orientations and grain boundary characters of experimental samples. In this technique the SEM beam is directed at the surface of the sample at an angle of 70°. The lattice symmetry is revealed by Kikuchi bands in the backscattered electrons that impinge a detector placed near the sample. The orientation of each grain can then be calculated from the Kikuchi band pattern, and the orientations are mapped. By calculating the angles between the orientations of each grain, the grain boundary character can be deduced. The Euler angles of each grain and grain cell centers estimated from the OIM scans are then used to create a set of virtual samples that mimic the experimental samples as can be seen in figure 1. The top row shows the OIM information, while the second row shows the virtual samples created to represent them. The two sets of samples share Euler orientations for each grain. This implies that the grain boundary characters should also be similar.

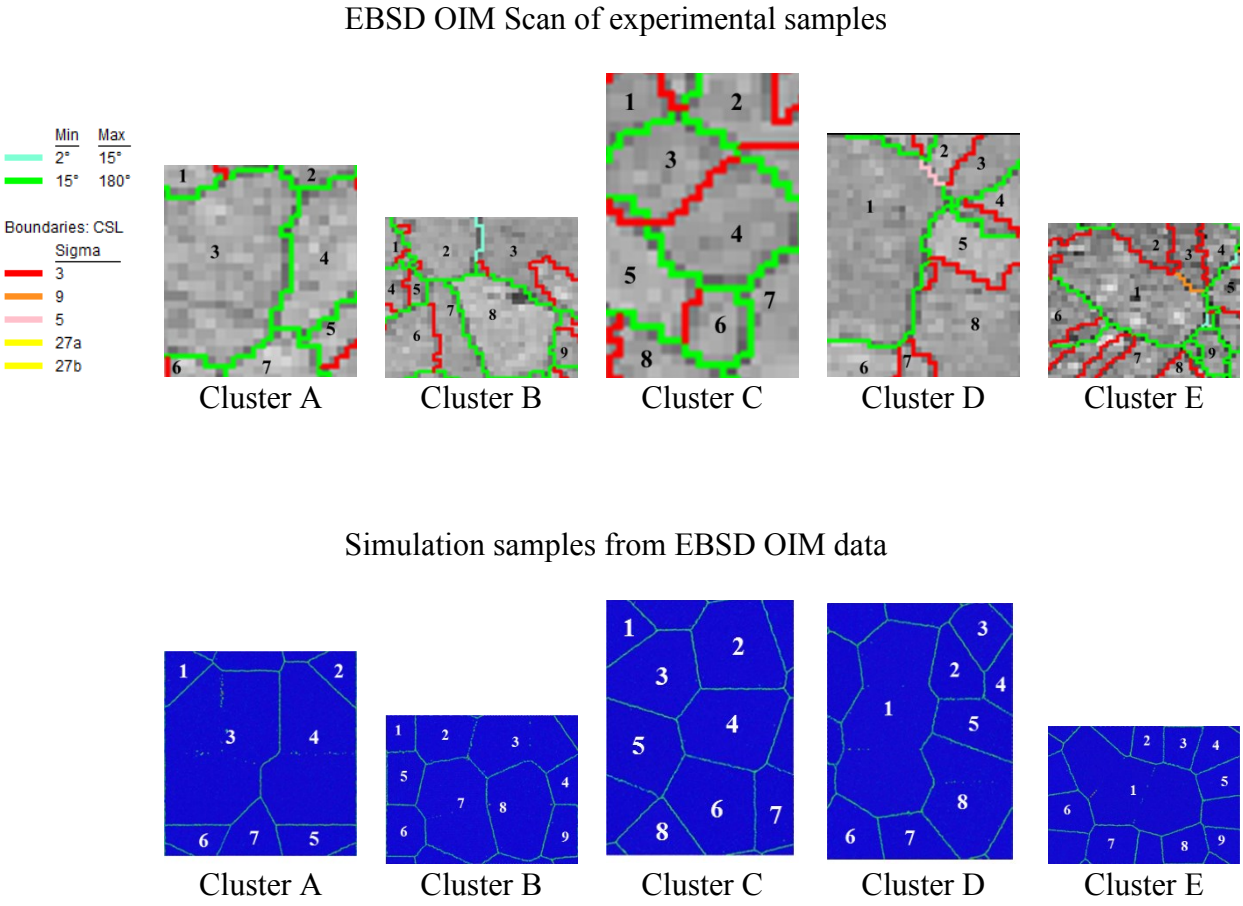

Figure 1: Experimental and simulated samples. Simulated samples were created from EBSD OIM data to obtain equivalent grain and boundary orientations. Top row shows results from OIM scans with boundary types coded by color. Bottom row shows simulated samples with coloration by centro-symmetry parameter [1] of each atom. Blue indicates perfect lattice, while green and red show increasing amounts of lattice disruption. The green atoms in this image indicate grain boundaries and small defects located within the bulk of the grain. Experimental OIM scans by McMurtrey. Simulation images by author.

3.2 Molecular dynamics

Molecular dynamics (MD) is a simulation technique that uses Newton's equations of force and motion to calculate the position, velocity, and force on each atom in a given simulated sample at a defined timestep. These calculations are used to determine how a sample responds to applied stress or strain. The MD software used in this work is the Large-scale Atomic/Molecular Massively Parallel Simulation written by Steve Plimpton at Sandia National Laboratories [2].

LAMMPS is a feature-rich MD software package that is widely considered the standard by computational materials researchers. LAMMPS is fully parallelized on multiple processors simultaneously, vastly increasing the computing power that can be used in each simulation. There are several advantages to MD simulations, including the number of atoms that can be simulated, the range of temperatures available to the simulation, and the variety of strain rates that can be used. MD simulations are capable of using up to a billion atoms at very fast strain rates of (greater than $10^7 s^{-1}$) or small samples of less than a million atoms at slower strain rates (less than $10^6 s^{-1}$). The limitations of molecular dynamics lie in the fast strain rates and short timescales available to MD simulations. The equations of motion are integrated with a femtosecond timestep, leading to simulations that have durations ranging from picoseconds to nanoseconds. This very short timescale prevents thermally-driven or time-dependent phenomena and presents difficulty with comparison to experiments.

Atoms in MD simulations are treated as hard spheres that react to the attractive or repulsive forces exerted on them by neighboring atoms. In order to initialize a simulation run, the starting atom positions, types, mass, and interactions are defined as inputs to the software. Next, initial velocities for each atom in the sample are set for each atom as a function of a given initial temperature. The first iteration calculates the force on each atom at t = 0. At each successive femtosecond the positions, forces, and velocities are recalculated for each atom until the total simulation time has elapsed.

A Nosé-Hoover thermostat and barostat were used to maintain the temperature and pressure in the system. The temperature in the system is rescaled periodically by modifying the velocities of each atom in the system according to the following relation:

$$\frac{1}{2}mv^2 = \frac{3}{2}NkT \qquad 3.1$$

Where m is the mass of each atom, v is the velocity, N is the number of atoms in the system, k is the Boltzmann constant, and T is the temperature. The pressure in each direction is controlled through the following relation:

$$P_{ij} = \frac{\sum_k^N m_k v_{ki} v_{kj}}{V} + \frac{\sum_k^N r_{ik} f_{jk}}{V} \quad 3.2$$

Where the first term uses specific terms from the kinetic energy tensor and the second term uses components of the virial tensor. In this equation, the terms i, j, and k equate to x, y, and z. In addition to the inputs listed above, an interatomic potential describing the interaction between atoms is necessary to complete the MD simulation. The potentials used in this work are described in the next section.

MD was used in this work to determine the virtual mechanical response to applied strain. The output from the software includes the deformed atom positions, the potential energy, and the stress on each atom. By considering the total stress of the sample (calculated as the sum of the stress of each atom in the system) as a function of strain, standard stress-strain curves can be developed for each simulation run. From the stress-strain diagram, the mechanical properties of the simulated system can be obtained, including quantities such as the yield and flow stress and the elastic modulus. Performing simulations at various strain rates and temperatures allows for the calculation of both strain rate sensitivities and the determination of Arrhenius behavior. Through these simple analysis techniques, the mechanical properties of simulated samples can be determined. Stress-strain curves were created for each virtual mechanical test in this work and combined with more complex analysis in order to detect deformation.

3.3 Interatomic potentials

Interatomic potentials are a method of defining the interactions between atoms in a simulated system. The first potentials, such as the Lennard-Jones potential, considered only the interactions of atom pairs, excluding the interactions between every atom in the sample. This technique is of limited accuracy in an N-body system with metallic bonding. The embedded atom method (EAM) interatomic potential is a many-body approach developed by Daw and Baskes [3] and is used to simulate the interaction between atoms in metals. The EAM potential model is an improvement on the Lennard-Jones mode because the EAM potentials incorporate a term that considers the effects of all atoms j on atom i.

Interatomic potentials describe how the potential energy of the system depends on the coordinates of all atoms. The total energy of the system in the EAM approach is written as

$$E_i = F_i \sum_{i \neq j} f_j(r_{ij}) + \frac{1}{2} \sum_{i \neq j} \varphi_{ij}(r_{ij}) \qquad 3.3$$

Where F is the embedding function that considers the contribution to the electron density at atom i from all atoms j, and φ is the pair potential. To reduce the computational load, the interaction energies are only calculated when atom separation radii are below a specific cutoff radius; beyond the cutoff radius the interaction energy is considered to be equal to zero.

When developing an EAM potential, the potential function is fit to both empirical and experimental parameters. These parameters include the lattice parameter (a_0), the cohesive energy (E_0), the vacancy formation energy (E_v^f), elastic constants (c11, c12, c44), stacking fault energy (γ_{SF} and γ_{USF}), and any other parameters that fall within the scope of the author's investigation.

The limitations of EAM potentials arise from the nature of metallic bonding. EAM potentials most accurately represent the behavior of fcc systems. EAM potentials have limited effectiveness

when simulating bcc metals due to both the orbital hybridization and angular nature of some bcc bonds. Covalent bonds are not well predicted with EAM potentials. Additional potential types have been developed to address these types of bonds, including the Tersoff [4] and Stillinger-Weber [5] potentials.

3.3.1 Empirical interatomic potentials used in this work

This work uses five model materials. These are aluminum, nickel, copper, palladium, and tantalum. The interatomic potentials used for each metal are discussed in detail below. The materials selected for this work have a wide range of lattice parameters, cohesive energies, stacking fault energies, and unstable stacking fault energies. This range will make the correlations between atomistic parameters and deformation behavior easier to identify by highlighting the differences in behavior at high and low values of each parameter.

3.3.1.1 EAM potentials for aluminum and nickel

In this work, the interatomic potentials of Mishin et al [6] and Voter and Chen [7] are used to describe the deformation of aluminum and nickel. To differentiate between the two nickel potentials and two aluminum potentials, the notations Al1 and Ni1 shall refer to the potentials developed by Mishin et al., while Al2 and Ni2 shall refer to those developed by Voter and Chen. As shown in Table 1, The Mishin et al. potentials more closely match the values obtained through ab initio techniques, indicating that they should predict behavior that is more representative of experimental deformation. In this work, we use both the Mishin et al. and Voter and Chen potentials in order to more fully explore the effect of the γ_{SF} and γ_{USF} energies on deformation.

Table 3: Fitting parameters and ab initio data for the Mishin et al. and Voter and Chen interatomic potentials for aluminum and nickel. All data from [6] except where otherwise noted.

	ab initio	Al1	Al2	*ab initio*	Ni1	Ni2
a_0 (nm)	0.405	0.405	0.405	0.352	0.352	0.352
E_0 (eV/atom)	-3.36	-3.36	-3.36	-4.45	-4.45	-4.45
B (10^{11} Pa)	0.79	0.79	0.79	1.81	1.81	1.81
c11 (10^{11} Pa)	1.14	1.14	1.07	2.47	2.47	2.44
c12 (10^{11} Pa)	0.619	0.616	0.652	1.47	1.48	1.49
c44 (10^{11} Pa)	0.316	0.316	0.322	1.25	1.25	1.26
E_v^f (eV)	0.68	0.68	0.63	1.60	1.60	1.56
γ_{SF} (mJ/m^2)	166, 120-144	146	76	125	125	58
γ_{USF} (mJ/m^2)	168-180 [8-11]	168	93	278-316 [9, 12]	366	225

3.3.1.2 EAM potentials for copper

The EAM potential of Mishin et al. [13] for copper was selected for this work due to the excellent agreement between the predicted atomistic parameters and *ab initio* calculations. Mishin et al. used a total of 23 fitting parameters, with a goal of making the potential as accurate as possible. The experimental parameters include a_0 , E_0, B, the elastic constants c_{ij} , the phonon frequencies $\nu_{L(X)}$ and $\nu_{T(X)}$ at the zone-boundary point X, the relaxed vacancy formation (E_f) and migration (E_m) energies, and the intrinsic stacking fault energy. The Rose equation of state [14] was used to ensure that the structural energy predicted by the potential was correct.

Table 2: Fitting parameters and ab initio data for the Mishin et al. copper interatomic potential. All data from [13] except where otherwise noted.

	ab initio	Cu
a_0 (nm)	0.3615	0.3615
E_0 (eV/atom)	-3.54	-3.54
B (10^{11} Pa)	1.383	1.383
c_{11} (10^{11} Pa)	1.700	1.699
c_{12} (10^{11} Pa)	1.225	1.226
c_{44} (10^{11} Pa)	0.758	0.762
E_v^f (eV)	1.27	1.272
γ_{SF} (mJ/m^2)	45	44.4
γ_{USF} (mJ/m^2)	164-180 [9, 11]	158

3.3.1.3 EAM potential for palladium

The EAM potential developed to represent palladium used in this work is by Foiles and Hoyt [15]. This potential was specifically developed to more accurately represent the stable and unstable stacking fault energies in palladium, and thus produce more accurate deformation behavior in tensile deformation simulations. The fitting parameters used by Foiles and Hoyt include a_0, E_0, the vacancy formation energy (E_f), the elastic constants c_{ij}, the stable stacking fault energy, the surface energy, and the Rose equation of state.

Table 3: Fitting parameters and ab initio data for Foiles and Hoyt palladium interatomic potential. All data from [15] except where otherwise noted.

	Desired	Pd
a_0 (nm)	0.389	0.389
E_0 (eV/atom)	-3.91	-3.91
c11 (10^{11} Pa)	2.341	2.392
c12 (10^{11} Pa)	1.76	1.735
c44 (10^{11} Pa)	0.712	0.656
E_v^f (eV)	1.54	1.58
γ_{SF} (mJ/m^2)	188	187
γ_{USF} (mJ/m^2)	260-439 [10, 16]	210

3.3.1.4 EAM potential for tantalum

The EAM potential of Li et al. [17] for tantalum was selected for this work due to its suitability for simulations at the temperatures and strain rates chosen for this work. This EAM potential does not address the angular components of bcc metallic bonding, including the orbital hybridization known to occur in tantalum. Potentials that account for the angular bonding in tantalum should, in theory, more accurately represent the deformation behavior of tantalum under uniaxial tension. An angular dependent potential (ADP) for tantalum has recently been developed by Mishin et al. [18], however initial testing showed that the ADP potential was too computationally expensive to be used in this work.

Li et al. used a force-matching method when constructing this potential that included a wide range of fitting parameters. The experimental and ab initio data included in the fit include a_0, E_0,

B, the unrelaxed vacancy formation energy (E_f), and the elastic constants c_{ij}. In addition, the Rose equation of state [14] was used to ensure that the structural energy predicted by thermal expansion of the unit cell was accurately modeled.

Table 4: Fitting parameters and ab initio data for the Li tantalum interatomic potential. All data from [17] except where otherwise noted.

	Desired	Ta
a_0 (nm)	0.3303	0.3306
E_0 (eV/atom)	-8.089	-8.089
B (10^{11} Pa)	194.2	179.2
c_{11}-c_{12} (10^{11} Pa)	108.2	103.9
c44 (10^{11} Pa)	87.4	86.5
E_v^f (eV)	1.54	1.58

3.4 Visualization and analysis techniques

The post-processing techniques used in this work are the Dislocation Extraction Algorithm (DXA) by Alexander Stukowski [19] and the slip vector technique written by Garett Tucker and Jon Zimmerman [20, 21].

DXA is an exceptionally powerful tool for materials research. DXA analyzes the bond lengths between pairs of atoms in the system, looking for bonds that are indicative of lattice disruption. When atypical bond lengths are found, the system attempts to find a path through the system with segments that consist of only these atypical bond lengths. When such a path is found, the system will connect the points of the path, indicating the specific limits of the disrupted lattice.

The region thus marked is the dislocation line. It is then smoothed and identified with a Burger's vector. In this way, DXA detects dislocations within the sample. The same process is used to identify dislocations, stacking faults, and twins in any cubic system, regardless of the crystal structure. Identified microstructural features are exported in a format suitable for visualization in Paraview.

In contrast, the slip vector analysis uses relative displacement vectors to detect crystallographic slip and twin formation. This software package creates neighbor lists and initial positions for each atom from a reference configuration. Subsequent configurations from snapshots at higher strain use these neighbor lists to compare the relative locations of pairs of atoms. Differences in the location of each atom relative to its neighbors are analyzed at each strain increment. Identified differences have characteristic Burger's vectors of crystallographic slip or twinning, allowing for the identification the deformation mechanism responsible for plastic strain. The identified slip vectors are output in a format suitable for importing into Paraview for analysis. Visualization of the results is achieved through use of OVITO [22], Paraview, and Amira. Paraview is a program with the capability of displaying various features, including simple representation of atom positions, to dislocation lines, stacking faults, and twin surfaces. It uses vector information output by both the DXA and slip vector programs to graphically display the desired information. For atomistic analyses, color coding of the individual atoms by centro-symmetry parameter [1] allows identification of various lattice features; blue atoms indicate occupation of a perfect lattice position, while atoms adjacent to stacking faults or surfaces would appear green or red, respectively. Through the use of this technique, stacking faults and grain boundaries are easily identified, making dislocation emission and grain boundary sliding readily detected.

3.5 Summary of tools used in this work, with reference to the corresponding websites.

1. Basic molecular dynamics implementation: LAMMPS www.lammps.sandia.gov
2. Interatomic potential database repository: www.ctcms.nist.gov/potentials/
3. Dislocation Extraction Algorithm: dxa.ovito.org
4. Visualization packages:
    a. OVITO: www.ovito.org
    b. Amira: www.vsg3d.com/amira/
    c. Paraview: www.paraview.org

References

[1] C. L. Kelchner, S. J. Plimpton, and J. C. Hamilton, "Dislocation nucleation and defect structure during surface indentation," *Physical Review B,* vol. 58, pp. 11085-11088, Nov 1998.

[2] S. Plimpton, "Fast parallel algorithms for short-range molecular-dynamics," *Journal of Computational Physics,* vol. 117, pp. 1-19, Mar 1995.

[3] M. S. Daw, S. M. Foiles, and M. I. Baskes, "The embedded-atom method - a review of theory and applications," *Materials Science Reports,* vol. 9, pp. 251-310, Mar 1993.

[4] J. Tersoff, "New empirical-approach for the structure and energy of covalent systems," *Physical Review B,* vol. 37, pp. 6991-7000, Apr 1988.

[5] F. H. Stillinger and T. A. Weber, "Computer-simulation of local order in condensed phases of silicon," *Physical Review B,* vol. 31, pp. 5262-5271, 1985.

[6] Y. Mishin, D. Farkas, M. J. Mehl, and D. A. Papaconstantopoulos, "Interatomic potentials for monoatomic metals from experimental data and ab initio calculations," *Physical Review B,* vol. 59, pp. 3393-3407, Feb 1999.

[7] A. F. a. C. Voter, S. P., "High temperature ordered intermetallic alloys," *Materials Research Society Symposium Proceedings,* vol. 82, p. 175, 1987.

[8] F. Apostol and Y. Mishin, "Hydrogen effect on shearing and cleavage of Al: A first-principles study," *Physical Review B,* vol. 84, Sep 2011.

[9] C. Brandl, P. M. Derlet, and H. Van Swygenhoven, "General-stacking-fault energies in highly strained metallic environments: Ab initio calculations," *Physical Review B,* vol. 76, Aug 2007.

[10] J. Hartford, B. von Sydow, G. Wahnstrom, and B. I. Lundqvist, "Peierls barriers and stresses for edge dislocations in Pd and Al calculated from first principles," *Physical Review B,* vol. 58, pp. 2487-2496, Aug 1998.

[11] M. Jahnatek, J. Hafner, and M. Krajci, "Shear deformation, ideal strength, and stacking fault formation of fcc metals: A density-functional study of Al and Cu," *Physical Review B,* vol. 79, Jun 2009.

[12] C. A. Becker, F. Tavazza, and L. E. Levine, "Implications of the choice of interatomic potential on calculated planar faults and surface properties in nickel," *Philosophical Magazine,* vol. 91, pp. 3578-3597, 2011.

[13] Y. Mishin, M. J. Mehl, D. A. Papaconstantopoulos, A. F. Voter, and J. D. Kress, "Structural stability and lattice defects in copper: Ab initio, tight-binding, and embedded-atom calculations," *Physical Review B,* vol. 63, Jun 2001.

[14] J. H. Rose, J. R. Smith, F. Guinea, and J. Ferrante, "Universal features of the equation of state of metals," *Physical Review B,* vol. 29, pp. 2963-2969, 1984.

[15] S. M. Foiles and J. J. Hoyt. (2001, Computer Simulation of Bubble Growth in Metals Due to He. *Sandia Report SAND2001-0661*.

[16] M. J. Mehl, D. A. Papaconstantopoulos, N. Kioussis, and M. Herbranson, "Tight-binding study of stacking fault energies and the Rice criterion of ductility in the fcc metals," *Physical Review B,* vol. 61, pp. 4894-4897, Feb 2000.

[17] Y. H. Li, D. J. Siegel, J. B. Adams, and X. Y. Liu, "Embedded-atom-method tantalum potential developed by the force-matching method," *Physical Review B,* vol. 67, p. 8, Mar 2003.

[18] Y. Mishin and A. Y. Lozovoi, "Angular-dependent interatomic potential for tantalum," *Acta Materialia,* vol. 54, pp. 5013-5026, Nov 2006.

[19] A. Stukowski and K. Albe, "Extracting dislocations and non-dislocation crystal defects from atomistic simulation data," *Modelling and Simulation in Materials Science and Engineering,* vol. 18, Dec 2010.

[20] G. J. Tucker, S. Tiwari, J. A. Zimmerman, and D. L. McDowell, "Investigating the deformation of nanocrystalline copper with microscale kinematic metrics and molecular dynamics," *Journal of the Mechanics and Physics of Solids,* vol. 60, pp. 471-486, Mar 2012.

[21] G. J. Tucker, J. A. Zimmerman, and D. L. McDowell, "Continuum metrics for deformation and microrotation from atomistic simulations: Application to grain boundaries," *International Journal of Engineering Science,* vol. 49, pp. 1424-1434, Dec 2011.

[22] A. Stukowski, "Visualization and analysis of atomistic simulation data with OVITO-the Open Visualization Tool," *Modelling and Simulation in Materials Science and Engineering,* vol. 18, Jan 2010.

4 Relationship between localized strain and irradiation assisted stress corrosion cracking in an austenitic alloy

M.D. McMurtrey[a], G.S. Was[a], L. Patrick[b], D. Farkas[b]

[a]Department of Nuclear Engineering and Radiological Sciences, University of Michigan, Ann Arbor, MI 48109, United States

[b]Department of Materials Science and Engineering, Virginia Tech, Blacksburg, VA 24061, United States

This chapter has been published in Materials Science and Engineering a-Structural Materials Properties Microstructure and Processing, 2011, Volume 528, Issue 10-11, pages 3730-3740. It is used here with permission.

4.1 Abstract

Irradiation assisted stress corrosion cracking may be linked to the local slip behavior near grain boundaries that exhibit high susceptibility to cracking. Fe-13Cr-15Ni austenitic steel was irradiated with 2 MeV protons at 360°C to 5 dpa and strained in 288°C simulated BWR conditions. Clusters of grains from the experiment were created in an atomistic simulation and then virtually strained using molecular dynamic simulation techniques. Cracking and grain orientation data were characterized in both the experiment and the simulation. Random high angle boundaries with high surface trace angles with respect to the tensile direction were found to be the most susceptible to cracking. Grain boundary cracking susceptibility was also found to correlate strongly with slip continuity, indicating that the strain accommodation at the boundary is related to cracking resistance. Higher cracking susceptibility was also found at grain boundaries adjacent to grains with low Schmid factor or high Taylor factor. The basic trends reported here are supported by both the experiments and the simulations. Keywords: austenite; intergranular cracking; localized deformation; strain accommodation

4.2 Introduction

Austenitic steels are widely used for structural components in current light water reactors (LWR), and are candidates for structural components in some Generation IV reactors. In high temperature water they suffer from susceptibility to irradiation assisted intergranular stress corrosion cracking (IASCC). This is a potentially life-limiting problem for current LWRs. Several irradiation-induced changes have been proposed as likely contributors to the increased susceptibility to cracking such as radiation induced segregation (RIS), radiation hardening and changes to the deformation mode. Recent results [1-6] show that localized deformation correlates strongly to IASCC.

Irradiation causes austenitic steels to harden by forming defect clusters that act as obstacles to dislocation motion under an applied stress. As dislocations move through the defects, they annihilate the defects, clearing paths for subsequent dislocations. Dislocations have been observed to annihilate stacking fault tetrahedra in in-situ TEM straining, which has been coupled with molecular dynamics models to explain the process by which dislocations clear defects to form channels [7-8].

Channels appear to originate and terminate at grain boundaries or at free surfaces where they create steps with heights proportional to the total strain in the channel. Channel strains can approach 100% for total sample strains of only a few percent [9]. Localized strain associated with the dislocation channels cannot always be accommodated by the grain boundaries through dislocation emission, and can lead to grain boundary deformation and cracking. Jiao and Was [1] recently showed that among the many parameters that could affect IASCC, intergranular cracking in irradiated stainless alloys correlates best with the degree of localized deformation as measured by the surface step height (Figure 1). It is likely that the ability of the grain boundary

to accommodate localized deformation is key to the cracking mechanism, though this connection is not currently well understood. Thus, measurements of the response of grain boundaries to dislocations in intersecting channels during straining in high temperature water are critical to understanding IASCC.

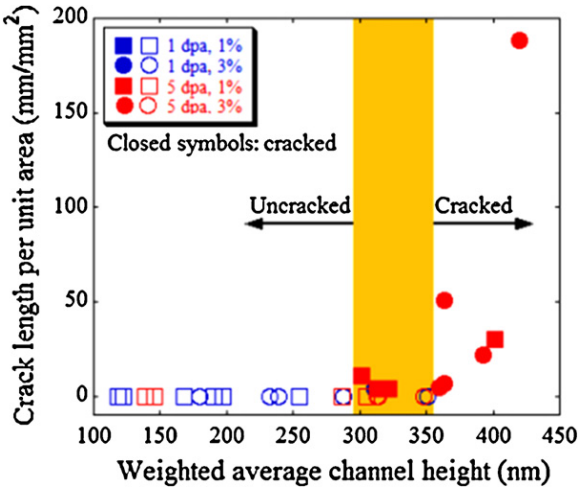

Figure 1 Correlation between IG cracking susceptibility and weighted average dislocation channel height, suggesting a strong connection between the degree of localized deformation and IASCC. [1]
Figure by McMurtrey and Was.

Atomistic simulations have been widely used to study the mechanical response of metallic materials, in particular, the structure and response of grain boundaries and dislocations and their role in fracture [10- 12]. Simulation accuracy is dependent upon the interatomic potentials of the materials being studied, particularly for the emission of dislocations from grain boundaries [13-17]. There have also been significant advances in the development of more accurate interatomic potentials [18]. The introduction of parallel large scale processing [19] and the accompanying increase in computer power has made it possible to conduct virtual mechanical response tests of realistic polycrystalline structures. Much progress has been made using these techniques to study crystalline nanomaterials properties [20-21]. Changes in the mechanical properties in polycrystalline materials are controlled by the atomistic nature of defects, including point defects (vacancies and interstitials), dislocation loops, and grain boundaries [22]. Detailed knowledge of

the mechanisms of interaction between these dislocations and grain boundaries is particularly important, as is the role of grain boundaries as a source of dislocations in metallic materials [23-24]. This study combines experimental observations with atomistic molecular dynamics simulations to understand the relationship between localized strain at the grain boundary and IASCC.

4.3 Experiment

Tensile bars were fabricated from a high purity austenitic steel of base composition Fe-13Cr-15Ni, which was known to exhibit moderate IASCC [4]. The composition is listed in Table 1.

Table 1: Composition of the austenitic stainless steel used in this work

Alloy	Cr	Ni	C	Mn	Si	P
13Cr15Ni	13.4	15.0	0.016	1.03	0.1	<0.01

Rectangular areas were "marked" in the gage section by using indents as reference points so that characterized areas could be relocated. The crystal orientation in each rectangular section was characterized using electron backscatter diffraction in the scanning electron microscope (SEM) [25-26]. From the orientation information, grain boundary misorientation, Schmid and Taylor factors were determined. Boundary misorientation is a measure of the difference in crystallographic orientation of the two grains adjacent to the boundary. The Schmid and Taylor factors describe the deformation behavior of the grains. Schmid factor describes individual slip systems, while Taylor factor models deformation assuming that five slip systems are active. A grain with a high Schmid factor deforms at lower applied stress, and a grain with low Taylor factor undergoes less shear deformation for a fixed tensile strain. Schmid and Taylor factor

values were divided into three bins, low (L), medium (M), and high (H). The bin limits, Table 2, were created by specifying that each bin have the same number of grains. The boundaries were then characterized by the pair of Schmid and Taylor factors of the adjacent grains that form the boundary (e.g. a L grain adjacent to a M grain form a LM boundary).

Table 2: Upper limits for Taylor and Schmid factor bins.

	Taylor Factor		Schmid Factor	
	Max bin value	% of grains[a]	Max bin value	% of grains[a]
L	2.89	33.3	0.44	34.6
M	3.32	33.1	0.47	33.8
H	3.67	33.6	0.5	31.6

Irradiations were performed using protons accelerated by a tandem particle accelerator to an energy of 2 MeV. Samples were irradiated at 360°C to a dose of 5 dpa at a damage rate of approximately 10-5 dpa/s. The irradiation damage peaked at approximately 20 μm below the sample surface, Figure 2. Dose calculations were performed at a depth of about 12 μm below the surface where the damage profile was flat, away from the damage peak. The temperature was monitored by a two-dimensional thermal imager that tracked surface temperatures of the samples at high spatial resolution throughout the irradiation.

After irradiation, the tensile bar was strained in a simulated boiling water reactor (BWR) normal water chemistry (NWC) environment. Water temperature was maintained at 288°C with a dissolved oxygen concentration of approximately 2 ppm and a conductivity of less than 0.1 μS/cm. The strain rate for the tests was approximately 3.5 x 10-7 s-1. The tensile bar was strained to 2% plastic strain in the irradiated region, at which point it was removed and the cracking behavior was characterized using an SEM to identify cracked boundaries. The oxide

layer was sufficiently thin so that it did not obscure the visibility of cracks in the metal. After characterization, the bar was strained a second strain increment to a total plastic strain of 6%. Following the second strain increment, the oxide layer was stripped off the sample using a chemical stripping process that consisted of two solutions: sodium hydroxide and potassium permanganate, and a solution of ammonium oxalate. The cracked boundaries were re-located and characterized in a SEM. Examples of cracks are shown in Figure 3.

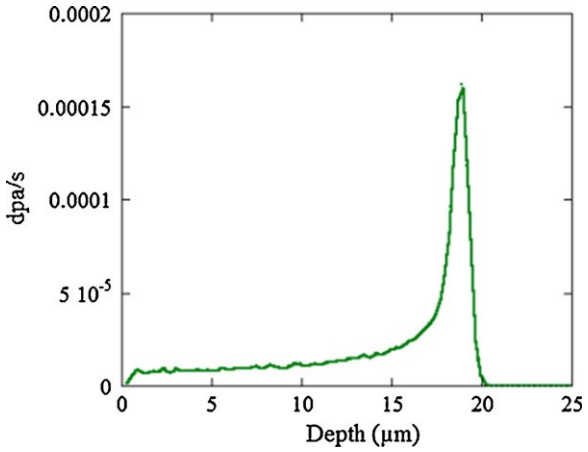

Figure 2 Damage profile for 2 MeV protons in austenitic steel. Calculations were performed using the SRIM program. [36]
Figure by McMurtrey and Was.

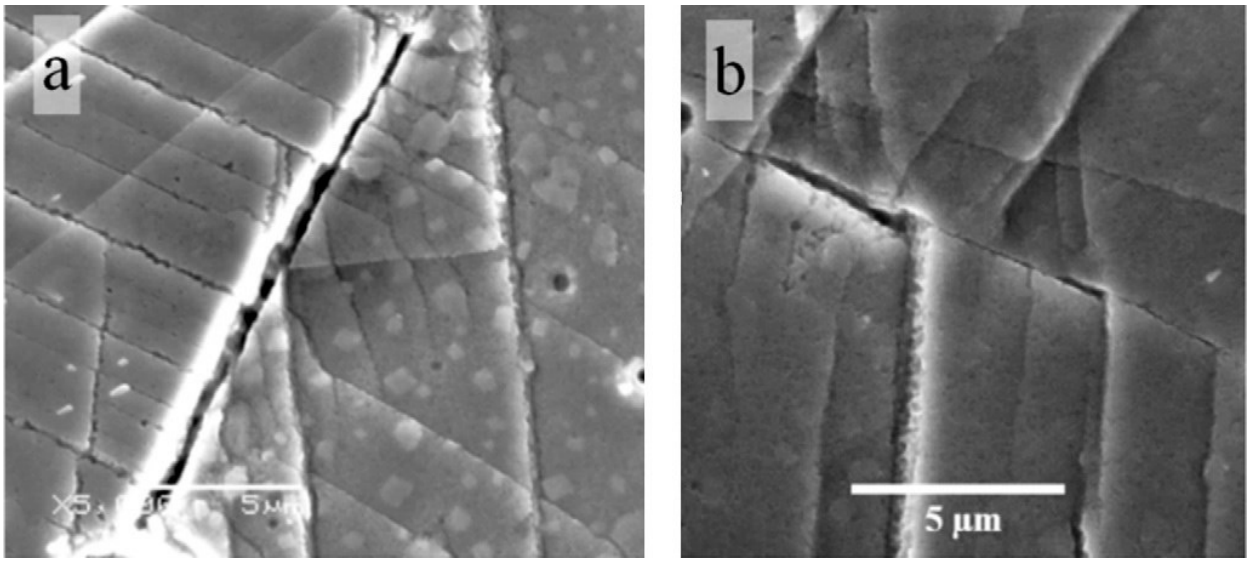

Figure 3 Examples of two types of cracking found in the Fe-13Cr15Ni alloy after 6% strain in BWR simulated water and the chemical oxide strip, (a) long cracks that propagated along the boundary and (b) small cracks localized near grain boundary-dislocation channel intersections.
Figure by McMurtrey and Was.

The orientations of the grains adjacent to a boundary were used to determine Schmid and Taylor factors, and to characterize the cracking behavior in terms of grain boundary type. The location of the crack on the boundary (mid boundary or at a triple junction) and the angle of the trace of the crack with respect to the tensile axis were measured directly from the SEM images. Certain grain boundary characteristics are unevenly distributed and so the data was normalized so as avoid unfairly weighting the data towards characteristics that were more strongly represented in the sample. Examples of this include the boundary type and Schmid factor. The majority of the boundaries in the sample are either random high angle boundaries (RHABs) or coincident site lattice boundaries (CSL), of which most are Σ3. There are few low angle boundaries (LAB). In these results, LABs and CSL boundaries will be grouped together as special boundaries. Though the Schmid factor for the most favorably oriented slip system was measured to be as low as 0.27, the vast majority of the grains had a Schmid factor greater than 0.45.

There is a statistical error associated with all of the collected data. This error decreases with an increasing amount of data collected, however, there is a limit to the amount of cracking data that it is feasible to collect, so it is important to calculate and include the statistical error with all cracking data. For binomial distributions, the standard deviation (σ) may be used to determine the amount of error in the measurements. Standard deviations for binomial distributions are calculated using eqn. (1),

$$\sigma = \frac{[x\times(1-\frac{x}{n})]^{1/2}}{n} \quad (1)$$

where x is the number of positive cases (e.g. cracks of a certain boundary type) and n is the total number cases examined (e.g. total number of cracks examined).

Slip continuity across grain boundaries was also characterized in the SEM. Dislocation channels that intersect the sample surface create ledges that are visible in the SEM. When these channels

appear to be continuous across a boundary (allowing for a change in angle at the boundary) slip is classified as continuous. If channels intersect the boundary on one side, but are not observed to "emerge" from the boundary in the adjacent grain, slip is classified as discontinuous. An example of distinguishable continuous and discontinuous slip at a boundary is shown in Figure 4. If it is possible to determine the continuity of slip across a boundary then the boundary is considered distinguishable and used in the data analysis. The number of slip systems activated in a random sampling of grains was also determined by examining the grains in the SEM and using the visible dislocation channels to identify the number of active slip systems.

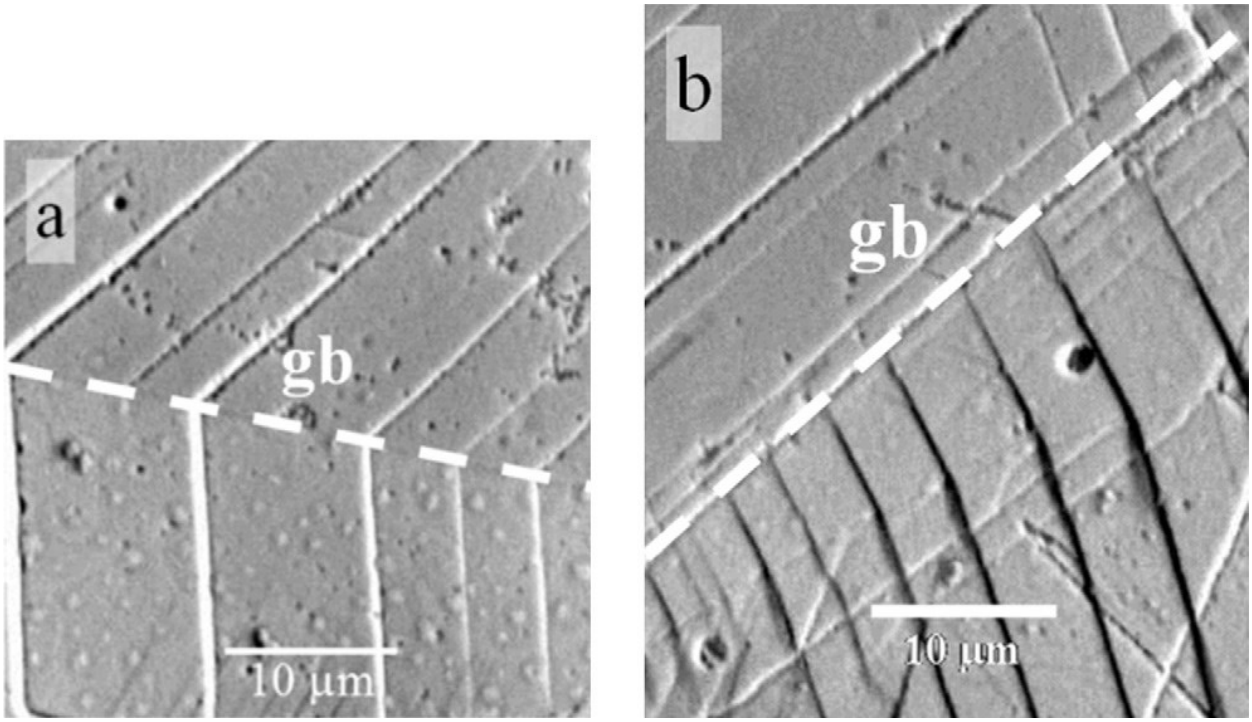

Figure 4. Examples of boundaries with (a) continuous slip and (b) discontinuous slip after 6% strain in BWR conditions and following the oxide strip. Figure by McMurtrey and Was.

4.4 Simulation

Virtual tensile tests were performed using LAMMPS [19] (Large-scale Atomic/Molecular Massively Parallel Simulator) software and System X at Virginia Tech. The samples used in this

simulation were generated using a Voronoi construction technique by specifying the grain centers and Euler angle data obtained from the OIM imaging. The samples were designed to mimic 4 clusters of grains chosen at random from the samples used in the experiments. The simulated grain clusters are shown in Figure 5. Each sample contained 5 to 7 grains and the grain size was approximately 40nm to avoid grain-boundary sliding as a deformation mechanism. The small grain size does not allow dislocation multiplication through Frank-Read sources mid-grain. While much smaller than the grain size of the experimental samples, the grain size of 40 nm is large enough to avoid most of the particular effects of the nano-scale, as reported in studies of the mechanical behavior of nanocrystalline materials [20] These small grain sizes allow for multiple grains to be atomistically modeled, while still avoiding many of the large effects of having nano-sized grains. The samples are fully periodic in the horizontal and vertical directions, with the direction orthogonal to the other two left as a free surface. The samples studied in this work had a total of 70 grain boundaries.

After sample generation, the boundary structure of each sample was relaxed for 50 picoseconds while being raised to 700K, and then cooled back to 300K. The interatomic potential used for both the relaxation and simulation was the nickel potential of Mishin et al [18]. The LAMMPS implementation uses a Nose-Hoover thermostat and barostat for temperature and pressure control. Once relaxation was complete, the samples are digitally deformed at 300K to induce dislocation emission from grain boundaries. The periodicity in the direction of tension allows control of the degree of deformation. The pressure is maintained at zero in the direction perpendicular to the applied stress so that the material reacts normally. Simulated strainings were also repeated at a higher temperature of 700 K and basic trends were found to be the same. The

majority of the simulations were run at the lower 300 K temperature and these are the results used in this analysis.

The samples were strained separately in both the horizontal and vertical directions up to 15% to observe dislocation emission and crack formation. This is a greater strain level than the 6% used in the experiments. The strain rate was $3x10^{8}s^{-1}$, which was the lowest possible given the available computing power. The high strain rate used in this work illustrates one of the main limitations of simulated tension tests, making it difficult to observe thermally-activated processes during the deformation. Another limitation of this technique is the small sample sizes that resulted in small numbers of grain boundaries available for study.

In order to analyze the results and compare with experiments, several visualization techniques were used. Results of this simulation work are visualized by color-coding the centro-symmetry parameter [27] using OVITO visualization software [28]. By showing only the atoms with a centro-symmetry number greater than 3, only the grain boundaries, stacking faults, and dislocation cores are shown. This technique clearly differentiates between atoms in perfect lattice conditions and atoms that have a disturbed crystal structure, such as those in grain boundaries and stacking faults.

A technique was developed to visualize strain localization by creating heterogeneous displacement maps. The map was calculated by dividing the atomic coordinates of each atom by the average deformation factor of the sample. The difference between the adjusted coordinates and the initial coordinates is the heterogeneous displacement of the atom. The magnitude of the difference indicates the strain experienced by the atom beyond the strain experienced by the entire sample. This is the heterogeneous strain. Color coding the sample based on the magnitude of the differences shows the strain localization of the whole sample [29].

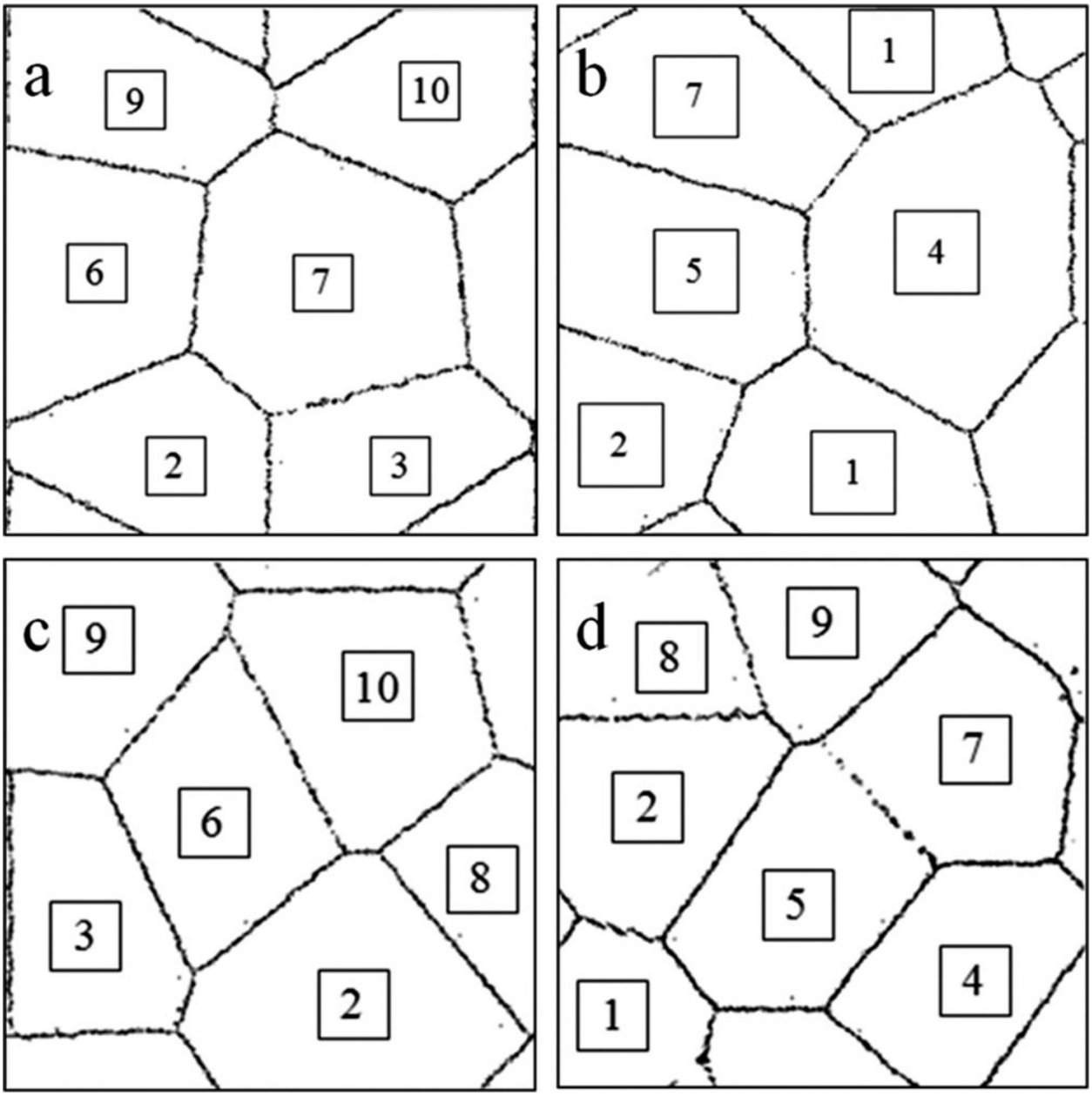

Figure 5 Simulation of fcc (nickel) samples showing periodicity in horizontal and vertical directions. (a) Cluster 13 (b) Cluster 36 (c) Cluster 42 (d) Cluster 70. Figure by author.

4.5 Results

4.5.1 Cracking behavior

4.5.1.1 Experiments

A total of 158 cracks were observed among approximately 260,000 grain boundaries characterized in the Fe-13Cr-15Ni sample after 6% total strain. Figure 6 shows the normalized fraction of the cracks for the different boundary types. The majority of the cracks at both strain increments were at RHABs. No LABs cracked, and only a few of the CSL boundaries were found to crack.

The more probable location for the cracks was found to be in the "mid-boundary" region between triple points, shown in Figure 7, irrespective of the strain level, though the distinction between locations was slightly greater after 6% strain.

The cracks tended to form on boundaries that made traces on the surface at angles greater than 70° to the tensile direction, as shown in Figure 8.

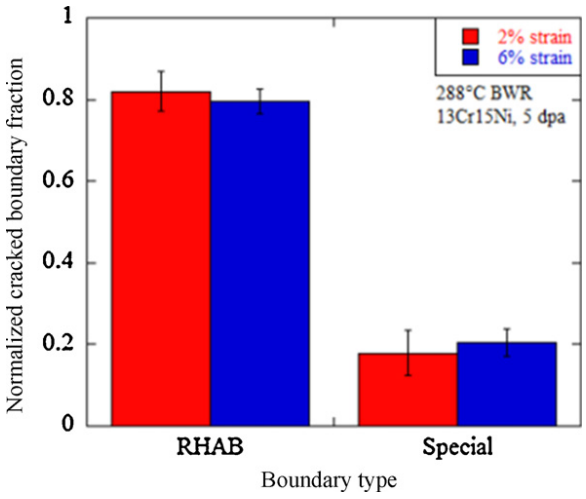

Figure 6 The fraction of cracked boundaries according to boundary type. The values have been normalized to account for the overall fraction of boundary types in the sample. In the simulations, all the cracks observed occurred in the RHABs. Figure by McMurtrey and Was.

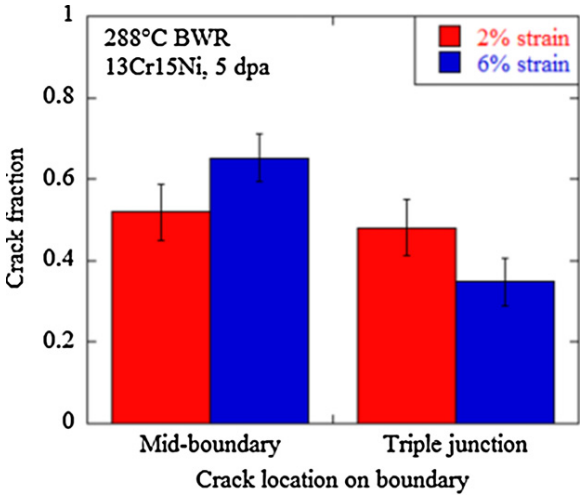

Figure 7 Fraction of cracks that appear "mid-boundary" between triple points, as compared to those that appear at the triple junction between three grains. Figure by McMurtrey and Was.

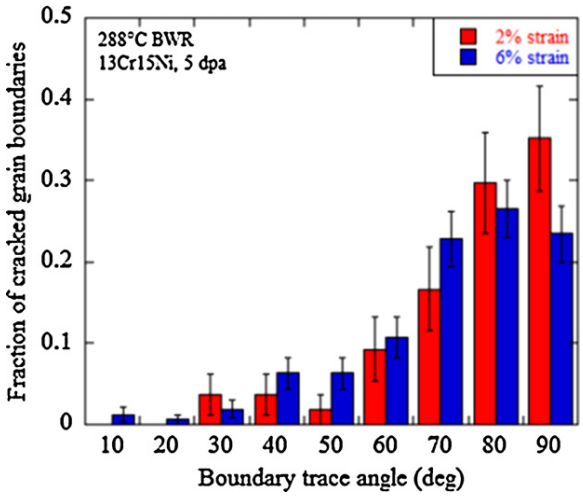

Figure 8 Fraction of grain boundaries that cracked as a function of the angle between the trace of the grain boundary on the sample surface and the tensile axis. Figure by McMurtrey and Was.

The angle dependence of cracking was strongest after 2% strain, but was still very evident after 6% strain. Schmid and Taylor factors both exhibited correlations with cracking frequency, shown in Figure 9, respectively. The higher Schmid factor bins demonstrate a trend towards lower cracking susceptibility. Cracking susceptibility is significantly decreased at boundaries for which at least one of the adjoining grains has a low Taylor factor. Taylor and Schmid factors are inversely related, so an inverse trend in cracking is expected. A grain with low Taylor factor is likely to have a high Schmid factor, and the boundaries surrounding it exhibit a high cracking resistance.

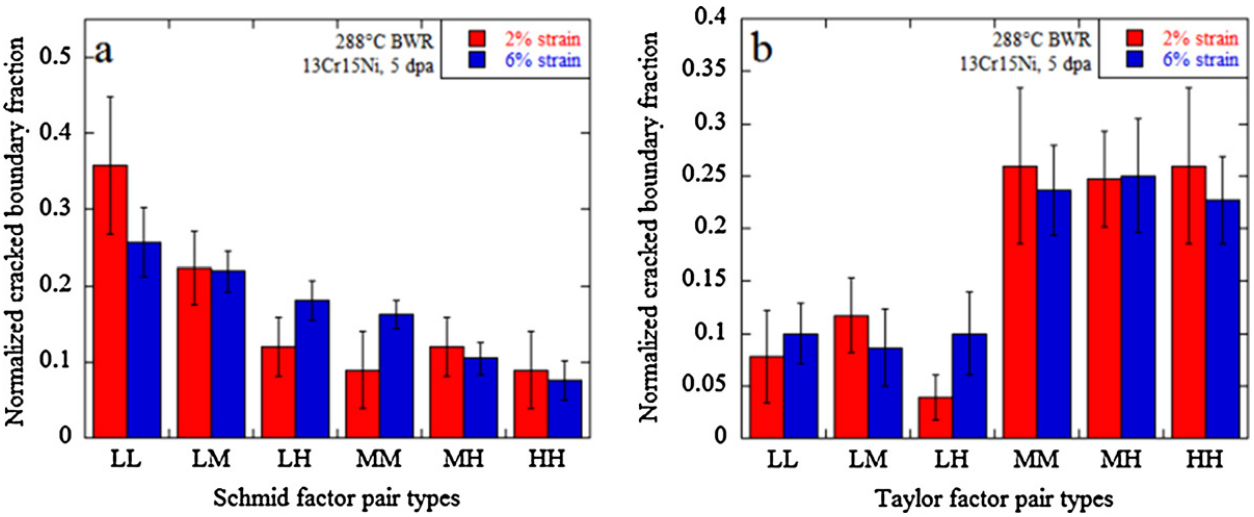

Figure 9 Fraction of grain boundaries that cracked as a function (a) Schmid factor pair types, and (b) Taylor factor pair types. Fractions at Schmid and Taylor factor pairs were normalized to account for the frequency of occurrence for each pair type in the sample. Figure by McMurtrey and Was.

4.5.1.2 Simulation:

Intergranular cracking was also observed in simulations. All cracked boundaries in the 4 clusters were RHABs, consistent with experimental results shown in Figure 6. The angle of the boundary with respect to the tensile axis showed that most of the cracks occurred in boundaries with angles greater than 50 degrees. The distribution is shown in Figure 10, which is very similar to the experimental results shown in Figure 8. Cracking occurred in 22 of the 70 grain boundaries studied, with 5 boundaries cracking at more than one location. A total of 30 cracks occurred during deformation, with 22 cracks initiating near triple junctions and the remaining 10 initiating mid-boundary. Figure 11 shows cracking in all samples strained in the horizontal direction to 15%.

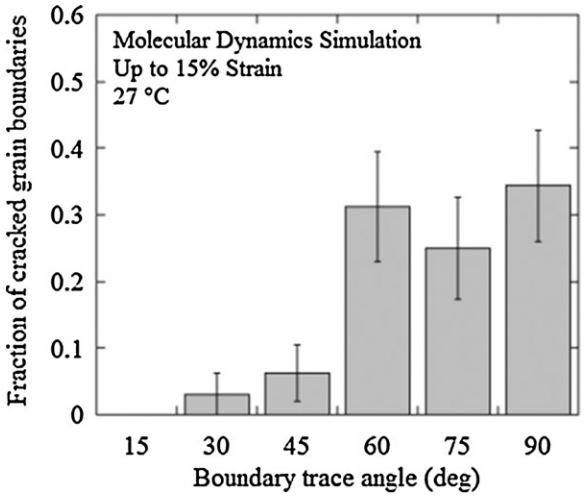

Figure 10 Fraction of simulated cracked boundaries as a function of the angle between that boundary and the tensile axis. These results are comparable to the experimental trends shown in Figure 8. Figure by author.

Schmid and Taylor factors for each grain were obtained during the OIM imaging of the samples used in the experiment. As the simulations were generated from these scans, the Schmid and Taylor factors for each simulated grain were gathered from that data. Schmid factors for the simulated grains ranged from 0.37 to 0.49 with most factors being above 0.4. The same bins used to divide Taylor and Schmid factors in the experiments (Table 2), were used in the model. Figure 12 shows the strain level at which a crack appeared vs. Taylor and Schmid factor pair types. A linear regression was performed on this data to determine the general trends which show that at higher Taylor Factors, (pair types MH and HH), cracking initiated at lower strain levels. The reverse was observed for the Schmid factor with cracking occurring preferentially at lower Schmid factors (pair types LL and LM). A statistical analysis of the regression shows that the trends may only be stated with a 60% confidence, due to the limited amount of data, and how the data is scattered. This does still suggest a trend, and these results are consistent with the experimental results as shown in Figure 9.

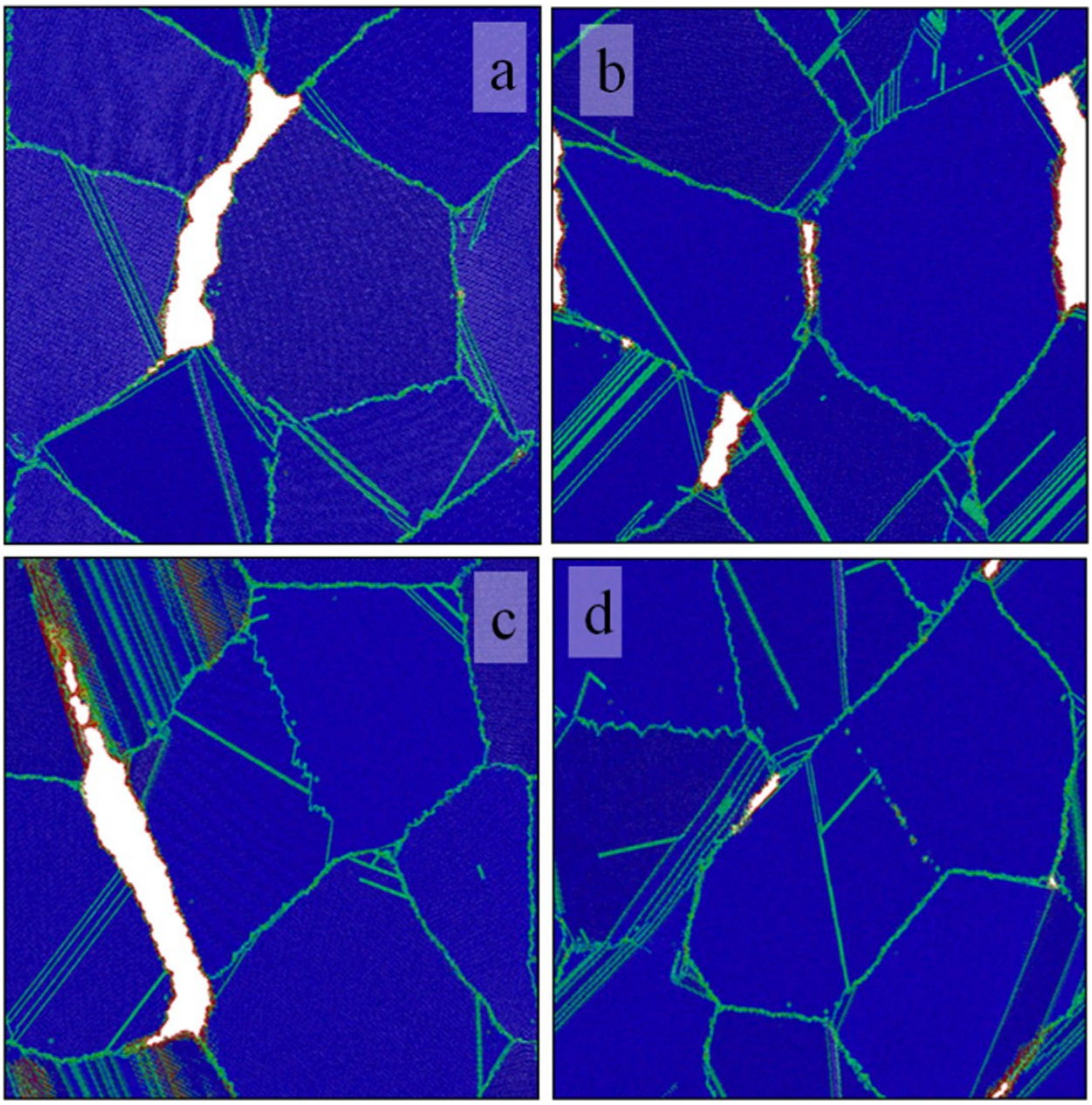

Figure 11 Examples of cracked boundaries (shown in white) in simulated fcc Ni samples at 15% strain in the horizontal direction. (a) Cluster 13, (b) Cluster 36, (c) Cluster 42, and (d) Cluster 70. Figure by author.

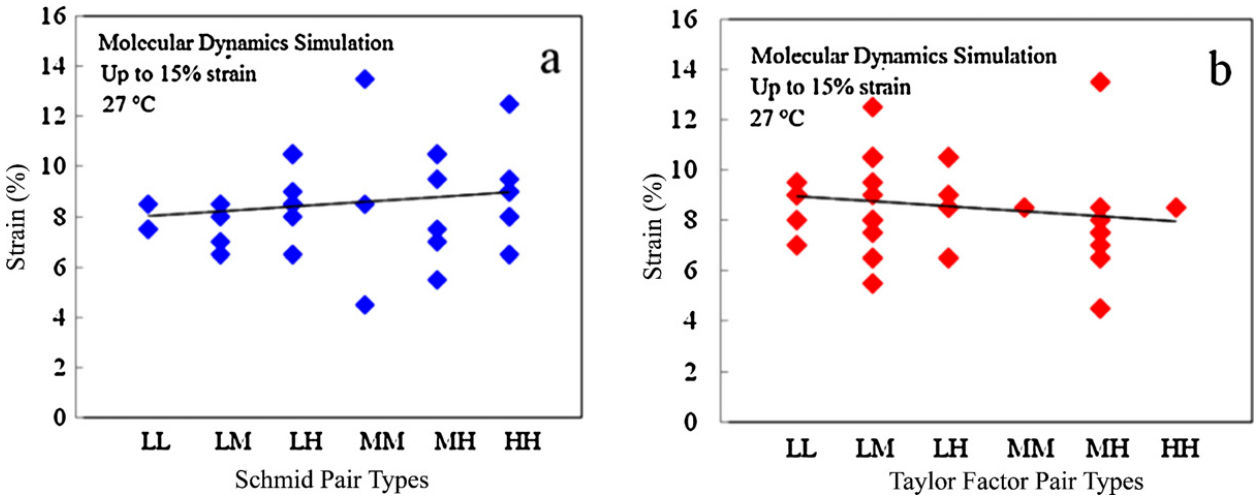

Figure 12 Strain at crack nucleation vs. (a) Schmid and (b) Taylor factor pair types, in simulated fcc (Ni) clusters. These results are consistent with the experimental trends shown in Figure 9. Figure by author.

4.5.2 Deformation

4.5.2.1 Experiments:

The ability of a boundary to accommodate strain is believed to be an important element in cracking susceptibility. A primary mechanism for accommodating strain from impinging dislocations is the transmission of dislocations into the adjacent grain. In these experiments, the continuation of a dislocation channel across a grain boundary is indicative of slip continuity and strain accommodation, where slip discontinuity represents a boundary that has not accommodated strain and must find another means to relieve the stress built up by the unaccommodated strain. Slip continuity was observed to vary with both boundary type and grain boundary trace inclination. Figure 13a shows that slip continuity across special boundaries was about 40% higher than across RHABs. Figure 13b shows that slip continuity was much stronger at boundary traces that made a low angle with respect to the tensile angle, which is opposite that of the cracking dependence.

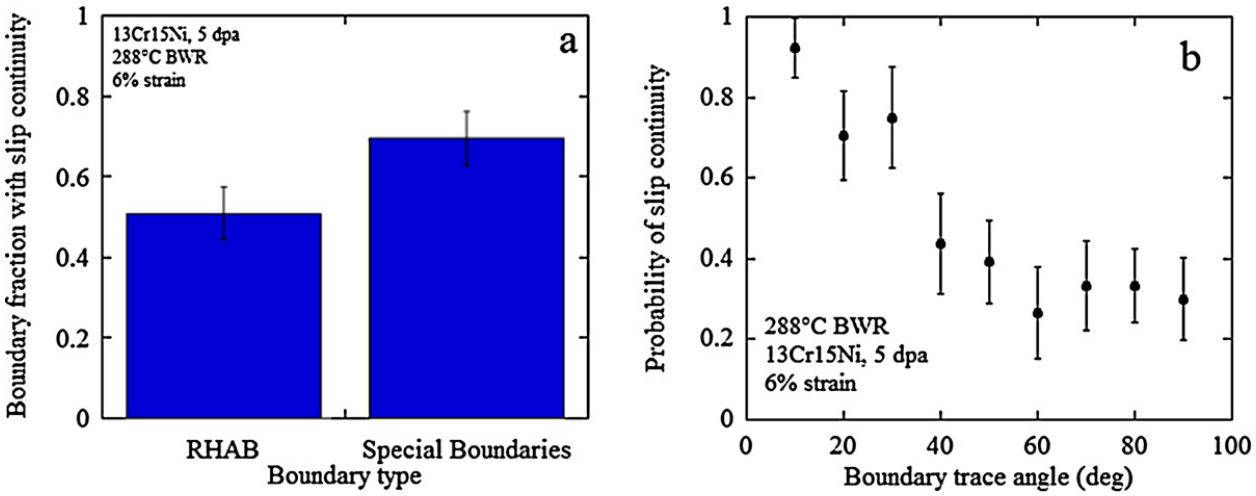

Figure 13 Fraction of boundaries exhibiting slip continuity after 6% plastic strain as a function of (a) boundary type, and (b) angle of grain boundary trace. Figure by McMurtrey and Was.

Another property that describes the deformation behavior of the grain is the number of slip systems that were activated during straining. Dislocation channels in the strained samples were examined to determine the number of slip systems that were active in a particular grain. Results were grouped by those with zero or one active slip systems, and those with more than one slip system active. Approximately half of the grains in the sample had one or no active slip systems, as shown in Figure 14a. Dividing the grains into the Schmid and Taylor factor bins, the number of active slip systems is shown in Figure 14b and c, respectively. The Schmid factor bins do not show much preference to activation of slip systems from one bin to another, but the low Taylor factor bin does tend to have multiple slip systems active.

4.5.2.2 Simulations:

The simulated samples were strained to 15% in the horizontal or vertical directions in separate deformation runs. Figure 15 shows the stress-strain curves for each of the 4 samples. The differences between the horizontal and vertical stress directions show that the grain boundaries respond differently to stress in the perpendicular direction. During the deformation of Cluster 36

in the vertical direction, the sample completely broke apart resulting in no additional strain after 10.3% strain.

In some boundaries, dislocations from one grain were absorbed by the grain boundary, while a corresponding dislocation is emitted from that boundary into the adjacent grain. Dislocation emission in these samples always originated from the grain boundaries and in the form of Shockley partials. Figure 16 shows an example of boundaries with and without slip continuity.

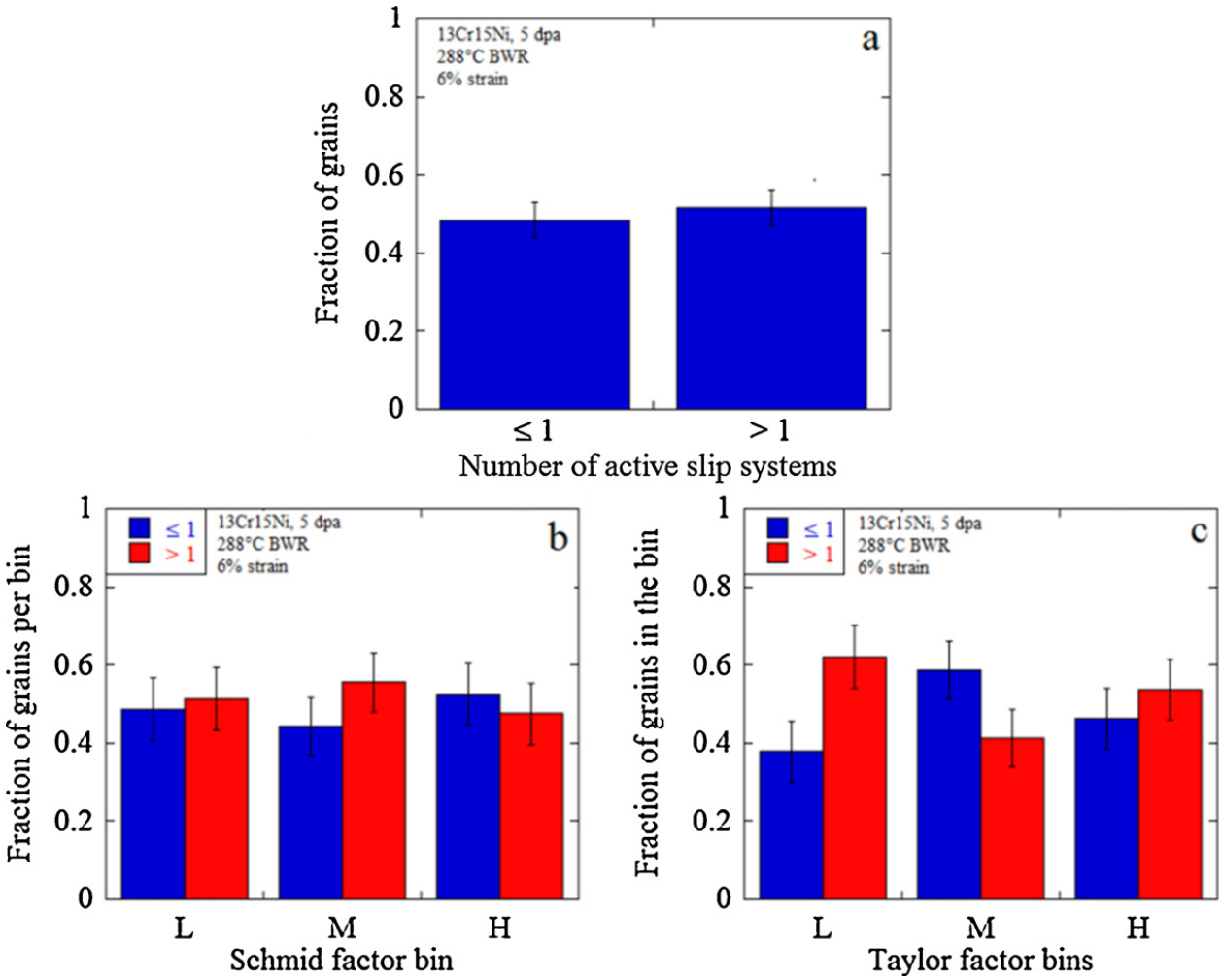

Figure 14 The fraction of grains (a) with one or no slip systems or with greater than one slip system, (b) as a function of Schmid factor, and (c) as a function of Taylor factor. Figure by McMurtrey and Was.

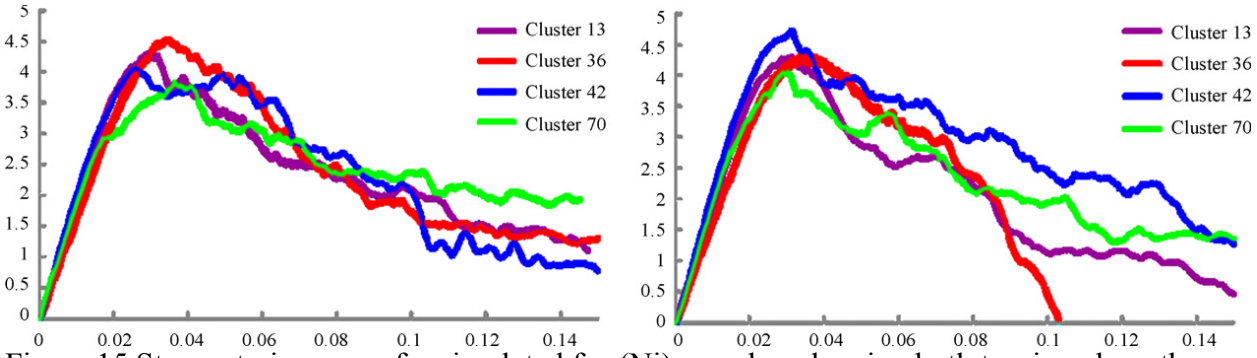

Figure 15 Stress-strain curves for simulated fcc (Ni) samples, showing both tension along the horizontal direction (a) and tension along the vertical direction (b).Figure by author.

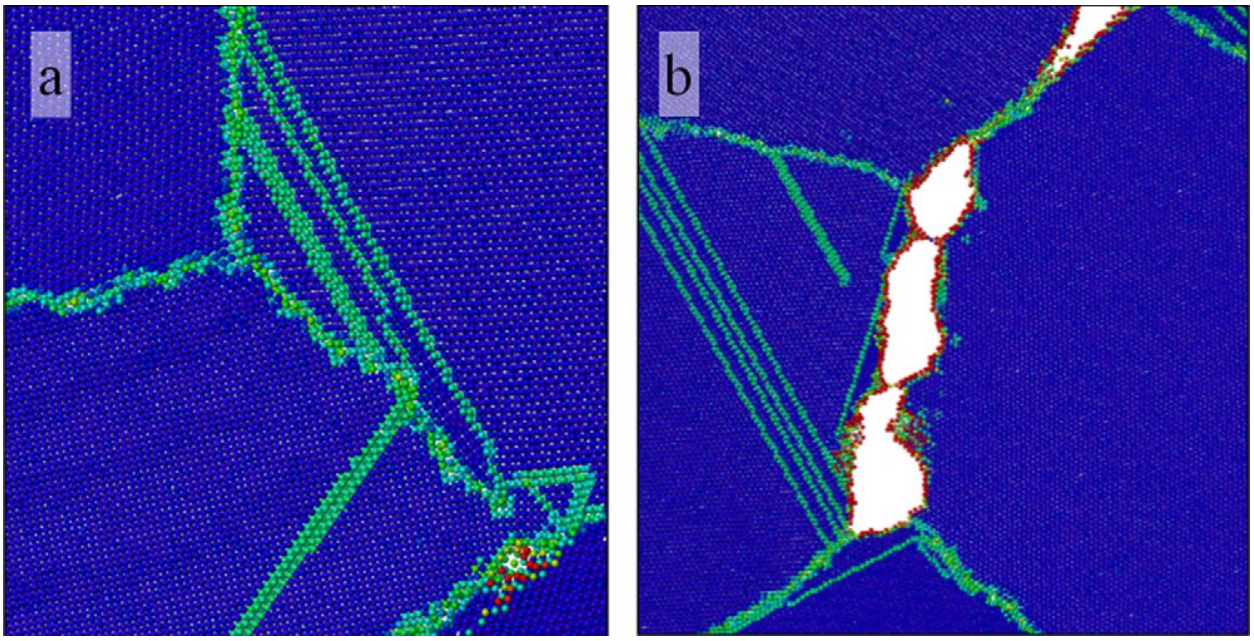

Figure 16 a) Continuous slip across grain boundary 36 in Cluster 13. b) Lack of slip continuity across boundary 67 contributed to cracking region. Figure by author.

Heterogeneous strain maps [29] created for each sample illustrate that strain localization occurred near crack initiation sites. The red indicates high strain relative to the overall strain, while blue indicates little strain relative to the overall strain. As an example, Figure 17 shows the strain localization in the sample created from Cluster 13 in grain boundary 67 at 6%, 7.5%, and 9% strain.

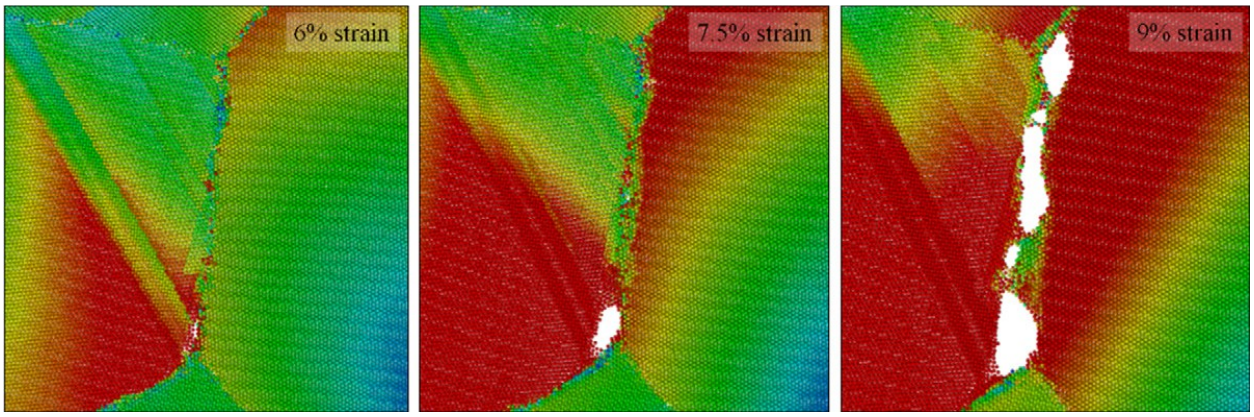

Figure 17 Grain boundary 67 in Cluster 13 at 6%, 7.5% and 9% strain showing strain localization around the boundary before and after crack initiation. Figure by author.

4.6 Discussion

Both experiment and simulation results showed that the type of boundary and the trace of the grain boundary angle with respect to the tensile direction strongly influence cracking behavior. It should be noted, however, that experiments were conducted in simulated BWR NWC and thus capture the combined effect of an irradiated microstructure and an aggressive environment. Irradiated samples strained in an inert environment under the same conditions do not exhibit IG cracking. Simulations are conducted in what could be considered to be an inert environment. Hence, cracking in these cases is indicative of the inherent weakness or susceptibility to decohesion than a true measure of the IASCC susceptibility of the boundary. The model also does not include compositional effects, as all of the atoms are modeled as identical atoms within an fcc crystal structure. Nevertheless, the propensity for cracking and the relation between local strain and cracking provide important insights into the processes that can lead to cracking in a more aggressive environment.

4.6.1 Dependence of cracking on boundary type and boundary inclination

A high cracking propensity of RHABs and of grain boundaries that are highly inclined to the tensile axis is exhibited in both sets of results. The high cracking susceptibility of RHABs is consistent with other intergranular corrosion studies of austenitic alloys [30-32]. Special boundaries have a high level of symmetry, smaller changes in atomic spacing from the normal lattice and less open volume. They also have significantly lower energy than RHABs [33]. The cusps in grain boundary energies at misorientation angles that coincide with special boundaries have been used to predict a higher cohesive strength in those boundaries, and a decreased susceptibility to cracking [33]. Results from this study show that RHABs do not transmit strain across the boundary as well as special boundaries (Figure 13a). The combination of a lower cohesive strength and a decreased probability of accommodating strain through slip continuity across the boundary may contribute to an increased cracking susceptibility in RHABs.

Grain boundaries inclined at high angles to the tensile axis will experience a high normal stress during straining. With a high fraction of cracks occurring at high angles, it is clear that the normal stress on the grain boundary is a factor in cracking susceptibility. West and Was [34] found that there was a critical normal stress for intergranular cracking to occur in irradiated materials. Boundaries perpendicular to the tensile stress direction would be the first to reach that critical normal stress. Within the boundaries normal to the applied stress, there is a preference for certain boundaries to crack prior to others. Nishioka et. al. [5] found that cracking occurred when high normal stress was coupled with dislocation pileups, which added an additional stress element to the boundary.

4.6.2 Linkage between slip continuity and grain boundary cracking

Dislocation pileups may occur where dislocation channels are discontinuous across the boundary and strain has not been accommodated. As shown in Figure 13b, slip continuity is highest at boundaries with the trace of the angle along the tensile axis, and these boundaries are least susceptible to cracking. The combination of high tensile stress and low slip continuity leads to high cracking susceptibility. Figure 18a shows the role of slip continuity in cracking of grain boundaries that are inclined between 70 and 90° with respect to the tensile axis. For similar grain boundary inclinations, cracking is three times more likely at boundaries where slip is discontinuous than at those exhibiting slip continuity. Slip discontinuity is an indication of the inability of the grain boundary to accommodate large amounts of strain. This strain can result in deformation of the boundary, slip in the boundary and rupture of the oxide film above the boundary, allowing for nucleation of a crack in the underlying alloy as described by the slip oxidation model for stress corrosion cracking [35]. As noted above, simulations cannot capture the effect of the environment, but the relation between IG cracking propensity and slip localization is essentially the same. Figure 18b shows that in the simulation, cracking at grain boundaries where slip is discontinuous is several times more likely than at boundaries where slip is continuous.

The link between cracking and deformation is further supported by trends in Taylor and Schmid factor pair types at the cracked boundaries (Figure 9). Taylor factor and Schmid factor both describe slip within a grain. A low Taylor factor is indicative of a grain that requires less shear strain to accommodate the overall tensile strain. For a fixed number of active slip systems, the shear strain on each slip system is low, and is consistent with a reduced severity of the localized strain accumulation at the grain boundary, as shown in Fig. 9b. Similarly, when the number of

slip systems varies, those grains that exhibit a larger number of active slip systems will also experience less shear strain per slip system, as shown in Figs 14a and c. The Schmid and Taylor factor trends are not observed in the simulation result, as the model does not account for irradiation damage. While dislocation emission is observed to occur, it does not reach the degree of localization required to form dislocation channels, as in the case in the experiments.

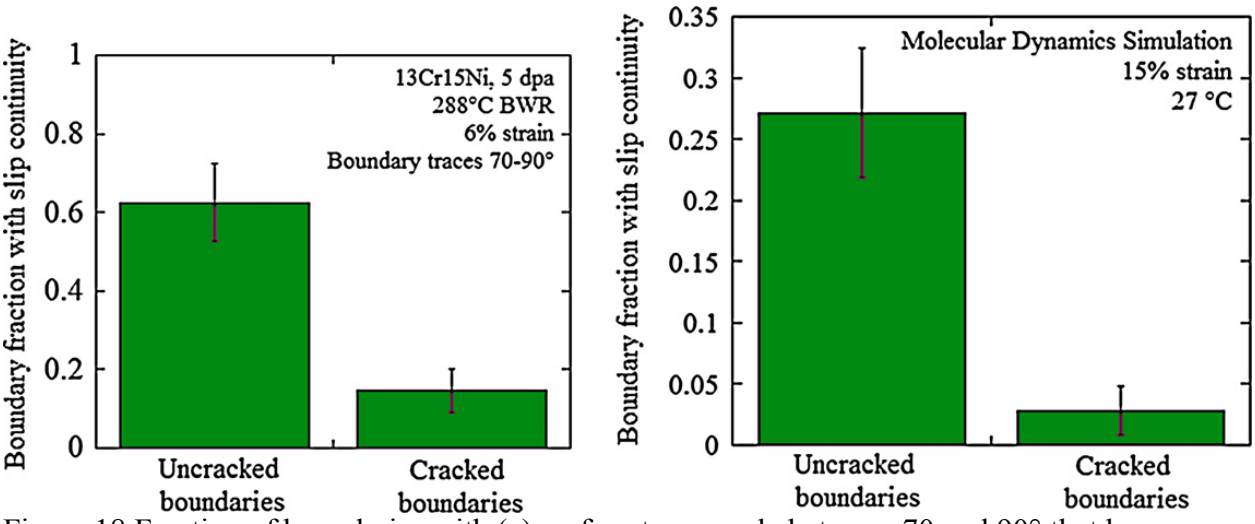

Figure 18 Fraction of boundaries with (a) surface trace angle between 70 and 90° that have continuous slip after experimentally straining to 6% and (b) from simulation of 15% strained fcc (Ni) samples. Figure (a) by McMurtrey and Was. (b) by author.

4.6.3 Location of localized deformation in experiment and simulation

While both the experimental and simulation results show that RHABs and grain boundaries highly inclined to the tensile axis are most susceptible to cracking, cracks tend to initiate at different locations. In the simulations, the majority of the cracks initiated at or near triple junctions. This is likely due to the constraint on deformation at the triple junction due to the intersection of multiple grains vs. a grain boundary where only two grains meet. The simulations provide the sequence of events in crack formation including the location at which the crack forms. Heterogeneous strain displacement maps (Figure 17) of the simulated grain boundary 67

in Cluster 13 showing significant inhomogenous strain building up at the grain boundary prior to crack development, starting at the triple junction at 6% strain. At 7.5% strain, a crack initiates near the triple junction while strain builds up in grain 6 above the crack. At 9% strain, the grain boundary has cracked due to the buildup of strain. It is significant that that buildup of strain at 7.5% was very noticeably confined to grain 6 prior to crack nucleation. The link between strain accommodation and cracking resistance is further supported by slip continuity results. Out of the 70 boundaries contained in the simulated samples, 21 showed slip continuity. Of these boundaries, 2 cracked. The results shown in Figure18b are consistent with experimental results given in Figure 18a, in that boundaries that cracked are less likely to have the strain accommodated through slip transmission across the boundary. The experimental results show that grain boundary cracking occurs between triple points. The experiments also show that strain is localized through dislocation channels, in particular at the boundaries with discontinuous slip, where a dislocation channel intersects a grain boundary. This is shown in Figure 18 and by the inverse relationship between slip continuity trends and cracking probability trends (Figure 6 and Figure 13a, and Figure 8 and Figure 13b). Dislocation channels do not form in the simulations, so the location of greatest strain is the triple junctions. In experiments, it is the dislocation channels that are primarily responsible for high strain localization. Therefore, though the location of crack initiation differs between the experiment and the simulation, both can be explained in terms of strain concentration. That is, both show that cracking occurs where the boundary is unable to accommodate the concentrated strain.

4.7 Conclusions

IASCC in Fe-13Cr-15Ni is caused by a combination of high normal stress acting on the boundary and the inability of the boundary to accommodate the localized strain from dislocation channels that form during straining. RHABs with high surface trace angles with respect to the tensile direction are inherently the most susceptible to cracking due to the higher normal stresses experienced at those angles and the lower cohesion strength of RHABs. Of the RHABs with high surface trace angles, the cracking preferentially occurs at the grain boundaries where slip is discontinuous. These boundaries are the least likely to accommodate strain. The ability of the grain boundary to accommodate stain is dependent on the following properties:

- Grain boundary type (RHAB or special boundary), with more strain buildup occurring at RHABs.
- Grain boundary surface trace angle with respect to the tensile direction. High surface trace angles not only experience higher levels of normal stress, but are also less likely to experience continuous slip across the grain boundary.
- The ability of the grain to deform to match overall strain and relieve strain at the boundary. This is measured by Schmid factor, Taylor factor and the number of activated slip systems. Grains with a low Schmid factor and a high Taylor factor do not deform easily and therefore are less able to accommodate strain at the boundary.

RHABs at high angles with respect to the tensile direction and with adjacent grains that have high Taylor factors and low Schmid factors are the least likely to accommodate strain and the most susceptible to IASCC.

4.8 Acknowledgements

The author acknowledges Alexander Flick for his assistance conducting the CERT tests in the Irradiated Materials Testing Laboratory at the University of Michigan, as well as the staff of the Michigan Ion Beam Laboratory, Ovidiu Toader and Fabian Naab for their assistance in performing the proton irradiations. EBSD equipment and support were provided by the University of Michigan Electron Microbeam Analysis Laboratory staff. This work was supported by the Department of Energy, Office of Basic Energy Sciences, under grant DE-FG02-08ER46525.

References

[1] Z. Jiao, G.S. Was, J. Nucl. Mater., paper in press.

[2] E. West, in: Nuclear Engineering and Radiological Sciences, University of Michigan, Ann Arbor, 2010.

[3] G.S. Was, B. Alexandreanu, J. Busby, Advances in Fracture and Failure Prevention, Pts 1 and 2, 261- 263 (2004) 885-901.

[4] Z. Jiao, G.S. Was, in: Symposium on Microstructural Processes in Irradiated Materials held at the 2007 TMS Annual Meeting, Elsevier Science Bv, Orlando, FL, 2007, pp. 203-209.

[5] H. Nishioka, K. Fukuya, K. Fujii, Y. Kitsunai, J. Nucl. Sci. Technol., 45 (2008) 274-287.

[6] T. Onchi, K. Dohi, N. Soneda, M. Navas, M.L. Castano, J. Nucl. Mater., 340 (2005) 219-236.

[7] Y. Matsukawa, Y.N. Osetsky, R.E. Stoller, S.J. Zinkle, Mater. Sci. Eng., A, 400-401 (2005) 366-369.

[8] Y. Matsukawa, Y.N. Osetsky, R.E. Stoller, S.J. Zinkle, Philos. Mag., 88 (2008) 581 - 597.

[9] Z. Jiao, J. Busby, R. Obata, G.S. Was, in: 12th International Conference on Degradation of Materials in Nuclear Power Systems, Warrendale, PA, 2005, pp. 379.

[10] D. Farkas, Philos. Mag. Lett., 80 (2000) 229-237.

[11] A. Latapie, D. Farkas, Phys. Rev. B, 69 (2004).

[12] S.J. Noronha, D. Farkas, Mater. Sci. Eng., A, 365 (2004) 156-165.

[13] M. Tschopp, D.L. McDowell, in: J.H. Fan, H.B. Chen (Eds.) International Conference on Heterogeneous Material Mechanics (ICHMM), Huangshan, PEOPLES R CHINA, 2008, pp. 97-104.

[14] M.A. Tschopp, D.L. McDowell, in: K.J. Hsia, M. Goken, T. Pollock, P.D. Portella, N.R. Moody (Eds.) Hael Mughrabi Honorary Symposium held at the 2008 Annual TMS Meeting and Exhibition, New Orleans, LA, 2008, pp. 29-34.

[15] M.A. Tschopp, D.L. McDowell, Scr. Mater., 58 (2008) 299-302.

[16] M.A. Tschopp, D.L. McDowell, International Journal of Plasticity, 24 (2008) 191-217.

[17] M.A. Tschopp, G.J. Tucker, D.L. McDowell, Comput. Mater. Sci., 44 (2008) 351-362.

[18] Y. Mishin, D. Farkas, M.J. Mehl, D.A. Papaconstantopoulos, Phys. Rev. B, 59 (1999) 3393-3407.

[19] S. Plimpton, J. Comput. Phys., 117 (1995) 1-19.

[20] H. Van Swygenhoven, A. Caro, D. Farkas, Mater. Sci. Eng. A, 309 (2001) 440-444.

[21] J. Schiotz, Scr. Mater., 51 (2004) 837-841.

[22] J.A. Moriarty, V. Vitek, V.V. Bulatov, S. Yip, J. Comput.-Aided Mater. Des., 9 (2002) 99-132.

[23] Z.H. Jin, P. Gumbsch, K. Albe, E. Ma, K. Lu, H. Gleiter, H. Hahn, Acta Mater., 56 (2008) 1126-1135.

[24] Z.H. Jin, P. Gumbsch, E. Ma, K. Albe, K. Lu, H. Hahn, H. Gleiter, Scr. Mater., 54 (2006) 1163-1168.

[25] B.L. Adams, S.I. Wright, K. Kunze, Metall. Mater. Trans. A, 24 (1993) 819-831.

[26] D.J. Dingley, V. Randle, J. Mater. Sci., 27 (1992) 4545-4566.

[27] C.L. Kelchner, S.J. Plimpton, J.C. Hamilton, Phys. Rev. B, 58 (1998) 11085-11088.

[28] A. Stukowski, Modelling and Simulation in Materials Science and Engineering, 18 (2010).

[29] D. Farkas, L. Patrick, Philos. Mag., 89 (2009) 3435-3450.

[30] G.S. Was, B. Alexandreanu, P. Andresen, M. Kumar, in: C.A. Schuh, M. Kumar, C.B. Carter, V. Randle (Eds.) Symposium on Interfacial Engineering for Optimized Properties III held at the 2004 MRS Spring Meeting, Materials Research Society, San Francisco, CA, 2004, pp. 87-100.

[31] M. Shimada, H. Kokawa, Z.J. Wang, Y.S. Sato, I. Karibe, in: Symposium on Computational Thermodynamics and Materials Design, Pergamon-Elsevier Science Ltd, New Orleans, Louisiana, 2001, pp. 2331-2341.

[32] S.M. Bruemmer, in: C.A. Schuh, M. Kumar, C.B. Carter, V. Randle (Eds.) Symposium on Interfacial Engineering for Optimized Properties III held at the 2004 MRS Spring Meeting, Materials Research Society, San Francisco, CA, 2004, pp. 101-110.

[33] D. Wolf, Acta Metallurgica, 37 (1989) 1983-1993.

[34] E.A. West, G.S. Was, J. Nucl. Mater., (Submitted 2010).

[35] Z. Jiao, J.T. Busby, G.S. Was, J. Nucl. Mater., 361 (2007) 218-227.

[36] J.F. Ziegler, J.P. Biersack, M.D. Ziegler, in, Yorktown, NY: IBM Corporation, 2008.

5 Strain localization at dislocation channel–grain boundary intersections in irradiated stainless steel

McMurtrey, MD; Was, GS; Cui, B; Robertson, I; Smith, L; Farkas, D.

Journal of Plasticity

This chapter has been published in International Journal of Plasticity 2014, Volume 56, pages 219-231. It is used here with permission.

5.1Abstract

The interaction of dislocation channels with grain boundaries in irradiated stainless steel was observed on multiple length scales using scanning electron microscopy (SEM) digital image correlation (DIC) and confocal microscopy (micro-scale), *in situ* straining in transmission electron microscopy (nano-scale), and atomistic modeling (atomic scale). Interactions were divided into three classifications; slip transmission, discontinuous slip, and discontinuous slip that induced grain boundary slip. DIC and confocal microscopy were used to quantify the plastic strain at dislocation channel - GB intersections. *In situ* TEM was used to image dislocations inside of channels as they interacted with the grain boundary. Slip in the dislocation channels, as observed by TEM, was found to involve cross slip between different slip planes, as well as the possibility of different slip systems activated on parallel slip planes. Atomistic simulations agreed well with experiments on the nature of channel-grain boundary interactions and also showed elevated levels of elastic stress at DC-GB intersections where slip was discontinuous with no slip transmission. The two distinct classifications of discontinuous slip are significant, suggesting two possible cracking mechanisms that both lead to rupture of the oxide over the grain boundary.

5.2 Introduction

The occurrence of stress corrosion cracking susceptibility of austenitic stainless steels under irradiation is known as irradiation assisted stress corrosion cracking (IASCC), and is a major concern for light water reactor component integrity, in particular as the lifetime of reactors is extended [1], [2]. Irradiation alters the microstructure of stainless steel, causes radiation-induced segregation of elements, dislocation loop and precipitate formation, increased hardness, and a transformation of the deformation mode from relatively homogeneous slip to heterogeneous slip in the form of coarse dislocation channels. The complexity of the irradiation effects on stainless steel makes it difficult to determine the cause of IASCC, however, there appears to be a connection between the localization of deformation into dislocation channels and cracking [1], [2], [3], [4], [5], [6], [7]. Recent results show that the degree of slip in dislocation channels correlates with cracking severity [3], but the mechanism still is not clear. This study seeks to better understand the interactions between dislocation channels and grain boundaries through a multi-length scale approach.

Dislocation channels are formed when the resolved shear stress reaches a magnitude sufficient to propagate dislocations through the damaged lattice. As the dislocation travels along the slip planes, small defects pin it temporarily and are eventually annihilated when the dislocation passes through, creating less resistance for subsequent dislocations to follow. As more dislocations travel through the channel, defects are progressively removed and the ease of slip in the channel increases. Typically, dislocation channels consist of parallel slip planes totaling 50-200 nm in thickness [8], and spaced one to three micrometers apart, though both spacing and thickness are dependent on straining temperature and irradiation dose [9]. Due to the high concentration of plastic deformation, it is possible to reach very high plastic strains within the

channels at low average macroscopic strains. Jiao et al. [10] used atomic force microscopy (AFM) measurements of the height of the channels protruding from the surface to estimate the average shear strains at nearly 100% in the channels of an irradiated steel strained to a macroscopic tensile strain of 3%.

While height measurements of surface steps provide out-of-plane strain values for the dislocation channels, the in-plane strain is more difficult to measure. Heterogeneous plastic strain has been studied in both unirradiated and irradiated alloys using digital image correlation (DIC) [7], [11]. DIC compares pre-strain and post-strain digital images of a region. With a speckle pattern made of nano-scale particles, sub-micron spatial resolution has been achieved. By using gold nano-particles on the order of 30-150 nm in size, Di Gioacchino and Quinta da Fonseca [11] were able to measure strain within slip bands, as well as visualize areas of strain localization in an unirradiated stainless steel.

The interaction of dislocation channels with grain boundaries is an area of active investigation. Using scanning electron microscopy (SEM) imaging of indentations near grain boundaries, Wo et al. [12] found that slip transmission was related to a misorientation factor based on the orientations of the closest {111} slip planes and <110> directions of the two neighboring grains. When slip does not transmit across the boundary, a dislocation pileup will form. Britton et al. [13] used high resolution EBSD to measure the stress caused by a pile-up of screw dislocations at the grain boundary and found a stress field ahead of the dislocation pile-up which decayed at a rate proportional to one over the square root of the distance from the pileup, similar to the model proposed by Eshelby et al. [14].

Transmission electron microscopy (TEM) has also been used to observe the interactions between dislocations and grain boundaries. Dislocations observed to absorb into the grain boundary may

either be glissile or sessile and retain the lattice Burgers vector or decompose into grain boundary dislocations [15]. In cases of slip transmission, except the special case of direct transmission, which occurs only for screw dislocations with a line direction parallel to the slip plane intersection in the grain boundary, the dislocations are absorbed into the grain boundary, and a new dislocation is nucleated in the grain boundary and ejected. By conducting *in situ* TEM straining experiments, it has been possible to develop a set of criteria to predict which slip system is activated to enable slip transmission across the grain boundary [16], [17]. It was found that the magnitude of the Burgers vector of the residual grain boundary dislocation was a dominating factor in predicting slip transmission with the magnitude of the local resolved shear stress playing a minor role.

Only recently have *in situ* TEM straining experiments been conducted on the interaction between dislocations and grain boundaries in irradiated materials. Briceno et al. [18] found that dislocation motion within a irradiated 304 stainless steel was different from that observed in the unirradiated state. Dislocation motion became irregular and jerky, and required higher levels of stress to push the dislocation through the grain. This was evident through the formation of dislocation pile-ups against invisible barriers in the grain interior and the tendency of dislocations to pile-up at the grain boundary dislocation source. When dislocations traverse the grain and reach the other grain boundary, a pile-up is formed. Initially, the dislocations in the pileup are evenly spaced, unlike the unirradiated case where the distance between dislocations rapidly decreases near the grain boundary. Eventually, as stress is increased, the dislocation pile-up in the irradiated sample develops in to a more conventional pileup, similar to those seen in the unirradiated case. This evolution of the pile-up structure is another manifestation of the need for higher stresses to push dislocations through the irradiation obstacle field.

Plastic deformation of a polycrystalline sample has been studied using different simulations and modeling techniques over various length scales [19], [20], [21]. In particular, atomistic studies are important as they can shed light on the details of fundamental atomistic mechanisms, such as dislocation/grain boundary interactions, at a length scale that is not accessible to experimental techniques. Atomistic techniques have been used to study the interaction of dissociated lattice dislocation with specific special grain boundaries [22], as well as the shearing of the interface when a dislocation arrives at a grain boundary [23].

To provide a sound statistical basis for identifying commonalities in dislocation interactions with grain boundaries in irradiated steels and at the same time understand the atomistic processing involved, a multi-scale experimental and simulation approach is employed in this study. Digital image correlation (DIC) and confocal microscopy are used to create a detailed image of the strain field at 23 dislocation channel-grain boundary (DC-GB) intersections on a 10-1000 nm scale, using scanning electron microscopy to provide a large sample area and more DC-GB intersections to be examined on each sample. This allows for a quantitative description of the strain in the dislocation channel, the grain boundary, and the area surrounding the intersection. To understand the interactions at the dislocation level, *in situ* TEM straining was employed to observe the interactions dynamically. These interactions were characterized in terms of the intersection angle, local resolved shear stress, and residual dislocation Burgers vector using methods described by Lee et al. [17]. Details of the specific interactions are described by Cui et al. [24]. Atomistic simulations of interactions at specific grain boundaries identified experimentally were employed to understand the processes and mechanism of strain transfer at the atomistic level. In particular, the modeling activity provide insight on the local elastic stress in the lattice at dislocation-grain boundary intersections, which is difficult to determine

experimentally. The objective of this work is to couple these multi-scale methods to obtain an understanding of channel interactions at grain boundaries to provide the basis for linkage to IASCC

5.3 Materials and methods

A tensile bar with a 23 mm gage section length and a cross section of 2.5 mm by 1.5 mm was cut using electrical discharge machining from a high-purity austenitic stainless steel with the composition shown in Table 1. The average grain size was 50 μm. The sample surface was prepared by a mechanical polish followed by electropolishing at 30V in a solution of 10% perchloric acid and 90% methanol at -40 °C for 90 sec. After polishing, the gage section of the tensile bar was characterized using a coarse EBSD scan in the SEM to determine grain orientation. The electron beam was rastered across the sample surface, pausing for 0.03 seconds to collect EBSD patterns every 5μm. This EBSD analysis was performed at the Michigan Electron Microscope Analysis Laboratory, using a Philips XL30 FEG SEM with a TSL OIM system for automated EBSD measurements.

Table 1. Composition of austenitic stainless steel (Heat # RAM-2191) used in this study, given in wt%.

Material designation	Fe	Cr	Ni	Mn	Si	P	C
13Cr15Ni	Bal.	13.41	15.04	1.03	0.1	<0.01	0.016

The tensile bar was irradiated with 3.2 MeV protons in a tandem accelerator at the Michigan Ion Beam Laboratory to a dose of 5 dpa at 360°C. After irradiation, gold nanoparticles were

deposited onto the surface using a technique developed originally for surface enhanced Raman spectroscopy by Grabar et al. [25], but later adapted by Kammers et al. [26] for use as a DIC speckle pattern. The sample was first soaked in a solution of 20% (3-aminopropyl) trimethoxysilane in methanol. The methoxy groups in the silane molecules react with the hydroxyl groups in the metal oxide to create a firmly attached silane layer over the sample surface. After immersion in the silane solution, the sample was placed in a gold nano-particle suspension (particles ~40 nm in diameter), created using the method developed by Frens [27]. The amines in the silane molecules attached to the gold, creating a random speckle pattern on firmly attached to the steel surface, as seen in figure 1. A random speckle pattern is ideal for DIC, as it allows for higher resolution than repeating patterns, such as grids. SEM analysis determined that the gold particle density varied greatly across the sample surface, from areas with zero particles/μm^2, to areas of 120 particles/μm^2, with an average of about 45 particles/μm^2. During the analysis, DC-GB intersections near areas of low particle density were avoided.

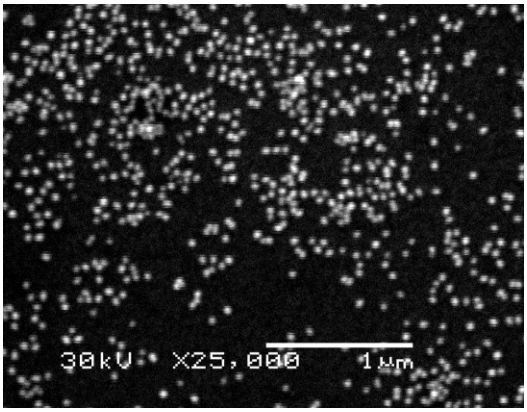

Figure 1. Gold speckle pattern (white) on stainless steel sample (black), as imaged in SEM prior to strain. Figure by McMurtrey and Was.

Using electron backscatter imaging to determine where grain boundaries were located, SEM secondary electron images of the grain boundaries were taken prior to deformation to use as references for the DIC analysis. To correct for the inherent distortion that occurs in SEM

imaging, an Ultrasharp TGX01 AFM calibration grid (3 μm grid spacing) was loaded alongside the tensile bar on the SEM stage and imaged at the same working distance as the gold pattern. Matlab® was used to determine a transformation function to correct the SEM distortion in the grid image, and the same transformation function was then applied to the gold speckle pattern images. Each time the tensile sample was loaded in to the SEM for imaging, the grid was also loaded and imaged so that a calibration image was available for each one.

To determine the amount of experimental error in the DIC process, the same area of the tensile bar was imaged multiple times by unloading and reloading the bar in the SEM between images. As no strain was applied between images, a perfect experimental setup would have shown zero displacement in a DIC analysis of the images. Prior to using the AFM calibration grid to correct the images, the DIC analysis revealed an average displacement of 61.2 nm across images ~7 μm x7μm in size. Using the correction grid, this error was reduced to an average displacement of 29.6 nm. This error analysis was performed in an area of high gold particle density (~80 particles/μm^2). Areas of lower density result in weighted correlations: i.e., if the gold density is higher in the top half of a subsection examined, than the correlation will give preference to that location when finding its match in the post-strained image. Areas where there were fewer than six particles/μm^2 could not be correlated successfully.

After imaging the grain boundaries prior to deformation, the tensile sample was loaded into a high temperature autoclave. The sample was strained at 288°C in a high-purity argon atmosphere at a strain rate of approximately $3x10^{-7}$ s^{-1} to 3.5% plastic strain. Post-strain images were taken in the SEM at the same locations imaged prior to loading. Images were analyzed using a DIC code developed in Matlab®. The first step in the analysis was to set up a grid of coordinates to be analyzed. The grid was set up around DC-GB intersections, with a spacing of ~100 nm between

each point. An aperture window of ~600x600 nm was placed around each point within the grid. The section of the image contained within this aperture was taken from the pre-strain image, and located within the post-strain image using the CPCORR function, part of the Matlab® image analysis library. Minor modifications were made to the CPCORR function to increase the accuracy of the image comparisons. Displacement of each point within the grid was determined, and a displacement map was created from this data. By taking the partial derivatives of the horizontal (X) and vertical (Y) displacements with respect to the X and Y axes, the partial plastic strain tensor was determined by assuming that the channels were 100 nm in width according to previous TEM observations [28] of dislocation channels in similar irradiated materials and similar straining conditions. With the in-plane strain measured, only the components in the direction normal to the surface (Z) were not accounted for.

Z displacement was determined using an Olympus LEXT confocal microscope in the Michigan Lurie Nanofabrication Facility. The Z displacement measurements were used to determine the partial derivatives of Z with respect to the X and Y axes, giving the XZ and YZ strains, which were combined with DIC measurements to produce a nearly complete plastic strain tensor (figure 2). As the collected measurements determine displacement on the measured surface only, it is not possible to determine the third column of the strain tensor, which would be calculated using the partial of the displacement measurements with respect to the Z axis.

Results of DIC measurements were compared to *in situ* TEM straining performed on the same alloy used in the SEM DIC studies, 13Cr15Ni, as well as other austenitic stainless steel alloys such as commercial purity 304 (18Cr8Ni), and 21Cr32Ni stainless steels. The geometrical dimensions of the TEM samples were typically 11.5 mm ×2.5 mm ×0.2 mm. The central section

was thinned to electron transparency using a twin jet polisher with a 6% perchloric acid, 39% butanol and 55% methanol electrolyte at -20 ºC. The ion irradiation experiments were performed *in situ* in the IVEM-Tandem microscope at Argonne National Laboratory [18], [29]. The samples were irradiated at room temperature with 1 MeV Kr ions to a dose of 3×10^{17} ions m^{-2}. TRIM simulations estimate that this dose can cause an average irradiation damage level of about 0.14 dpa in a 100 nm-thick foil of these stainless steel samples. The irradiation dose is lower than that of the tensile bar used in the SEM study, however it was found that dislocation channels still form in the TEM samples under strain, allowing for the DC-GBs to be studied. The deformation experiments were performed *in situ* in the IVEM microscope at Argonne National Laboratory and in a JEOL 2010 LaB_6 TEM operating at 200 keV at the University of Illinois. The *in situ* TEM straining was accomplished using a single-tilt heat/strain stage (Gatan Model 672, Gatan Inc., Warrendale, PA) allowing samples to be deformed *in situ* under tension [29]. TEM images were taken using two-beam bright-field imaging conditions.

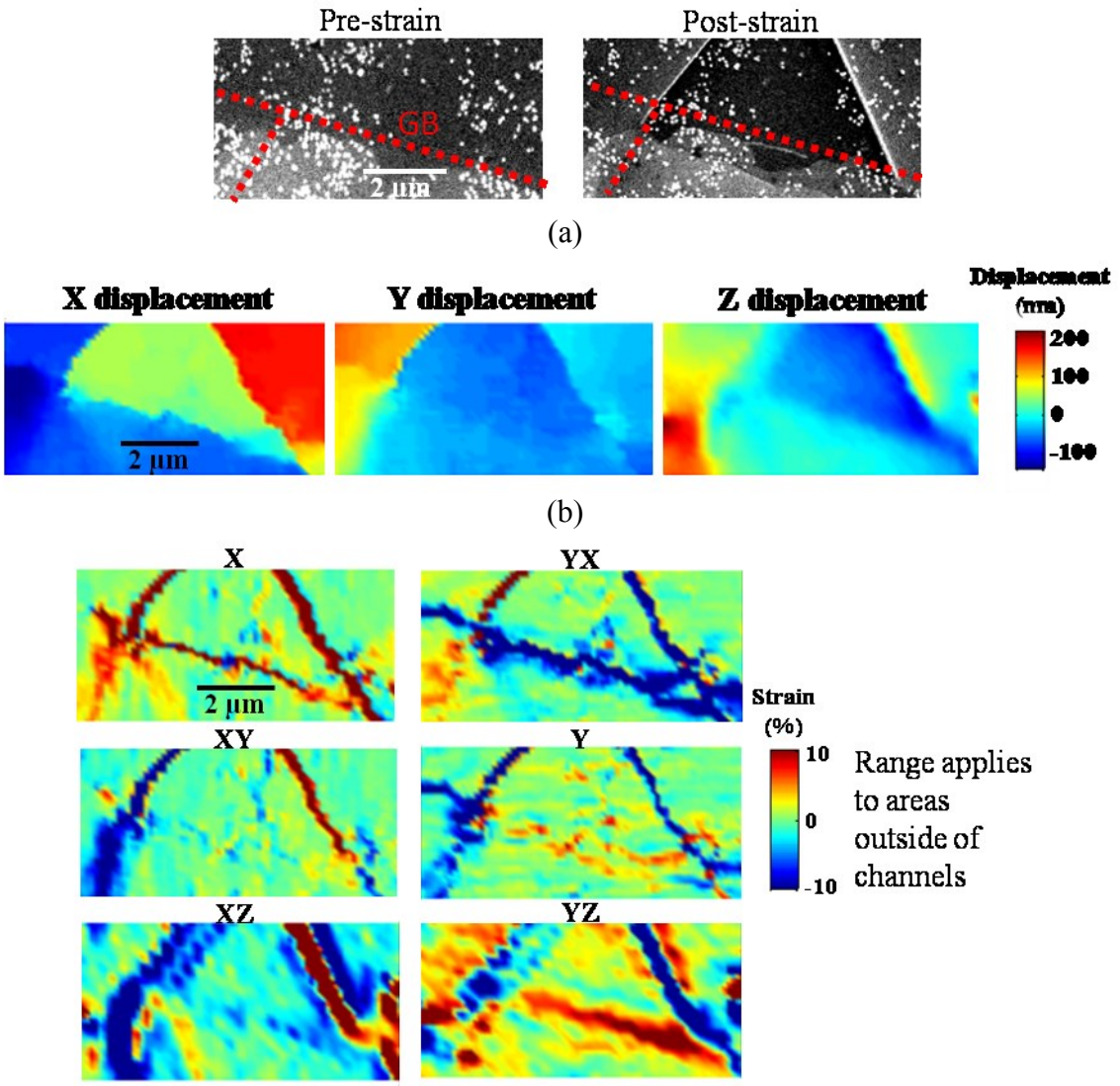

Figure 2. Example of data from a DC-GB intersection area showing (a) the SEM images taken before and after straining (grain boundaries shown with dashed red line), (b) the DIC and confocal microscopy displacement measurement results, and (c) the 6 components of the strain tensor calculated from the displacement measurements. Figure by McMurtrey and Was.

The dynamic interactions between matrix dislocations and grain boundaries were recorded as videos using a CCD camera. The recorded video, together with still frame micrographs, was used to determine the active slip systems. By using the conventional g·b invisibility condition, the Burgers vectors of the incoming and outgoing dislocations were determined. The character of the dislocations and their slip planes were identified using trace analysis techniques. Grain boundary

misorientation (i.e., the axis/angle pair) was calculated using sets of Kikuchi patterns acquired at different tilts on either side of the grain boundary and following the procedure outlined in Edington [30]. The Burgers vector of the residual dislocation created in the grain boundary (b_r) is the difference between the Burgers vector of the incoming (b_{in}) and outgoing (b_{out}) dislocations:

$$\mathrm{b_r} = \mathrm{b_{in}} - \mathrm{b_{out}}\,, \qquad (1)$$

where the Burgers vectors are expressed in the same frame-of-reference.

Atomistic modeling was conducted using thin-film, columnar grains with a Voronoi construction, as described in [6], using the grain centers and grain orientations from the macroscopic tensile sample EBSD data. An example of the grain clusters modeled based on orientation information obtained from the experimental sample are shown in figure 3. The crystals in the simulation are oriented in alignment with the Euler angles observed in the experimental sample. This technique aims to create grain boundaries that share similar properties and alignments as those in the tested experimental sample prepared for the DIC analysis.

The sample was then relaxed using molecular dynamics and embedded atom interatomic force laws in order to achieve equilibrium grain boundary structures. Using this relaxed sample as initial configuration, the model performs uniaxial strain-controlled virtual tensile tests at constant temperature using large-scale atomic/molecular massively parallel simulator (LAMMPS) code [31] and the Virginia Tech supercomputer infrastructure, at a strain rate of $3\text{x}10^{8}\ \text{s}^{-1}$. The Mishin nickel potential [32] was used as a model potential. The main limitations intrinsic to the technique arise from the use of model interatomic potentials and strain rates that are much faster than experimental ones. The constraints of available computing power place limits on the size of

the sample that may be modeled using molecular dynamics. As a result, the simulated grain size is ~50 nm, instead of 50 μm, as it is in the experimental sample. This size is sufficient to avoid the most common of the nano-crystalline mechanical effects, such as significant effects of grain boundary sliding.

Dislocation activity and crystallographic slip is observed and analyzed as a result of these simulations. Visualization and analysis of the simulation can be achieved by colorization of atoms by their centro-symmetry parameter [33]. This technique clearly reveals grain boundaries and stacking faults. Local strain can also be obtained and used as a visualization technique. In particular, inhomogeneous strain across the sample can be analyzed to reveal areas of strain localization. In addition, the simulations also provide information on the local stress of individual atoms, and this can be used to observe areas of stress concentration.

5.4 Results

Figure 4 shows an example of the simulation results for deformation to 4% applied strain corresponding to the same area as the experimental results shown in figure 2. The grain boundary is shown with a black dashed line and color is used to depict local strain. There is good agreement between the slip system activation shown by the simulation at 4% strain and the experimental observations at 3% strain. Slip planes appear at similar angles in the simulation as were observed experimentally, and similar levels of X strain, Y strain and XY shear strains were observed. The differences in the stress levels required for slip activations are minor, and may be due to the very fast strain rates necessitated by the simulation method.

The plastic strain tensors were analyzed for 23 DC-GB intersections. The intersections were divided into three classifications; slip transmission, discontinuous slip, and discontinuous slip-

inducing grain boundary slip. These classifications are similar to those described by Shen et al. [16] in their work studying unirradiated materials using *in situ* TEM straining. Examples of these classifications are shown in figures 5a-5c for the different techniques employed in this study. Slip transmission was readily identified by the continuation of a dislocation channel through the grain boundary. When two channels in adjacent grains coincided at the same point on a grain boundary, it was considered a result of slip transmission. In the cases of discontinuous slip, the intersection was considered to include grain boundary slip when there was a discernable amount of displacement in the grain boundary (>25nm), which was clearly visible above any noise in the displacement map. Of the 23 DC-GB cases, 9 exhibited slip transmission, 5 resulted in discontinuous slip, and 9 were characterized by discontinuous slip-inducing grain boundary slip. In some cases, slip in the grain boundary was observed to occur only along a segment of the grain boundary near the point of intersection with the discontinuous channel, resulting in the activation of a channel in the adjoining grain at a location away from the intersection site, as shown in figure 6. In order for the glissile dislocations in the grain boundary plane to be re-emitted into the adjoining grain, the dislocations would have to be screw dislocations and the grain boundary would have to be the conjugate plane of the slip plane in the lattice [34]. Alternatively, the passage of grain boundary dislocations may be blocked within the grain boundary such that a pile-up is formed, activating a grain boundary source and then ejecting dislocations into the grain. For the purpose of characterizing the strain field around the DC-GB intersection, the 9 DC-GB cases were considered as discontinuous slip-inducing grain boundary slip, regardless of what happened elsewhere along the grain boundary.

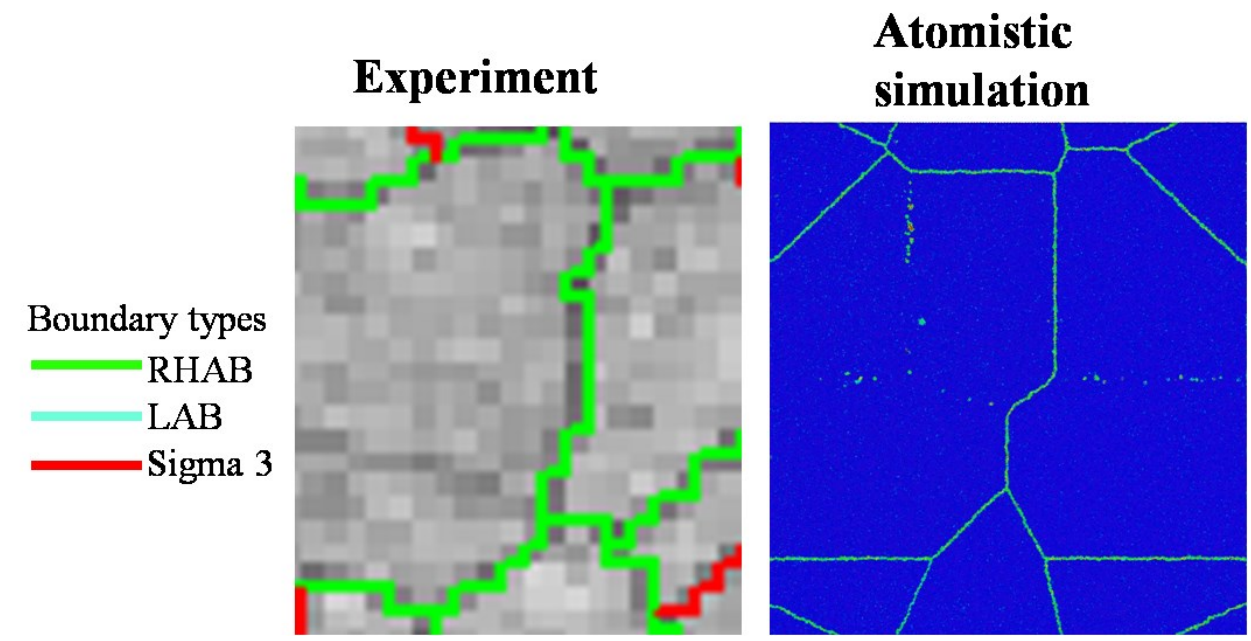

Figure 3. Example of simulating grain clusters using the EBSD grain orientation measurements from the experimental sample as an input so that the simulated clusters match experimental grain clusters. OIM image by McMurtrey and Was. Simulation image by author.

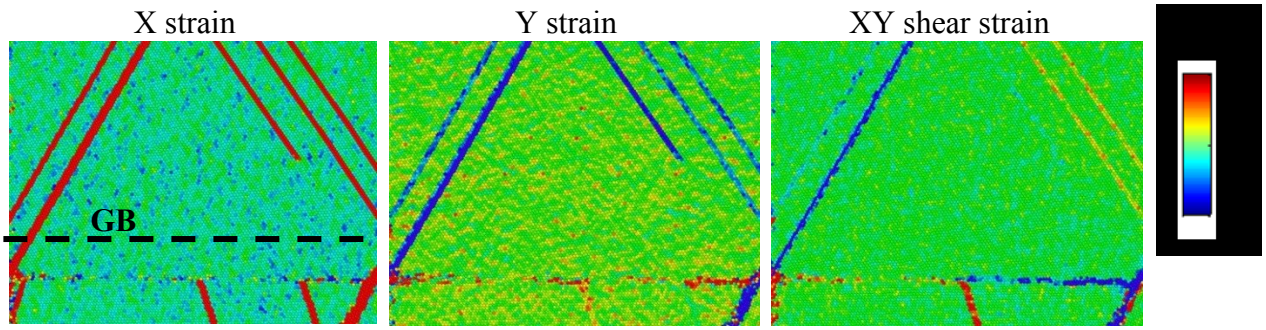

Figure 4. Simulation results of a 4% straining for the same grains as the experimental results shown in figure 2. Color corresponds to atomic strain. Similar slip systems were found to activate in the simulation as seen in the experiment. Figure by author.

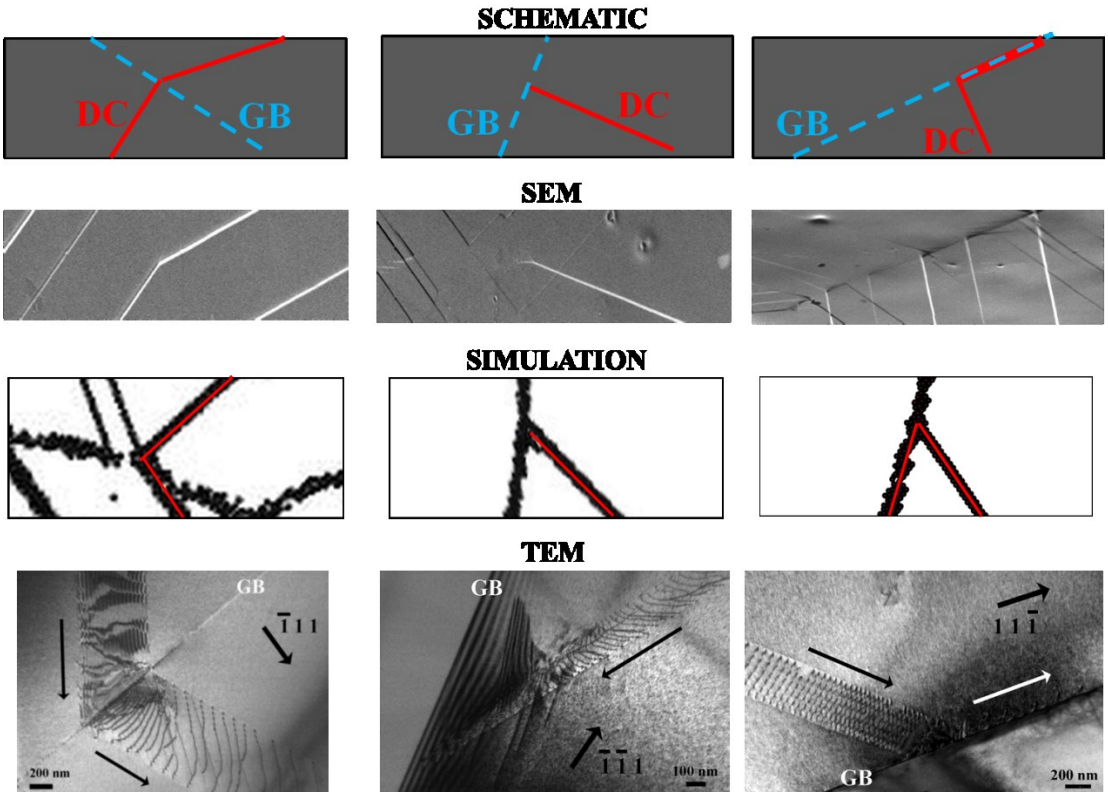

(a) (b) (c)

Figure 5. Schematic diagram, SEM, simulated example and TEM images of the DC-GB classifications; (a) slip transmission, (b) discontinuous slip, (c) discontinuous slip-inducing grain boundary slip. In the TEM images, Kr+ irradiated 304 was used in (a), and Kr+ irradiated 13Cr15Ni was used in (b) and (c). The moving directions of the dislocations are indicated by the thin arrows. The thick arrows indicate the **g** vectors used in the two beam bright field imaging conditions. Slip is highlighted in red for the simulated examples. Figure by McMurtrey and Was. Simulation by author.

Total displacement in the dislocation channels was measured and compared to out-of-plane channel heights, which have previously been used to determine the amount of strain in the channel [3]. Total displacement is the magnitude of all three measured displacement vectors (X, Y, Z) combined, and calculated as the square root of the sum of the squares of the three displacement vectors. Figure 7 shows that the total deformation is related to the channel height measurements, though it is generally greater in magnitude. This is expected as the channel height does not account for in-plane strain. The total strains of the channels were also examined for each of the DC-GB classifications, as shown in figure 8. For the strain calculations, channels

were assumed to be 100 nm wide. Channels with discontinuous slip at the grain boundary were found to have undergone significantly less plastic strain than the other types of DC-GB classifications.

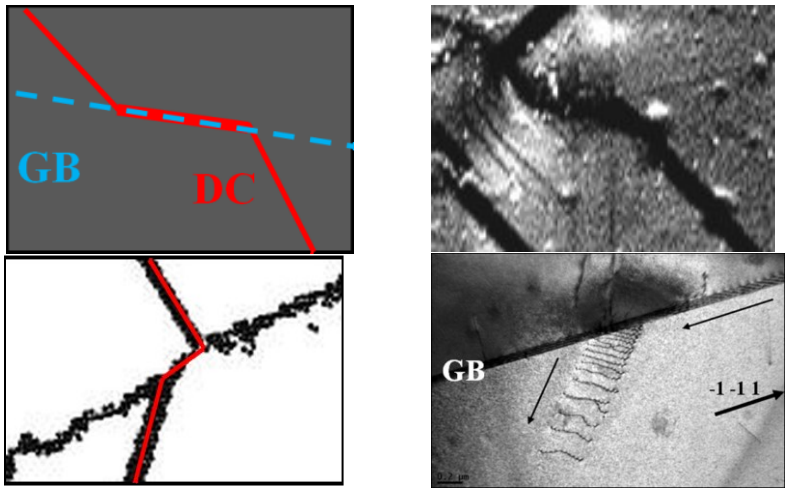

Figure 6. Grain boundary absorption with subsequent re-emission in a 13Cr15Ni allow, shown in (clockwise from upper left image) schematic, SEM, TEM, and simulation. Figure by McMurtrey and Was. Simulation by author.

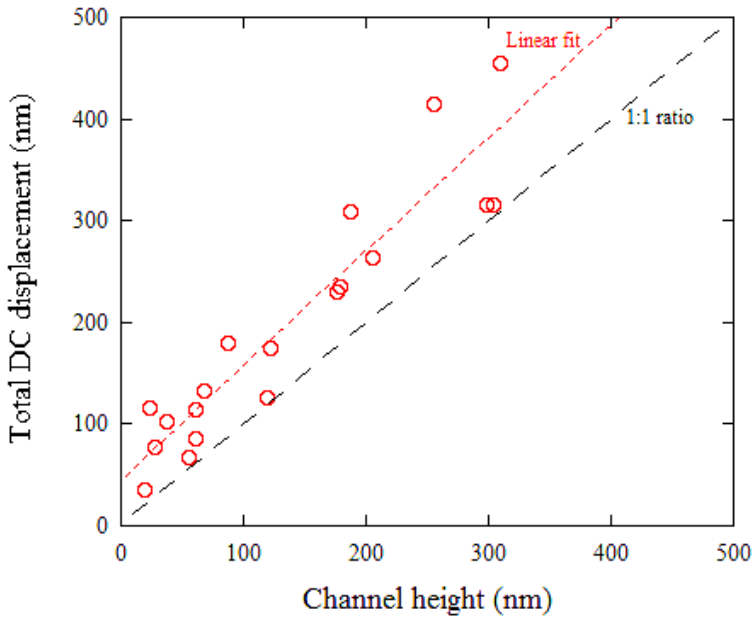

Figure 7. Total displacement in a dislocation channel compared to out-of-plane channel height measurements. Dashed line shows 45° line where channel height is equal to total displacement. Figure by McMurtrey and Was.

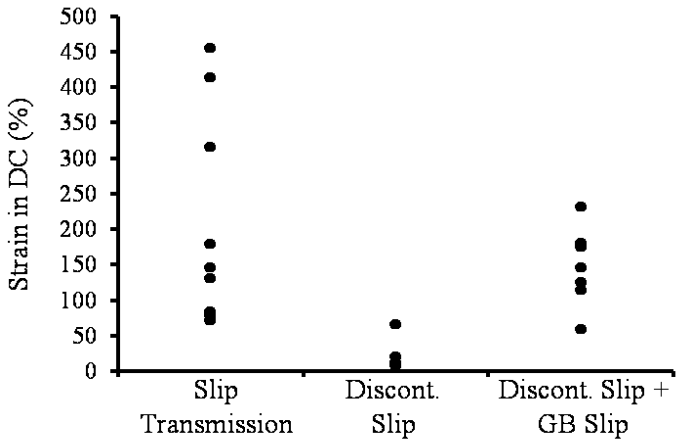

Figure 8. Total strain of dislocation channels, divided into the three DC-GB classifications. Channel width was assumed to be 100 nm for the strain calculations. Figure by McMurtrey and Was.

As IASCC is intergranular in nature, the effects of dislocations on grain boundaries need to be understood. The amount of displacement in the grain boundary was measured in the area adjacent to the dislocation channel. As expected, and as shown in figure 9, near intersections where discontinuous channels induce grain boundary slip, the grain boundaries experienced large amounts of displacement. Also shown in figure 9 that slip transmission resulted in low amounts of grain boundary displacement, similar to discontinuous channels that did not result in GB slip.

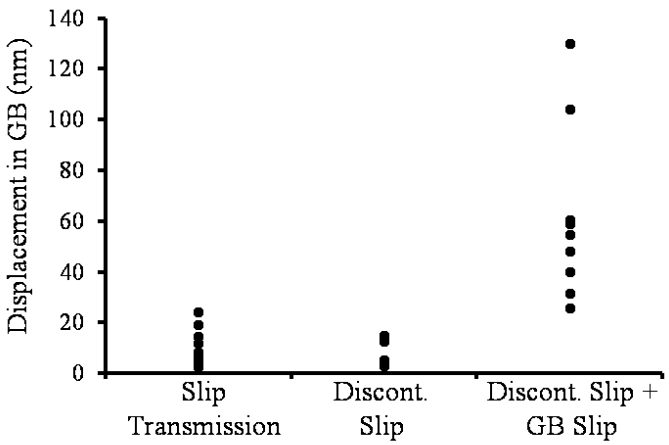

Figure 9. The amount of displacement within the grain boundary, measured adjacent to the dislocation channel in the DC-GB intersection. Figure by McMurtrey and Was.

Simulations were conducted to determine the localized stresses where dislocation channels intersect grain boundaries. In particular, of interest in this study was the difference in stress levels caused by the three classifications of DC-GB observed in the experiments. While true dislocation channels do not form in the atomistic simulation, interactions of dislocations in slip planes with the grain boundary were observed. Figure 10a shows dislocations that were impeded by the grain boundary when the simulated sample was taken to 4% tensile strain. Upon additional straining, figure 10b, slip occurred in the grain boundary and the dislocation was re-emitted into the adjacent grain. Additional details are given in figure 11, which shows this interaction at the grain boundary in more detail. A case of slip transmission is shown in figure 12 for a simulated sample strained to 3%.

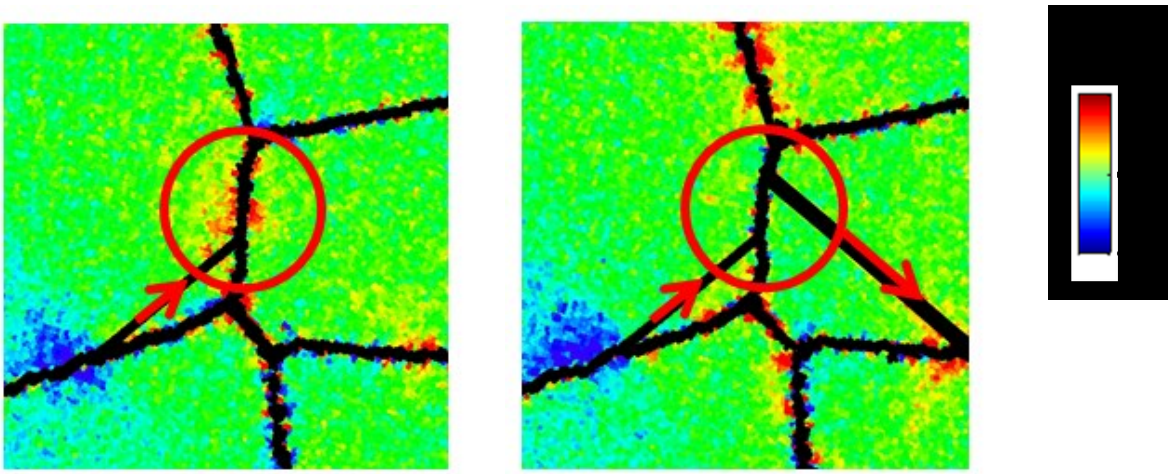

(a) (b)

Figure 10. Simulated sample at (a) 4% and (b) 4.5% applied tensile strain, the black lines are stacking faults created by the passage of partial dislocations. At 4% strain, the slip terminates at the grain boundary, similar to a discontinuous dislocation observed in the experiments. By 4.5% strain, the dislocation has moved through the boundary and emitted into the adjacent grain. Figure by author.

Simulation results were colored to highlight areas of high stress, such as the dislocation-grain boundary intersection in figures 10a and 11c. Stress states were observed throughout the

simulated straining and at times, areas of high stress were alleviated through slip transmission, such as in figures 10b and 11d. In general, areas where slip transmitted through the boundary (figure 12) were found to exhibit lower levels of stress than areas where slip terminated at the boundary.

As discontinuous DC-GB sites have a higher probability of cracking, the processes controlling slip transmission needs to be better understood. The active slip planes could be determined by examining the angle of the trace of the dislocation channel on the surface of the tensile bar observed in the SEM, and comparing it to the possible slip plane traces as determined from EBSD crystal orientation measurements. Attempts to determine the slip direction, however, were not successful using the SEM techniques applied in this paper. Displacement vectors measured by DIC and the confocal microscope were compared to possible slip direction vectors along the active slip plane, as determined by EBSD. While some slip directions matched with the measured displacement vector better than others, on average, only 64% of the total slip could be accounted for by assuming a single slip system. Some of the mismatch may be attributed to error with the measurements, however, the majority of the displacement that cannot be accounted for by a single active slip system is expected to be due to the complexity of the slip within the dislocation channels.

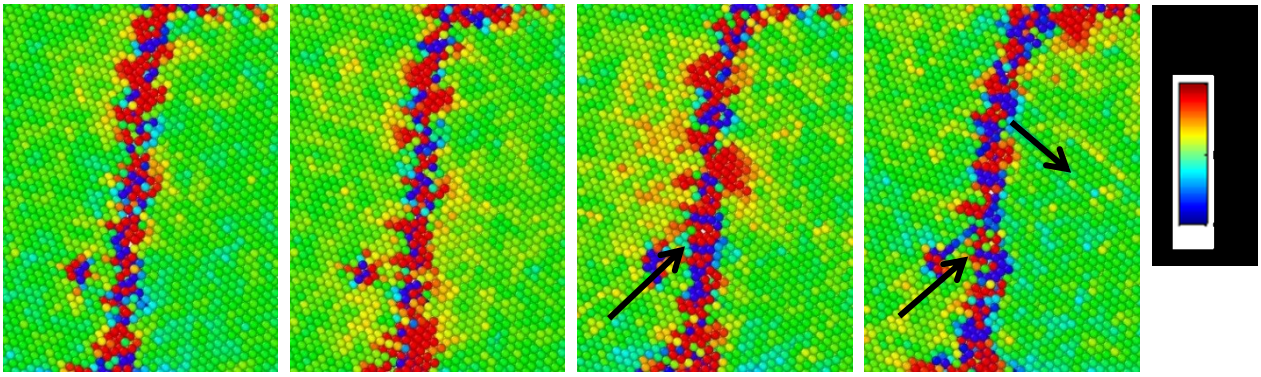

(a) (b) (c) (d)

Figure 11. More detailed simulations results depicting the area circled in figure 10 showing the average local stress evolution in the selected grain boundary region of 37.5 nm^3. The total applied tensile strain, as well as the average stress in each image is (a) 3% Strain, 1.49GPa, (b) 3.5% Strain, 2.95GPa, (c) 4% Strain, 2.78GPa, and (d) 4.5% Strain, 1.47GPa. Figure by author.

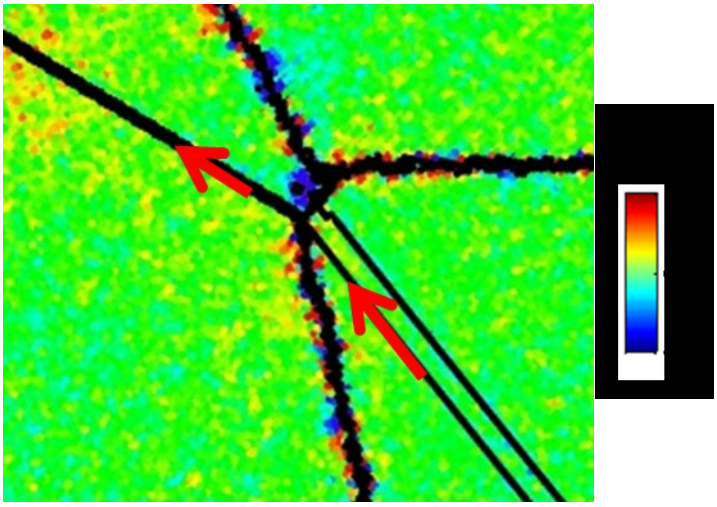

Figure 12. Simulated sample strained to 3%. Dislocations intersecting the grain boundary were transmitted into the adjacent grain. Figure by author.

In fact, cross slip events within a channel can contribute to obstacle bypass [29], widening of a channel, and creation of a new channel on the conjugate plane. It also was observed that a channel could be arrested within a grain, presumably a manifestation of the presence of strong obstacles. These different scenarios are consistent with the SEM observations in figure 13a, and are further supported by the *in situ* TEM straining observations in which cross slip between slip

planes within the channel and multiple active slip systems have been seen to operate within a single channel, as seen in figures 13b and 13c.

Due to the complexity of slip, it was not possible to determine which slip systems were active in the slip transmission process observed in the SEM, and therefore little additional information was gathered with respect to the slip transmission mechanism from the SEM/confocal microscope measurements. It was noted, however, that the Schmid factor (related to resolved shear stress) of the grains adjacent to discontinuous channels tended to be lower than that of the Schmid factors of the grains involved in slip transmission. In fact, as shown in figure 14, the lower the Schmid factor in the adjacent grain, the higher the strain in the discontinuous channel impinging on that grain. This is consistent with the TEM results reported elsewhere by Cui et al. [24]. Cui found slip transmission in irradiated metal to be governed by the Burgers vector of the

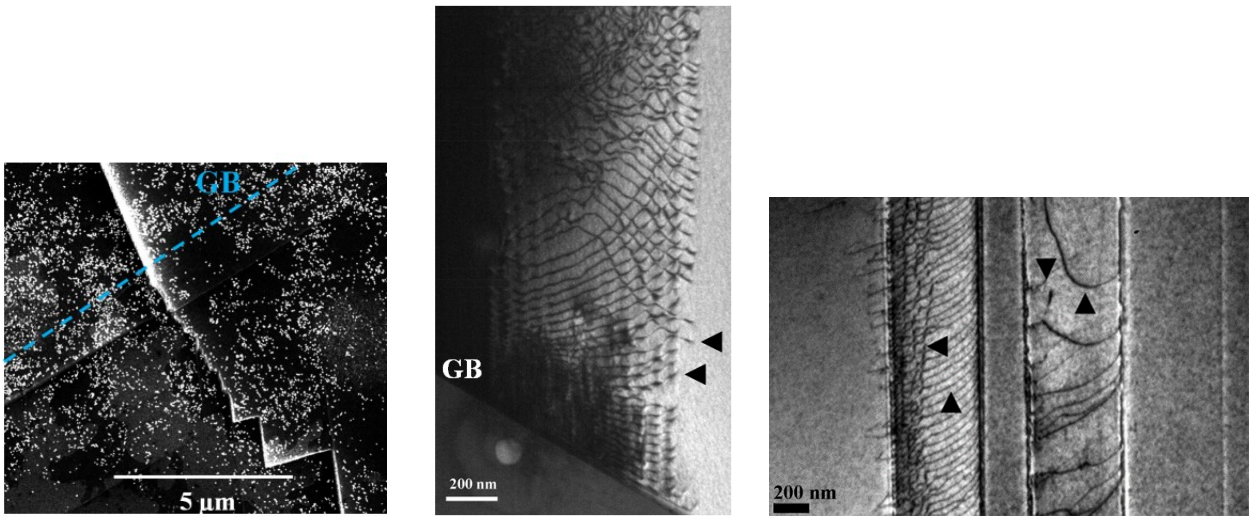

(a) (b) (c)

Figure 13. (a) SEM image showing cross slip between slip planes, away from the grain boundary (b) TEM images of a dislocation channel near the grain boundary in Kr+ irradiated 304 stainless steels. (c) TEM image of two dislocation channels in Kr+ irradiated 21Cr32Ni stainless steels. In b and c, complex dislocation structures and more than one slip systems (indicated by arrowheads) are active in the dislocation channels. Figure by McMurtrey and Was.

residual GB dislocation, as well as the shear stress on the slip system in the adjacent grain. This is similar to the governing characteristics of slip transmission in unirradiated metal. However, in the irradiated case more importance is attributed to the shear stress on the outgoing slip system.

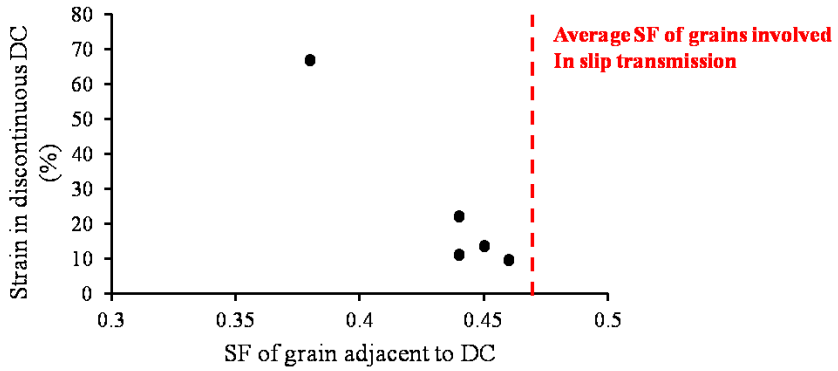

Figure 14. Schmid factor analysis of grains adjacent to discontinuous channels. The red line depicts the average Schmid factor of all the grains involved in slip transmission. Figure by McMurtrey and Was.

5.5 Discussion

In previous work [6], dislocation channels at DC-GB intersections were considered discontinuous or continuous across a grain boundary, and it was found that discontinuous channels were more likely to induce cracking. In this work, the characterization of dislocation channels was augmented with an additional case: discontinuous channels that induce grain boundary slip. With the DIC measurements of in-plane displacement, it was possible to more accurately determine displacement, whether in the channel or in the grain boundary, and to observe slip in the grain boundary. Other than discontinuous slip that induces grain boundary slip, DC-GB intersections were found to cause very little displacement in the grain boundary plane (figure 9).

As noted in the Results section, discontinuous channels undergo less strain than channels in which slip is accommodated either through transmission or absorption into the grain boundary. This is expected, and confirmed through experiments shown in figure 8. As the dislocations form

a pile-up at the grain boundary, the back stress will limit the activity of the dislocation source. The high stress caused by discontinuous slip was observed in the simulation, as shown in figures 10a and 11c. This back stress was relieved by slip transmission *across* the grain boundary (figure 12), or absorption *into* the grain boundary (figures 10b and 11d). Absent these processes, slip is not relieved, and the back stress continues to limit the activity of the dislocation source. These high stress states were observed in the simulation and could be confirmed experimentally by measuring elastic strain/stress tensors in conjunction with the plastic strain tensors collected in this work. Even though the slip is accommodated in figure 12, high stress levels are still observed near the triple junction of the grain boundaries close to the slip transmission event. Slip systems could not be fully characterized using these SEM techniques, as there is ambiguity as to which slip directions are active. Slip within the channel was found to be complex, with cross slip within the channel between slip planes, and the possibility of multiple slip directions existing on parallel slip planes (figure 13) all observed in the TEM. Without the ability to identify the active slip systems in the SEM, it was not possible to determine the residual Burgers vector between the two active slip systems in the case of slip transmission, nor the resolved shear stress on the active slip systems. This type of analysis was instead conducted using *in situ* TEM straining. Results from the study [24] showed that slip transmission is controlled by both minimization of the strain energy density in the grain boundary (by minimizing the Burgers vector of the residual grain boundary dislocation) and the resolved shear stress with the latter increasing in importance as the dislocations must be able to propagate through the obstacles. SEM observations reported in this work support the increased emphasis on resolved shear stress in the outgoing channel. Discontinuous slip at the DC-GB intersection occurred in locations

where the adjacent grain had a lower Schmid factor, confirming that in the case of irradiated metals the resolved shear stress plays a significant role.

The two forms of discontinuous channels (where one induces grain boundary slip and one does not) result in two possible mechanisms that could account for the increase in IASCC susceptibility at discontinuous channel - grain boundary intersections. Discontinuous channels that induce grain boundary slip could cause IASCC by rupturing the oxide layer above the grain boundary, exposing it to the environment. Discontinuous channels that terminate at the boundary result in high elastic stresses that could also rupture the oxide and expose the boundary to the environment.

5.6 Conclusion

Plastic strain was measured for several dislocation channel - grain boundary intersections, including both cases of continuous and discontinuous slip at the grain boundary. Atomistic model result exhibited the same types of intersection modes as experiment. Two distinct types of discontinuous dislocation channels were found; discontinuous with no slip accommodation, and discontinuous but with transfer of slip into the grain boundary followed by emission of a channel away from the original intersection. The displacement tensor resulting from slip within the dislocation channels was compared to the dislocation channel height and it was found that the full tensor is needed to accurately describe the strain of the dislocation channel. Dislocations within the channels were found to undergo cross slip as well as exhibiting multiple slip directions within a single channel. All measurable grain boundary slip occurred from discontinuous channels that induced grain boundary slip. Discontinuous channels where slip is not accommodated by inducing slip into the grain boundary exhibited significantly less plastic

strain than other classifications of channels, as well as high levels of stress at the grain boundary intersection. Discontinuous channels were also found to form adjacent to low Schmid factor grains, as expected given the increased importance of shear stress on slip transmission in irradiated steel found in the TEM studies.

5.7 Acknowledgements

The authors acknowledge Alexander Flick for his assistance conducting the CERT tests in the Irradiated Materials Testing Laboratory at the University of Michigan, as well as the staff of the Michigan Ion Beam Laboratory, Ovidiu Toader and Fabian Naab for their assistance in performing the proton irradiations. J. Kacher is thanked for providing Figure 13c. The electron microscopy was accomplished at the Electron Microscopy Center at Argonne National Laboratory (a U.S. Department of Energy Office of Science Laboratory operated under Contract No. DE-AC02-06CH11357 by U Chicago Argonne, LLC). The NSF IRD program is also acknowledged for support. The authors acknowledge Advanced Research Computing at Virginia Tech for providing computational resources and technical support that have contributed to the results reported within this paper. URL: http://www.arc.vt.edu. Research supported by the U.S. Department of Energy, Office of Basic Energy Sciences, Division of Materials Sciences and Engineering under Award DE-FG02-08ER46525 (McMurtrey, Was, Robertson, Cui: experimental studies and Smith: computational studies) and the NSF IRD program (Farkas: computational studies).

References

[1] S. J. Zinkle and G. S. Was, "Materials challenges in nuclear energy," *Acta Materialia*, vol. 61, no. 3, pp. 735–758, Feb. 2013.

[2] K. Fukuya, "Current understanding of radiation-induced degradation in light water reactor structural materials," *Journal of Nuclear Science and Technology*, vol. 50, no. 3, pp. 213–254, 2013.

[3] Z. Jiao and G. S. Was, "Impact of localized deformation on IASCC in austenitic stainless steels," *Journal of Nuclear Materials*, vol. 408, no. 3, pp. 246–256, 2011.

[4] T. Onchi, K. Dohi, N. Soneda, M. Navas, and M. L. Castano, "Mechanism of irradiation assisted stress corrosion crack initiation in thermally sensitized 304 stainless steel," *Journal of Nuclear Materials*, vol. 340, no. 2–3, pp. 219–236, 2005.

[5] E. A. West and G. S. Was, "Strain Incompatibilities and Intergranular Fracture of Irradiated 316L Stainless Steel," *Journal of Nuclear Materials*.

[6] M. D. McMurtrey, G. S. Was, L. Patrick, and D. Farkas, "Relationship between localized strain and irradiation assisted stress corrosion cracking in an austenitic alloy," *Materials Science and Engineering: A*, vol. 528, no. 10–11, pp. 3730–3740, 2011.

[7] M. Le Millier, O. Calonne, J. Crépin, and C. Duhamel, "Irradiation assisted stress corrosion cracking of stainless steels in a PWR environment (A combined approach)," *Proceedings of the fifteenth international conference on environmental degradation of materials in nuclear power systems water reactors*, pp. 1–15, 2011.

[8] D. J. Edwards, B. N. Singh, and J. B. Bilde-Sørensen, "Initiation and propagation of cleared channels in neutron-irradiated pure copper and a precipitation hardened CuCrZr alloy," *Journal of Nuclear Materials*, vol. 342, no. 1–3, pp. 164–178, 2005.

[9] L. M. Howe, “Irradiation hardening and annealing in copper at high neutron fluences,” *Radiation Effects*, vol. 23, pp. 181–195, 1974.

[10] Z. Jiao, J. Busby, R. Obata, and G. S. Was, “Influence of Localized Deformation on Irradiation-assisted Stress Corrosion Cracking of Proton-Irradiated Austenitic Alloys,” in *12th International Conference on Degradation of Materials in Nuclear Power Systems*, 2005, p. 379.

[11] F. Gioacchino and J. Quinta da Fonseca, “Plastic Strain Mapping with Sub-micron Resolution Using Digital Image Correlation,” *Experimental Mechanics*, Oct. 2012.

[12] P. Wo and A. Ngan, “Investigation of slip transmission behavior across grain boundaries in polycrystalline Ni3Al using nanoindentation.pdf,” *Journal of Materials Research*, vol. 19, no. 1, pp. 189–201, 2004.

[13] T. Benjamin Britton and A. J. Wilkinson, “Stress fields and geometrically necessary dislocation density distributions near the head of a blocked slip band,” *Acta Materialia*, vol. 60, no. 16, pp. 5773–5782, Sep. 2012.

[14] J. D. Eshelby, F. C. Frank, and F. R. N. Nabarro, “The equilibrium of linear arrays of dislocations,” *Philosophical Magazine*, vol. 42, no. 327, pp. 351–364, 1951.

[15] B. Lagow, I. Robertson, M. Jouiad, D. Lassila, T. Lee, and H. Birnbaum, “Observation of dislocation dynamics in the electron microscope,” *Materials Science and Engineering: A*, vol. 309–310, pp. 445–450, Jul. 2001.

[16] Z. Shen, R. Wagoner, and W. Clark, “Dislocation and grain boundary interactions in metals,” *Acta Metallurgica*, vol. 36, no. 12, pp. 3231–3242, 1988.

[17] T. C. Lee, I. M. Robertson, and H. K. Birnbaum, “Prediction of slip transfer mechanisms across grain boundaries,” *Scripta Metallurgica*, vol. 23, no. 5, pp. 799–803, 1989.

[18] M. Briceño, J. Fenske, M. Dadfarnia, P. Sofronis, and I. M. Robertson, “Effect of ion irradiation-produced defects on the mobility of dislocations in 304 stainless steel,” *Journal of Nuclear Materials*, vol. 409, no. 1, pp. 18–26, Feb. 2011.

[19] H. Lim, M. G. Lee, J. H. Kim, B. L. Adams, and R. H. Wagoner, “Simulation of polycrystal deformation with grain and grain boundary effects,” *International Journal of Plasticity*, vol. 27, no. 9, pp. 1328–1354, Sep. 2011.

[20] D. L. McDowell, “A perspective on trends in multiscale plasticity,” *International Journal of Plasticity*, vol. 26, no. 9, pp. 1280–1309, Sep. 2010.

[21] D. H. Warner, F. Sansoz, and J. F. Molinari, “Atomistic based continuum investigation of plastic deformation in nanocrystalline copper,” *International Journal of Plasticity*, vol. 22, no. 4, pp. 754–774, Apr. 2006.

[22] J. P. Couzinié, B. Décamps, and L. Priester, “Interaction of dissociated lattice dislocations with a Σ=3 grain boundary in copper,” *International Journal of Plasticity*, vol. 21, no. 4, pp. 759–775, Apr. 2005.

[23] H. J. Chu, J. Wang, I. J. Beyerlein, and E. Pan, “Dislocation models of interfacial shearing induced by an approaching lattice glide dislocation,” *International Journal of Plasticity*, vol. 41, pp. 1–13, Feb. 2013.

[24] B. Cui, J. Kacher, M. McMurtrey, G. Was, and I. Robertson, “The influence of Irradiation Damage on Slip Transfer across Grain Boundaries,” *Acta Materialia*, vol. Submitted, 2013.

[25] K. C. Grabar, R. G. Freeman, M. B. Hommer, and M. J. Natan, “Preparation and Characterization Monolayers,” vol. 67, no. 4, pp. 1217–1225, 1995.

[26] A. D. Kammers and S. Daly, “Self-Assembled Nanoparticle Surface Patterning for Improved Digital Image Correlation in a Scanning Electron Microscope,” *Experimental Mechanics*, Mar. 2013.

[27] G. Frens, “Controlled Nucleation for the Regulation of the Particle Size in Monodisperse Gold Suspension,” *Nature Physical Science*, vol. 241, pp. 20–22, 1973.

[28] Z. Jiao and G. S. Was, “The role of irradiated microstructure in the localized deformation of austenitic stainless steels,” *Journal of Nuclear Materials*, vol. 407, no. 1, pp. 34–43, 2010.

[29] J. Kacher, G. S. Liu, and I. M. Robertson, “In situ and tomographic observations of defect free channel formation in ion irradiated stainless steels.,” *Micron*, vol. 43, pp. 1099–1107, 2012.

[30] J. Edington, *Practical Electron Microscopy in Materials Science*, vol. Submitted. New York, 1976.

[31] S. Plimpton, “Fast Parallel Algorithms for Short Range Molecular Dynamics.pdf,” *Journal of Computational Physics*, vol. 117, pp. 1–19, 1995.

[32] Y. Mishin, D. Farkas, and M. Mehl, “Interatomic potentials for monoatomic metals from experimental data and ab initio calculations,” *Physical Review B*, vol. 59, no. 5, pp. 3393–3407, 1999.

[33] C. Kelchner, S. Plimpton, and J. Hamilton, “Dislocation nucleation and defect structure during surface indentation,” *Physical Review B*, vol. 58, pp. 11085–11088, 1998.

[34] J. Kacher and I. M. Robertson, “Quasi-four-dimensional analysis of dislocation interactions with grain boundaries in 304 stainless steel,” *Acta Materialia*, vol. 60, no. 19, pp. 6657–6672, Nov. 2012.

6: Tensile deformation of fcc Ni as described by an EAM potential

DIANA FARKAS and LAURA PATRICK

Department of Materials Science and Engineering

Virginia Tech

Blacksburg, VA 24061

This chapter has been published in Philosophical Magazine, 2009, Volume 89, Issue 34-36, pages 3435-3450. It is used here with permission.

6.1 Abstract

We present the results of a large scale atomistic study of tensile deformation in a virtual FCC polycrystalline sample with columnar grain structure and a [110] texture. The atomic interaction was described by a volume dependent central interatomic potential based on first principle calculations and experimental data for FCC Ni. The sample contained 9 grains of 40 nm average size and was created using a Voronoi construction with a common [110] axis, so that the grain boundaries were all pure tilt with random misorientation angles and crystallographic orientation of the grain boundary plane. We report the stress-strain behavior of the sample and the particular details of dislocation emission and dislocation interaction. Different grain boundaries acted as emission sites at different stresses, due to their different local structure and orientation with respect to the applied stress. It was found that boundaries close to a twin misorientation can emit dislocations easily and become closer to the twin misorientation as a result of the emission process. Low angle boundaries were observed to disappear as a result of the deformation process. The emission of leading and trailing Shockley partials was observed and as the deformation proceeds, dislocation debris accumulates in the sample. The results also show that as the deformation proceeds the strain can localize in certain grains and grain regions, driven solely by the particular local structure and orientation of the various grain boundaries.

6.2 Introduction

Atomistic simulation has been used for many years to study the mechanical response of metallic materials at a nano-scale level, in particular the structure of grain boundaries and dislocations. The initial studies of dislocation core structure in various materials used pair potential models to understand the role of the atomic level structure of the defective region [1]. Over the years, the simulations have become more realistic due to advances in computing power, allowing the simulation of digital samples with larger number of atoms, including polycrystalline structures and defect interaction. However, the accuracy of the simulation results depends critically on the interatomic potential models. The introduction of volume dependent potentials [2-4] has been a major breakthrough in the description of metallic materials, for example the structure of dislocation cores [5-8], the interaction of lattice dislocations with grain boundaries [9-11], and the emission of dislocations from grain boundaries [12-16].

Since their introduction in 1984, significant progress has been made in developing accurate volume dependent potentials that are based on first principle calculations [17]. For example, first principle calculations of the energies of metastable phases have been used to develop more accurate EAM (embedded atom method) potentials for Ni and Al [18]. The use of large scale massively parallel simulations [19] using these accurate interatomic potentials makes it possible to conduct virtual mechanical tests of realistic polycrystalline structures. Great success has been achieved in studying the properties of nanocrystalline materials using these techniques [20-24]. Significant mechanical property changes are controlled by the atomistic nature of defects, from point defects to dislocation loops and grain boundaries [25]. One area of particular importance is the detailed knowledge of the interaction mechanisms between dislocations and grain boundaries and the role of grain boundaries and other defects as dislocation sources in metallic materials

[26-32]. Most of the work done on the simulation modeling of the interaction of dislocations and grain boundaries and the nucleation of grain boundaries from dislocations has been performed in bicrystal samples containing special boundaries [12-16, 33-35].

Previous work on polycrystalline structures mostly concentrated on the role of grain boundary sliding as a particular deformation mechanism that operates at very small grain sizes, mostly less than 20 nm [22]. The existence of this additional mechanism results in the maximum hardness for grain sizes of around 20 nm. The aim of the present work is to study deformation mechanism beyond the maximum hardness. In particular we focus on the inhomogeneity of the deformation in the various grains. The inhomogeneity of the deformation is a significant factor in the ductility of these materials.

The simulation work presented here was geared towards contributing to the understanding of the fundamental mechanisms of dislocation emission from random grain boundaries in polycrystalline FCC structures [36], and the interaction of the dislocations with grain boundaries. Atomistic simulation can provide details at the nanometer length scale and insight into basic mechanisms. An important consideration in our simulation work was to create digital samples that were as similar as possible to the experimental ones in order to perform a direct comparison with the experimental results. We also wanted to study grain sizes for which grain boundary sliding was not a major deformation mechanism, that is, significantly larger than 20 nm. We report virtual tensile tests of polycrystalline columnar grain samples with a random distribution of tilt grain boundaries and study the dislocation emission process from these boundaries in detail, followed by their interaction.

6.3 Simulation technique

The samples for the simulations reported here were generated using a Voronoi construction with random misorientation angles around the <110> axis. The procedure to generate the sample is similar to that used in our previous work on columnar structures [37]. The sample contained 9 grains of 40 nm average grain size and a total of about one million atoms. In this way, all the grain boundaries in the sample were of tilt character with random misorientation angles. Figure 1 shows the initial structure of the sample, indicating the nine grains. The sample is fully periodic in all directions. The grain size is large enough to avoid significant effects of grain boundary sliding as a deformation mechanism in the sample. We note that the 40 nm grain size is still too small to support dislocation multiplication through Frank-Read source type mechanisms.

The sample represents a columnar grain structure with a <110> texture. Figure 1 also shows the various misorientation angles around <110> for 17 grain boundaries in the sample. Four of these boundaries are low angle, with misorientation angles less than 15 degrees. Three boundaries have misorientation angles within 10 degrees of the perfect twin misorientation and one more is within 15 degrees.

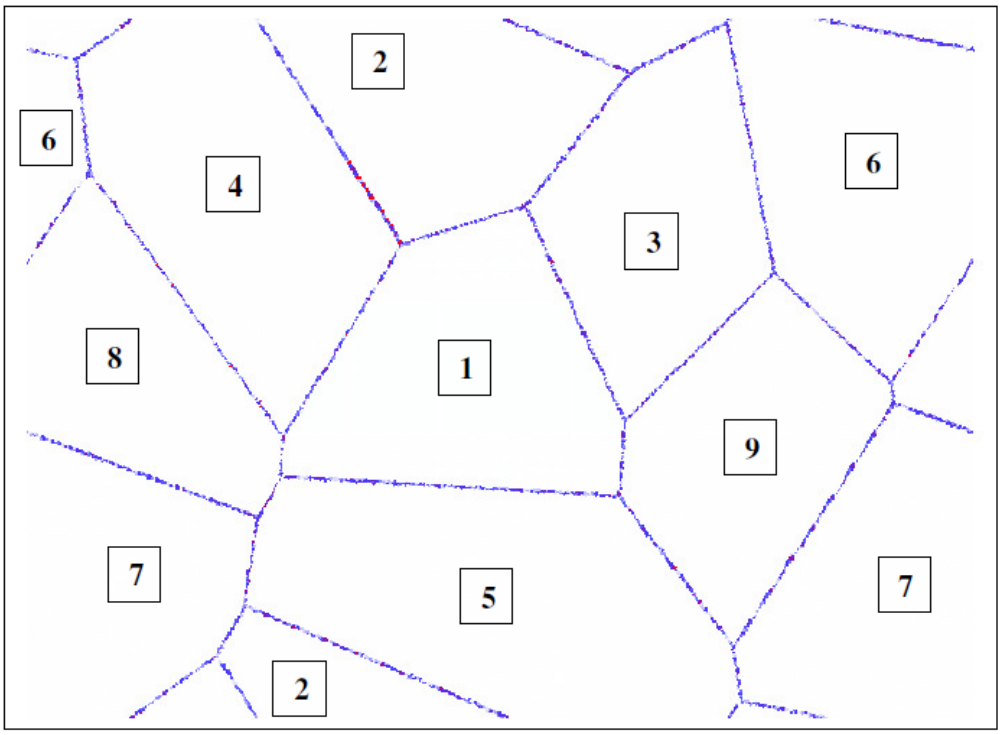

GB	θ(°)
12	80.19
13	54.58
14	88.93
15	23.49
24	8.74
23	25.61
25	76.32
36	77.47
39	85.57
46	68.18
48	58.82
57	21.34
59	7.51
68	9.37
69	8.11
78	30.11
79	28.85

Figure 1: Initial periodic sample generated using the Voronoi construction. The 9 grains are indicated as well as the various misorientation angles around [110] for 17 different grain boundaries in the sample. Figure by author.

After they were generated, the samples were relaxed using molecular dynamics for 100 ps at 300 K in order to achieve a relaxed grain boundary structure. The interatomic potential used for the relaxation was that of Mishin et al. for Ni [18]. The code used is LAMMPS [19] with a Nose-Hoover thermostat and barostat. After relaxation, the samples were digitally deformed in order to induce the emission of dislocations from the grain boundaries. The displacement-controlled deformation of the digital samples was performed using standard molecular dynamics at room temperature, using periodicity in all directions. The periodicity in the direction of the tensile axis was used to control the deformation level and the pressure was maintained at zero in the direction perpendicular to the tensile axis. In this process, we utilized strain rates that are as slow as possible with the available computing power, in our case $3x10^{8}$ s^{-1}. The main limitation of molecular dynamics techniques is the very fast strain rates used as compared with experimental

techniques. This makes it difficult to observe thermally activated processes which take longer than the nanosecond timeframe.

As the deformation proceeded, the dislocation emission process was followed by monitoring the centrosymmetry parameter [38]. This allows detailed visualizations of the mechanisms of dislocation emission and interaction as the deformation proceeds. We performed virtual tensile tests of the same sample in both directions (x and y) that were perpendicular to the tilt axis of the boundaries (z). In this way, we could study the response of the same boundaries to different applied loading directions.

6.4 Results

Figure 2 shows the stress-strain behavior of the sample. The values of the flow stress obtained are very high due to the fast strain rates used and the small grain sizes; as compared to experiments. When the loading direction is changed, we do not obtain exactly the same tensile behavior because the sample contains a limited number of grain boundaries and each has a particular response to loading. The difference in the two stress-strain curves shown in Figure 2 highlights the fact that each boundary responds differently to the applied stress in each direction, and the sample contains only a limited number of grains.

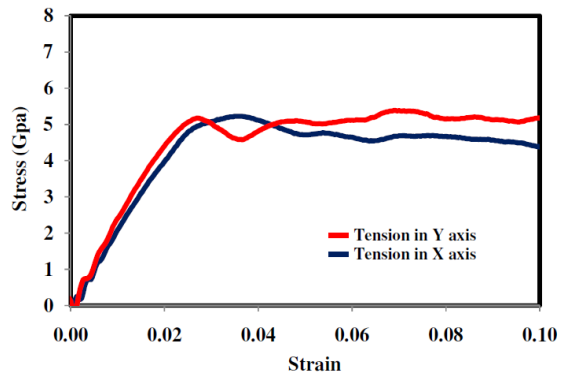

Figure 2: Stress-strain curves obtained for the tensile deformation of the sample in the horizontal (x) and vertical (y) directions. The strain rate utilized is 3.3×10^{8} s^{-1}. Figure by author.

Figure 3 shows the sequence of tensile deformation at 3, 6, and 9% strain in the horizontal direction (x). The simulations show the emission of dislocations from particular grain boundaries first, and how the different boundaries in the sample were activated as the deformation level is increased. Figure 4 shows similar results for the same sample but under tensile loading in the vertical direction (y).

Figures 3 and 4 show the atoms with centrosymmetry parameter greater than 3, therefore filtering out all the atoms in perfect lattice configurations. In this way, we only plot the atoms in the grain boundaries, dislocation cores, and stacking faults. The boundaries react differently depending on the direction of the applied load. Our results show that grain 4 is the first one to deform plastically under tensile loading in the x direction, whereas grain 1 is the first to deform plastically under tensile loading along the y direction. As the deformation level increases, other grain boundaries start emitting dislocations and all grains deform.

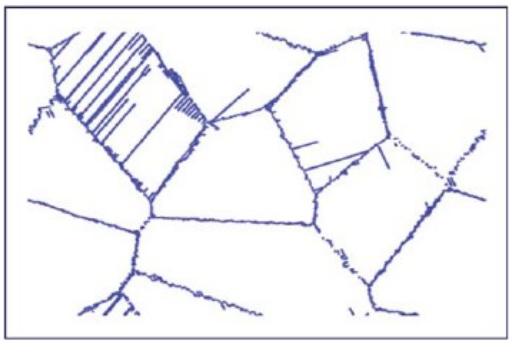

(a)

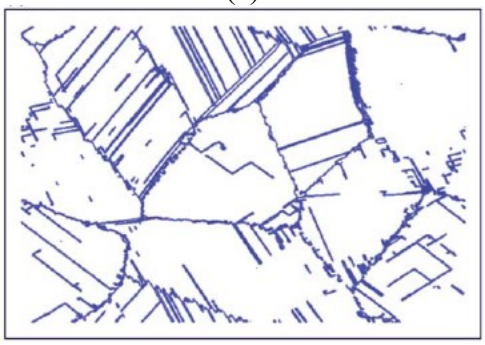

(b)

(c)

Figure 3. Grain boundaries, dislocations and stacking faults in the sample after 3, 6 and 9%deformation in the x direction. The atoms shown are those with centrosymmetry parameters greater than 3 and, therefore, not including the atoms in perfect lattice positions. Figure by author.

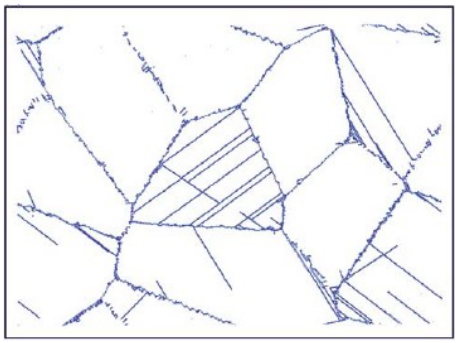

(a)

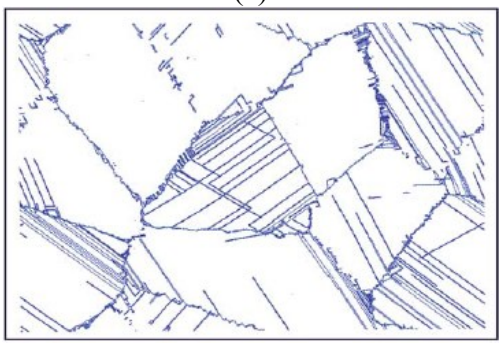

(b)

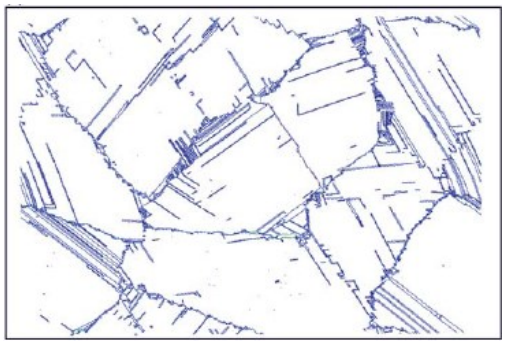

(c)

Figure 4. Grain boundaries, dislocations, and stacking faults in the sample after 3, 6 and 9% deformation in the y direction. The atoms shown are those with centrosymmetry parameters greater than 3 and, therefore, not including the atoms in perfect lattice positions. Figure by author.

For deformation in the x direction, the deformation is initiated in grain 4 from grain boundary 48. Only one slip system is activated, and the dislocations are absorbed by grain boundary 24. For deformation in the y direction two slip systems are activated in grain 1 from various grain boundaries. The response in the two different loading directions cannot be explained by the different Schmid factors alone, but rather is a result of the combination of the Schmid factors and local structures of the grain boundaries. Table 1 shows the Schmid factors for the most favorable slip systems within each grain for tensile deformation in the x direction.

6.4.1 Emission of dislocations from grain boundaries and dislocation debris

The emission of the dislocations is always from the grain boundaries in our simulations and always happens in the form of Shockley partials. It is interesting to note that we observe the emission of both leading and trailing partials, in contrast to simulations performed for smaller grain sizes, where only leading partials are seen [37]. In the sequences of Figures 3 and 4, the emission of leading partials creates stacking faults that disappear upon the emission of the trailing partial in the same slip plane. In the geometry of our samples each grain has two possible slip systems and both can be activated in many grains depending on the loading direction.

Table 1: Schmid Factors for Each Grain

Grain ID	Schmid Factor
1	0.47
2	0.5
3	0.31
4	0.48
5	0.45
6	0.45
7	0.48
8	0.35
9	0.37

Table 2 shows critical resolved shear stress for emission of dislocations during tensile deformation in the x direction from various boundaries. The average critical resolved shear stress for dislocation emission for the various boundaries was 1.7 GPa with a standard deviation of 0.7 GPa. The wide range of values for the critical resolved shear stress shows how significant the atomistic grain boundary structure is for grain boundary dislocation emission.

When both slip systems are activated in a grain, we see the intersection of stacking faults in both slip systems. The process generates dislocation debris that is accumulated as the deformation level is increased. The grains that first emit dislocations are not necessarily those where more debris is accumulated later in the deformation process. This indicates that some of the dislocation sources in the boundaries are exhausted and other sources in different grain boundaries become active.

In our results, transmission of individual dislocations across grain boundaries is a relatively rare event. Most of the dislocations are absorbed by the grain boundaries, without re-emission on the

other side of the boundary in the same location. We do observe that as the grain boundaries emit and absorb dislocations, the local structure changes. These changes can affect the stress necessary for the boundary to emit additional dislocations.

Table 2: Critical Resolved Sheer Stress for Selected Boundaries

Boundary ID	CRSS in Y (GPa)	CRSS in X (Gpa)
12	2.5	2.5
13	0.6	0.6
14	2.4	2.4
15	2.2	2.2
23	1.6	1.6
24	1.0	1.0
25	2.5	2.5
36	1.1	1.1
39	0.7	1.9
46	1.0	1.0
48	1.0	2.4
57	2.4	1.9
59	2.2	0.9
68	1.4	1.8
69	1.9	1.5
78	2.4	2.4
79	1.9	1.5

6.4.2 Formation of deformation twins.

After the emission of a leading Shockley partial, it is possible that instead of the emission of a trailing partial along the same plane, the emission of a second leading partial in an adjacent slip plane occurs. In this case, the formation of a deformation twin occurs. This process is illustrated in Figure 5, which shows the formation of twins in grain 2. The process is similar to that observed at crack tips in previous studies [39]. The formation of twins has also been seen in simulations of nanocrystalline FCC metals as a result of deformation [40] or annealing [41]. The

presence of the twins can stop the glide of other dislocations in the grain, as seen in Figure 5. This can have a significant hardening effect [42]. On the other hand, twinning itself contributes to the deformation process as the width of the twin increases through the emission of leading partial dislocations in subsequent planes.

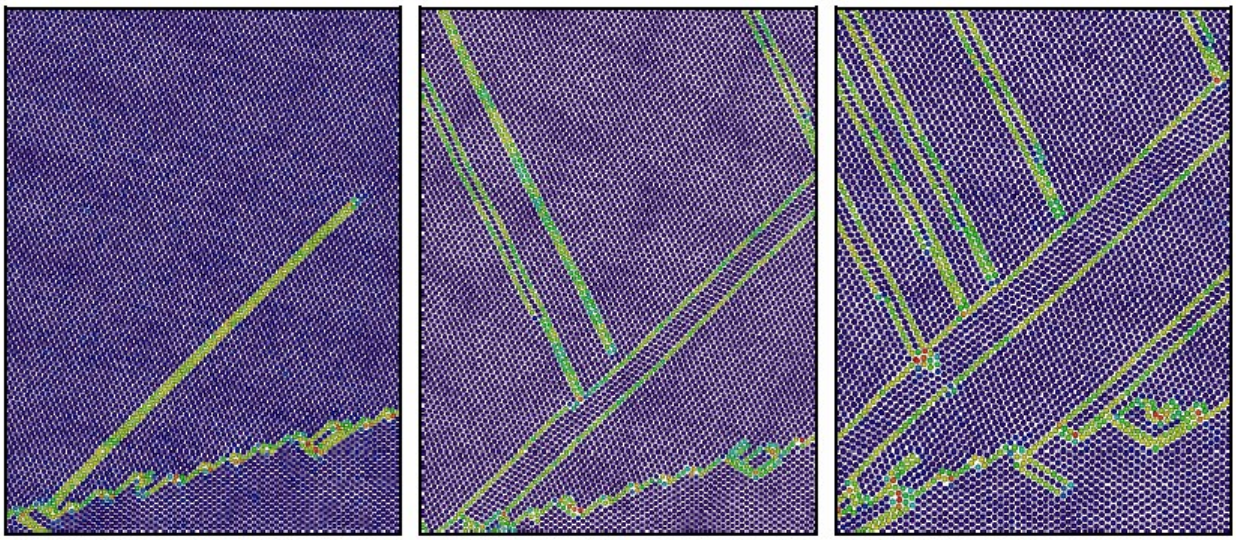

Detail of grain 2 and grain boundary 12 showing the emission of dislocations, the formation of deformation twins, and the intersection of stacking faults and deformation twins. The atoms are colored according to the centrosymmetry parameter, with blue corresponding to values less than 3 (perfect lattice) and green and red showing higher values, up to 10. Figure by author.

6.4.3 Behavior of low angle boundaries

In an effort to understand the role of grain boundary structure on the relative ease of emission of dislocations, we analyzed the particular behavior of special grain boundaries. As mentioned in section 2, the sample contains several low angle boundaries. These are boundaries 24, 59, 68, and 69. Our results show that these low angle boundaries can disappear as a response to the deformation. This is illustrated in the example of Figure 6, where we show the evolution of a region of grain boundary 68 as the deformation level in the x direction is increased. This is a low angle grain boundary of 9.37 degrees misorientation, and its structure consists of a series of

dislocation cores as shown in Figure 6 (a). These dislocation cores that constitute the boundary start gliding at deformation levels larger than 3% and the grain boundary disappears. At the deformation level of 9% shown in Figure 6(c), no boundary is seen, and the structure only shows two stacking faults resulting from emission from a different boundary. This observation points to the idea that for low angle boundaries the emission of dislocations can be thought of as the glide of the existing dislocations that constituted the boundary in the first place. Note that the other low angle boundaries in the sample also tend to disappear or start to disappear as the deformation level is increased. This effect is observed for deformation both in the x and y directions, with the exception of grain boundary 59 under deformation in the y direction. This indicates that both grain boundary structure and load orientation are important. In the next section, we analyze the case of another special grain boundary, vicinal to a twin configuration.

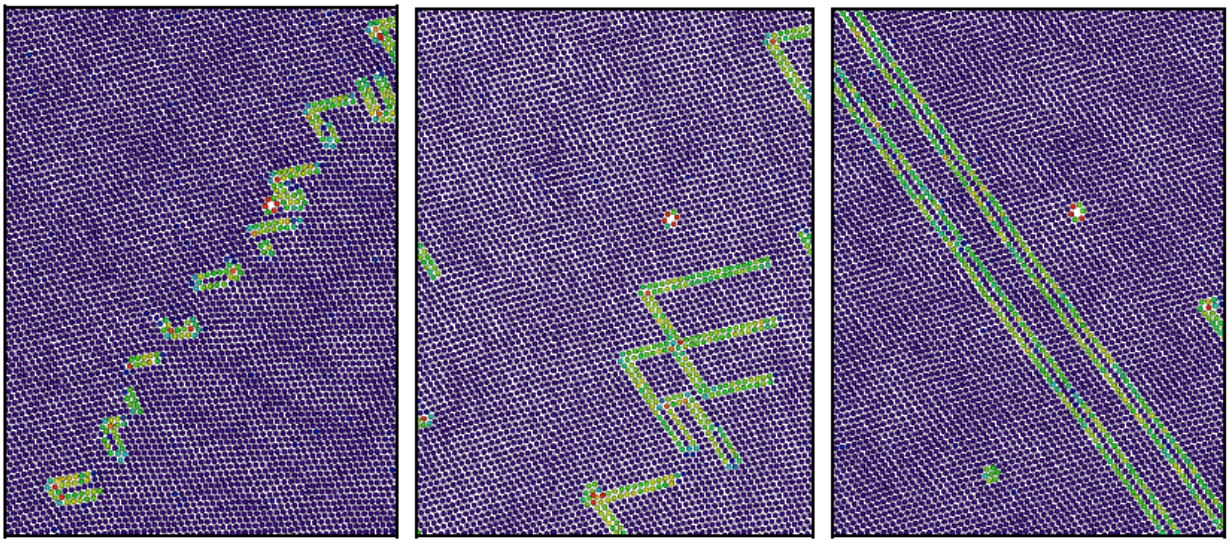

Figure 6: Detail of grain boundary 68, a low angle boundary that disappears as a result of deformation. The atoms are colored according to the centrosymmetry parameter, as in Figure 5. Figure by author.

6.4.4 Behavior of vicinal twin boundaries

The sample contains several boundaries with misorientation angles that are close to that of a Σ=3 twin. Our results show that these boundaries can emit dislocations at relatively low stresses. During deformation along the x axis, one of these boundaries (grain boundary 48) is actually the first one to emit dislocations. Grain boundary 48 is particularly interesting because its misorientation is 58.8 degrees, and the grain boundary plane is actually close to a {111} type plane for grain 8 and {334} type for grain 4. As a result of the emission of dislocations into grain 4, the misorientation becomes closer to that of a twin and the boundary presents regions that have the structure of a perfect twin boundary. This is shown in Figure 7. One could think of the emission process in this particular case as the emission of the secondary grain boundary dislocations that accommodate the deviation of the boundary from the perfect twin. Under a favorable load orientation, these are the first dislocations to be emitted.

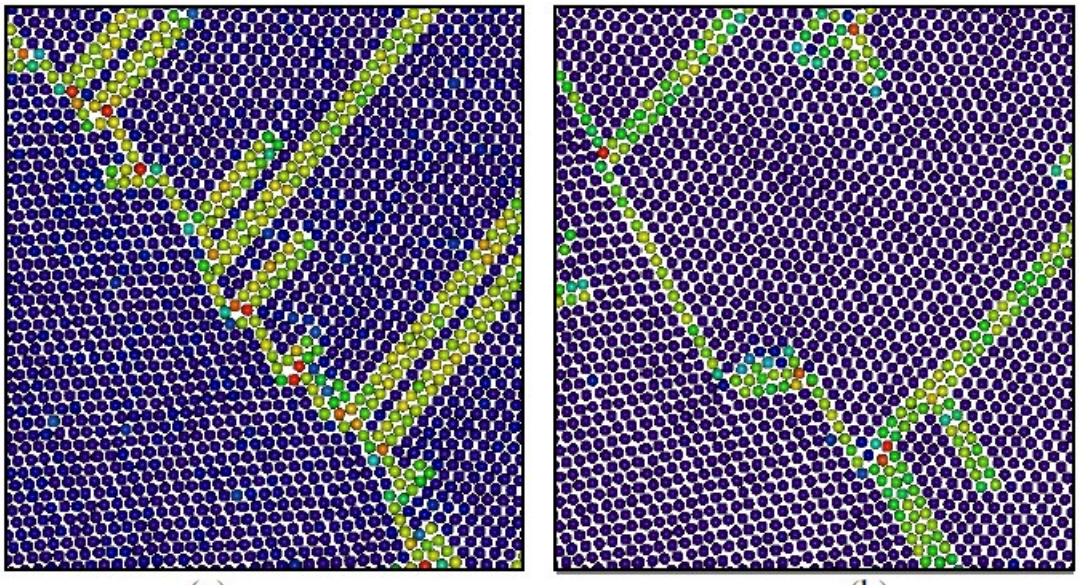

Detail of grain boundary 48, a vicinal twin boundary with a structure that moves closer to a perfect twin as a result of deformation. The atoms are colored according to the centrosymmetry parameter, as in Figures 5 and 6. Figure by author.

6.4.5 Strain Localization

In order to study the development of strain localization during the tensile tests, we generated heterogeneous displacements maps. The heterogeneous displacement was calculated by first dividing all deformed atomic coordinates by the average deformation factor of the sample. The heterogeneous displacement is then the difference between these adjusted deformed coordinates and the initial position of the atom. In this way, the magnitude of the excess displacements represents the local strain over and above the average homogeneous strain of the sample, indicating strain localization. For nanocrystalline metals where grain boundary sliding is a major deformation mechanism, these maps show the different deformation of individual grains resulting from the sliding process. For the results presented here, grain boundary sliding is not a major deformation mechanism. The maps showing heterogeneous strain therefore indicate that the strain localization within the grains is a result of the emission of dislocations. As opposed to simply looking at the dislocation debris in the manner shown in Figures 3 and 4, these maps show where full dislocations have been emitted. Through analyzing the heterogeneous displacement of individual atoms, it is possible to see where the local strain is significantly greater than the overall strain seen by the sample. This allows the identification of areas where large numbers of dislocations have occurred.

Figure 8 shows the strain localization maps obtained for deformation levels of 3, 6 and 9% in the y direction. The color map used is from blue to red where red indicates heterogeneous displacements over 0.4, 0.8, and 1.2 nm for Figures 8 (a), (b), and (c), respectively.

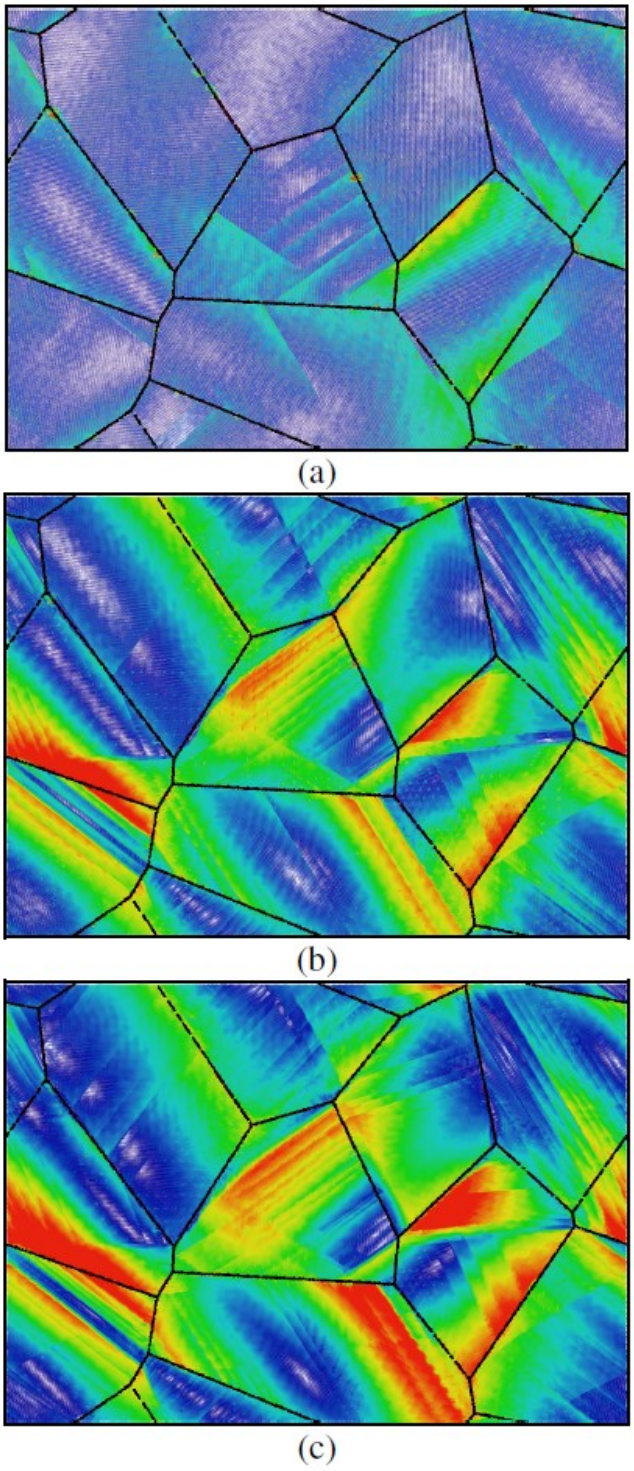

Figure 8: Heterogeneous deformation map for deformation levels of 3, 6, and 9%. The initial positions of the grain boundaries are also shown. The color map used is from blue to red where red indicates heterogeneous displacements over 0.4, 0.8, and 1.2 nm, respectively.
Figure by author.

Strain localization develops as the deformation level is increased due to the fact that each individual boundary or boundary region responds in a different way to applied loading. Figure 8 shows the heterogeneous strain maps and the initial positions of the grain boundaries, but not the

dislocation debris. A detail of the strain localization process for two individual boundaries can be seen in the maps of Figures 9 and 10. Here we show the grain boundaries, dislocation cores, and stacking faults at each deformation level. The color differences indicate the heterogeneous displacements and strain localization, clearly showing that it is caused by the emission of dislocations from the boundaries. Color gradients seen without the presence of stacking faults indicate the emission of full dislocations. In Figure 9, two slip systems become active in grain 1 changing the boundary structure. At a later stage, dislocations are emitted from the same boundary now into grain 4. The top right corner constitutes a favored site for dislocation emission, and therefore creates a site for heterogeneous strain and localized deformation. Figure 10 shows the example of grains 3 (top) and 9 (bottom). Grain 9 has more dislocation activity than grain 3 and heterogeneous strains develop.

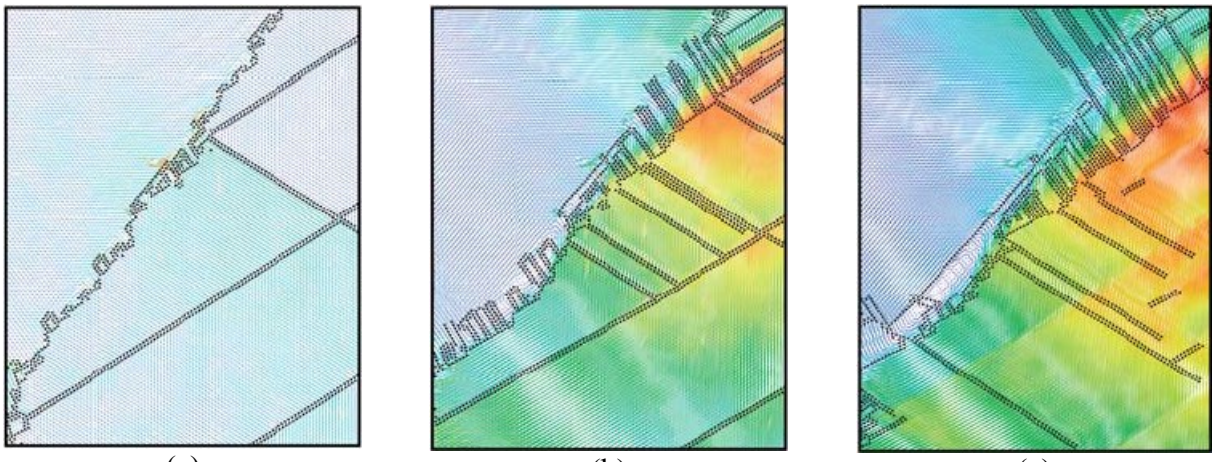

(a) (b) (c)

Figure 9: Details of the heterogeneous deformation map for boundary 14. Deformation levels of 3, 6, and 9%. The color map used is from blue to red where red indicates heterogeneous displacements over 0.4, 0.8, and 1.2 nm, respectively. Atoms with centrosymmetry parameter greater than 3 are also shown, indicating grain boundaries, twins, dislocation cores and stacking faults. Figure by author.

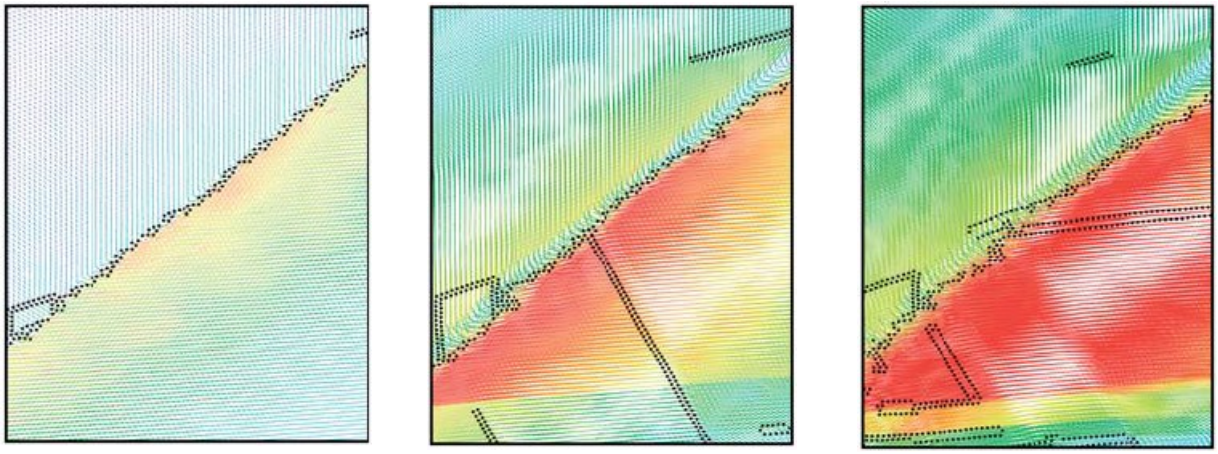

(a) (b) (c)

Figure 10: Details of heterogeneous deformation map for boundary 39. Deformation levels of 3, 6, and 9%. The color map used is from blue to red where red indicates heterogeneous displacements over 0.4, 0.8, and 1.2 nm, respectively. Atoms with centrosymmetry parameter greater than 3 are also shown, indicating grain boundaries, twins, dislocation cores and stacking faults. Figure by author.

6.5 Discussion

We have presented atomic level simulations of the tensile behavior of polycrystalline samples with grains that are large enough to avoid the particular effects of nano-sized grains, namely grain boundary sliding. This is important because these are simulations that are expected to be in the normal Hall-Petch regime, instead of the inverse Hall-Petch observed for very small grain sizes (less than 20 nm) [43]. Atomistic simulation techniques can further the understanding of the deformation process in great detail, including the initiation of plastic deformation through dislocation emission from the grain boundaries, the changes occurring in the grain boundaries as a result of the process, and the interaction of dislocations observed within the grains. The results presented here show the power of the technique, but are subject to limitations arising for the available computing power. The first limitation is one that is common to all molecular dynamics techniques, namely the very fast strain rates used, as compared with experimental technique. This limitation results in higher stresses needed for dislocation emission due to the fact that we

cannot observe thermally activated processes which take longer than the nanosecond timeframe attainable with the simulation technique.

A second important consideration in our simulations is that we have addressed columnar grain structures where all the grain boundaries are of pure tilt character. Most importantly, the columnar structure and the periodicity used along the z axis limits all dislocation lines to be parallel to the Z axis. This makes the nucleation of dislocations more difficult. On the other hand, the columnar grain structure facilitates visualization of the various elements of the sample and it narrows down the spectrum of grain boundaries possible. In that sense, columnar grain structures represent an ideal way to extend simulation work done in bicrystals containing special boundaries to polycrystals with more general boundaries. Other limitations are related to the Voronoi technique used in creating the sample, which may not fully represent experimental microstructures. Finally, one should keep in mind that the grain sizes used here are still not large enough to allow dislocation multiplication through mechanisms such as Frank-Read sources. In experimental samples other defects and impurities may be present that aid in the emission of dislocations.

6.6 Conclusions

Our results represent a study of deformation mainly occurring through dislocations as emitted from random tilt boundaries. The most important result of our simulations is the fact that the local structure of the boundary plays a significant role in the boundary response to loading, and this response is very different for different boundaries as shown in Table 2. This is true even if all boundaries are of pure tilt character. As a result of that, different grain boundaries emit dislocations at significantly different values of the applied stress. The range of critical resolved

shear stress for various boundaries is from 0.63 GPa to 2.5 GPa with an average value of 1.7 GPa and a standard deviation of 0.7. This standard deviation is large compared to the average value. This indicates how significant the individual atomistic structure of each boundary is in responding to tensile stress.

The second major result is that grain boundary structures undergo significant local changes as a result of dislocation emission. The most dramatic case is that of low angle boundaries which are observed to disappear as a result of the deformation process. Dramatic changes are also seen in vicinal twin boundaries, which tend to change to be closer to a perfect twin as a result of the emission process. Vicinal twin boundaries have also been shown to play a role as dislocation sources in nanocrystalline Al [44]. The different response of different boundaries and of different regions of the same boundary results in heterogeneous strain in the sample and strain localization. We show the development of strain localization by mapping the heterogeneous strain in the sample. These heterogeneous strain effects can be very important for the ductility of the material, since strain localization can play a major role in crack nucleation. These effects will be studied in separate work, involving larger deformation levels.

This research shows that grain boundaries play a very important role in dislocation emission and absorption during deformation. Grain boundary response depends upon the characteristics of the individual boundary, including the misorientation angle between grains and orientation with respect to the tensile axis. The different response of the various boundaries can lead to significant strain localization.

6.7 Acknowledgements:

This work was supported by the Department of Energy, Office of Basic Energy Sciences, under grant DE-FG02-08ER46525 and the National Science Foundation, IRD program. The authors acknowledge Advanced Research Computing at Virginia Tech for providing computational resources and technical support that have contributed to the results reported within this paper. URL: http://www.arc.vt.edu

References:

[1] V. Vitek, A. P. Sutton, D. A. Smith, and R. C. Pond, "Structure of grain-boundary dislocations," *Philosophical Magazine a-Physics of Condensed Matter Structure Defects and Mechanical Properties,* vol. 39, pp. 213-224, 1979.

[2] M. W. Finnis and J. E. Sinclair, "A simple empirical n-body potential for transition-metals," *Philosophical Magazine a-Physics of Condensed Matter Structure Defects and Mechanical Properties,* vol. 50, pp. 45-55, 1984.

[3] M. S. Daw, S. M. Foiles, and M. I. Baskes, "The embedded-atom method - a review of theory and applications," *Materials Science Reports,* vol. 9, pp. 251-310, Mar 1993.

[4] F. Ercolessi and J. B. Adams, "Interatomic potentials from 1st-principles calculations - the force-matching method," *Europhysics Letters,* vol. 26, pp. 583-588, Jun 1994.

[5] V. Vitek, "Interatomic forces in relation to the theory of dislocations," *Philosophical Magazine a-Physics of Condensed Matter Structure Defects and Mechanical Properties,* vol. 58, pp. 193-212, Jul 1988.

[6] C. H. Henager and R. G. Hoagland, "Dislocation and stacking fault core fields in fcc metals," *Philosophical Magazine,* vol. 85, pp. 4477-4508, Dec 2005.

[7] S. G. Srinivasan, X. Z. Liao, M. I. Baskes, R. J. McCabe, Y. H. Zhao, and Y. T. Zhu, "Compact and Dissociated Dislocations in Aluminum: Implications for Deformation," *Physical Review Letters,* vol. 94, p. 125502, 2005.

[8] P. Szelestey, M. Patriarca, and Y. Kaski, "Computational study of core structure and Peierls stress of dissociated dislocations in nickel," *Modelling and Simulation in*

Materials Science and Engineering, vol. 11, pp. 883-895, Nov 2003.

[9] B. J. Pestman, J. T. M. Dehosson, V. Vitek, and F. W. Schapink, "Interaction between lattice dislocations and grain-boundaries in fcc materials," *Scripta Metallurgica,* vol. 23, pp. 1431-1435, Aug 1989.

[10] B. J. Pestman, J. T. M. Dehosson, V. Vitek, and F. W. Schapink, "Atomic-structure calculations of the interaction between lattice dislocations and grain-boundaries," in *Symp on Atomic Scale Calculations of Structure in Materials*, San Francisco, Ca, 1990, pp. 205-210.

[11] A. P. Sutton, D. A. Smith, and V. Vitek, "Atomistic study of the structure of grain-boundary dislocations," *Journal of Microscopy-Oxford,* vol. 116, pp. 97-104, 1979.

[12] M. Tschopp and D. L. McDowell, "Atomistic simulations of grain boundary dislocation nucleation," in *International Conference on Heterogeneous Material Mechanics (ICHMM)*, Huangshan, Peoples R China, 2008, pp. 97-104.

[13] M. A. Tschopp and D. L. McDowell, "Atomistic simulations of grain boundary dislocation nucleation," in *Hael Mughrabi Honorary Symposium held at the 2008 Annual TMS Meeting and Exhibition*, New Orleans, LA, 2008, pp. 29-34.

[14] M. A. Tschopp and D. L. McDowell, "Grain boundary dislocation sources in nanocrystalline copper," *Scripta Materialia,* vol. 58, pp. 299-302, Feb 2008.

[15] M. A. Tschopp and D. L. McDowell, "Dislocation nucleation in Sigma 3 asymmetric tilt grain boundaries," *International Journal of Plasticity,* vol. 24, pp. 191-217, 2008.

[16] M. A. Tschopp, G. J. Tucker, and D. L. McDowell, "Atomistic simulations of tension-compression asymmetry in dislocation nucleation for copper grain boundaries," *Computational Materials Science,* vol. 44, pp. 351-362, Dec 2008.

[17] M. Finnis, "Interatomic Forces in Condensed Matter," *Oxford University Press,* pp. 129-186, 2003.

[18] Y. Mishin, D. Farkas, M. J. Mehl, and D. A. Papaconstantopoulos, "Interatomic potentials for monoatomic metals from experimental data and ab initio calculations," *Physical Review B,* vol. 59, pp. 3393-3407, Feb 1999.

[19] S. Plimpton, "Fast parallel algorithms for short-range molecular-dynamics," *Journal of Computational Physics,* vol. 117, pp. 1-19, Mar 1995.

[20] H. Van Swygenhoven, A. Caro, and D. Farkas, "A molecular dynamics study of

polycrystalline fcc metals at the nanoscale: grain boundary structure and its influence on plastic deformation," *Materials Science and Engineering a-Structural Materials Properties Microstructure and Processing,* vol. 309, pp. 440-444, 2001.

[21] J. Schiotz, "Atomic-scale modeling of plastic deformation of nanocrystalline copper," *Scripta Materialia,* vol. 51, pp. 837-841, Oct 2004.

[22] J. Schiotz and K. W. Jacobsen, "A maximum in the strength of nanocrystalline copper," *Science,* vol. 301, pp. 1357-1359, Sep 2003.

[23] D. Wolf, V. Yamakov, S. R. Phillpot, A. Mukherjee, and H. Gleiter, "Deformation of nanocrystalline materials by molecular-dynamics simulation: relationship to experiments?," *Acta Materialia,* vol. 53, pp. 1-40, Jan 2005.

[24] V. Yamakov, D. Wolf, S. R. Phillpot, A. K. Mukherjee, and H. Gleiter, "Deformation-mechanism map for nanocrystalline metals by molecular-dynamics simulation," *Nature Materials,* vol. 3, pp. 43-47, Jan 2004.

[25] J. A. Moriarty, V. Vitek, V. V. Bulatov, and S. Yip, "Atomistic simulations of dislocations and defects," *Journal of Computer-Aided Materials Design,* vol. 9, pp. 99-132, 2002.

[26] Z. H. Jin, P. Gumbsch, K. Albe, E. Ma, K. Lu, H. Gleiter*, et al.*, "Interactions between non-screw lattice dislocations and coherent twin boundaries in face-centered cubic metals," *Acta Materialia,* vol. 56, pp. 1126-1135, Mar 2008.

[27] Z. H. Jin, P. Gumbsch, E. Ma, K. Albe, K. Lu, H. Hahn*, et al.*, "The interaction mechanism of screw dislocations with coherent twin boundaries in different face-centred cubic metals," *Scripta Materialia,* vol. 54, pp. 1163-1168, Mar 2006.

[28] M. de Koning, R. J. Kurtz, V. V. Bulatov, C. H. Henager, R. G. Hoagland, W. Cai*, et al.*, "Modeling of dislocation-grain boundary interactions in FCC metals," in *Workshop on Modeling and Experimental Validation*, Les Diableret, Switzerland, 2002, pp. 281-289.

[29] J. P. Hirth, "Influence of grain boundaries on mechanical properties," *Metallurgical Transactions,* vol. 3, pp. 3047-3067, 1972.

[30] J. P. Hirth, "Defect structures in grain boundaries," *Acta Metall,* vol. 22, pp. 1023-1031, 1974.

[31] L. E. Murr, "Some observations of grain-boundary ledges and ledges as dislocation sources in metals and alloys," *Metallurgical Transactions,* vol. A 6, pp. 505-513, 1975.

[32] Y. Shen and P. M. Anderson, "Transmission of a screw dislocation across a coherent, non-

slipping interface," *Journal of the Mechanics and Physics of Solids,* vol. 55, pp. 956-979, May 2007.

[33] D. E. Spearot, K. I. Jacob, and D. L. McDowell, "Dislocation nucleation from bicrystal interfaces with dissociated structure," *International Journal of Plasticity,* vol. 23, pp. 143-160, 2007.

[34] D. E. Spearot, K. I. Jacob, and D. L. McDowell, "Nucleation of dislocations from [001] bicrystal interfaces in aluminum," *Acta Materialia,* vol. 53, pp. 3579-3589, Aug 2005.

[35] D. E. Spearot, M. A. Tschopp, and D. L. McDowell, "Orientation and rate dependence of dislocation nucleation stress computed using molecular dynamics," *Scripta Materialia,* vol. 60, pp. 675-678, Apr 2009.

[36] H. Van Swygenhoven, D. Farkas, and A. Caro, "Grain-boundary structures in polycrystalline metals at the nanoscale," *Physical Review B,* vol. 62, pp. 831-838, 2000.

[37] D. Farkas and W. A. Curtin, "Plastic deformation mechanisms in nanocrystalline columnar grain structures," *Materails Science and Engineering A* vol. 412, pp. 316-322, Dec 17-19 2005.

[38] C. L. Kelchner, S. J. Plimpton, and J. C. Hamilton, "Dislocation nucleation and defect structure during surface indentation," *Physical Review B,* vol. 58, pp. 11085-11088, Nov 1998.

[39] D. Farkas, M. Duranduru, W. A. Curtin, and C. Ribbens, "Multiple-dislocation emission from the crack tip in the ductile fracture of Al," *Philosophical Magazine a-Physics of Condensed Matter Structure Defects and Mechanical Properties,* vol. 81, pp. 1241-1255, May 2001.

[40] A. G. Froseth, P. M. Derlet, and H. Van Swygenhoven, "Twinning in nanocrystalline fcc metals," *Advanced Engineering Materials,* vol. 7, pp. 16-20, Jan 2005.

[41] D. Farkas, E. Bringa, and A. Caro, "Annealing twins in nanocrystalline fcc metals: A molecular dynamics simulation," *Physical Review B,* vol. 75, p. 5, May 2007.

[42] L. Lan and M. G. Nasr, "Twin-size effects on the deformation of nanotwinned copper," *Physical Review B (Condensed Matter and Materials Physics),* vol. 79, p. 075444, 2009.

[43] K. S. Kumar, H. Van Swygenhoven, and S. Suresh, "Mechanical behavior of nanocrystalline metals and alloys," *Acta Materialia,* vol. 51, pp. 5743-5774, Nov 2003.

[44] A. G. Froseth, P. M. Derlet, and H. Van Swygenhoven, "Vicinal twin boundaries

providing dislocation sources in nanocrystalline Al," *Scripta Materialia,* vol. 54, pp. 477-481, Feb 2006.

7. Non-planar grain boundary structures in fcc metals and their role in nanoscale deformation mechanisms

Laura Smith and Diana Farkas

This chapter has been published in Philosophical Magazine 2014, Volume 94, Issue 2, pages 152-173. It is used here with permission.

7.1 Abstract

This work presents the results of a comparative molecular dynamics study showing that relaxed random grain boundary structures can be significantly non-planar at the nano-scale in fcc metals characterized by low stacking fault values. We studied the relaxed structures of random [110] tilt boundaries in a poly-crystal using interatomic potentials describing Cu and Pd. Grain boundaries presenting non-planar features were observed predominantly for the Cu potential but not for the Pd potential and we relate these differences to the stacking fault values. We also show that these non-planar structures can have a strong influence on dislocation emission from the grain boundaries as well as on grain boundary strain accommodation processes, such as grain boundary sliding. We studied the loading response in polycrystals of 40nm grain size to a level of 9% strain and found that the non-planar grain boundaries favor dislocation emission as a deformation mechanism and hinder grain boundary sliding. This has strong implications for the mechanical behavior of nanocrystalline materials, which is determined by the competition between dislocation activity and grain boundary accommodation of the strain. Thus, the two interatomic potentials for Cu and Pd considered in this work resulted in the same overall stress-strain curve, but significantly different fractions of the strain accommodated by the inter-granular versus intra-granular deformation mechanisms. Strain localization patterns are also influenced by the non-planarity of the grain boundary structures.

7.2 Introduction

It is well known that specific grain boundary structure and its constituent defects[1] can significantly affect the properties of metallic materials[2]. This is particularly true in materials with features at the nano-scale[3]. Using atomistic techniques, significant progress has been made in understanding the structures of general grain boundaries in fcc materials. Van Swygenhoven, Farkas and Caro[4] have shown that the structure of random boundaries is composed of regions of highly ordered structures, similar to special coincident site boundaries, and regions that are highly disordered in nature. Tschopp and McDowell[5] studied the structure and energy of asymmetric tilt grain boundaries in Cu and Al, finding that some asymmetric boundaries faceted as part of the relaxation process. Brown and Mishin[6] found dissociation and faceting of asymmetrical grain boundaries in Cu. Yet, no specific study has been performed on the possibility and consequences of non-planar features in the grain boundary structure of metallic materials. These consequences can be particularly important in nano-crystalline materials with a large fraction of grain boundaries.

A large effort has been devoted to studying the relationship between grain boundary structure and mechanical response of the grain boundaries, because of the great interest in the mechanical properties of nanocrystalline materials. These relationships have been investigated via both experimental and simulation methods[7-12]. Several deformation mechanisms are known to occur in the nano-scale regime, including dislocation emission and motion, deformation twinning, grain boundary sliding with coupled migration, and grain rotation. Previous work has focused on deformation twinning in Al[7] and Cu[13], dislocation nucleation and propagation[14], and grain boundary sliding[15] as deformation mechanisms. Understanding how deformation processes proceed at the nanoscale may help explain the mechanisms by which

the Hall-Petch and the inverse Hall-Petch effect for smaller grain sizes are active. For example, Godon et al[16] discuss the Hall-Petch effect down to the nanoscale region by postulating a combination of grain boundary sliding and dislocation emission. Van Swygenhoven and co-workers[17] postulated this competition in 1999. Vo and co-workers[18] recognized the importance of this work as well and also showed that dislocation emission and grain boundary sliding are competing processes in deformation at the nano-scale and proposed a method to quantify this competition. Schiotz and Jacobsen[19] furthered this work by analyzing deformation mechanism shifts in copper with grain sizes ranging from 5 to 50nm, finding that the shift from grain boundary sliding to crystallographic slip occurs as the grain size increases.

It is also known that different interatomic potentials can produce different behavior when a digital sample is subject to strain. For example, in studies conducted via molecular dynamics simulations, Becker and co-workers[20] showed that the accuracy of the results of simulated mechanical behavior is dependent on the stacking fault energies predicted by the potentials used in the simulation. It is therefore logical to expect some possible effects of the interatomic potential on grain boundary structure. Holm, Olmstead and Foiles[21] performed a comparative study of grain boundary energetics in various fcc metals. They found that, in general, grain boundary energies in different elements are strongly correlated. Consistent with a dislocation model for grain boundary structure, the boundary energy scales with the shear modulus. Most interestingly, they found that when a series of boundaries is considered, there is more scatter in the data for high stacking fault energy metals than for the low stacking fault energy elements. This suggests there is an effect of stacking fault energy on grain boundary structure.

In the present work, we present a molecular dynamics study using interatomic potentials developed for two fcc metals with significantly different stable stacking fault energies: Cu and

Pd. Despite the differences in stable stacking fault energies, these potentials result in similar stress-strain behavior. We report noticeably different relaxed grain boundary structures with Cu presenting significantly non-planar grain boundaries. As a consequence of the difference in grain boundary structures, each responds to applied strain with different predominant deformation mechanisms, yet present substantially similar stress-strain behavior.

7.3 Simulation techniques

The Voronoi construction used to generate the columnar samples used in this work is similar to that used in our previous work[22-24]. The samples have 9 grains with an average 40nm grain size and about a million atoms. The sample is fully periodic in all directions; the periodicity along the z axis is the lattice periodicity along the [110] direction common to all grains. All the grain boundaries in the sample are of pure tilt character around the [110] axis with random misorientation angles as well as random orientations of the grain boundary planes. We note that this generation technique creates a quasi-2D sample in which only straight line dislocations are possible. Also, the 40 nm grain size is too small to encourage dislocation multiplication and generation through Frank-Read source type mechanisms. For an adequate comparison, exactly the same sample and deformation procedure was used with the two different interatomic potentials. The only procedure needed to ensure that the exact same generated sample was appropriate for simulation runs using different interatomic potentials was to adjust the size of the sample to accommodate the different lattice parameters of the potentials of interest. In this way any differences observed in the sample relaxed structure and response are a result of using different interatomic potentials. This is true despite the standard limitations of the molecular dynamics techniques, such as the high strain rate resulting from the extremely short timescale

imposed by computational time constraints. This limitation also prevents the observation of thermally-activated deformation mechanisms and presents difficulty in comparing this work to experimentally-generated results.

The molecular dynamics (MD) implementation used in this simulation work is that of LAMMPS [25], with a Nosé-Hoover thermostat and barostat. The two EAM interatomic potentials used in this work were that of Mishin et al. for Cu [26] and that of Foiles et al. for Pd [27].

The samples were equilibrated using molecular dynamics for 100 ps at 300 K in order to achieve a relaxed grain boundary structure. Once relaxed samples were obtained, virtual mechanical testing was performed. The deformation was strain-controlled utilizing standard MD at 300K along the horizontal axis up to 9% strain with a constant strain rate of $3x10^{8}s^{-1}$. The pressure was maintained at zero in the directions perpendicular to the tensile axis. The total stress on the sample can be calculated from the simulation, obtaining standard stress-strain curves for the strain controlled virtual tensile testing. Note that the tensile axis is perpendicular to the [110] direction common to all grains in the sample.

Simulation results were visualized utilizing the centrosymmetry [28] parameter in molecular visualization packages, such as OVITO [29]. This allowed visualization of grain boundary structure as well as the dislocation emission process and twin formation. The strain level at which a particular boundary emits the first dislocation can also be monitored in this way, and the number of dislocations emitted thereafter can be assessed quantitatively.

Grain boundary sliding was investigated using a simple technique where a group of atoms containing the particular grain boundary to be studied is extracted from the sample. The same group of atoms is visualized as the deformation proceeds. Grain boundary sliding becomes evident as atoms in the two different grains are displaced in different directions parallel to the

plane of the grain boundary. This method allows a quantitative measure of the extent of grain boundary sliding. In this way we could observe the difference in the grain boundary sliding distances for the same boundary using the two different interatomic potentials. Coupled grain boundary motion was also evident using this technique.

In order to study the possible localization of the response to strain, we used a technique in which the local atomic displacement for each atom is compared with what it would have been in a totally homogeneous deformation of the sample, obtaining the heterogeneous displacement magnitude for each atom. Based on this comparison, heterogeneous strain distribution maps can be created by color-coding the sample microstructure by the magnitude of the heterogeneous displacement vectors. This simple technique does not actually analyze elastic versus plastic processes [30] but it does give a picture of how the strain is distributed in the sample. This technique is similar to that developed in our previous work[8, 10]. For homogeneous deformation this magnitude should be zero and it is increasingly larger in areas where the deformation process was not homogeneous. Color-coding by the length of the displacement vector calculated in this way reveals regions of heterogeneous deformation in the sample.

Table I shows tabulated critical parameters for the two potentials utilized in this work. The elastic constants C_{11}, C_{12}, and C_{44} were checked for consistency by using the method of Mehl et al [31]. The values obtained agree well with the values reported in the work of Mishin[26] and Foiles [32], respectively. The stable stacking fault (γ_{SF}) values for these two potentials are significantly different: the Cu potential having a γ_{SF} of 44.4mJ/m^2 [26] and the Pd potential γ_{SF} being 187mJ/m^2 [32]. While the stable stacking fault values differ by a factor of about 4, the unstable stacking fault values for these two potentials are more similar, differing only by about 30%. Twinning energies are also similar, differing by about 12%

Table I: Critical parameters for the Cu and Pd potentials utilized in this work.

Potential	Cohesive Energy (eV)	Lattice Constant (Å)	C_{11} (GPa)	C_{12} (GPa)	C_{44} (GPa)	Stable SFE (mJ/m^2)	Unstable SFE (mJ/m^2)	Twinning Energy (mJ/m^2)
Cu	-3.54	3.61	169.88	122.59	76.21	44.4[26]	158[26]	160[11]
Pd	-3.91	3.89	239.49	173.72	65.73	187[32]	210[32]	180[11]

7.4 Results

7.4.1. Grain boundary relaxation structure

Local structures of the grain boundaries obtained following relaxation with the two potentials show significant differences. Figures 1(a) and 1(b) show the overall structures of the sample after relaxation using the Cu and Pd potentials, respectively. Coloration in the images is based on the centrosymmetry parameter [28], with blue indicating perfect fcc structure while green and red show increasing levels of lattice disruption. Stacking faults are shown in green. Figure 1(a) shows close-up views of example regions of several grain boundaries in the Cu sample. Grain boundaries in the sample are labeled by the grains they interface. For example, the boundary between grains 1 and 2 will be labeled as grain boundary 1-2. In grain boundary 4-8, shown on the far left, non-planar boundary structures have developed during the relaxation process and include features not contained in the gran boundary plane that extend into the surrounding grain. Examples are shown for grain boundaries 4-8, 1-4, 1-3, and 4-7. All show non-planar grain boundary structures in Cu and planar grain boundary structures in Pd. Locally, these non-planar features resemble nascent stacking faults. Orange lines indicate the disruption of the local structure in the grain at right. On the far right, there is little disruption, while in the non-planar structure the offset can be clearly noted. These features can be seen as caused by the glide into the grain of intrinsic grain boundary dislocations with Burgers vector of the Shockley partial

type. This process lowers the energy of the atomic arrangement in the grain boundary plane but involves the creation of extra stacking fault area inside the grain. The presence or absence of these features in the relaxed grain boundary structure will be dictated by the balance of these two energy terms. The low stacking fault energy of Cu makes it much more energetically favorable for these features to appear when compared to the case of Pd with much higher stacking fault energy. The 9R structure that has been observed both experimentally and in simulation [33, 34] is a possible explanation for non-planarity, but was not found in our samples. Figure 1(b) shows the same region of grain boundary 4-8 in the Pd sample, with a more planar relaxed grain boundary structure. Examining the same regions in Pd where the non-planar features appeared in Cu shows structural regions with high excess volume that can be recognized as structural units found in studies of [110] symmetrical tilt boundaries and known as E-units[5]. These are noted in the figure by the red triangular outlines. This grain boundary structure is clearly confined to the plane of the boundary and does not extend into the surrounding grain. The non-planar structures are observed in all shown Cu boundaries, while when the same boundary region is inspected for Pd, they are present for only grain boundaries 4-8 and 1-3. The average length of the the non-planar features or nascent stacking faults found in the relaxed Cu grain boundaries is 0.941nm whereas non-planar features were hardly present in the same boundaries relaxed using the Pd potential.

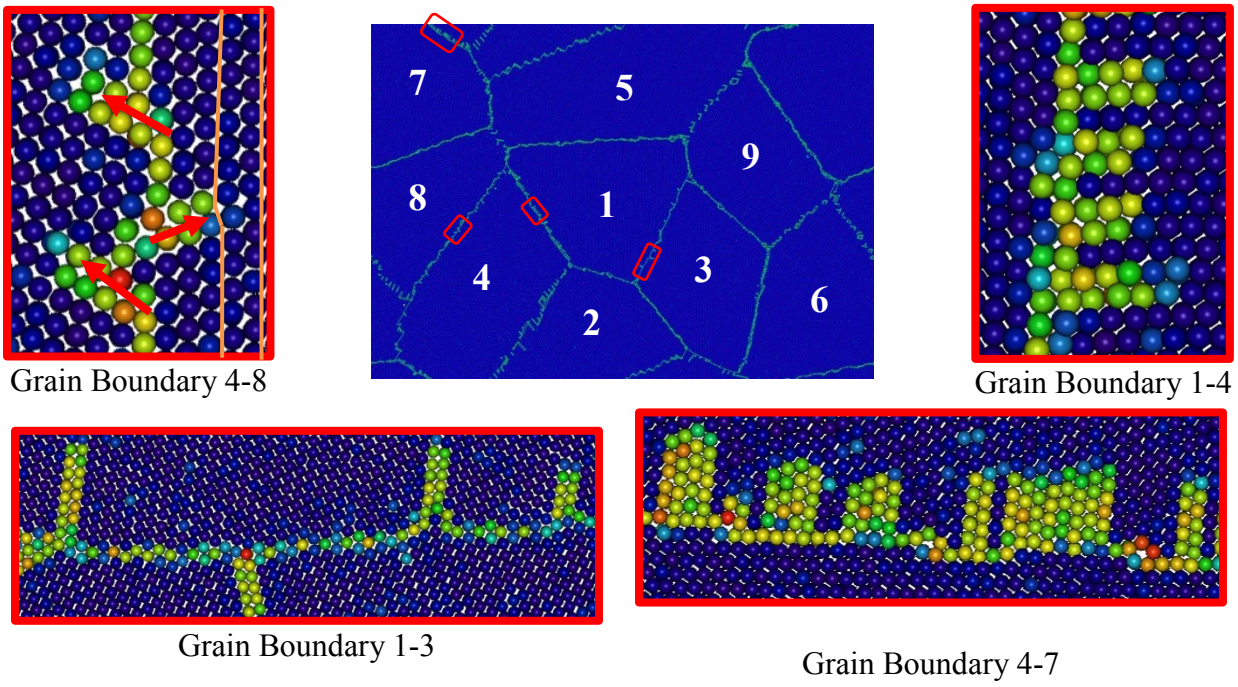

(a)

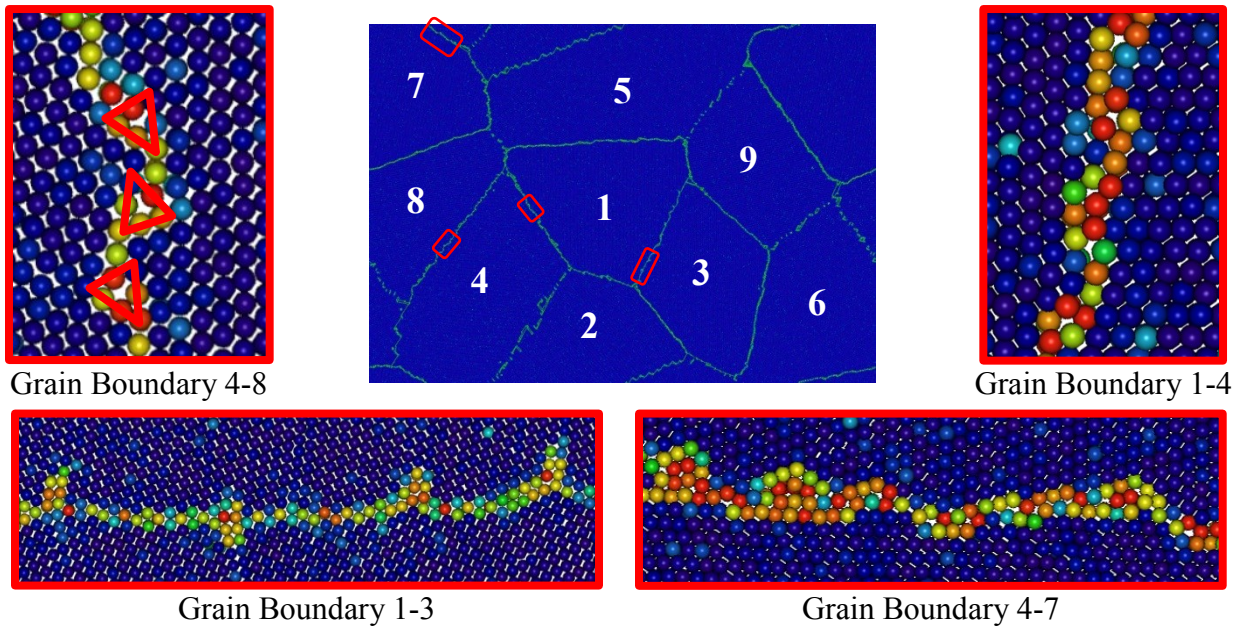

(b)

Figure 1: Post-relaxation grain boundary configurations. Callouts highlight grain boundaries 1-4. 1-3, 4-8, and 4-7. (a) The Cu sample shows significantly more non-planar structures in all highlighted regions. (b) The Pd sample shows fewer non-planar structures in each region and an increase in the planar e-unit structures. Figure by author.

7.4.2 Stress-strain behavior

Stress-strain curves were generated for each potential as the strain level on the samples was increased. As shown in Figure 2, the two curves obtained are essentially similar up to 5% deformation, and show a difference of less than 15% for later deformation levels. Using the method shown in Hopcroft, Nix, and Kenny[35] which uses the elastic constants of the material (Table 1) and accounts for the [110] texture in these samples, the elastic modulus of Cu was predicted to be 131 GPa, and 145 GPa for Pd. The elastic modulus for each curve was calculated by doing a linear fit to the data up to 0.5% strain. Results show a modulus of 113 GPa for the Cu potential and 100 GPa for the Pd potential. This represents a 14% difference for Cu and a 30% difference for Pd which may be accounted for by the high proportion of grain boundaries in our sample.

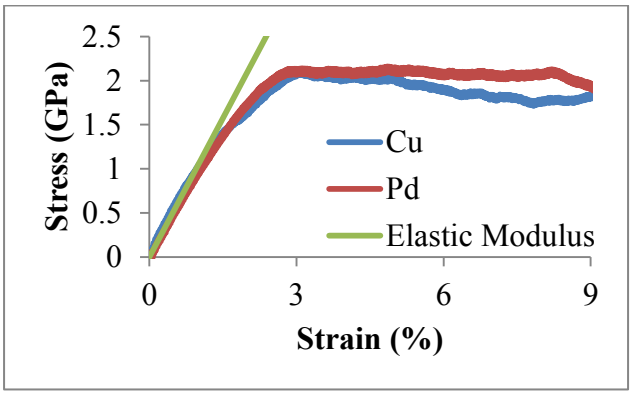

Figure 2: Stress-strain curves obtained for the Cu and Pd potentials showing similar behavior. Differences are not noted until about 5% strain. Figure by author.

The yield strengths observed in this simulation for Cu and Pd are 1.3 GPa and 1.6 GPa, respectively. These values were obtained by the 0.2% offset yield strength criteria. The values of the yield strength differ by about 30%, which correlates well with the difference that the two potentials have in unstable stacking fault energy values. The details of the deformation

mechanisms were analyzed to see any major differences that can be attributed to different grain boundary structures observed in the two samples.

7.4.3 Dislocation emission as a deformation mechanism

Figure 3 shows the behavior of grain boundary 4-8, shown in Figure 1, as strain is applied. The images contain the exact same group of atoms at three different strain levels. In each image atoms are color-coded by centrosymmetry[28] parameter; with blue indicating atoms in perfect lattice positions. Green and red atoms indicate increasing amounts of lattice disruption. Figure 3(a) shows the relaxed boundary of the Cu sample at 0% strain. Figures 3(b) and 3(c) show the boundary at 1 and 2% strain. The boundary response to the low levels of strain shown in these images indicates that the non-planar grain boundary structures in the Cu sample constitute the favored sites for dislocation emission. As the non-planar features grow, the boundary becomes increasingly non-planar. The non-planar structures have extended and grown into stacking faults left by the emission of Shockley partial dislocations. The partial dislocations emitted in these cases are not necessarily part of a full dislocation that has dissociated located in the grain boundary. In contrast, the grain boundaries shown in Figures 3(d), 3(e), and 3(f) that show the same group of atoms in the Pd sample contain E-units with excess volume. The boundary structures observed for Pd at 0 and 1% strain do not shown the same type of stacking fault formation as in the Cu case. A higher, 2% strain level must be reached before dislocations begin to be emitted from this grain boundary. The dislocations are emitted from the E-unit sites, in a process that is consistent with findings for special boundaries where the E-units are the favored sites for dislocation nucleation[36-41]. Our findings show that the E-structural units are preferred sites for the nucleation of Shockley partial dislocations from random grain boundaries. The non-

planar boundary structures observed in the low stacking fault potential constitute sites for dislocation emission at stress levels that are clearly lower than those required for the emission from the planar grain boundary e-unit structures.

In order to understand the implications of the non-planar structures for the overall deformation behavior of the sample, a quantitative evaluation of the dislocation emission process was performed by counting the total number of partial dislocations emitted from grain boundaries in the sample as the strain was increased. Figure 4 shows the cumulative number of dislocations emitted from 0 to 9% strain. The Cu sample emits significantly more dislocations than the Pd sample under the same strain loading conditions by a factor of approximately 1.6. At 1% strain both samples emit similar numbers of dislocations. By about 2% strain, the Cu sample emits more dislocations than Pd at each strain level observed. Over the course of the straining process Cu emitted a total of 1245 partial dislocations. In contrast, Pd emitted 818. This is due to the difference in relaxed grain boundary structure, which in turn can be attributed to the lower stacking fault energy for Cu as compared to Pd. Our results therefore clearly show that there is a greatly reduced dislocation activity in the Pd sample as compared to the Cu sample. Since the overall mechanical response of the two model samples is about the same, as indicated in Figure 2, we conclude that deformation mechanisms other than dislocation emission have to be more active in Pd than in Cu. In the next section we discuss twinning observed in both model materials.

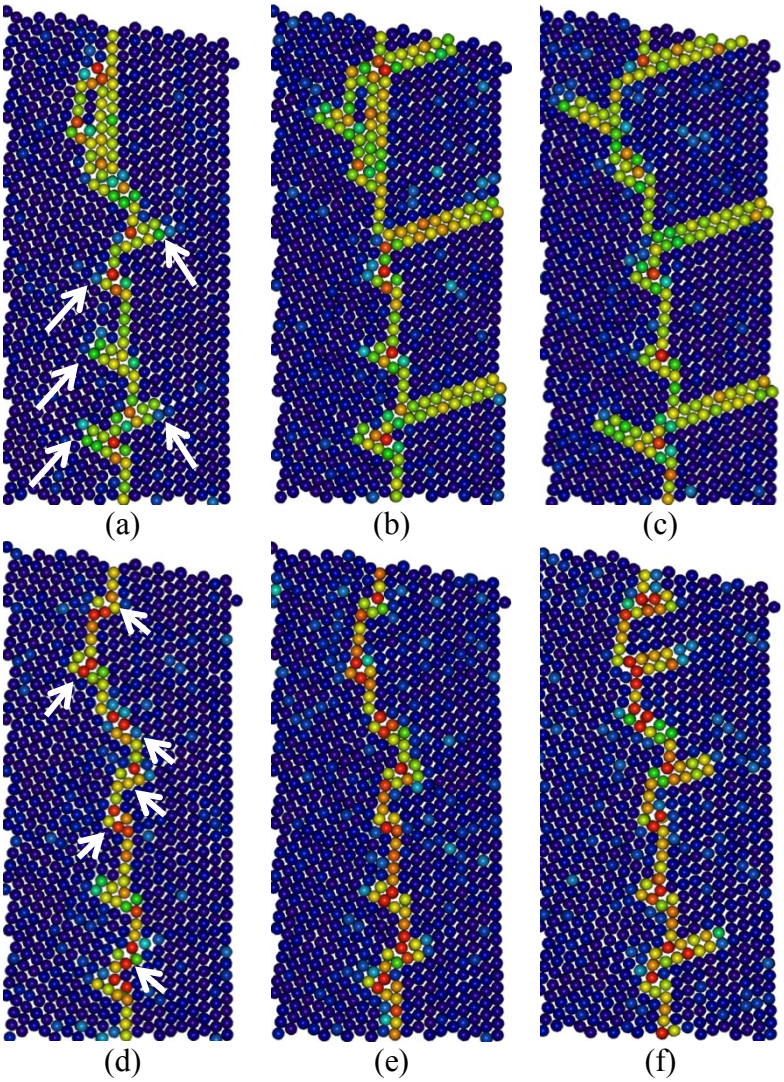

Figure 3: Boundary 4-8 deformation behavior in the Cu and Pd samples. Images show the exact same atoms for each sample at each strain level. Color is by centrosymmetry. Blue shows perfect fcc structure while green indicates lattice disruption consistent with stacking faults. (a-c) show Cu while (d-f) shows Pd. (a) 0% strain showing initial relaxation configuration featuring 5 incipient stacking faults. (b) 1% strain indicating the stacking faults have started to extend. (c) 2% strain, showing the extension of the stacking faults has continued under increasing deformation. (d) 0% strain, showing fewer incipient stacking faults and a higher proportion of planar E structural units. (e) 1% strain, showing little change in the structure of the boundary. (f) 2% strain. 4 of the non-planar e-units have emitted partial dislocations to form short stacking faults. Figure by author.

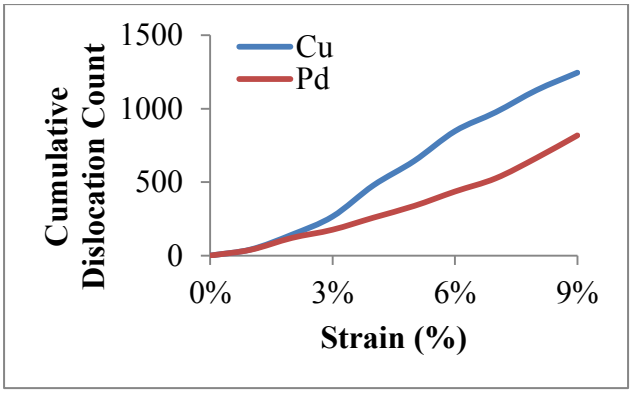

Figure 4: Cumulative number of partial dislocations emitted in the sample as a function of strain. As strain increases, the Cu sample is emitting significantly more dislocations in order to accommodate the applied strain than the Pd sample. Figure by author.

7.4.4 Twin formation

A second deformation mechanism active at the nano-scale is the formation of deformation twins. Twinning occurs when a series of leading partial dislocations are emitted in adjacent compact planes with each additional dislocation broadening the twinned region without any additional planar defect energy. Twin boundaries present in nanocrystalline materials are known to significantly affect deformation behavior[42-44]. In many fcc materials, such as Cu, twins typically increase strength by acting as obstacles to the motion of dislocations within the grains[45-48]. In a recent study Stukowski, Albe and Farkas compared twinned and non-twinned samples studying the effect of twins on the deformation behavior of nanocrystalline Cu and Pd. While Cu shows hardening due to the presence of twins, Pd shows the opposite effect. A quantitative dislocation analysis method was applied and a statistical analysis of the occurring dislocation types showed that twin boundaries can be effective sources for twinning dislocations, which are the reason for the observed softening in some fcc materials. An important conclusion of that work showed that twins can contribute to deformation in Pd by producing a softening effect. We have found that this effect is also present in the Pd sample used in the present work, with twinning contributing to deformation.

This phenomenon is shown in Figure 5. Figures 5(a) and 5(e) show the grain at 0% strain, just after relaxation, for the Cu and Pd samples respectively. In Figures 5(b) and 5(f) at 3% strain, dislocations have begun to be emitted from a grain boundary (2-5, not shown) and from grain boundary 1-2. An important difference in behavior in Cu is that the dislocations from grain boundaries 2-4 and 2-5 have intersected and pinned, while in Pd there is no interaction between emitted dislocations. In Figures 5(c) and 5(g) at 6% strain a twin has formed in both materials and is broadening in grain 2. The Cu sample presents only the twin formed from the grain

boundary between grains1 and 2 while dislocation pinning seems to be preventing the development of other twins. In the Pd sample no pinning effect is observed in dislocations from other grain boundaries leading the dislocations coming from grain boundary 2-5 to have formed a series of twins. In Figures 5(d) and (h) at 9% strain the interaction of dislocations in the Cu sample prevented twin formation, while the twins formed in the Pd sample in grain 2 are clearly seen. Most importantly, we see in Pd how the width of the twinned regions increases, constituting a clear deformation mechanism. Our findings here are consistent with experimental work showing a high twin density in Pd films[49]. However, the differences we observe in twinning behavior are not significant enough to compensate for the very different rates of dislocation emission in the two model materials, even though they show similar stress-strain response. In order to explain these results, we consider grain boundary sliding.

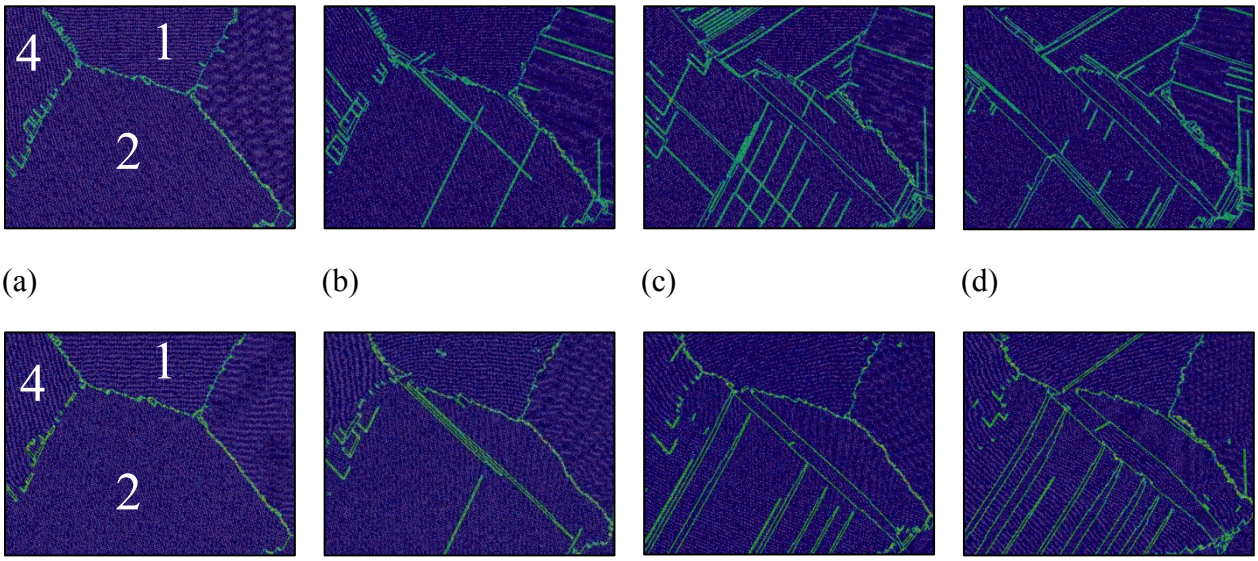

Figure 5: Twinning behavior in grain 2 in Cu and Pd. (a-d) show the Cu sample while (e-h) shows Pd. (a, e) 0% strain. Here the initial structure of the grains can be seen in both samples. (b, f) 3% strain. Partial dislocations have begun to emit from the 1-2 grain boundary into grain 2. Partial dislocations emitted from the 2-5 grain boundary (not shown) are also crossing grain 2. In copper the dislocations have intersected with dislocations emitted from the 2-4 grain boundary while in Pd the dislocations are proceeding unhindered. (c, g) 6% strain. In Cu one dislocation emitted from the 1-2 grain boundary has begun to form a twin while the others have become pinned, preventing additional twin development. In Pd, the same dislocation emitted from grain boundary 1-2 has formed a twin, as have the dislocations coming from grain boundary 2-5. (d, h) 9% strain. Significant differences exist between the Cu and Pd samples. The Cu sample shows a disordered collection of stacking faults while the Pd sample shows a collection of deformation twins. Figure by author.

7.4.5. Grain boundary sliding as a deformation mechanism

A significant deformation mechanism in nanocrystalline metals is grain boundary sliding[50]. Sliding is expected to be critical for very small grain sizes and can still be important for the grain size of 40 nm used here. In order to study the sliding behavior of the grain boundaries in our two model materials we utilized the simple technique of following a specific group of atoms containing the grain boundary as the samples are deformed.

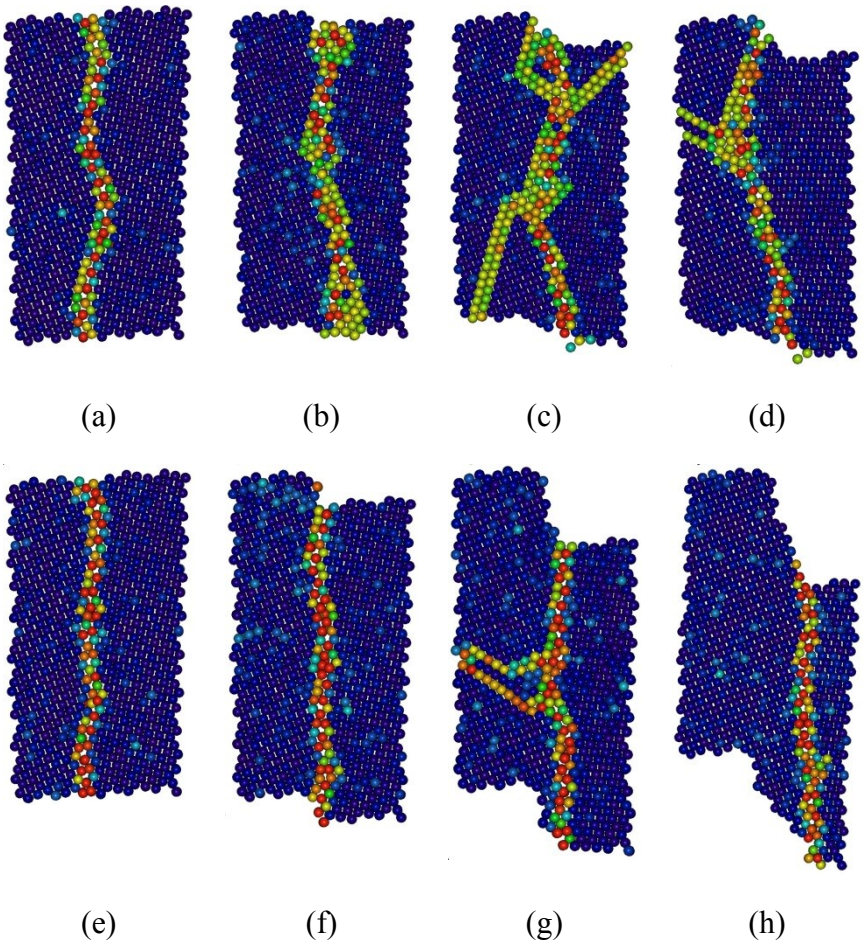

Figure 6: Grain boundary sliding in boundary 7-8. (a-d) shows Cu; (e-h) shows Pd. (a, e) 0% strain. Relaxed boundary shown. (b, f) 3% strain. Cu shows no sliding while Pd shows nascent sliding. (c, g) 6% strain. Cu has begun to slide at the top while Pd shows significant sliding. (d, h) 9% strain. Sliding has occurred in both samples, with Pd having slid notably further. Figure by author.

Figures 6, 7, and 8 show examples of grain boundary sliding in three different grain boundaries in both the Cu and Pd samples. Figure 6 shows grain boundary 7-8 at (a, e) 0, (b, f) 3, (c, g) 6, and (d, h) 9% strain for the Cu and Pd samples, respectively. The Cu sample shows significantly less sliding than that demonstrated by the Pd sample. This pattern is repeated in Figure 7 for grain boundary 1-5, and in Figure 8 for grain boundary 7-9. In each of these examples, the Pd sample has experienced notably more sliding than the Cu samples, while the Cu samples have emitted more dislocations.

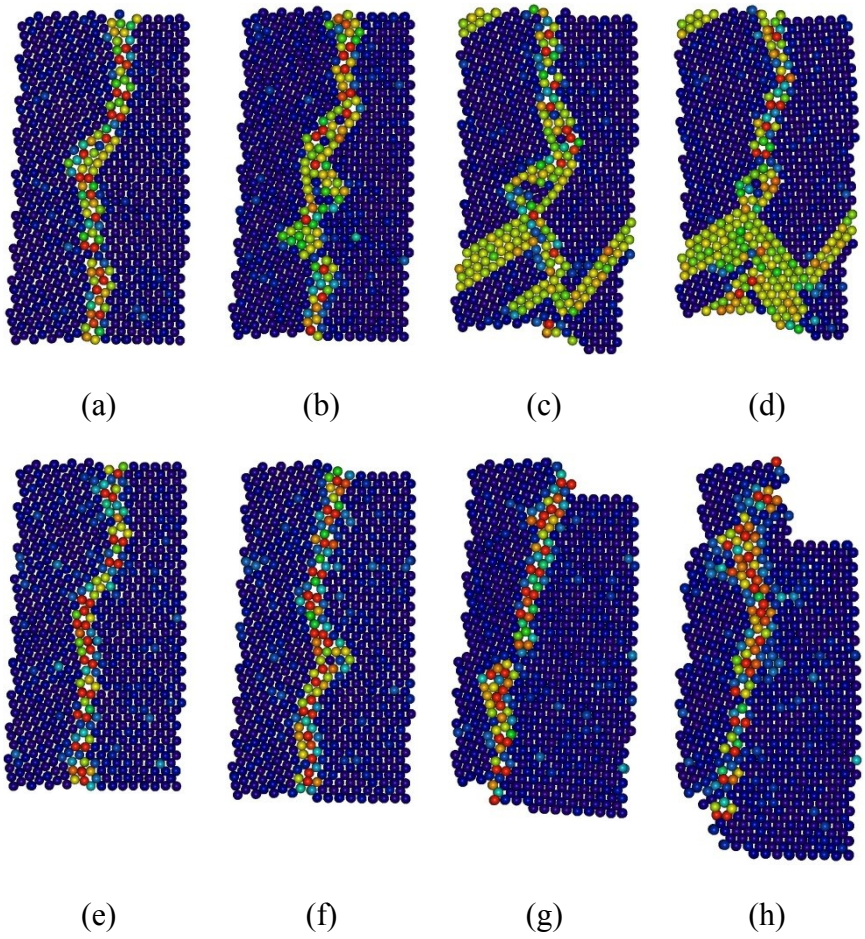

Figure 7: Grain boundary sliding in boundary 1-5. (a-d) shows Cu; (e-h) shows Pd. (a, e) 0% strain. Relaxed boundary shown. (b, f) 3% strain. Cu shows no sliding while Pd shows incipient sliding. (c, g) 6% strain. Cu is emitting dislocations while Pd shows some sliding and coupled boundary migration. (d, h) 9% strain. Sliding has occurred in both samples, with Pd having greater sliding, while Cu shows increased dislocation emission. Figure by author.

Comparing the initial shape of the atom group with the shape observed after deformation, a quantitative measure of the sliding distance as a function of strain can be obtained. This quantified sliding information is shown in Figure 9, plotting the sliding distances observed in each boundary as a function of strain for both model materials. As expected, with increasing strain, the amount of grain boundary sliding increases as well. In all cases the grain boundaries in the Pd sample showed significantly more sliding than in the Cu sample. In Figures 6 through 8 it can also be seen that grain boundary sliding can be accompanied by coupled motion of the boundary parallel to itself, particularly in the Pd sample. This is a phenomenon that has been studied extensively in special boundaries[51-53] and has also been observed in polycrystalline

simulation work, including grain boundary networks similar to the ones studied in this work[54-56].

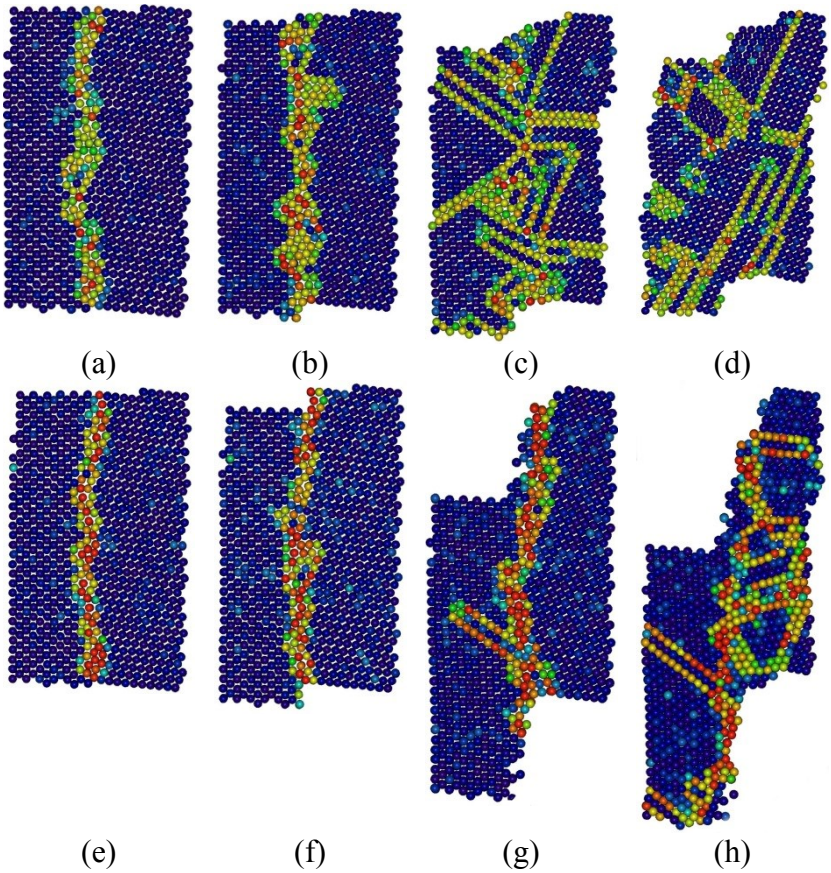

Figure 8: Grain boundary sliding in boundary 7-9. (a-d) shows Cu; (e-h) shows Pd. (a, e) 0% strain. Relaxed boundary shown. (b, f) 3% strain. Cu shows small amounts of sliding while Pd shows increased sliding. (c, g) 6% strain. Cu is emitting dislocations while Pd continues to slide. (d, h) 9% strain. Sliding and dislocation emission have occurred in both samples, with Pd having greater sliding, while Cu shows increased dislocation emission. Figure by author.

As discussed in the work by Velasco et al.[56], grain boundary motion is possible even in boundaries bounded by triple junctions. Grain boundary migration and grain growth have also been observed experimentally and modeled for general boundaries[57-61]. The present results show that it occurs in these digital samples with a coupling factor (β) of approximately 0.3 to 0.6 for the set of boundaries analyzed in Pd and shown in Figures 6-8. β is the ratio of the velocity of grain boundary motion perpendicular to the grain boundary plane over the velocity of the grain boundary motion parallel to the grain boundary plane. The coupling factors cannot be analyzed with any accuracy in Cu because the extent of sliding observed is much smaller.

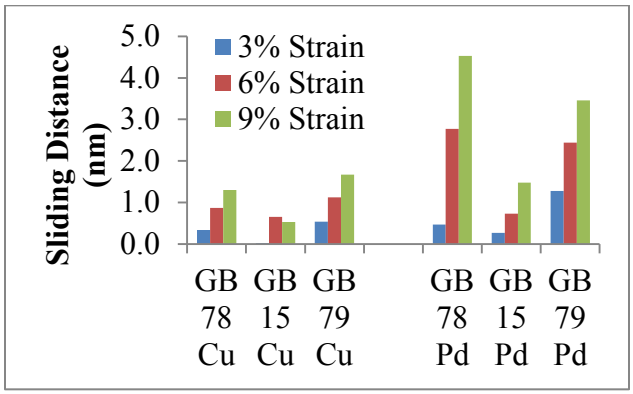

Figure 9: Observed grain boundary sliding distances in the Cu and Pd samples for 3 representative grain boundaries at 3, 6, and 9% strain. Grain boundary sliding was observed to have a greater magnitude in the Pd samples for each grain boundary studied. Figure by author.

Figure 10 shows grain boundary sliding distance in the sample versus strain. This data was obtained by measuring the slide in each boundary at each percent strain level. It is again clear that the Pd sample presents significantly more sliding than the Cu sample. At 9% strain, with a total of 20.7nm of sliding observed, Pd has about 3 times more sliding than Cu with a total of 7.9nm of sliding. The Pd sample is also shown to begin sliding at 1%, while significant sliding begins in the Cu sample at a strain of 3%. These results can be interpreted as directly related to the non-planar structure of the grain boundaries in Cu. Non-planar grain boundary structures are expected to be more difficult to slide due to the structural features that extend into the grains, out of the grain boundary plane itself. This effect is quite significant and a picture emerges of our model materials as two cases that have similar overall deformation response but with very different contributions of dislocation processes and grain boundary mediated processes.

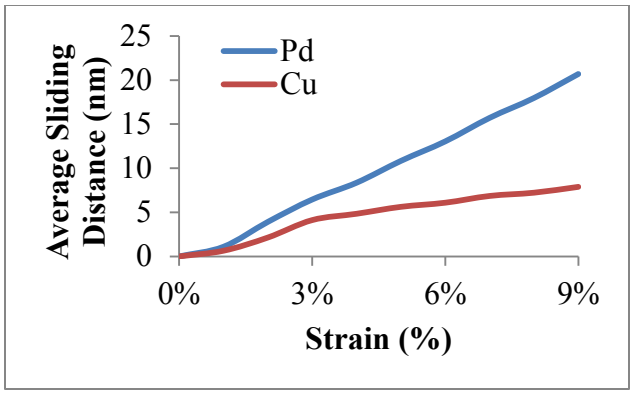

Figure 10: Average grain boundary sliding distance vs strain. Pd uniformly slides further than Cu at each strain level measured. Sliding begins at 1% for the Pd sample, while sliding doesn't become a significant factor for Cu until 2% strain is applied. Figure by author.

7.4.6 Contribution of grain boundary sliding and dislocation emission to overall plasticity

The contribution of dislocation emission to the overall plastic strain was estimated from the Burger's vector, the average distance traveled by the dislocations, the number of dislocations observed, and the cosine of the average angle of the active slip systems with respect to the tension axis. The contribution to plastic strain from grain boundary sliding was estimated from the measured average sliding in each grain boundary and the cosine of the average angle of the grain boundary with respect to the tension axis. The results are shown in Figure 11, where the respective strain due to each of these two processes is compared in Cu and Pd for (a) 3, (b) 6, and (c) 9% strain. At 3% strain, dislocation emission is the dominant deformation mechanism in Cu, contributing about 52% of the applied strain, while grain boundary sliding and migration is the dominant mechanism in Pd, contributing about 70% of the applied strain. At 6% strain, dislocation emission accounts for 70% of the applied strain in Cu. In contrast, grain boundary processes are the dominant mechanism in Pd, with about 65% of the applied strain. At 9%, the vast majority of the strain in Cu is still from dislocation emission, contributing to about 70% of the strain. In Pd, the contributions of dislocation emission and grain boundary sliding are more evenly matched, with about 60% of the applied strain coming from grain boundary processes and the remaining 40% from dislocation emission.

The competitive nature of deformation mechanisms is further shown in Figure 12. Figure 12(a) shows the behavior of Cu. At 1% strain, dislocation emission and grain boundary sliding contribute approximately equally to the overall deformation. At 4% strain and above, a trend can be identified where dislocations prevail over grain boundary sliding as a deformation mechanism, rising to a rate of about 4 to 1. Figure 12(b) shows the same information for Pd. Dislocation emission and grain boundary sliding and coupled migration are more consistently noted for all strain levels observed, with dislocation emission contributing about 35% of the applied strain and the remaining applied strain coming from grain boundary sliding and coupled migration.

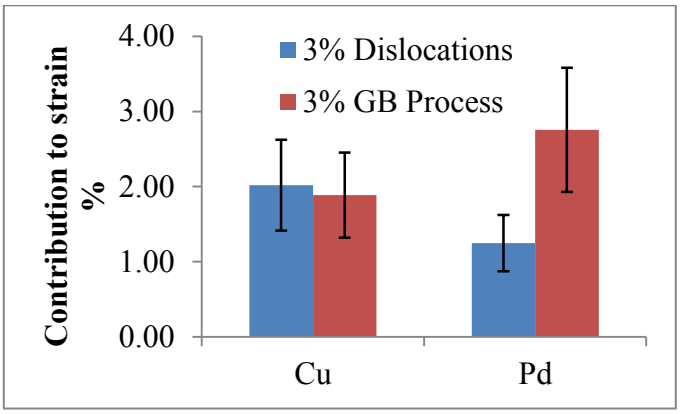

(a)

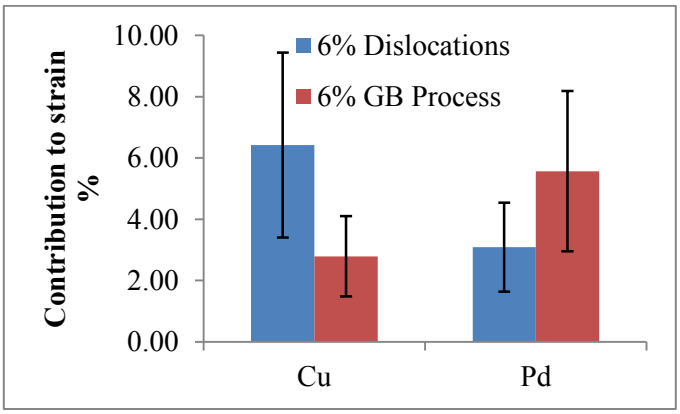

(b)

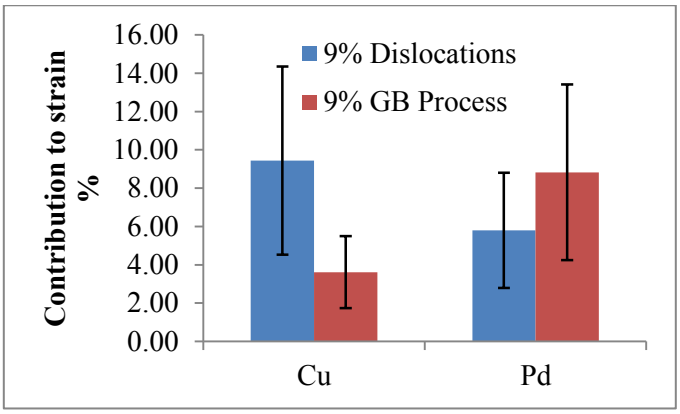

(c)

Figure 11: Estimated contributions from dislocations and grain boundary processes to total strain observed. (a) 3% applied strain. Dislocation emission is the preferred method of deformation mechanisms in Cu, while in Pd grain boundary sliding or migration is the dominating mechanism. (b) 6% strain. Dislocation emission continues to be the overwhelming technique in Cu, in Pd dislocation emission and grain boundary processes are both in effect, with a preference for grain boundary process. (c) 9% strain. Dislocation emission and grain boundary processes continue to contribute at about the same rate as at 6% strain. Figure by author.

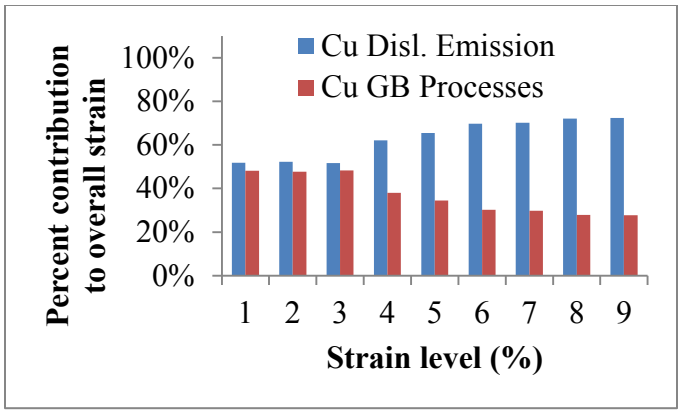

(a)

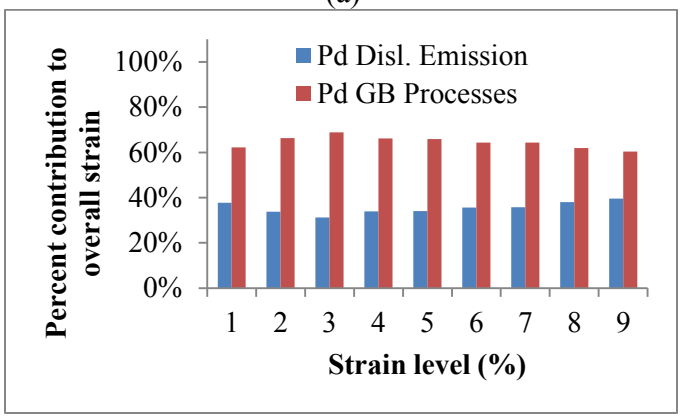

(b)

Figure 12: Contributions from dislocations and grain boundary processes to total applied strain. (a) In the Cu sample, dislocation emission is the preferred method of deformation mechanisms. At low levels of strain, below 4%, dislocation emission is slightly dominant. Starting at 4% strain, dislocation emission becomes strongly dominant over grain boundary processes. At high strain, the ratio of dislocation emission to GB sliding is about 4:1. (b) In the Pd sample, grain boundary processes are dominant at all strain levels with a ratio of about 1:2. There is little change in the ratio as the strain level increases. Figure by author.

7.4.7 Heterogeneous strain displacement

Finally, we investigated the effects of these different grain boundary structures on the distribution of strain in the sample. We utilized a technique where the local atomic displacement for each atom is compared with what it would have been in a totally homogeneous deformation of the sample, obtaining the heterogeneous displacement magnitude for each atom. Based on this comparison, heterogeneous strain distribution maps can be created by color-coding the sample microstructure by the magnitude of the heterogeneous displacement vectors. This simple technique does not actually analyze elastic versus plastic processes[30] but it does give a picture of how the strain is distributed in the sample.

Figure 13 shows the heterogeneous strain displacement maps for the Cu and Pd samples. The color scale measures the magnitude of the heterogeneous displacement for each atom, with white and dark blue showing very little deviation from homogeneous strain, while red shows 2nm or greater heterogeneous displacement. Figures 13(a), 13(b), and 13(c) show the Cu sample at 3, 6, and 9% strain. For the Cu case, the local strain can be seen to be more concentrated in grain centers, particularly in some grains. This is consistent with a significant role of dislocation-mediated deformation, occurring inside the grains as the dislocation glides. In contrast, Figures 13(d), 13(e), and 13(f) show that in the Pd sample, the strain has localized around grain boundaries. This is consistent with the finding of grain boundary accommodation playing a major role in the deformation of the Pd sample. These differences in the distribution of the strain can have important implications for ductility, since strain localization is an important factor in crack nucleation.

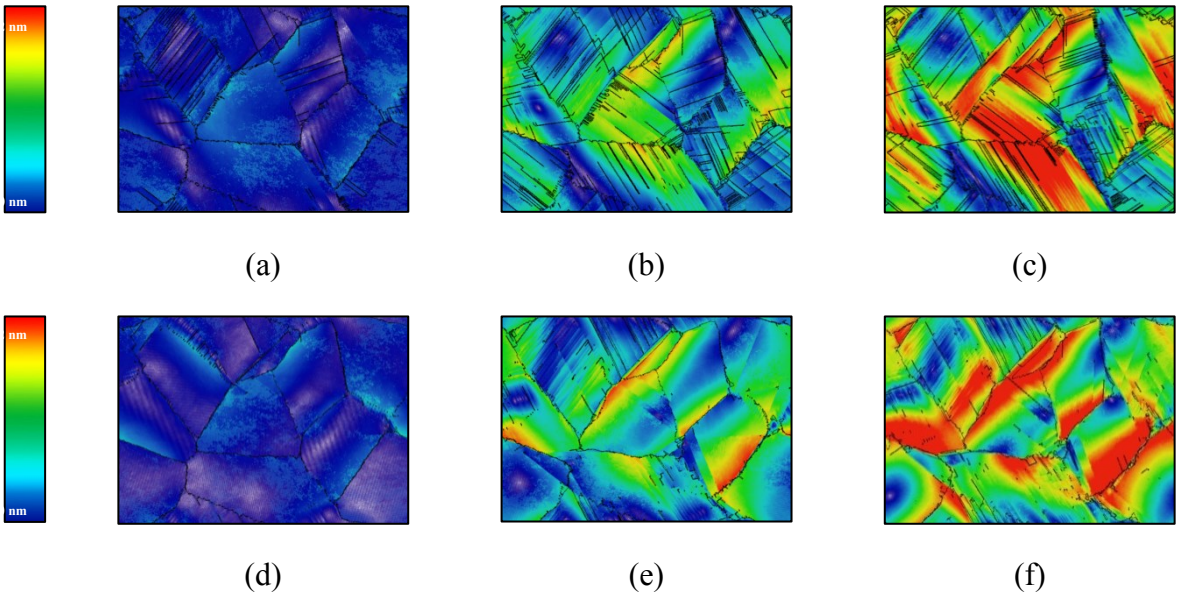

Figure 13: Heterogeneous displacement maps for Cu and Pd. (a-c) shows Cu; (d-f) shows Pd. The color map indicates 0 to 2nm heterogeneous displacement shown in blue to red. (a, d) 3% strain, indicating mostly homogenous strain. (b, e) 6% strain showing some strain localization with greater amounts noted in Pd near grain boundaries. (c, f) 9% strain. Strain localization is noted in both the Cu and Pd samples. In Pd the strain localization is observed near grain boundaries, whereas in Cu it is mostly inside the grains. Figure by author.

7.5 Discussion

The stress-strain curves predicted by the Cu and Pd potentials used in this paper are very similar despite the significant difference in the value of the stacking fault. The two different potentials predict different relaxed grain boundary structures, including structures with features that are non-planar, extending into the grain for the case of Cu. These features resemble incipient stacking faults and therefore can be correlated with the fact that Cu has a much smaller value of the stacking fault energy. In a study of the shear response of a special incoherent twin boundary in various fcc metals[62] a correlation was found between stacking fault energies and relaxed grain boundary structure. Our results seem to suggest that such dependence is present for the case of randomly generated general tilt boundaries. More importantly, these structures for low stacking fault energy materials include non-planar features that extend into the grain. These

differences in the grain boundary relaxed structure were observed for exactly the same relaxation treatment and identical grain boundary characteristics, so that they can be clearly linked to the different interatomic potential utilized and, in particular their corresponding widely different stacking fault energies.

The deformation mechanisms observed in the samples under applied strain were critically affected by the relaxed structure of the boundaries. As expected for nanocrystalline materials, the deformation processes observed in this work include dislocation emission, twin formation, and grain boundary sliding, but the relative importance of these mechanisms is controlled by the grain boundary structure, which in turn correlates with the stacking fault energy. It is important to point out that the non-planar structures observed here occur in random boundaries, are not expected, and have not been seen in studies of symmetrical tilt boundaries using different interatomic potentials[63]. This is because the non-planar features are associated with the accommodation of deviations from of a coincidence misorientation. A recent study [64] examined dislocation emission dependence on grain boundary structure and found that emission is highly dependent on the presence of intrinsic grain boundary dislocations that form the equilibrium grain boundaries.

Because the more non-planar grain boundary structures that occur in the Cu sample (with the lower γ_{SF} of 44 mJ/m^2) resemble stacking faults locally, they make it easier for the Cu boundary to emit a leading Shockley partial dislocation in order to accommodate the applied strain. Pd, with its higher γ_{SF} (187mJ/m^2) shows fewer of the non-planar structures. In place of the non-planar structures, the boundaries contain more of the high excess volume E structural units. Although we observe that the E-units are favored sites for the emission of dislocations, we find that they operate at a higher level of stress than the non-planar features observed for the low

stacking fault energy material, and Pd grain boundaries cannot emit dislocations as easily as the same boundaries in Cu.

Another consequence of the non-planar structure of defects and an important observation of the present work is that while all the grain boundaries exhibited some sliding, the sliding observed in Pd, with the more planar grain boundaries, progressed significantly further than in Cu. This is clearly seen when the same sections of grain boundary are compared for identical strain. The non-planar structure of extended defects has been known to influence mechanical behavior ever since the effects of non-planar dislocation cores were initially studied when atomistic computer simulations were becoming possible decades ago[65]. The non-planar nature of bcc dislocation cores have been confirmed by ab initio work done by Woodward[66], Groger et al. [67], and Ismail-Beigi et al.[68] We theorize that grain boundaries with non-planar cores cannot slide as easily as more planar structured grain boundaries due to the non-planarity, in a clear analogy to dislocation with non-planar cores, such as pure screw dislocations in bcc materials, not gliding as easily as planar core dislocations.

Our results highlight the critical role of grain boundary sliding in nanocrystalline Pd, consistent with previous studies[69, 70]. We also observed coupled grain boundary migration occurring in Pd as shown in previous work[70]. The heterogeneous strain displacement maps also show differences between how the Cu and Pd samples accommodated the applied strain, pointing out the predominant role that grain boundary sliding plays as a deformation mechanism in Pd is shown as being more localized near the grain boundaries. By contrast, increased dislocation emission is observed in the Cu samples with corresponding concentration of localized strain in the grain centers.

These differences in deformation mechanisms can be linked to the value of the stacking fault energy through the increased presence of non-planar structures in relaxed random grain boundaries for materials with low stacking fault values. The relationship between stacking fault energy and overall mechanical behavior is well documented experimentally[71] and investigated in mesoscale simulations[72]. Our results suggest that grain boundary structure, which in turn depends on the stacking fault energy values, also needs to be incorporated in the complete understanding of the role of stacking fault energy values in deformation. The present results are important for models that require assumptions regarding the emission of dislocations, such as crystal plasticity models[73, 74].

In an experimental study of the effect of stacking fault energy on the mechanical properties of Ni-Co alloys[75, 76] reduced stacking fault energy was found to promote grain refinement and increase dislocation emission and density. These experimental results are consistent with our findings here that lower stacking fault energies promote grain boundary structures with non-planar features with less excess volume that are more effective as dislocation sources. It must also be remembered that our model, as with all models, may not fully represent the behavior of these materials in a macroscopic sense due to the limitations imposed by the model itself. These limitations include the quasi-2D nature of our sample and the strain rate utilized by molecular dynamics which prevents the occurrence of thermally-activated deformation mechanisms.

In the present study, we have concentrated on the role of stable stacking fault energies. For that purpose we have chosen two model potentials that are characterized by very similar unstable stacking fault energy values. Stacking fault energy plays only a part in the deformation mechanisms that activate. Clearly, the processes of dislocation emission, twinning, and grain

boundary sliding will also be greatly affected by the values of the unstable stacking fault energy and the generalized stacking fault energy curve. This will be the subject of a separate study.

7.6 Acknowledgments

This work was supported by the Department of Energy, Office of Basic Energy Sciences, under grant DE-FG02-08ER46525 and the National Science Foundation, IRD program. The authors acknowledge Advanced Research Computing at Virginia Tech for providing computational resources and technical support that have contributed to the results reported within this paper. URL: http://www.arc.vt.edu

References

[1] J. P. Hirth, "Defect structures in grain boundaries," *Acta Metall,* vol. 22, pp. 1023-1031, 1974.

[2] J. P. Hirth, "Influence of grain boundaries on mechanical properties," *Metallurgical Transactions,* vol. 3, pp. 3047-3067, 1972.

[3] H. Van Swygenhoven, A. Caro, and D. Farkas, "A molecular dynamics study of polycrystalline fcc metals at the nanoscale: grain boundary structure and its influence on plastic deformation," *Materials Science and Engineering a-Structural Materials Properties Microstructure and Processing,* vol. 309, pp. 440-444, 2001.

[4] H. Van Swygenhoven, D. Farkas, and A. Caro, "Grain-boundary structures in polycrystalline metals at the nanoscale," *Physical Review B,* vol. 62, pp. 831-838, 2000.

[5] M. A. Tschopp and D. L. McDowell, "Asymmetric tilt grain boundary structure and energy in copper and aluminium," *Philosophical Magazine,* vol. 87, pp. 3871-3892, 2007 2007.

[6] J. A. Brown and Y. Mishin, "Dissociation and faceting of asymmetrical tilt grain boundaries: Molecular dynamics simulations of copper," *Physical Review B,* vol. 76, Oct

2007.

[7] M. W. Chen, E. Ma, K. J. Hemker, H. W. Sheng, Y. M. Wang, and X. M. Cheng, "Deformation twinning in nanocrystalline aluminum," *Science,* vol. 300, pp. 1275-1277, May 2003.

[8] D. Farkas and L. Patrick, "Tensile deformation of fcc Ni as described by an EAM potential," *Philosophical Magazine,* vol. 89, pp. 3435-3450, 2009 2009.

[9] J. B. Jeon, B.-J. Lee, and Y. W. Chang, "Molecular dynamics simulation study of the effect of grain size on the deformation behavior of nanocrystalline body-centered cubic iron," *Scripta Materialia,* vol. 64, pp. 494-497, Mar 2011.

[10] M. D. McMurtrey, G. S. Was, L. Patrick, and D. Farkas, "Relationship between localized strain and irradiation assisted stress corrosion cracking in an austenitic alloy," *Materials Science and Engineering a-Structural Materials Properties Microstructure and Processing,* vol. 528, pp. 3730-3740, Apr 2011.

[11] A. Stukowski, K. Albe, and D. Farkas, "Nanotwinned fcc metals: Strengthening versus softening mechanisms," *Physical Review B,* vol. 82, Dec 2010.

[12] N. Q. Vo, R. S. Averback, P. Bellon, and A. Caro, "Yield strength in nanocrystalline Cu during high strain rate deformation," *Scripta Materialia,* vol. 61, pp. 76-79, Jul 2009.

[13] X. Z. Liao, Y. H. Zhao, S. G. Srinivasan, Y. T. Zhu, R. Z. Valiev, and D. V. Gunderov, "Deformation twinning in nanocrystalline copper at room temperature and low strain rate," *Applied Physics Letters,* vol. 84, pp. 592-594, Jan 2004.

[14] H. Van Swygenhoven, P. M. Derlet, and A. G. Froseth, "Nucleation and propagation of dislocations in nanocrystalline fcc metals," *Acta Materialia,* vol. 54, pp. 1975-1983, Apr 2006.

[15] H. Van Swygenhoven, P. M. Derlet, and A. G. Froseth, "Stacking fault energies and slip in nanocrystalline metals," *Nature Materials,* vol. 3, pp. 399-403, Jun 2004.

[16] A. Godon, J. Creus, S. Cohendoz, E. Conforto, X. Feaugas, P. Girault*, et al.*, "Effects of grain orientation on the Hall-Petch relationship in electrodeposited nickel with nanocrystalline grains," *Scripta Materialia,* vol. 62, pp. 403-406, Mar 2010.

[17] H. Van Swygenhoven, M. Spaczer, A. Caro, and D. Farkas, "Competing plastic deformation mechanisms in nanophase metals," *Physical Review B,* vol. 60, pp. 22-25, 1999.

[18] N. Q. Vo, R. S. Averback, P. Bellon, S. Odunuga, and A. Caro, "Quantitative description of plastic deformation in nanocrystalline Cu: Dislocation glide versus grain boundary sliding," *Physical Review B,* vol. 77, Apr 2008.

[19] J. Schiotz and K. W. Jacobsen, "A maximum in the strength of nanocrystalline copper," *Science,* vol. 301, pp. 1357-1359, Sep 2003.

[20] C. A. Becker, F. Tavazza, and L. E. Levine, "Implications of the choice of interatomic potential on calculated planar faults and surface properties in nickel," *Philosophical Magazine,* vol. 91, pp. 3578-3597, 2011.

[21] E. A. Holm, D. L. Olmsted, and S. M. Foiles, "Comparing grain boundary energies in face-centered cubic metals: Al, Au, Cu and Ni," *Scripta Materialia,* vol. 63, pp. 905-908, Nov 2010.

[22] D. Farkas and W. A. Curtin, "Plastic deformation mechanisms in nanocrystalline columnar grain structures," *Materials Science and Engineering a-Structural Materials Properties Microstructure and Processing,* vol. 412, pp. 316-322, Dec 2005.

[23] I. Shabib and R. E. Miller, "A molecular dynamics study of twin width, grain size and temperature effects on the toughness of 2D-columnar nanotwinned copper," *Modelling and Simulation in Materials Science and Engineering,* vol. 17, Jul 2009.

[24] V. Yamakov, D. Wolf, S. R. Phillpot, A. K. Mukherjee, and H. Gleiter, "Deformation-mechanism map for nanocrystalline metals by molecular-dynamics simulation," *Nature Materials,* vol. 3, pp. 43-47, Jan 2004.

[25] S. Plimpton, "Fast parallel algorithms for short-range molecular-dynamics," *Journal of Computational Physics,* vol. 117, pp. 1-19, Mar 1995.

[26] Y. Mishin, M. J. Mehl, D. A. Papaconstantopoulos, A. F. Voter, and J. D. Kress, "Structural stability and lattice defects in copper: Ab initio, tight-binding, and embedded-atom calculations," *Physical Review B,* vol. 63, Jun 2001.

[27] S. M. Foiles and J. J. Hoyt. (2001, Computer Simulation of Bubble Growth in Metals Due to He. *Sandia Report SAND2001-0661*.

[28] C. L. Kelchner, S. J. Plimpton, and J. C. Hamilton, "Dislocation nucleation and defect structure during surface indentation," *Physical Review B,* vol. 58, pp. 11085-11088, Nov 1998.

[29] A. Stukowski, "Visualization and analysis of atomistic simulation data with OVITO-the

Open Visualization Tool," *Modelling and Simulation in Materials Science and Engineering,* vol. 18, Jan 2010.

[30] A. Stukowski and A. Arsenlis, "On the elastic-plastic decomposition of crystal deformation at the atomic scale," *Modelling and Simulation in Materials Science and Engineering,* vol. 20, Apr 2012.

[31] M. J. Mehl, J. E. Osburn, D. A. Papaconstantopoulos, and B. M. Klein, "Structural properties of ordered high-melting-temperature intermetallic alloys from 1st-principles total-energy calulations," *Physical Review B,* vol. 41, pp. 10311-10323, May 1990.

[32] S. Foiles, "Computer Simulation of Bubble Growth in Metals Due to He," ed. Albuquerque, NM: Sandia National Laboratories, 2001.

[33] F. Ernst, M. W. Finnis, D. Hofmann, T. Muschik, U. Schonberger, U. Wolf*, et al.*, "Theoretical prediction and direct observation of the 9R structure in Ag," *Physical Review Letters,* vol. 69, pp. 620-623, Jul 1992.

[34] U. Wolf, F. Ernst, T. Muschik, M. W. Finnis, and H. F. Fischmeister, "The influence of grain-boundary inclination on the structure and energy of sigma=3 grain-boundaries in copper," *Philosophical Magazine a-Physics of Condensed Matter Structure Defects and Mechanical Properties,* vol. 66, pp. 991-1016, Dec 1992.

[35] M. A. Hopcroft, W. D. Nix, and T. W. Kenny, "What is the young's modulus of silicon?," *Journal of Microelectromechanical Systems,* vol. 19, pp. 229-238, Apr 2010.

[36] M. A. Tschopp, G. J. Tucker, and D. L. McDowell, "Atomistic simulations of tension-compression asymmetry in dislocation nucleation for copper grain boundaries," *Computational Materials Science,* vol. 44, pp. 351-362, Dec 2008.

[37] M. Tschopp and D. L. McDowell, "Atomistic simulations of grain boundary dislocation nucleation," in *International Conference on Heterogeneous Material Mechanics (ICHMM)*, Huangshan, Peoples R China, 2008, pp. 97-104.

[38] D. E. Spearot and D. L. McDowell, "Atomistic modeling of grain boundaries and dislocation processes in metallic polycrystalline materials," *Journal of Engineering Materials and Technology-Transactions of the Asme,* vol. 131, Oct 2009.

[39] G. J. Tucker, M. A. Tschopp, and D. L. McDowell, "Evolution of structure and free volume in symmetric tilt grain boundaries during dislocation nucleation," *Acta Materialia,* vol. 58, pp. 6464-6473, Nov 2010.

[40] M. A. Tschopp, G. J. Tucker, and D. L. McDowell, "Structure and free volume of < 110 > symmetric tilt grain boundaries with the E structural unit," *Acta Materialia,* vol. 55, pp. 3959-3969, Jun 2007.

[41] D. E. Spearot, "Evolution of the E structural unit during uniaxial and constrained tensile deformation," *Mechanics Research Communications,* vol. 35, pp. 81-88, Jan-Mar 2008.

[42] A. Froseth, H. Van Swygenhoven, and P. M. Derlet, "The influence of twins on the mechanical properties of nc-Al," *Acta Materialia,* vol. 52, pp. 2259-2268, May 2004.

[43] A. G. Froseth, P. M. Derlet, and H. Van Swygenhoven, "Grown-in twin boundaries affecting deformation mechanisms in nc-metals," *Applied Physics Letters,* vol. 85, pp. 5863-5865, Dec 2004.

[44] A. G. Froseth, P. M. Derlet, and H. Van Swygenhoven, "Twinning in nanocrystalline fcc metals," *Advanced Engineering Materials,* vol. 7, pp. 16-20, Jan 2005.

[45] Y. Kulkarni, R. J. Asaro, and D. Farkas, "Are nanotwinned structures in fcc metals optimal for strength, ductility and grain stability?," *Scripta Materialia,* vol. 60, pp. 532-535, 2009.

[46] L. Lan and M. G. Nasr, "Twin-size effects on the deformation of nanotwinned copper," *Physical Review B (Condensed Matter and Materials Physics),* vol. 79, p. 075444, 2009.

[47] L. Lu, "Current progress of mechanical properties of metals with nano-scale twins," *Journal of Materials Science & Technology,* vol. 24, pp. 473-482, Jul 2008.

[48] L. Lu, X. Chen, X. Huang, and K. Lu, "Revealing the maximum strength in nanotwinned copper," *Science,* vol. 323, pp. 607-610, Jan 2009.

[49] B. Wang, H. Idrissi, H. Shi, M. S. Colla, S. Michotte, J. P. Raskin*, et al.*, "Texture-dependent twin formation in nanocrystalline thin Pd films," *Scripta Materialia,* vol. 66, pp. 866-871, Jun 2012.

[50] J. Weissmueller, J. Markmann, M. Grewer, and R. Birringer, "Kinematics of polycrystal deformation by grain boundary sliding," *Acta Materialia,* vol. 59, pp. 4366-4377, Jun 2011.

[51] J. W. Cahn, Y. Mishin, and A. Suzuki, "Coupling grain boundary motion to shear deformation," *Acta Materialia,* vol. 54, pp. 4953-4975, Nov 2006.

[52] J. W. Cahn, Y. Mishin, and A. Suzuki, "Duality of dislocation content of grain boundaries," *Philosophical Magazine,* vol. 86, pp. 3965-3980, Sep 1 2006.

[53] J. W. Cahn and Y. Mishin, "Recrystallization initiated by low-temperature grain boundary motion coupled to stress," *International Journal of Materials Research,* vol. 100, pp. 510-515, Apr 2009.

[54] D. Farkas, S. Mohanty, and J. Monk, "Strain-driven grain boundary motion in nanocrystalline materials," *Materials Science and Engineering a-Structural Materials Properties Microstructure and Processing,* vol. 493, pp. 33-40, Oct 15 2008.

[55] D. Farkas, A. Froseth, and H. Van Swygenhoven, "Grain boundary migration during room temperature deformation of nanocrystalline Ni," *Scripta Materialia,* vol. 55, pp. 695-698, 2006.

[56] M. Velasco, H. Van Swygenhoven, and C. Brandl, "Coupled grain boundary motion in a nanocrystalline grain boundary network," *Scripta Materialia,* vol. 65, pp. 151-154, Jul 2011.

[57] F. Mompiou, M. Legros, and D. Caillard, "Direct observation and quantification of grain boundary shear-migration coupling in polycrystalline Al," *Journal of Materials Science,* vol. 46, pp. 4308-4313, Jun 2011.

[58] F. Mompiou, M. Legros, and D. Caillard, "SMIG model: A new geometrical model to quantify grain boundary-based plasticity," *Acta Materialia,* vol. 58, pp. 3676-3689, Jun 2010.

[59] M. Legros, D. S. Gianola, and K. J. Hemker, "In situ TEM observations of fast grain-boundary motion in stressed nanocrystalline aluminum films," *Acta Materialia,* vol. 56, pp. 3380-3393, Aug 2008.

[60] D. S. Gianola, S. Van Petegem, M. Legros, S. Brandstetter, H. Van Swygenhoven, and K. J. Hemker, "Stress-assisted discontinuous grain growth and its effect on the deformation behavior of nanocrystalline aluminum thin films," *Acta Materialia,* vol. 54, pp. 2253-2263, May 2006.

[61] D. Caillard, F. Mompiou, and M. Legros, "Grain-boundary shear-migration coupling. II. Geometrical model for general boundaries," *Acta Materialia,* vol. 57, pp. 2390-2402, May 2009.

[62] J. Wang, A. Misra, and J. P. Hirth, "Shear response of Sigma 3{112} twin boundaries in face-centered-cubic metals," *Physical Review B,* vol. 83, Feb 18 2011.

[63] L. Wan and S. Wang, "Shear response of the Sigma 9 < 110 > {221} symmetric tilt grain

boundary in fcc metals studied by atomistic simulation methods," *Physical Review B,* vol. 82, Dec 20 2010.

[64] K. Kinoshita, T. Shimokawa, and T. Kinari, "Grain boundary structure dependence of extrinsic grain boundary dislocation emission phenomena: A molecular dynamics study," *Materials Transactions,* vol. 53, pp. 147-155, Jan 2012.

[65] V. Vitek, "Structure of dislocation cores in metallic materials and its impact on their plastic behavior," *Progress in Materials Science,* vol. 36, pp. 1-27, 1992.

[66] C. Woodward, "First-principles simulations of dislocation cores," *Materials Science and Engineering a-Structural Materials Properties Microstructure and Processing,* vol. 400, pp. 59-67, Jul 2005.

[67] R. Groger, A. G. Bailey, and V. Vitek, "Multiscale modeling of plastic deformation of molybdenum and tungsten: I. Atomistic studies of the core structure and glide of 1/2 < 111 > screw dislocations at 0 K," *Acta Materialia,* vol. 56, pp. 5401-5411, Nov 2008.

[68] S. Ismail-Beigi and T. A. Arias, "Ab initio study of screw dislocations in Mo and Ta: A new picture of plasticity in bcc transition metals," *Physical Review Letters,* vol. 84, pp. 1499-1502, Feb 2000.

[69] Y. Ivanisenko, L. Kurmanaeva, J. Weissmueller, K. Yang, J. Markmann, H. Roesner*, et al.*, "Deformation mechanisms in nanocrystalline palladium at large strains," *Acta Materialia,* vol. 57, pp. 3391-3401, Jun 2009.

[70] Y. Wang, X. Liao, and Y. Zhu, "Grain refinement and growth induced by severe plastic deformation," *International Journal of Materials Research,* vol. 100, pp. 1632-1637, Dec 2009.

[71] X. H. An, Q. Y. Lin, S. D. Wu, Z. F. Zhang, R. B. Figueiredo, N. Gao*, et al.*, "Significance of stacking fault energy on microstructural evolution in Cu and Cu-Al alloys processed by high-pressure torsion," *Philosophical Magazine,* vol. 91, pp. 3307-3326, 2011 2011.

[72] A. Hunter, I. J. Beyerlein, T. C. Germann, and M. Koslowski, "Influence of the stacking fault energy surface on partial dislocations in fcc metals with a three-dimensional phase field dislocations dynamics model," *Physical Review B,* vol. 84, Oct 10 2011.

[73] J. Shi and M. A. Zikry, "Modeling of grain boundary transmission, emission, absorption and overall crystalline behavior in Sigma 1, Sigma 3, and Sigma 17b bicrystals," *Journal*

of Materials Research, vol. 26, pp. 1676-1687, Jul 2011.

[74] J. Shi and M. A. Zikry, "Grain size, grain boundary sliding, and grain boundary interaction effects on nanocrystalline behavior," *Materials Science and Engineering a-Structural Materials Properties Microstructure and Processing,* vol. 520, pp. 121-133, Sep 15 2009.

[75] P. L. Sun, Y. H. Zhao, J. C. Cooley, M. E. Kassner, Z. Horita, T. G. Langdon*, et al.*, "Effect of stacking fault energy on strength and ductility of nanostructured alloys: An evaluation with minimum solution hardening," *Materials Science and Engineering a-Structural Materials Properties Microstructure and Processing,* vol. 525, pp. 83-86, Nov 15 2009.

[76] Z. W. Wang, Y. B. Wang, X. Z. Liao, Y. H. Zhao, E. J. Lavernia, Y. T. Zhu*, et al.*, "Influence of stacking fault energy on deformation mechanism and dislocation storage capacity in ultrafine-grained materials," *Scripta Materialia,* vol. 60, pp. 52-55, Jan 2009.

8 Molecular dynamics study of deformation and fracture in a tantalum nano-crystalline thin film

Laura Smith[1,3], Jonathan A. Zimmerman[2], Lucas M. Hale[2], and Diana Farkas[1]

[1]Virginia Polytechnic Institute and State University 445 Old Turner St Blacksburg VA 24061

[2]Sandia National Laboratories P.O. Box 969 Livermore CA 94551-0969

This chapter has been accepted for publication in Modelling and Simulation in Materials Science and Engineering, 2014. It is used here with permission

[3]Corresponding Author: lauramse@vt.edu (540) 629-4449

8.1 Abstract

We present results from molecular dynamics simulations of two nano-crystalline tantalum thin films that illuminate the variety of atomic-scale mechanisms of incipient plasticity. Sample 1 contains approximately 500K atoms and three grains, chosen to facilitate study at $10^5 s^{-1}$ strain rate; sample 2 has 4.6M atoms and 30 grains. The samples are loaded in uniaxial tension at deformation rates of $10^5 s^{-1}$ to $10^9 s^{-1}$, and display phenomena including emission of perfect ½<111>-type dislocations and the formation and migration of twin boundaries. It was found that screw dislocation emission is the first deformation mechanism activated at strain rates below $10^8 s^{-1}$. Deformation twins emerge as a deformation mechanism at higher strains, with twins observed to cross grain boundaries as larger strains are reached. At high strain rates atoms are displaced with the characteristic twin vector at a ratio of 3:1 ($10^8 s^{-1}$) or 4:1 ($10^9 s^{-1}$) to characteristic dislocation vectors. Fracture is nucleated through a nano-void growth process. Grain boundary sliding does not scale with increasing strain rate. Detailed analysis of nano-scale deformation using these tools enhances our understanding of deformation mechanisms in tantalum.

PACS: 07.05.Tp, 31.15.xv, 83.10.Rs, 83.50.-v, 62.25.-g

Submitted to: Modelling and Simulation in Materials Science and Engineering

8.2 Introduction

There has been considerable interest in the mechanical properties of nano-crystalline metals in recent years [1-9]. Deformation mechanisms that activate in crystalline materials under applied stress and strain have significant effects on the mechanical response of the material. The strength of a material is closely related to how the material deforms, thus understanding the various deformation mechanisms activated in crystalline materials is key to understanding the interrelated phenomena of deformation processes and material properties.

Previous work on the deformation mechanisms in bcc metals at a variety of grain sizes in the nano-crystalline regime indicate that deformation twinning [9-11], grain boundary sliding [3, 12], and dislocation emission and transmission [3, 7, 13] are all activated at different levels of strain. Molecular simulations have revealed many of the deformation mechanisms that are activated in bcc materials. Work by Rudd [14] shows that both dislocation emission and twinning are seen in tantalum when deformed at high strain rates. Pan, Li and Wei [15] also modeled tantalum and observed that deformation twinning is a primary dislocation mechanism, but the mechanisms of grain boundary sliding, grain rotation, and dislocation emission are also active. Pan et al. were also able to identify a strain rate sensitivity of the maximum tensile stress of approximately 0.14. Zhang et al. [11] noted that twinning dislocations emitted from grain boundaries are the first deformation mechanisms observed in the molecular dynamics simulations done in bcc molybdenum. For molecular dynamics simulations of tantalum nano-wires, Ajing Cao [10] observed deformation twinning to be the primary deformation mechanism in both tension and compression. Deformation twinning has also been observed to be the dominant deformation mechanism in simulation work performed by Fredriksen et al. [3] in their work on nano-crystalline molybdenum. Experimentally, deformation twinning in nano-

crystalline tantalum has also been observed in nano-indentation experiments, such as those done by Wang et al. [9].

Dislocation emission as a deformation mechanism has also been investigated in bcc nano-crystalline materials through molecular dynamics simulations. Frederiksen et al. [3] observed this mechanism in nano-crystalline molybdenum subjected to a very high strain rate ($10^9 s^{-1}$). It has also been observed by Jeon, Lee and Chang [13], in bcc iron at very high levels of strain (>15%). Experimentally, Zhenhua et al. [12] found that dislocation emission was the primary deformation mechanism in nano-crystalline tantalum during nano-indentation experiments with grain sizes of 10 to 20nm. Dislocation emission as the initial deformation mechanism hasn't been explored at lower strain rates, or in the absence of inter-granular cracking. Further understanding the competing relationship between deformation twinning and dislocation emission will give a more complete picture of deformation at the nano-scale in bcc materials.

Grain boundaries slide in response to applied stress and strain by moving the grains on either side of the grain boundary parallel to the grain boundary plane in opposite directions. Using molecular dynamics, Frederiksen et al. [3] noted grain boundary sliding as a key deformation mechanism in their work with bcc molybdenum with an approximate grain size of about 12nm. Dislocation emission and grain boundary sliding were also observed as important deformation mechanisms in the simulation work of Jeon, Lee and Chang [13] in of nano-crystalline iron. They observed that below a critical grain size, deformation dominated by dislocation emission converts to grain boundary sliding. In experimental nano-indentation, Cao et al. [16] note grain boundary sliding as a key deformation mechanism in their work on tetragonal and bcc thin-film tantalum.

Grain boundaries slide in response to applied stress and strain by moving the grains on either side of the grain boundary parallel to the grain boundary plane in opposite directions. Using molecular dynamics, Frederiksen et al. [3] noted grain boundary sliding as a key deformation mechanism in their work with bcc molybdenum with an approximate grain size of about 12nm. Dislocation emission and grain boundary sliding were also observed as important deformation mechanisms in the simulation work of Jeon, Lee and Chang [13] in of nano-crystalline iron. They observed that below a critical grain size, deformation dominated by dislocation emission converts to grain boundary sliding. In experimental nano-indentation, Cao et al. [16] note grain boundary sliding as a key deformation mechanism in their work on tetragonal and bcc thin-film tantalum.

Fracture in nano-crystalline tantalum is known to happen through the nucleation and growth of nano-voids. In molecular dynamics simulations, Tang, Bringa, and Meyers [17, 18] note that failure through nano-voids has been observed in tantalum through the emission of dislocation loops and twinning from the void surface. Rudd [19] has analyzed this phenomenon in both fcc and bcc materials, finding that bcc materials tend to grow through bursts of deformation emission, finally resulting in fracture of the material. Nano-voids carved out of grain interfaces in tantalum have been studied by Traiviratana et al. [20], finding that the voids can emit dislocations and twins into both neighboring grains.

In the current effort, we aim to shed additional light on the deformation of nano-crystalline thin-film tantalum under uniaxial tension at several strain rates. We seek to determine the strain rate dependence of the initial deformation mechanism observed the degree of grain boundary sliding, and the overall response of the material to the applied strain.

In this paper, we examine the deformation mechanisms observed in polycrystalline samples of tantalum with an average grain size of 20nm subjected to a uniaxial strain rate of $10^6 s^{-1}$ and up to 30% strain with a focus on the first deformation mechanism observed. Dislocation slip was seen at a lower strain than previously observed, and prior to deformation twin emission. Fracture was observed at higher strain levels, nucleated via a nano-void process. We then extend our analysis to examine strain rates ranging from 10^5 to 10^9 s^{-1}, in order to assess how the applied loading rate impacts the type and ordering of deformation mechanisms that become active.

8.3 Simulation and analysis techniques

The polycrystalline samples used in this work, shown in figure 1, consists of one sample with 3 columnar grains of tantalum, and a similarly constructed sample one order of magnitude larger containing 30 grains. A Voronoi construction technique similar to that used in previous work by Farkas and Patrick [2] was employed to create the samples. Sample 1 contains 463607 atoms with an average in-plane grain size of 20nm, total dimensions of 34.5nm in both the x and y directions, and a thickness of 7nm. The small number of atoms (<500K) in sample 1 was specifically chosen to facilitate the study of deformation at a strain rate of $10^5 s^{-1}$. This sample size is necessary given the limitations of computational power available to the authors. Sample 2 is an order of magnitude larger than sample 1, with random grain orientations and boundaries. This sample consists of 30 grains, with an average in-plane grain size of about 20nm, total dimensions of 110.6 nm in both the x and y directions, and about 4.6 million atoms. Each sample was used in several simulation runs at increasing strain rates in order to isolate the effects of strain rate on deformation mechanisms. Periodic boundary conditions are applied along the x and y directions, while free surface conditions exist in the z directions. Grain boundary analysis has

determined that the boundaries in sample 1 are random high-angle boundaries. The random distribution of grain orientations used in this work is similar to that commonly used in simulation work investigating the properties of nanocrystalline metals [3, 7, 8, 13].

Grain boundaries in sample 1 will be referred to using the grain indices; for example, grain boundary 1-2 describes the grain boundary between grains 1 and 2. This also holds true for grain boundary 1-3 as referring to the grain boundary between grains 1 and 3, and grain boundary 2-3 as meaning the grain boundary between grains 2 and 3. The left and right grain boundary 1-3 will be designated as such, as will be the upper and lower grain boundary 1-2.

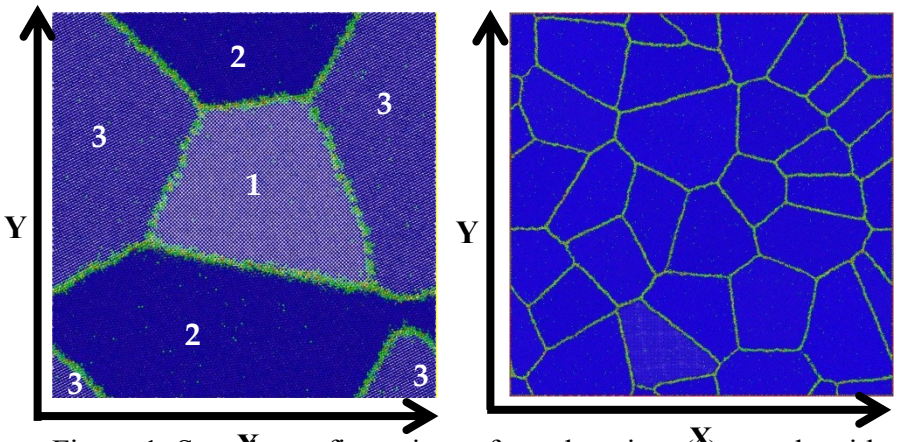

Figure 1: Sample configurations after relaxation. (a) sample with 464k atoms and three grains. (b) sample with 4.6M atoms and 30 grains. Colour coding is by centro-symmetry [21] parameter, with blue indicating perfect lattice and green atoms indicating moderate lattice disruption characteristic of grain boundaries. Figure by author.

Molecular dynamics is used to deform the samples using the Large-Scale Atomic/Molecular Massively Parallel Simulation (LAMMPS) software [22] developed at Sandia National Labs. Several embedded atom method potentials exist for tantalum, including those by Li et al. [23], and Mishin and Lozovoi [24]. The Mishin potential includes angular-dependent terms; however the extra computational time required made the force-matched, embedded atom method potential by Li et al. the best choice for these simulations, given that both potentials display similar

crystallographic slip behavior and have similar energetic properties. The behavior of the Li potential has been explored in depth by Alleman et al. [25], in particular noting that the Li potential satisfied their criteria of accurate estimations of the elastic moduli, appropriate predictions of gamma surfaces, and accurate simulation of the bcc screw dislocation core. The Li potential displays good agreement with the unstable stacking fault energy barrier determined by DFT calculations. Mishin et al. [24] determined that the Li potential underestimates the surface energies of the (100) and (110) surfaces by 12-29% as compared with DFT. In addition, the twin boundary energy in the Li potential calculated in this work is 550 mJ/m^2, which is considerably higher than the DFT value of 304 mJ/m^2 calculated by Mishin [24].

A relaxed and equilibrated boundary structure is obtained by heating each sample to 1700K for 200ps, then cooling to 300K over an additional 200ps using a Nosé-Hoover thermostat and barostat while maintaining the pressure at 0 bar in all directions. After relaxation, the samples are subjected to strain-controlled virtual mechanical tension along the x axis at a finite temperature of 300K and at a selected strain rate from $10^5 s^{-1}$ to $10^9 s^{-1}$ with a timestep of one femtosecond. Sample 1 was deformed at all strain rates, while sample 2 was deformed at strain rates from $10^6 s^{-1}$ to $10^9 s^{-1}$. Pressure in the perpendicular direction (along the y axis) is maintained at 0 to enforce uniaxial stress loading. Elastic constants and behaviour of the potential at 0K as reported in Li et al. [23] are confirmed in this work. Calculation of the elastic constants at 300K predicts C_{11} equaling 261GPa and C_{12} equaling 175GPa. The calculated elastic modulus for this polycrystalline system is 121GPa. No intrinsic stacking faults are observed, and unstable stacking fault energy barriers for the {112}/<111> and {110}/<111> directions are estimated to be 1096 mJ/m^2 and 938 mJ/m^2 respectively.

Results from the simulation are visualized using the software packages OVITO [26] and Paraview [27]. Additional post-processing work is conducted with the Dislocation Extraction Algorithm (DXA) [28], slip vector analysis [29], and the atoms-to-continuum user-package (AtC) for LAMMPS [30]. DXA operates on output/dump files from LAMMPS to identify discrete dislocation lines, stacking faults, and arbitrary interfaces such as free surfaces, grain boundaries, and twin boundaries. DXA quantifies both Burgers vector and line directions for dislocations and surface normal vectors for stacking faults and other types of interfaces. DXA is ideal for visualizing dislocations sufficiently isolated from structural features (e.g. grain boundaries, triple junctions) and those dislocations that exist as distinct components of grain boundary sub-structure, as well as for identifying the slip paths of partial dislocations as indicated by the presence of stacking faults. Since tantalum has bcc lattice structure, there are no stacking faults for DXA to detect. In addition, our nano-sized grains emit and absorb dislocations within narrow strain intervals. Thus, for cases where dislocations have been created at specific structural features, pass through a grain, and are absorbed by a different feature, the slip path can be identified by utilizing slip vector analysis. Slip vector analysis enables the identification of slip planes between individual sets of atoms, and calculates the magnitude and direction of slip for defects such as dislocations, stacking faults, and twin boundaries. With the slip vector package, the slip planes used by passing dislocations are shown, and whether the slip is caused by a perfect dislocation or a twinning dislocation is easily deduced from the magnitude of the vector.

The AtC user-package uses the formalism by Hardy [30, 31] to extract local values of Cauchy stress from atomistic simulation data. A grid consisting of 40 x 40 x 8 elements is superimposed onto the simulation domain, with element sizes of about 0.9nm. Using the atoms within the

elements adjacent to grid vertices (nodes), the AtC package computes spatially averaged continuum stress values via a tri-linear weighting function. More information on this method can be found in articles by Webb, Zimmerman, and Seel [32] and by Zimmerman, Jones, and Templeton [33].

8.4 Simulation results

8.4.1 Stress-strain behaviour

A stress-strain curve is calculated from sample 1 (at 300K and under uniaxial stress conditions) at the $10^6 s^{-1}$ strain rate and is shown in figure 2(a). The majority of this paper will concentrate on analysis of the deformation observed at the $10^6 s^{-1}$ strain rate, with section 3.7 devoted to noting differences obtained by varying the loading rate. The slope of the linear portion of the stress strain curves for sample 1 reveals the elastic modulus and the yield stress, using the 0.2% offset criteria, to be 121.9GPa and 3.85GPa respectively. When compared to experimental values, this value of the elastic modulus is lower than the ~170GPa elastic modulus and 1.6GPa yield stress seen in tantalum wires at 300K [34-36]. The elastic modulus and yield strength for sample 2 at $10^6 s^{-1}$ strain rate are 146.4GPa and 4.165GPa respectively. These values approach the experimentally observed values. Work by Guisbiers et al. [36] shows a yield stress of 4.06GPa from nano-indentation of a 100nm thick thin film.

In the stress-curves generated for sample 1, sharp stress drops are noted at 4.5 %, 8%, and 11.5% strain. These drops are related to the nucleation and transmission of dislocation and twinning events described in the next section. In sample 2, deformed to 15% strain, the specific strain levels at which dislocation emission (3.5%), twin formation (4%), and nano-void nucleation

(4.5%) are initiated are noted with arrow. No plastic deformation occurred before the 0.2% offset yield point in any of the virtual mechanical tests reported in this work.

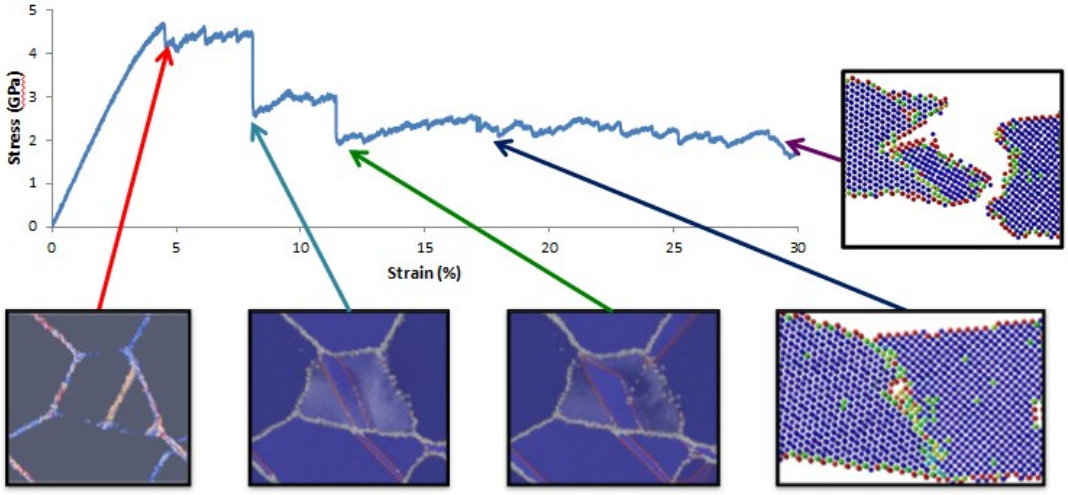

(a)

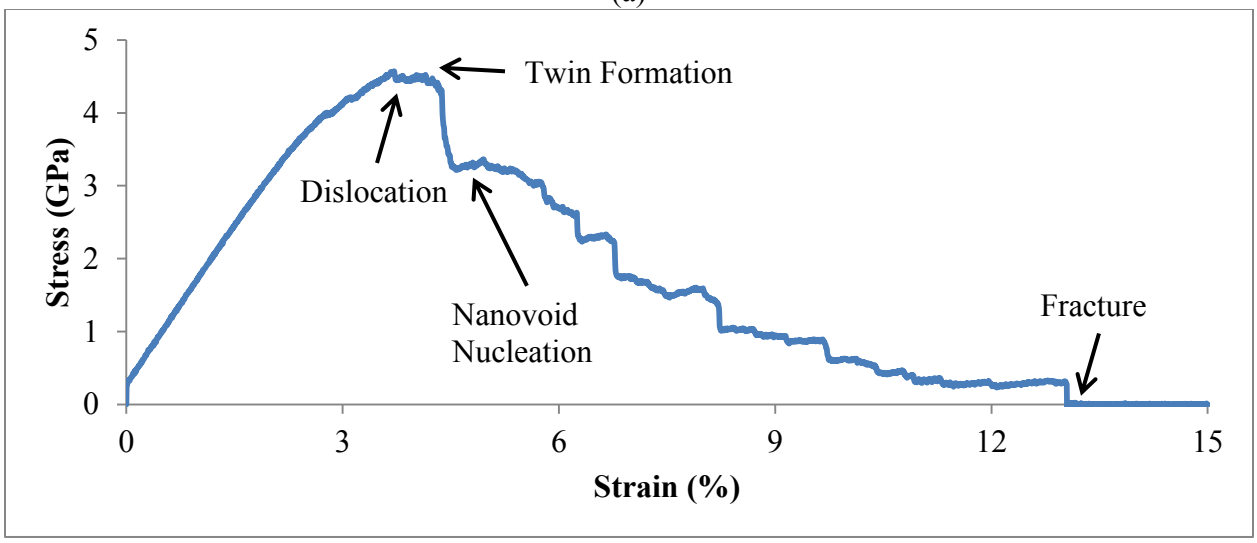

(b)

Figure 2: Stress-strain curves for (a) the nano-crystalline thin film simulated geometry in sample 1 at $10^6 s^{-1}$. The inset images indicate the deformation thresholds. The first, denoted with the red line, indicates emission of a perfect dislocation at about 4.5% strain. The second (light blue line) shows the first twin formation at about 9% strain. The third (green line) shows a second twin formation and transmission into a second grain at about 12% strain. The fourth (dark blue line) indicates initial nano-void formation at about 17.5% strain. The last inset (purple line) indicates final fracture of the sample in the region of the nano-void at 28% strain. (b) shows the stress-strain curve for sample 2 at $10^6 s^{-1}$. Initial dislocation emission occurred at 3.5%, initial twin formation at 4%, nano-void nucleation at 4.5%, and fracture occurred at 13%. Figure by author.

8.4.2 Dislocation emission

In both samples at $10^6 s^{-1}$, dislocation emission is the first deformation mechanism observed. In sample 1, the initial dislocation emission was observed at 4.5% strain. As the strain increases, the grain boundary accommodates the deformation by additional dislocation emission from the same grain boundary at 6, 7, and 8% strain. Slip vector analysis is performed on the data at 4.5, 5, and 6% strain in order to analyze the dislocations observed. Figure 3(a) shows the sample prior to dislocation emission (left) at 4.5% strain and after emission of two perfect dislocations at 5% strain from the right grain boundary, 1-3 traversing the center grain, and being absorbed by the lower grain boundary 1-2 (right). A red arrow shows the direction of the dislocation propagation. The pink colour shown in the images reflects a displacement of about 0.29nm, which matches well with the tantalum perfect dislocation Burgers vector of 0.286nm, and given that the grain is subjected to unequal, biaxial strain. Also shown in figure 3(a) is dislocation emission at 5% strain from the triple junction circled in red and extending into grain 2, indicated by a yellow arrow. This dislocation extends along the grain boundary, with very little separation between the grain boundary and the dislocation path. In figure 3(b) at 6% strain the paths of several dislocations emitted between 5 and 6 % strain not captured by DXA analysis are shown. The dislocations pass through the crystal, again being emitted by the right grain boundary 1-3 and absorbed by the lower grain boundary 1-2. The pink colour of the slip vectors again indicates that these are perfect $\frac{a}{2}|< 111 >|$ dislocations. Figure 3(c) show that the initial deformation mechanism is dislocation emission in sample 2 at $10^6 s^{-1}$ at 3.5% strain. The deformation behaves qualitatively similar to the dislocation studied in sample 1, with emission from one boundary, travel across the grain, and absorption by a different grain boundary. The pink color of the slip vector reveals that this is also a perfect $\frac{a}{2}|< 111 >|$ dislocation.

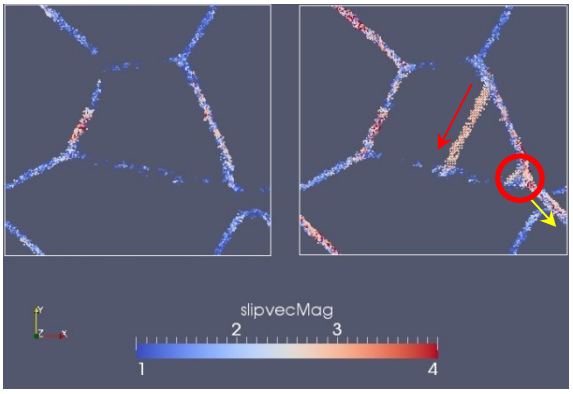

(a)

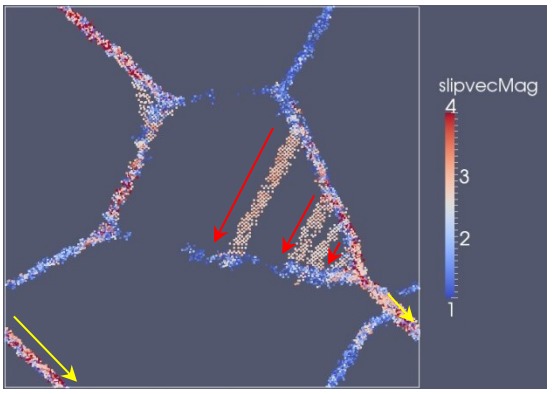

(b)

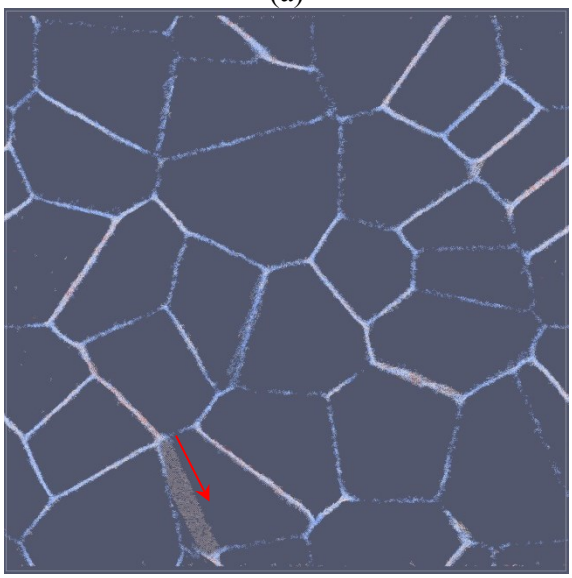

(c)

Figure 3: Slip vector analysis at (a) 4.5 to 5% strain in sample 1 and (b) 6% strain in sample 1. (c) 3.5% strain in sample 2 The scale bar goes from 0 to 0.4nm (0-4Å), with the pink lines in the figure indicating perfect dislocations with a slip vector of about 0.292nm. Figure (a,b) by Zimmerman, (c) by author.

Further analysis is conducted on the dislocation emission process in sample 1, figure 3(a), observed between 4.5 and 5% strain shown in figure 3(a). The dislocation was tracked for each .005% strain. Through this technique, the dislocation was observed as it lengthened and crossed the center grain to be observed by the lower 1-2 grain boundary. The dislocation emission process was also analyzed using slip vector analysis. The Burgers vector of the dislocation was analyzed through DXA analysis. It was found that the Burgers vector of the dislocation is parallel to the dislocation line, clearly indicating the screw nature of the dislocation. Screw dislocations in bcc materials have a non-planar dislocation core [37]. This non-planar nature

causes a high lattice friction, making the motion of screw dislocations the rate-controlling deformation mechanism in bcc materials [38]. This explains the overall screw nature of the dislocations observed in this work.

8.4.3 Twin formation

Below 9% strain at $10^6 s^{-1}$, dislocation emission is the primary means of deformation in sample 1. Above 9%, the nucleation of deformation twins becomes available as an additional deformation mechanism. At 9% strain, a twin has emitted from the upper grain boundary 1-2, and extends across the center grain. A second twin has emitted from the lower grain boundary 1-2 and extends across grain 2 to the right grain boundary 2-3. This is shown in figure 4(a). Slip vector analysis of the sample at 9% strain indicates the twins have a slip vector of about 0.1nm. This correlates well to the ideal twinning Burgers vector of 0.095nm. This analysis is shown in figure 4(a) where the twins are indicated by light blue slip planes. Figure 4(b) shows DXA analysis at 9% strain, indicating twin boundaries as interfaces within the grain. Careful analysis shows that the twin plane in grain 1 is confirmed to be (211) for the left and right twin boundary segments, while the segment closest to the top grain boundary 1-2 is $(12\bar{1})$. Twin formation as a deformation mechanism is also seen in sample 2. Figure 4 (e) shows sample 2 at 5% strain. A twin has emitted from a grain boundary and extends across the grain. At 6% strain, figure 4 (f), both twin formation and dislocation emission are activated.

Twin transmission across grain boundaries is noted as deformation increased. In figures 4(c) and 4(d) the interaction between the twin in grain 3 and the right grain boundary 1-3 is detailed. In figure 4(c), a twin dislocation has emitted from the red-circled region and extended across the diameter of the grain to grain boundary 1-3, show with a red arrow. The twin begins to cross the

grain boundary here. Figure 4(d) shows the twin has clearly crossed into grain 1 and is beginning to spread into the grain.

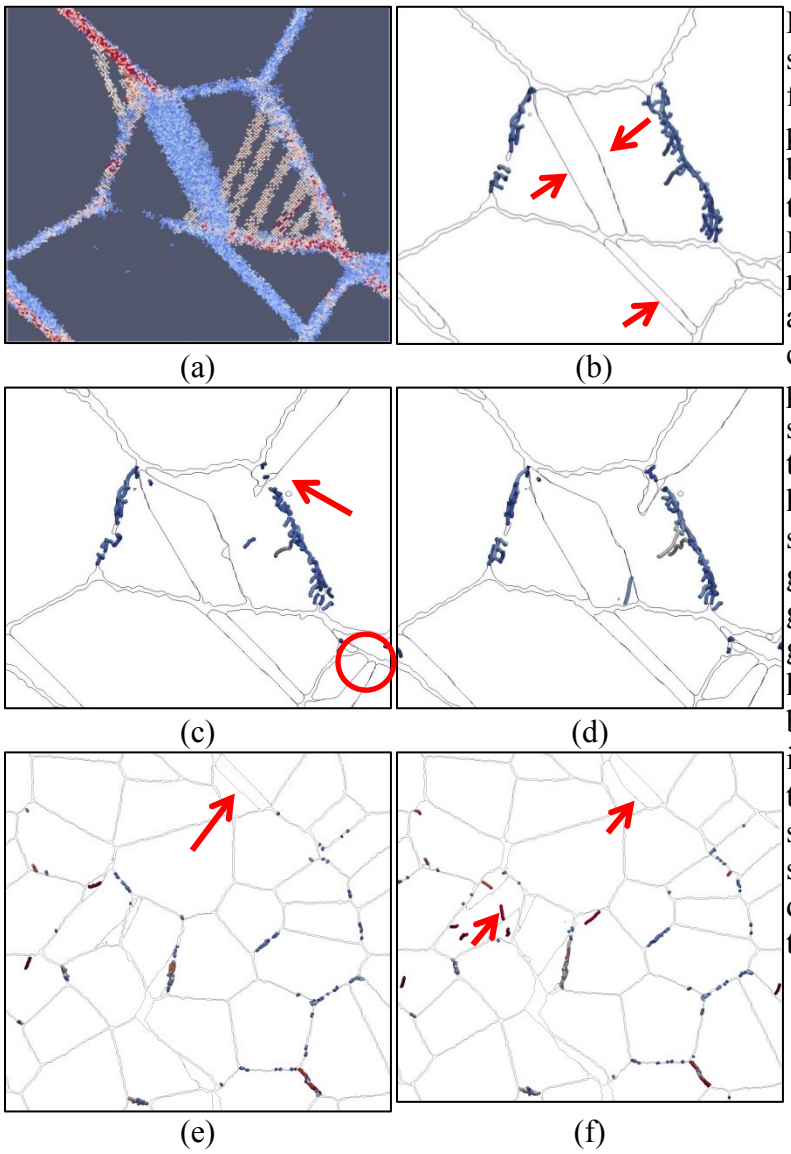

Figure 4: Deformation twinning in sample 1 (a-d) and in sample 2 (e-f). (a) 9% strain, twins are clearly present in the sample, shown in blue. Atoms shown coloured by their value of slip vector magnitude. Blue indicates about 0.1nm slip and marks twins, while the pink shows about 0.3nm magnitude of slip, characteristic of perfect dislocation passage. (b) DXA analysis of the sample at 9% strain displays the twin boundaries as thin lines, highlighted with arrows. (c) At 12% strain a new twin has originated in grain 3 and is beginning to cross the grain boundary into the center grain. (d) at 13% strain, the twin has clearly crossed the grain boundary into the center grain and is growing towards the existing twin. (e) show twin formation in sample 2 at 5% strain. At (f) 6% strain, both twin formation and dislocation emission (shown as red tubes) are active. Figure by author.

8.4.4 Grain boundary sliding

Grain boundary sliding was investigated in three grain boundaries present in sample 1. In order to perform this analysis, the same atoms are isolated and analyzed from both strain levels to accurately measure the sliding in each grain boundary. The sliding observed at 15% strain was

compared to the grain configuration at 0% strain. Grain boundary 2-3 shows the most sliding at 3.69nm. Grain boundary 1-3 demonstrates both grain boundary sliding and grain boundary m .igration [39-42] normal to the grain boundary plane. Cahn and Taylor [43] have proposed that grain boundary sliding is proportional to grain boundary migration. The proportionality constant is referred to as the coupling factor, □. In this work, the total extent of sliding parallel to the grain boundary plane is 1.26nm, with 1.84nm of motion in the perpendicular direction. This gives a coupling factor (β) of 0.68. Grain boundary sliding in sample 2 was observed in four grain boundaries, with a total of 2.96 nm of sliding. Very little grain boundary migration was observed, thus no coupling factor could be calculated.

8.4.5 Stress analysis

Stress analysis is performed on the snapshots of deformation in sample 1 captured at 4.5 and 5% strain to clarify local stress conditions prior to the initial dislocation emissions. As mentioned in Section 2, the local Cauchy stress tensor is calculated at the vertices of a grid that overlays the atomic system. Element size for this grid is approximately 0.9nm. This stress tensor is used to determine local values of effective or von Mises stress, shown in figure 5. The boxed region on the right side of figure 5 at 4.5% strain shows a locally high concentration of stress equal to or greater than 8GPa in magnitude. By 5% strain, a dislocation has been emitted from this locally stressed area, shown as a pink line. As in figure 4, the colour of the dislocation line corresponds to the magnitude of the slip vector, with pink indicating a displacement of about 0.3nm, corresponding to the slip of a perfect dislocation. After the dislocation emits, the local stress has been significantly reduced, and a new segment of boundary has been introduced within grain 2.

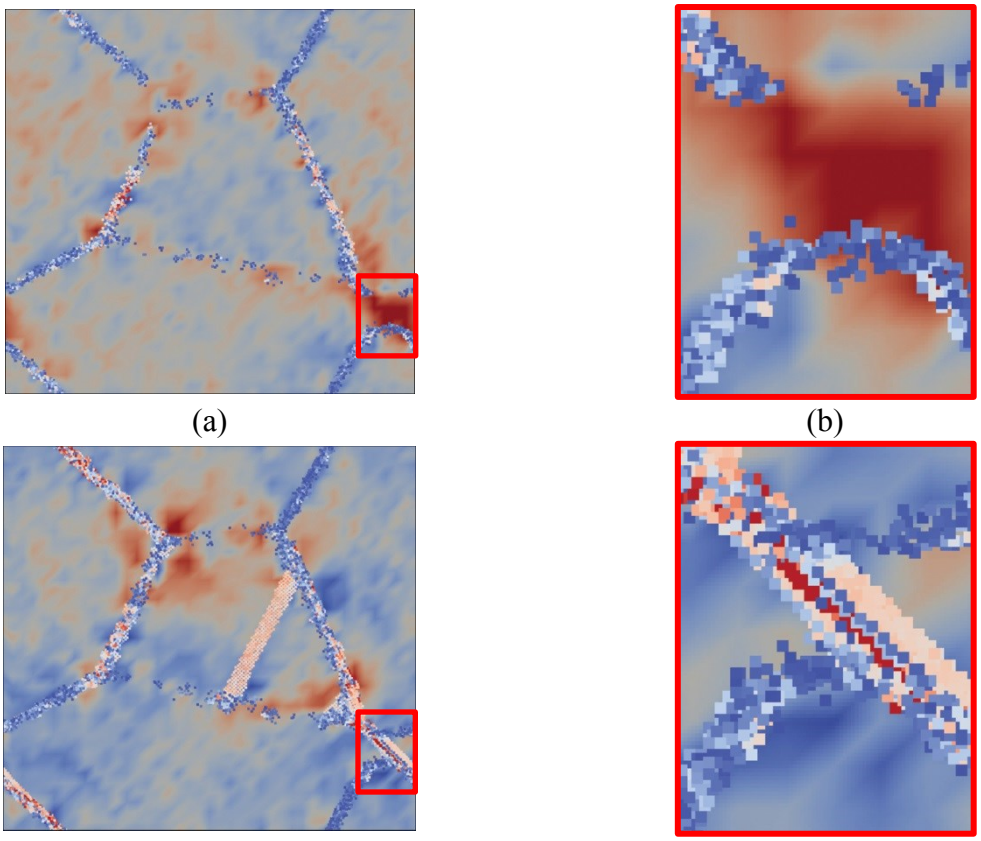

Figure 5: Visualization of local effective (von Mises) stress before and after dislocation emission. The colour scale of the stress field goes from blue at 2 GPa to red at 8 GPa. (a) The effective stress field over the entire sample at 4.5% strain. (b) shows the area outlined in red in more detail, showing locally high stress (>8GPa). For clarity, the atomic configuration shown in figure 5(a) is superimposed to correlate the grain boundary structure and dislocation paths with the stress field values. (c) The effective stress field over the entire sample at 5% strain. (d) shows the area outlined in red in more detail after dislocation emission, showing that the local stress has been relieved and a dislocation has emitted and extends into grain 2. Figure by author.

8.4.6 Nano-void formation and fracture

Figure 6(a) shows the top view of sample 1 at 17.5% strain. The twin first noted in figure 4(c) has transmitted across the right grain boundary 1-3 and intersects the right boundary of the twin in grain 1. A thin red line indicates the region viewed in figure 6(b). When a thin slice of the sample showing the xz plane is viewed in figure 6(b) it is seen that a nano-void has formed in the

interface created between the two twin boundaries that have intersected. The nano-void of interest is in the center of the image, outlined with a red box and has a size of 0.55nm. The size of the nano-void is determined by measuring the diameter of the void in the commercial software package Amira. The red outlines of this void correlate well with the work done by Kumar et al. [44] in nano-crystalline nickel. In their work, they observed that a step in the grain boundary is created by dislocation slip. Grain boundary sliding then operates to open a void within the boundary. Void growth has been studied by Rudd [19], Bringa [45], and Ahn [46]. Their work (both experimental and simulation) indicates that voids similar to this one grow through the emission of dislocation loops.

In figure 6, the growth of the nano-void is observed as strain increases. In figure 6(c) at 23% strain, the void has clearly grown when compared to figure 6(b), both along the line of the twin boundary and into the surrounding grain structure. The void has grown to the extent that only a small barrier remains between the void and the upper surface of the thin film. From 17.5% to 23% strain the nano-void grew by 1.63nm to a diameter of 2.18nm. It is not clear by which mechanism this nano-void grows, although the question merits further study.

Additional nano-void growth and critical thinning of the material is shown in figure 6(d) at 27% strain. The top layer of material has separated, opening the nano-void to the surface. As strain progresses, the cross-sectional area of the sample in this region is significantly reduced, lowering its ability to withstand stress. An additional, smaller nano-void can be seen to have formed in this remaining material, circled in red. Under increasing amounts of strain, this secondary nano-void is seen to persist and reaches a maximum size of 3.84nm before the sample fully pulls apart as shown in figure 6(e). Figure 7 shows the growth of the initial nano-void as a function of increasing strain. It shows that there is a linear relationship between the diameter of the void and

increasing strain, with a growth rate of 28.9mm/s. Bringa and co-workers [17, 18, 20, 45, 47, 48] have done very detailed analysis of the growth and fracture of nano-voids in tantalum, showing that in their work, the voids grow through the emission of dislocation loops. The work by Traiviratana [20] shows expansion of the void along the grain boundary similar to the growth shown in this work.

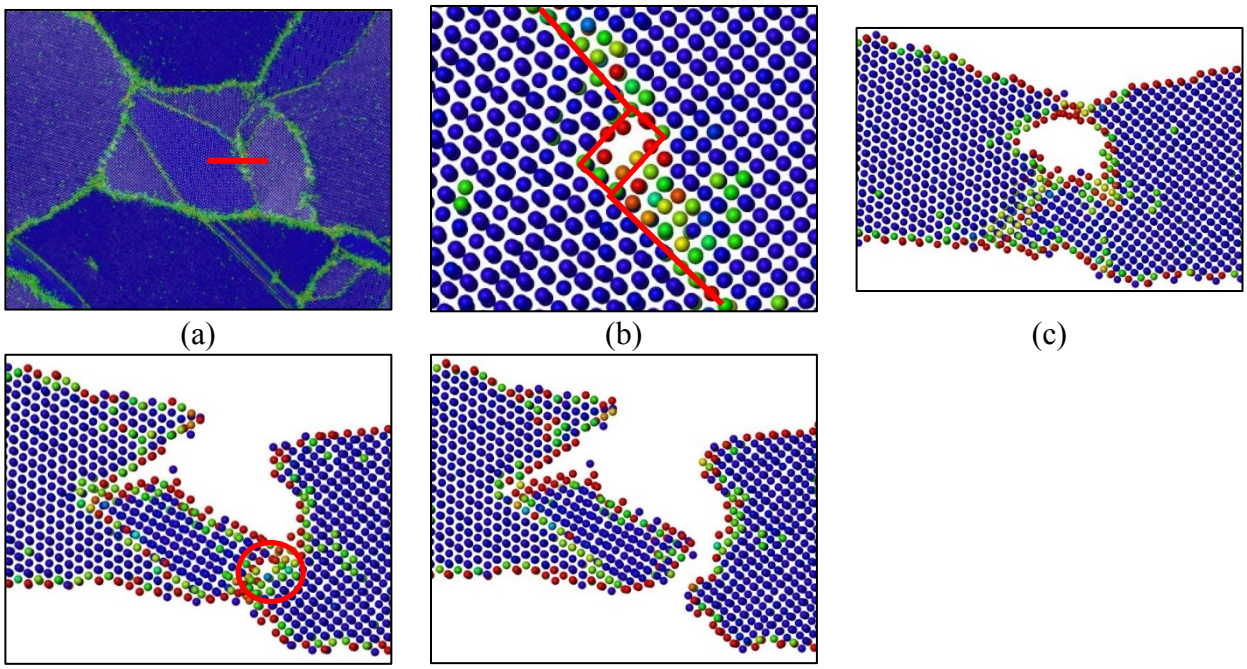

Figure 6: Nano-void formation, growth, and fracture in sample. (a)Top view of the sample at 17.5% strain. Red line indicates section of sample shown in following figures. (b) Front view of selected section of sample. (c) 23% strain showing nano-void growth. At 23% strain the top of the sample is 1-2 atoms thick. (d) 27% strain, showing an additional nano-void forming. (e) 29% strain. Fracture has breached both surfaces. Colour coding of (a-d) is by centrosymmetry parameter, with blue showing atoms in perfect lattice, green showing atoms with moderate disruption, as in grain boundaries, and red showing little lattice symmetry. Figure by author.

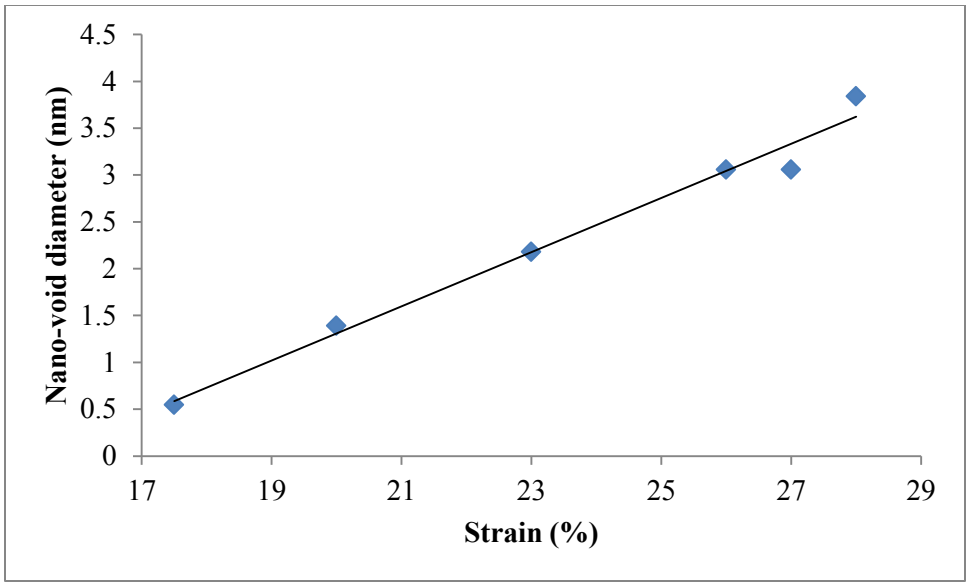

Figure 7: Nano-void growth in sample 1 as a function of strain. The nano-void grows at a rate of 0.289nm per 1% strain. Figure by author.

Intergranular fracture was also observed in sample 2. The same boundary was observed to fracture at each strain rate; beginning with nano-void formation and leading to full-thickness fracture. Analysis of the crack as it developed showed that nano-void formation and growth is the mechanism responsible for crack initiation and progression in this sample, similar to that observed for sample 1. Figure 8(a) shows sample 2 deformed using the $10^6 s^{-1}$ strain rate. The intergranular crack that initiated in the same grain boundary at each strain rate is circled in red. Figure 8 (b) shows an edge-on slice through the cracked region of the sample just prior to breaching both surfaces of the film, similar to that shown in figure 6.

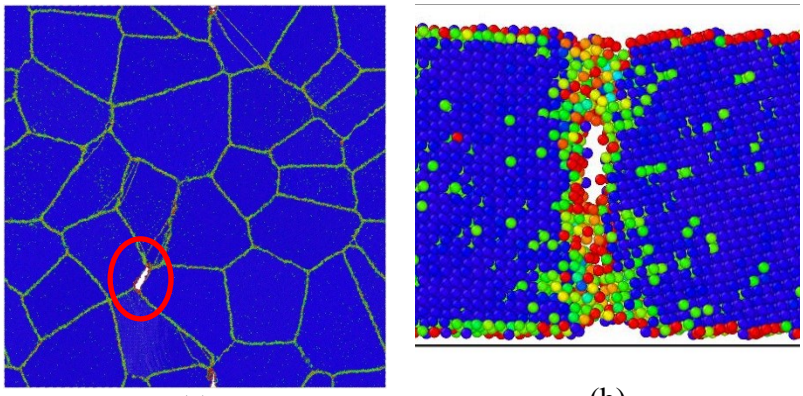

(a) (b)

Figure 8: Intergranular crack nucleation and progression in sample 2. Each crack shows evidence of forming through nano-void formation and growth. (a) Crack of interest that formed at each strain rate studied. (b) Slice through the crack at $10^9 s^{-1}$.Nano-void formation is clearly seen. Colour coding as in figure 6. Figure by author.

8.4.7 Strain rate effects

The samples were deformed at different strain rates to determine the effect of strain rate on plasticity. The strain rates increased in orders of magnitude from $10^5 s^{-1}$ to $10^9 s^{-1}$ for sample 1 and from $10^6 s^{-1}$ to $10^9 s^{-1}$ for sample 2. The combined stress-strain curves for each strain rate are seen in figure 9. The curves for sample 1 have been separated by similar behaviour, with the 10^5, 10^6, and 10^7 s^{-1} strain rates grouped in figure 9(a). The higher two strain rates, 10^8 and $10^9 s^{-1}$ are shown in figure 9(b). Stress-strain curves for sample 2 are shown in figure 9(c). Marked in the figures are the strain level at which notable deformation mechanisms occur, including dislocation emission, twin formation, and twin transmission. In sample 1, the first mechanism to activate is dislocation emission for the slower three strain rates (10^5, 10^6, and $10^7 s^{-1}$). At the higher strain rates (10^8 and 10^9 s^{-1}), the initial deformation mechanism is twin formation with the initial dislocation emission occurring at higher strain levels. In sample 2, the initial deformation mechanism at 10^6 and $10^7 s^{-1}$ is dislocation emission, while at 10^8 and $10^9 s^{-1}$ it is twin formation. The strain levels at which these mechanisms activate are marked with arrows. These results are similar to that seen by Pan et al.[7] who also observed twinning as the initial deformation

mechanism at a strain rate on the order of $10^8 s^{-1}$. Work by Meyers et al. [49] showed that there is a distinct relationship between strain rate and deformation twins as the initial deformation mechanism at high strain rates. This agrees well with the work presented in this article.

It is notable that the maximum stress reached by each curve in sample 1 lessens as the strain rate slows, as shown in figure 10(a). The maximum stress reached in each simulation increased with strain rate, with the $10^5 s^{-1}$ strain rate also having the lowest maximum stress of 4.5GPa. There is a distinct change in slope that can be seen at the point corresponding to the $10^7 s^{-1}$ strain rate. The strain rate sensitivity has been determined to be 0.015 up to $10^7 s^{-1}$, and 0.049 after. A similar plot for sample 2 is shown in figure 10 (b). The results are qualitatively similar to those observed in sample 1, with the change in slope occurring at $10^8 s^{-1}$. The strain rate sensitivity up to $10^8 s^{-1}$ is 0.04, and 0.08 after. These are comparable to the 0.02 to 0.05 range measured in experiments by Wei et al. [35] and Cao et al. [50]. The noted change in slope at about $10^7 s^{-1}$ for sample 1, and $10^8 s^{-1}$ for sample 2, along with the observed change in initial deformation mechanism indicates that strain rate effects become much more pronounced at strain rates at or above $10^8 s^{-1}$. The change from crystallographic slip to twin formation in this work agrees well with previous work [18, 19, 51-53], particularly that of Tang and co-workers [18] who saw a similar change from crystallographic slip to twin formation at $10^8 s^{-1}$ strain rate.

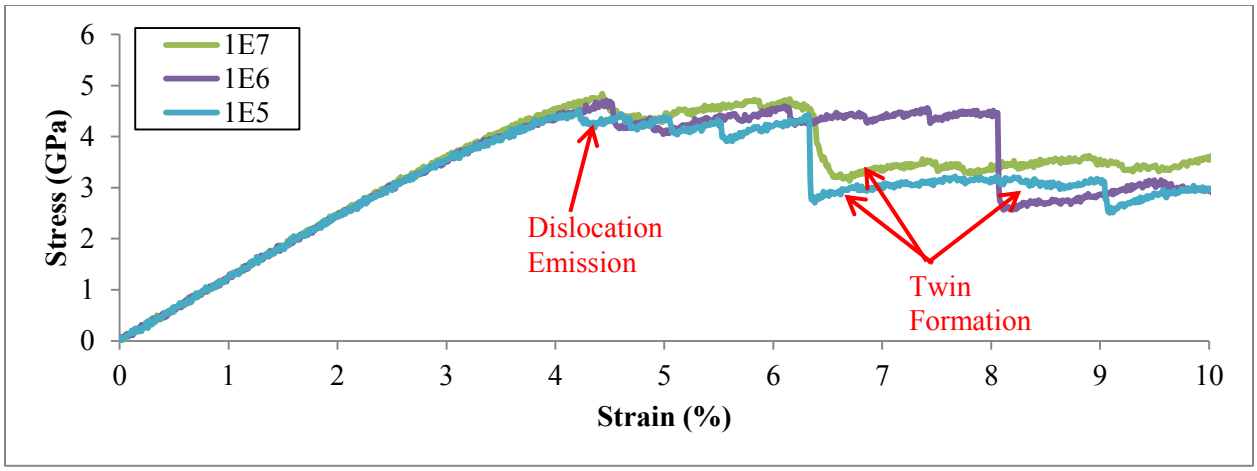

(a)

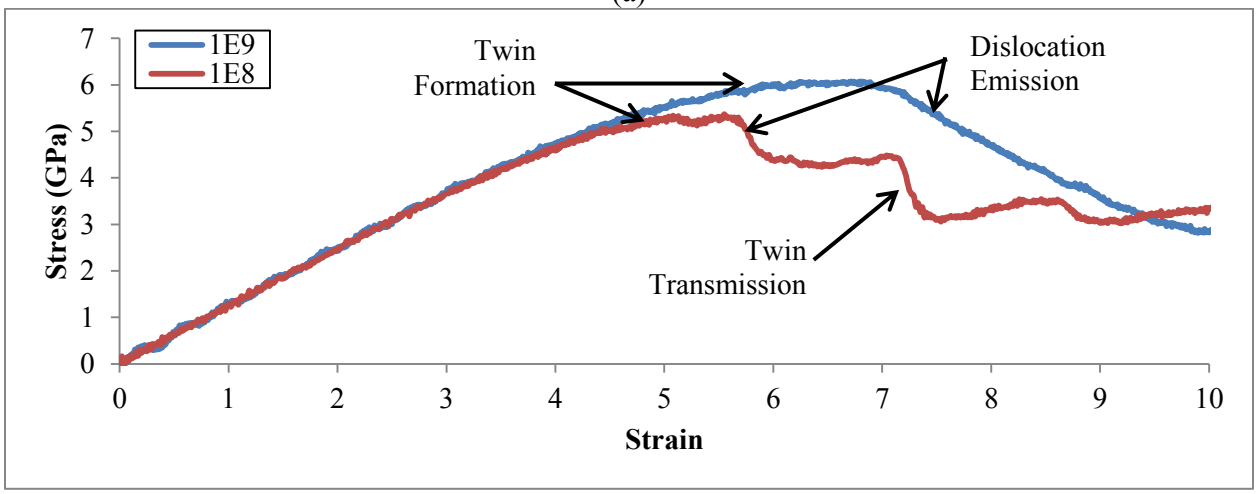

(b)

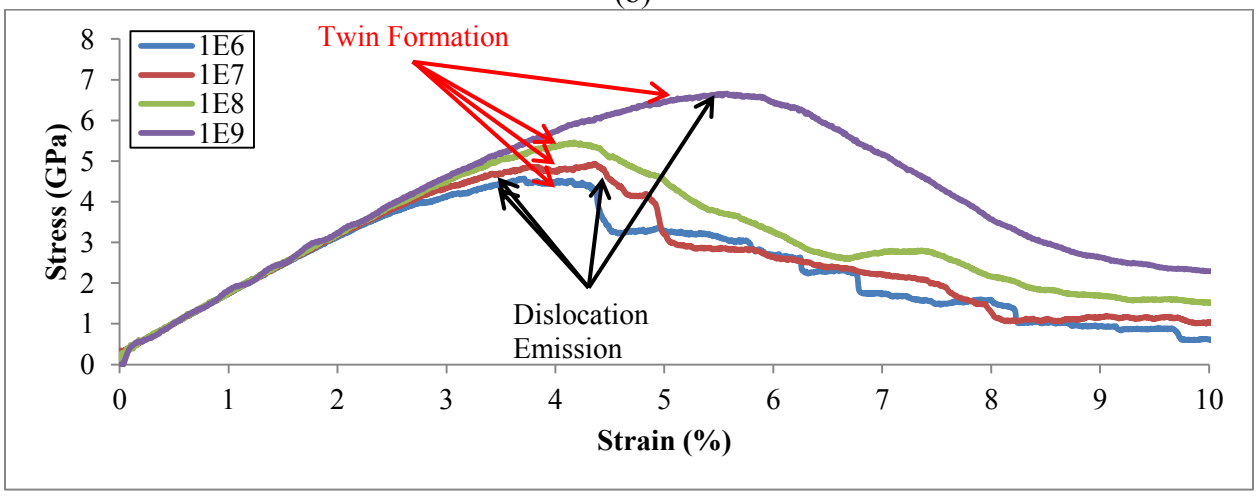

(c)

Figure 9: Combined stress-strain curves for sample 1 for the five strain rates used in this work. (a) shows the stress-strain curves for the slower three rates, 10^5, 10^6, and 10^7 s^{-1}. (b) shows the stress-strain curves for the higher two rates: 10^8 and 10^9 s^{-1} strain rates. (c) Stress-strain curves for sample 2 showing all strain rates. Deformation events are noted on each curve. Figure by author.

Figures 10(c) and (d) show the number of atoms with the characteristic slip of both twinning and perfect dislocations as a function of strain for sample 2. At the higher strain rates of 10^8 and $10^9 s^{-1}$, the number of atoms with the characteristic slip of a twinning dislocation is observed to have increased by 3:1 for $10^8 s^{-1}$ and 4:1 for $10^9 s^{-1}$ strain rates. This observation greatly supports our claim that twinning is the dominant deformation mechanism at very fast strain rates and becomes a factor at strain rates of $10^8 s^{-1}$ and higher.

Activation volumes were calculated for both dislocation emission and twin formation in sample 1. Dislocation emission has an activation volume of about $5b^3$ with the activation volume for twin formation about 3 times less. The activation volume for twin formation is smaller because the Burgers vector for twin formation is about 3 times smaller than that for dislocation emission. This is consistent with the values observed by Asaro and Suresh [54] in their work on nano-crystalline fcc metals.

We examined the sensitivity of grain boundary sliding to strain rate. In each sample, sets of atoms containing a grain boundary were isolated and examined at each percent strain to determine if any sliding occurred. The sliding was measured and then plotted as a function of strain, shown in figure 11. In sample 1, the majority of the sliding occurred in grain boundary 2-3, while in sample 2, four boundaries showed evidence of sliding. We found that there was little sensitivity to strain rate in either sample, however, with additional sample geometries and a greater statistical variation in future work, a trend may become clear.

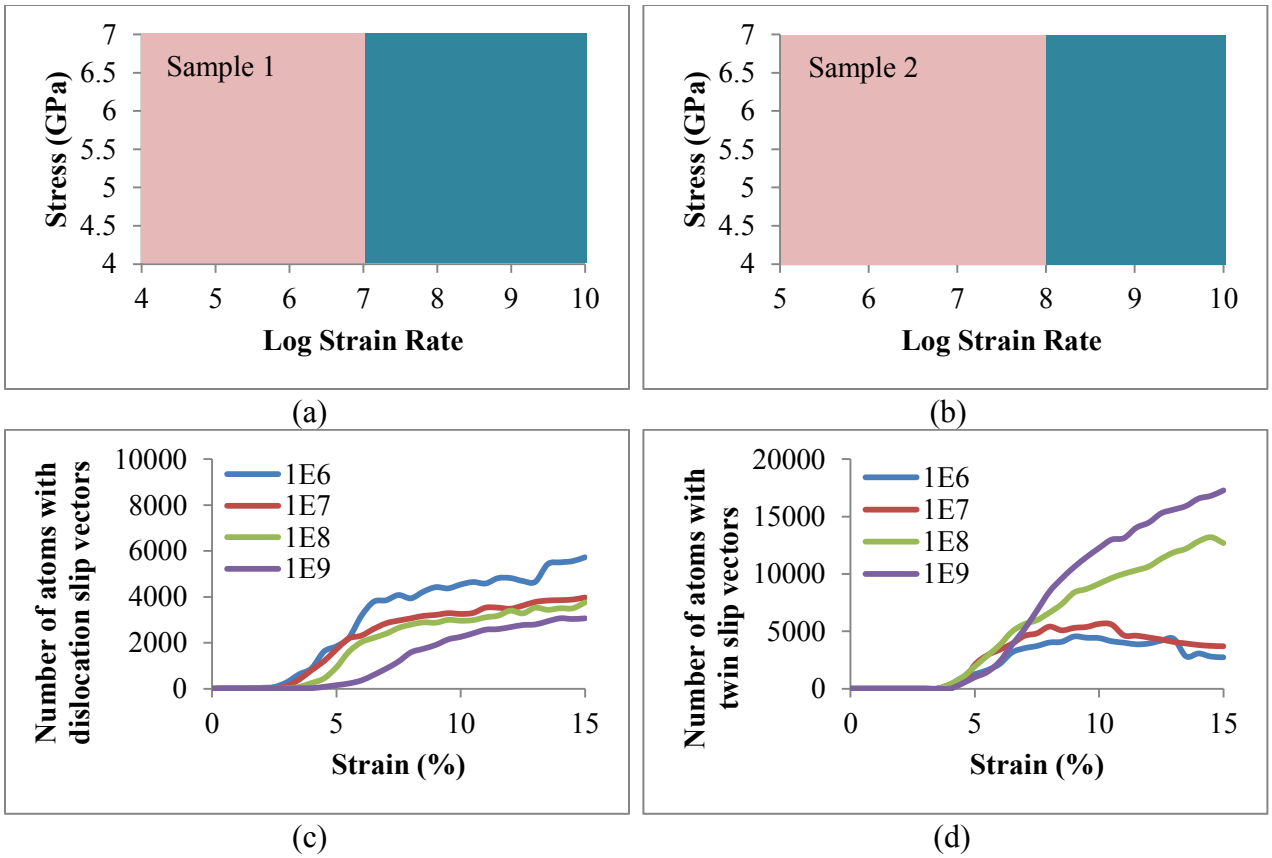

Figure 10: Effects of strain rate on the maximum stress and number of atoms with the characteristic slip of both the twinning and dislocation emission deformation mechanisms. (a) Max stress at yield vs the log of the strain rate for sample 1 and (b) sample 2. The two slopes of the graph are highlighted with coloured boxes, indicating the strain rate regime where dislocation emission is the first active mechanism (red) and the regime where twin boundary formation is the first (blue). (c) Number of atoms displaced by the characteristic slip vector of dislocation in sample 2 and (d) twinning dislocations in sample 2. Figure by author.

Figure 12(a) shows grain boundary 2-3 in sample 1 before deformation has occurred. Figure 12 (b-d) shows this same grain boundary at 15% strain at 3 different strain rates: 10^5, 10^7, and $10^9 s^{-1}$. There is no clear trend relating grain boundary sliding and strain rate. The strain rate with the greatest amount of sliding was the 10^6 s^{-1} simulation (not shown) at 3.69nm, while that with the least sliding was the 10^8 s^{-1} simulation (not shown) at 0.95nm. The sliding observed in grain

boundary 2-3 at the three strain rates shown in figure 12 are the ones with the most similar sliding, within a 1nm range.

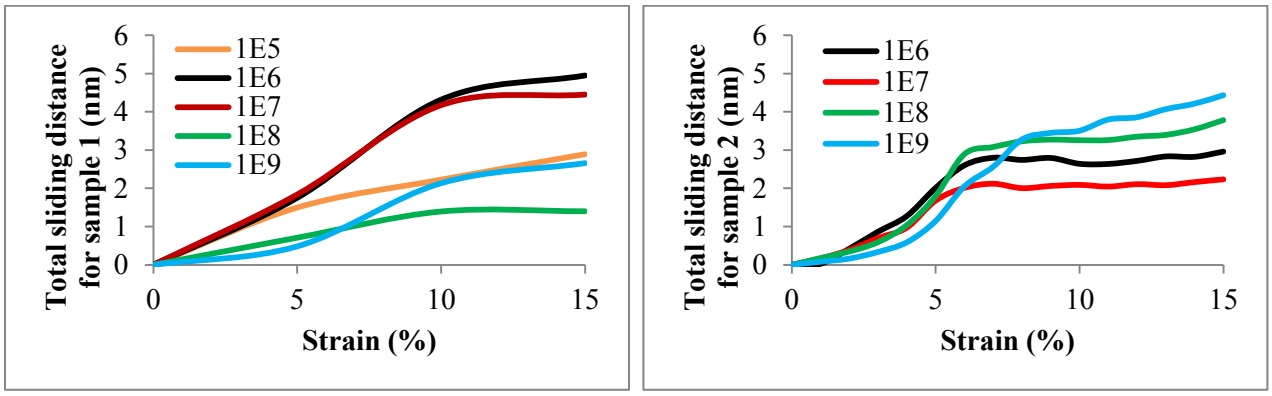

(a) (b)

Figure 11: Grain boundary sliding as a function of strain in (a) sample 1 and (b) sample 2. There is no clear trend correlating grain boundary sliding and strain rate. Figure by author.

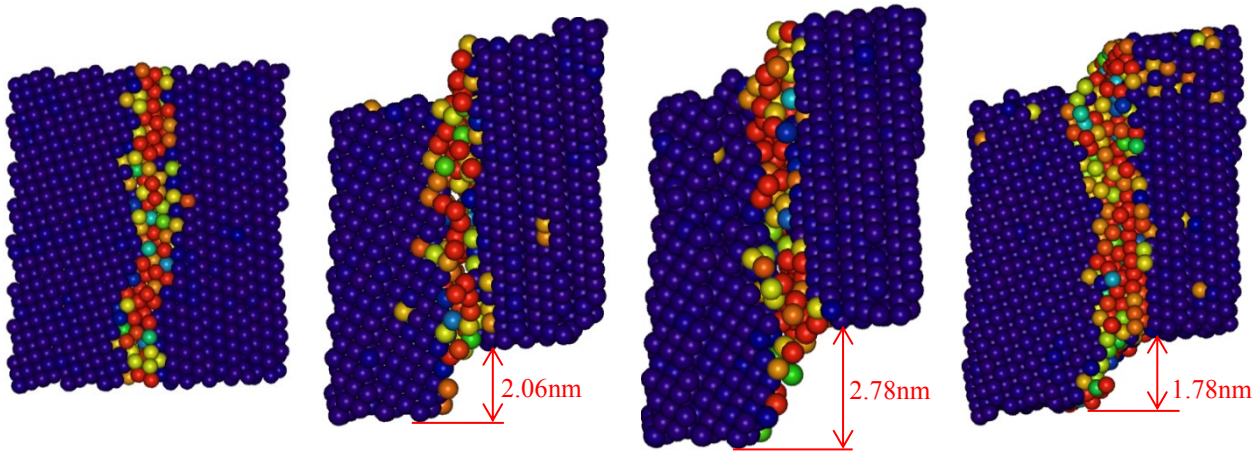

(a) (b) (c) (d)

Figure 12: Grain boundary sliding in sample 1 at several strain rates. shown at 15% deformation. (a) The sample before deformation. (b) Sample deformed at 10^5 s^{-1}. (c) Sample deformed at 10^7 s^{-1}. (d) Sample deformed at 10^9 s^{-1}. Colour coding as in figure 6. Figure by author.

8.5 Discussion & summary

In this article, we have presented the mechanisms of deformation observed within a molecular dynamics simulation framework for two polycrystalline, randomly misoriented, thin-film

samples of tantalum subjected to uniaxial tension stress loading. Sample 1 contains 464K atoms, chosen to facilitate study at $10^5 s^{-1}$ strain rate; sample 2 is one order of magnitude larger than sample 1, with 4.6M atoms, and 30 grains. Both samples were tested at strain rates increasing in orders of magnitude from 10^6 to $10^9 s^{-1}$. Elastic testing of the Li [23] potential confirms that it gives reasonable elastic constants at zero and finite temperature.

We have observed that deformation at the nano-scale is a competing process between dislocation emission and twin formation. Unlike previously reported results, the work presented here indicates that in sample 1 and at the relatively low strain rate of $10^6 s^{-1}$, dislocation emission is the initial deformation mechanism at 4.5% strain and is the dominating mechanism below 9% strain with several perfect dislocations observed to have both emitted from the right grain boundary between grains 1 and 3, and traveled through the grain to be absorbed by the lower 1-2 grain boundary. Dislocation emission as the initial deformation mechanism was also observed in sample 2 at 3.5% strain. The more commonly observed deformation twin formation, in both experiments and simulation work, begins at higher levels of strain, above 9% in sample 1, while in sample 2 twin formation began much earlier, at 4% strain. Twins were also observed to be transmitted across grain boundaries and to extend into new grain structures, if the local structure is favorable. Dislocations are emitted from and absorbed by grain boundaries, while twins originate in grain boundaries and can grow to consume the majority of the original grain. The dislocations were observed to be slipping on the {112}/<111> slip system. This is somewhat unexpected, since the generalized stacking fault curves generated for this particular tantalum potential at 0K would indicate that the energy barrier is lower on the {110}/<111> slip system. Lower stacking fault energy implies that crystallographic slip on this slip system should be easier than crystallographic slip on a different slip system. However, slip on the {112}/<111> plane has

been observed in all the potentials developed for tantalum to date [55]. Therefore, our results showing {112}/<111> slip is consistent with the results of other investigators. Full investigation at finite temperatures involving the energy barriers that must be overcome for dislocation slip, the critical resolved shear stresses necessary, and the study of competing mechanisms in bcc dislocation core motion is a complex task currently being undertaken by Hale et al. [55].

As shown in previous work [2], grain boundaries have a significant effect on deformation processes at the nano-scale. With grain boundaries comprising a greater proportion of a nano-crystalline sample than in a coarse-grained material, a greater understanding of the conditions necessary for dislocation emission and twin formation, and the interactions between twins and grain boundaries will further the scientific understanding of their role in nano-crystalline deformation.

Analysis of strain rate effects on this sample configuration have revealed that the initial deformation mechanism observed at lower strain rates (10^5 s^{-1} to 10^7 s^{-1}) is dislocation emission while at the higher two strain rates (10^8 s^{-1} and 10^9 s^{-1}) it is deformation twinning. Analysis of characteristic slip vectors shows that at $10^8 s^{-1}$, three times as many atoms exhibit characteristic twin deformation as crystallographic slip, while at $10^9 s^{-1}$ this ratio rises to 4:1. Strain rate effects appear to become much more pronounced at strain rates of $10^8 s^{-1}$ or faster. Grain boundary sliding analysis in this work reveals that there is little to no dependence of sliding on strain rate. The qualitative and quantitative similarities in results between the two samples shows that despite its limited number of both atoms and grains, sample 1 is an adequate subject for study at low strain rates using molecular dynamics.

8.6 Acknowledgements

The authors would like to acknowledge the invaluable assistance of Christopher Weinberger and Alexander Stukowski, the author of the DXA and OVITO programs, as well as Christopher Lammi and Stephanie Pitts for their fruitful discussions. We also acknowledge the support of the Enabling Predictive Simulation Research Institute (EPSRI) and the Predicting Performance Margins (PPM) program. Sandia National Laboratories is a multi-program laboratory managed and operated by Sandia Corporation, a wholly owned subsidiary of Lockheed Martin Corporation, for the U.S. Department of Energy's National Nuclear Security Administration under contract DE-AC04-94AL85000. Also contributing vital support is the Department of Energy grant – DE-FG02-08ER46525.

References

[1] M. W. Chen, E. Ma, K. J. Hemker, H. W. Sheng, Y. M. Wang, and X. M. Cheng, "Deformation twinning in nanocrystalline aluminum," *Science,* vol. 300, pp. 1275-1277, May 2003.

[2] D. Farkas and L. Patrick, "Tensile deformation of fcc Ni as described by an EAM potential," *Philosophical Magazine,* vol. 89, pp. 3435-3450, 2009 2009.

[3] S. L. Frederiksen, K. W. Jacobsen, and J. Schiotz, "Simulations of intergranular fracture in nanocrystalline molybdenum," *Acta Materialia,* vol. 52, pp. 5019-5029, Oct 2004.

[4] A. Godon, J. Creus, S. Cohendoz, E. Conforto, X. Feaugas, P. Girault*, et al.*, "Effects of grain orientation on the Hall-Petch relationship in electrodeposited nickel with nanocrystalline grains," *Scripta Materialia,* vol. 62, pp. 403-406, Mar 2010.

[5] X. Z. Liao, Y. H. Zhao, S. G. Srinivasan, Y. T. Zhu, R. Z. Valiev, and D. V. Gunderov, "Deformation twinning in nanocrystalline copper at room temperature and low strain rate," *Applied Physics Letters,* vol. 84, pp. 592-594, Jan 2004.

[6] M. D. McMurtrey, G. S. Was, L. Patrick, and D. Farkas, "Relationship between localized strain and irradiation assisted stress corrosion cracking in an austenitic alloy," *Materials*

Science and Engineering a-Structural Materials Properties Microstructure and Processing, vol. 528, pp. 3730-3740, Apr 2011.

[7] Z. Pan, Y. Li, and Q. Wei, "Tensile properties of nanocrystalline tantalum from molecular dynamics simulations," *Acta Materialia,* vol. 56, pp. 3470-3480, Aug 2008.

[8] H. Van Swygenhoven, P. M. Derlet, and A. G. Froseth, "Nucleation and propagation of dislocations in nanocrystalline fcc metals," *Acta Materialia,* vol. 54, pp. 1975-1983, Apr 2006.

[9] Y. M. Wang, A. M. Hodge, J. Biener, A. V. Hamza, D. E. Barnes, K. Liu*, et al.*, "Deformation twinning during nanoindentation of nanocrystalline Ta," *Applied Physics Letters,* vol. 86, p. 3, Mar 2005.

[10] C. Ajing, "Shape memory effects and pseudoelasticity in bcc metallic nanowires," *Journal of Applied Physics,* vol. 108, 1 Dec. 2010.

[11] Y. Zhang, P. C. Millett, M. Tonks, and B. Biner, "Deformation-twin-induced grain boundary failure," *Scripta Materialia,* vol. 66, pp. 117-120, Jan 2012.

[12] C. Zhenhua, S. Qianwei, H. Yongli, and M. Xiangkang, "The rate sensitivity and plastic deformation of nanocrystalline tantalum films at nanoscale," *Nano Scale Research Letters,* vol. 6, pp. 186-92, 2011 2011.

[13] J. B. Jeon, B.-J. Lee, and Y. W. Chang, "Molecular dynamics simulation study of the effect of grain size on the deformation behavior of nanocrystalline body-centered cubic iron," *Scripta Materialia,* vol. 64, pp. 494-497, Mar 2011.

[14] R. E. Rudd, "High-rate Plastic Deformation of Nanocrystalline Tantalum to Large Strains: Molecular Dynamics Simulation," in *Ductility of Bulk Nanostructured Materials*. vol. 633-634, Y. Zhao and X. Liao, Eds., ed, 2010, pp. 3-19.

[15] P. Zhiliang, L. Yulong, and W. Qiuming, "Molecular dynamics simulation of nanocrystalline tantalum under uniaxial tension," *Diffusion and Defect Data Part B (Solid State Phenomena),* vol. 139, pp. 83-8888, 2008 2008.

[16] Z. H. Cao, P. Y. Li, and X. K. Meng, "Nanoindentation creep behaviors of amorphous, tetragonal, and bcc Ta films," *Materials Science and Engineering a-Structural Materials Properties Microstructure and Processing,* vol. 516, pp. 253-258, Aug 2009.

[17] Y. Z. Tang, E. M. Bringa, and M. A. Meyers, "Ductile tensile failure in metals through initiation and growth of nanosized voids," *Acta Materialia,* vol. 60, pp. 4856-4865, Jul

2012.

[18] Y. Z. Tang, E. M. Bringa, B. A. Remington, and M. A. Meyers, "Growth and collapse of nanovoids in tantalum monocrystals," *Acta Materialia,* vol. 59, pp. 1354-1372, Feb 2011.

[19] R. E. Rudd, "Void growth in bcc metals simulated with molecular dynamics using the Finnis-Sinclair potential," *Philosophical Magazine,* vol. 89, pp. 3133-3161, 2009 2009.

[20] S. Traiviratana, E. M. Bringa, D. J. Benson, and M. A. Meyers, "Void growth in metals: Atomistic calculations," *Acta Materialia,* vol. 56, pp. 3874-3886, Sep 2008.

[21] C. L. Kelchner, S. J. Plimpton, and J. C. Hamilton, "Dislocation nucleation and defect structure during surface indentation," *Physical Review B,* vol. 58, pp. 11085-11088, Nov 1998.

[22] S. Plimpton, "Fast Parallel Algorithms for Short-Range Molecular Dynamics," *Journal of Computational Physics,* vol. 117, pp. 1-19, Mar 1 1995.

[23] Y. H. Li, D. J. Siegel, J. B. Adams, and X. Y. Liu, "Embedded-atom-method tantalum potential developed by the force-matching method," *Physical Review B,* vol. 67, p. 8, Mar 2003.

[24] Y. Mishin and A. Y. Lozovoi, "Angular-dependent interatomic potential for tantalum," *Acta Materialia,* vol. 54, pp. 5013-5026, Nov 2006.

[25] C. Alleman, S. Ghosh, D. J. Luscher, and C. A. Bronkhorst, "Evaluating the effects of loading parameters on single-crystal slip in tantalum using molecular mechanics," *Philosophical Magazine,* vol. 94, pp. 92-116, Jan 2014.

[26] A. Stukowski, "Visualization and analysis of atomistic simulation data with OVITO-the Open Visualization Tool," *Modelling and Simulation in Materials Science and Engineering,* vol. 18, Jan 2010.

[27] A. Henderson, *ParaView Guide, A Parallel Visualization Application.*: Kitware Inc., 2007.

[28] A. Stukowski and K. Albe, "Extracting dislocations and non-dislocation crystal defects from atomistic simulation data," *Modelling and Simulation in Materials Science and Engineering,* vol. 18, Dec 2010.

[29] J. A. Zimmerman, C. L. Kelchner, P. A. Klein, J. C. Hamilton, and S. M. Foiles, "Surface step effects on nanoindentation," *Physical Review Letters,* vol. 87, pp. art. no.-165507, Oct 2001.

[30] J. A. Zimmerman, E. B. Webb, J. J. Hoyt, R. E. Jones, P. A. Klein, and D. J. Bammann, "Calculation of stress in atomistic simulation," *Modelling and Simulation in Materials Science and Engineering,* vol. 12, pp. S319-S332, Jul 2004.

[31] R. J. Hardy, "Formulas for determining local properties in molecular-dynamics simulations - shock waves," *Journal of Chemical Physics,* vol. 76, pp. 622-628, 1982.

[32] E. B. Webb, J. A. Zimmerman, and S. C. Seel, "Reconsideration of continuum thermomechanical quantities in atomic scale simulations," *Mathematics and Mechanics of Solids,* vol. 13, pp. 221-266, May-Jun 2008.

[33] J. A. Zimmerman, R. E. Jones, and J. A. Templeton, "A material frame approach for evaluating continuum variables in atomistic simulations," *Journal of Computational Physics,* vol. 229, pp. 2364-2389, Mar 2010.

[34] G. P. Scaronkoro, J. R. J. Bennett, T. R. Edgecock, S. A. Gray, A. J. McFarland, C. N. Booth*, et al.*, "Dynamic Young's moduli of tungsten and tantalum at high temperature and stress," *Journal of Nuclear Materials,* vol. 409, 1 Feb. 2011.

[35] Q. Wei, Z. L. Pan, X. L. Wu, B. E. Schuster, L. J. Kecskes, and R. Z. Valiev, "Microstructure and mechanical properties at different length scales and strain rates of nanocrystalline tantalum produced by high-pressure torsion," *Acta Materialia,* vol. 59, pp. 2423-2436, Apr 2011.

[36] G. Guisbiers, E. Herth, L. Buchaillot, and T. Pardoen, "Fracture toughness, hardness, and Young's modulus of tantalum nanocrystalline films," *Applied Physics Letters,* vol. 97, Oct 2010.

[37] R. Groger and V. Vitek, "Temperature and strain rate dependent flow criterion for bcc transition metals based on atomistic analysis of dislocation glide," *International Journal of Materials Research,* vol. 100, pp. 315-321, Mar 2009.

[38] C. R. Weinberger, B. L. Boyce, and C. C. Battaile, "Slip planes in bcc transition metals," *International Materials Reviews,* vol. 58, pp. 296-314, Jun 2013.

[39] J. W. Cahn, Y. Mishin, and A. Suzuki, "Coupling grain boundary motion to shear deformation," *Acta Materialia,* vol. 54, pp. 4953-4975, Nov 2006.

[40] D. Caillard, F. Mompiou, and M. Legros, "Grain-boundary shear-migration coupling. II. Geometrical model for general boundaries," *Acta Materialia,* vol. 57, pp. 2390-2402, May 2009.

[41] D. Farkas, A. Froseth, and H. Van Swygenhoven, "Grain boundary migration during room temperature deformation of nanocrystalline Ni," *Scripta Materialia,* vol. 55, pp. 695-698, 2006.

[42] D. Farkas, S. Mohanty, and J. Monk, "Strain-driven grain boundary motion in nanocrystalline materials," *Materials Science and Engineering a-Structural Materials Properties Microstructure and Processing,* vol. 493, pp. 33-40, Oct 15 2008.

[43] J. W. Cahn and J. E. Taylor, "A unified approach to motion of grain boundaries, relative tangential translation along grain boundaries, and grain rotation," *Acta Materialia,* vol. 52, pp. 4887-4898, Sep 2004.

[44] K. S. Kumar, S. Suresh, M. F. Chisholm, J. A. Horton, and P. Wang, "Deformation of electrodeposited nanocrystalline nickel," *Acta Materialia,* vol. 51, pp. 387-405, Jan 2003.

[45] E. M. Bringa, S. Traiviratana, and M. A. Meyers, "Void initiation in fcc metals: Effect of loading orientation and nanocrystalline effects," *Acta Materialia,* vol. 58, pp. 4458-4477, Aug 2010.

[46] D. C. Ahn, P. Sofronis, M. Kumar, J. Belak, and R. Minich, "Void growth by dislocation-loop emission," *Journal of Applied Physics,* vol. 101, Mar 2007.

[47] R. A. Lebensohn, E. M. Bringa, and A. Caro, "Continuum mesoscale modelling of nanocrystalline fcc metals under shock-loading using an spectral formulation fed by molecular dynamics results," *Journal De Physique Iv,* vol. 134, pp. 17-22, Aug 2006.

[48] M. A. Meyers, S. Traiviratana, V. A. Lubarda, D. J. Benson, and E. M. Bringa, "The role of dislocations in the growth of nanosized voids in ductile failure of metals," *Jom,* vol. 61, pp. 35-41, Feb 2009.

[49] M. A. Meyers, O. Vohringer, and V. A. Lubarda, "The onset of twinning in metals: A constitutive description," *Acta Materialia,* vol. 49, pp. 4025-4039, Nov 2001.

[50] Z. Cao, Q. She, Y. Huang, and X. Meng, "The rate sensitivity and plastic deformation of nanocrystalline tantalum films at nanoscale," *Nanoscale Research Letters,* vol. 6, 2011 2011.

[51] J. Alcala, R. Dalmau, O. Franke, M. Biener, J. Biener, and A. Hodge, "Planar defect nucleation and annihilation mechanisms in nanocontact plasticity of metal surfaces," *Physical Review Letters,* vol. 109, Aug 2012.

[52] J. Marian, W. Cai, and V. V. Bulatov, "Dynamic transitions from smooth to rough to

twinning in dislocation motion," *Nature Materials,* vol. 3, pp. 158-163, Mar 2004.

[53] D. H. Warner, W. A. Curtin, and S. Qu, "Rate dependence of crack-tip processes predicts twinning trends in f.c.c. metals," *Nature Materials,* vol. 6, pp. 876-881, Nov 2007.

[54] R. J. Asaro and S. Suresh, "Mechanistic models for the activation volume and rate sensitivity in metals with nanocrystalline grains and nano-scale twins," *Acta Materialia,* vol. 53, pp. 3369-3382, Jul 2005.

[55] L. Hale, J. A. Zimmerman, and C. Weinberger, "Simulations of bcc tantalum screw dislocations: why classical inter-atomic potentials predict {112} slip," *Computational Materials Science,* vol. Accepted, 2014.

9 Connecting Atomistic Parameters with the Energetics and Deformation Response of Grain Boundary Networks

Laura Smith[a], Niklas Floyd[a], and Diana Farkas[a]

Virginia Polytechnic Institute and State University

445 Old Turner Street

Blacksburg VA 24061

Corresponding Author:

Laura Smith

445 Old Turner St

Blacksburg, VA 24061

(540) 629-4449

lauramse@vt.edu

9.1 Abstract

We present a molecular dynamics study of the relationship between specific interatomic force law characteristics and the corresponding deformation behavior of simulated nanoscale grain boundary networks. We used a fully periodic polycrystalline quasi-2D sample created using Voronoi tessellation with random [1 1 0] tilt boundaries, adjusted for the lattice parameter given by six different fcc model embedded atom method potentials. We subjected the samples to virtual tensile deformation using the same exact simulation parameters for each of the potentials considered. This procedure enabled us to isolate and attribute differences in deformation behavior to the specific potential used. We considered possible correlations between a set of atomistic parameters, predicted by the interatomic potentials used, with the resulting grain boundary structure, energetics and mechanical response. We have found non-planar grain boundary structures to be common for some of the potentials utilized and show that non-planarity in grain boundaries is correlated with low values of the stable stacking fault energy. We also found that the yield and flow stress correlate with the unstable stacking fault energy, whereas the grain boundary energy correlates with the cohesive energy and shear modulus characteristic of the potential.

Keywords: molecular dynamics, interatomic potential, mechanical behavior, stacking fault energy, grain boundaries, fcc materials

9.2 Introduction

Grain boundaries in nanocrystalline materials are critical contributors to deformation behavior, including grain boundary sliding and dislocation emission. Grain boundaries introduce excess energy in nanocrystalline materials that may contribute to the nucleation of deformation mechanisms, such as dislocation emission and grain boundary sliding. The grain boundary energy of specific boundary types has been established in tilt [1-3] and twist boundaries [4-9] through both simulation and experimental work. Grain boundary energies from molecular dynamics simulations of Ni have been compared to and validated by experimental results through the work of Holm [10, 11], Olmstead[12], and Rohrer [13]. They found that for experimentally prevalent grain boundary types, there is good agreement between calculated and observed energies. Further work by Holm [10] shows that grain boundary energies in several fcc materials scale with the shear modulus. Vo and co-workers [14] observed that lowering the grain boundary energy of Cu through the addition of alloying solute atoms increased the yield strength of nano-crystalline Cu to nearly its theoretical limit. It is clear from these results that grain boundary energy affects deformation, though the specific role of grain boundary energy in deformation is not well understood. Previous experimental work by Monzen [15] in Cu-Fe-Co bicrystals and simulation work by Chandra [16] in Al bicrystals indicates that the incidence of grain boundary sliding increased with higher grain boundary energy. There is little reference in the literature to the effect of grain boundary energy on dislocation emission.

The relationship between grain boundary structure, deformation mechanisms, and atomistic parameters at the nanoscale is an important field of research. Simulation work by de Koning et al. [17] showed that local grain boundary structure affects dislocation emission and interaction. Tschopp et al [18, 19] showed how structural units in the grain boundary dissociate into partial

dislocations, which can then emit into the grain. Jin et al. [20, 21] showed that slip transfer across grain boundaries is related to a resistance parameter R that is dependent upon the stable and unstable stacking fault energy. Deng et al. [22] expanded on this work with Au, Ag, Al, Cu, Pd, and Ni nanowires. Deng expanded on the work of Jin et al. and was able to show that the unstable stacking fault energy was directly proportional to the yield stress and to the stress at which leading partial dislocations emit from interfaces. Simulations by Asaro et al. [23] in Cu, Al, and Ni showed that the ratio of the stable and unstable stacking fault energies significantly affects the emission of a trailing partial dislocation from grain boundaries, which in turn affects the equilibrium partial separation distance. Stable and unstable stacking fault energies are clearly critical in the deformation of nanocrystalline fcc materials, though work to determine how the stable and unstable stacking fault energy correlates to both grain boundary structures and subsequent deformation has yet to be performed.

In this work, we seek to explore how atomistic parameters given by the interatomic potentials used correlate to specific deformation mechanisms and mechanical properties observed in virtual tensile tests using standard molecular dynamics. Six different empirical interatomic potentials are used, originally developed to represent the fcc metals Ni, Al, Cu, and Pd [24-27]. We study the correlations among interatomic potential properties (cohesive energy, shear modulus, melting temperature, stable and unstable stacking fault energy values) and the resulting grain boundary structure and energetics as well as deformation behavior as given by yield and flow stress, dislocation emission and grain boundary sliding. We organized this paper as follows: Section 2 presents a brief description of our simulation techniques. Section 3 describes the correlation results obtained for the grain boundary structure and energetics. Section 4 discusses the

correlation results for deformation behavior and various mechanisms observed. Section 5 presents a summary of all the correlations found, followed by discussion and conclusions.

9.3 Simulation techniques

We generated the fully periodic samples used in this work with a Voronoi tessellation construction technique, similar to the one used in our previous work [28, 29]. The samples have 9 columnar grains with an average grain size of 40nm and 719 598 atoms. The samples are periodic in all directions; the periodicity in the z direction is the periodicity of the lattice along the [1 1 0] direction, imposing a [1 1 0] texture on the entire sample. The grain boundaries in the sample have pure tilt character around the [1 1 0] axis with random misorientation angles. Box dimensions for each sample are proportional to the lattice parameter produced by each interatomic potential used in this work. The box sizes range from 150 nm by 106 nm for Ni to 173 nm by 122 nm for Al with a 0.5 nm thickness for each sample. For adequate comparison, we adjusted the size of the initial generated sample to accommodate the lattice parameters of the interatomic potentials of interest. Using this procedure, we ensured that the samples are identical apart from their size. This technique isolates differences in deformation behavior to the specific interatomic parameters of the potential used. This is true, even when considering the standard limitations of molecular dynamics techniques, such as the high strain rate due to the extremely short timescale imposed by computational constraints. The limitations of molecular dynamics also prevent the observation of thermally activated deformation mechanisms and needs to be considered when comparing our results to experiments. The samples have a quasi-2D nature, seen in figure 1, in which only straight-line dislocations are possible. The grain size also precludes the possibility of dislocation generation or multiplication through Frank-Read sources.

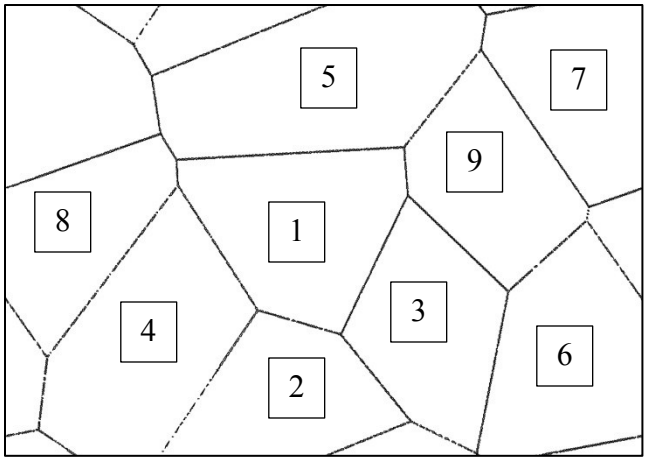

Figure 1: Unrelaxed sample configuration with artificially straight grain boundaries.

We used the molecular dynamics software LAMMPS [30] with a Nosé-Hoover thermostat and barostat to equilibrate the samples and to perform the virtual mechanical testing reported. To achieve relaxed grain boundary structures, we equilibrated each sample at 300K for 100ps with its corresponding potential. Once we obtained relaxed grain boundary structures, we deformed each sample using virtual strain-controlled mechanical testing via standard molecular dynamics. We performed the strain-controlled deformations at 300K, with uniaxial tension along the horizontal axis up to 9% strain, at a constant strain rate of $3x10^{8}s^{-1}$. Note that the tensile direction is perpendicular to the [1 1 0] direction common to all grains in each sample. We maintained the pressure at zero bars in the directions perpendicular to the tension axis during deformation.

We selected six embedded atom method potentials developed to represent model fcc materials with various energetic properties which produce differing mechanical behavior. We list the critical parameters for each potential in table 1. The authors of each potential used a semi-empirical method to develop each potential, requiring accurate representation of the experimentally-determined lattice parameter, the cohesive energy, the stable stacking fault energy, the elastic constants, and the vacancy formation energy. We refer to the results reported in this work by the element represented: the Mishin aluminum and nickel potential results are

labelled Al1 [25] and Ni1 [25], respectively. Similarly, we refer to the Voter aluminum and nickel potentials as Al2 [27] and Ni2 [27] respectively. The Mishin et al. potential for Cu [26], and the Foiles and Hoyt potential for Pd [24] are simply referred to as Cu and Pd. We selected these specific potentials in order to consider a range of stable stacking fault energies in this work. Cu has the lowest stable stacking fault energy, 44 mJ/m^2, while Pd has the highest, 187 mJ/m^2. We checked the elastic constants, C_{11}, C_{12}, C_{44}, produced by each potential using the method of Mehl et al. [31]. The values we obtained agree well with the values reported by Mishin et al. [25, 26] Foiles and Hoyt [24] and Voter and Chen [27].

Table 1: Critical parameters for the potentials used in this work. The potential melting temperature is the temperature at which the sample melted in molecular dynamic simulation. These temperatures can vary from the experimental melting temperatures by up to 40%.

Potential	Cohesive Energy (eV)	Lattice Constant (Å)	C_{11} (GPa)	C_{12} (GPa)	C_{44} (GPa)	Stable SFE (mJ/m^2)	Unstable SFE (mJ/m^2)	Potential Tm (K)
Al1	-3.36	4.05	114	62	32	146[25]	168[25]	1166
Al2	-3.36	4.05	107	65	32	76[25]	93[25]	560
Cu	-3.54	3.61	170	123	76	44[26]	158[26]	1222
Ni1	-4.45	3.52	247	148	125	125[25]	366[25]	2160
Ni2	-4.45	3.52	244	149	126	58[25]	225[25]	1469
Pd	-3.91	3.89	239	174	66	187[24]	210[24]	1280

We visualized the simulation results using the centrosymmetry [32] parameter to color code each atom in molecular visualization packages like OVITO [33]. This procedure allowed visualization of grain boundary structure as well as the dislocation emission and grain boundary sliding processes. In this way, the stress level at which a particular boundary emits the first dislocation can also be monitored, and the number of dislocations emitted and extent of grain boundary sliding thereafter can be quantitatively assessed.

9.4 Grain boundary structure and energetics

9.4.1 Grain boundary structure

We first investigated the overall planarity of relaxed grain boundary structures in each potential as a function of stacking fault energy. In our previously published work on deformation in Cu and Pd [29], we show the effect of the stable stacking fault energy on local grain boundary structures in detail. Similarly, in this work, we considered planarity with respect to grain boundary structures as the presence or absence of nascent stacking faults extending from the grain boundary plane into the bulk of the grain. We show relaxed grain boundary structures in the Al1 (146 mJ/m^2) and Ni1 (125 mJ/m^2) samples in figures 2 (a) and (b). We color coded the atoms based on the centro-symmetry parameter [32], with blue indicating perfect lattice structure, green indicating grain boundaries and stacking faults, and red atoms showing the highest amounts of local lattice disruption. Red and yellow boxes highlight the same grain boundaries in each sample, extracted and magnified. Figure 2 (a) shows detailed views of two example grain boundaries in the Al1 sample. These boundaries contain few non-planar features, while the same grain boundaries in the Ni1 sample show significant non-planarity. The non-planar regions in the Ni1 sample may represent the glide of intrinsic grain boundary dislocations with a Shockley partial Burgers vector type. We theorize that he non-planar features may lower the overall atomic energy in the boundary but introduce nascent stacking faults into the neighboring grains. These nascent stacking faults can ease dislocation emission into the grains at low strains, a phenomenon discussed further in section 4.5. Examination of each sample did not reveal the presence of the 9R structure, a possible explanation of local non-planarity that has been observed both experimentally and in simulations [34, 35]. When we combine these results

with our previously reported results in Cu and Pd it becomes clear that low stacking fault energy promotes significant non-planarity in grain boundary features.

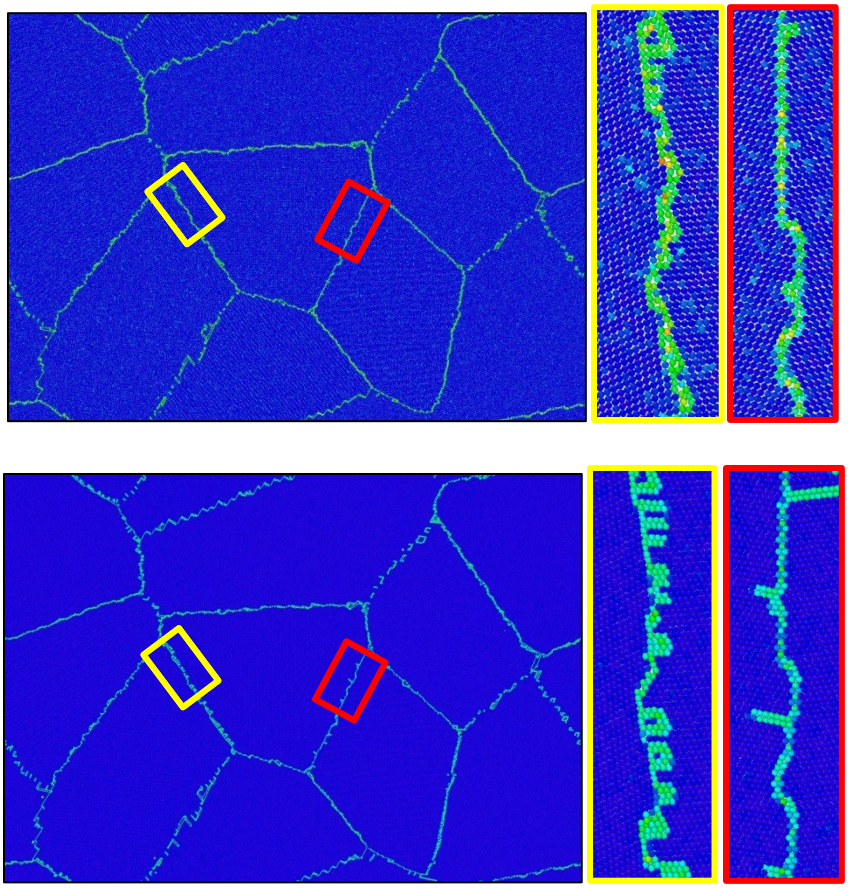

Figure 2: Relaxed grain boundary structure showing differences in planarity for the featured boundaries. (a) Sample relaxed with the Al1 potential. (b) Sample relaxed with the Ni1 potential. Callouts highlight differences in grain boundary structure, with the Al1 boundaries displaying increased planarity.

We then considered the overall fraction of grain boundaries with non-planar features in each sample as a function of stacking fault energy. We found that the fraction of non-planar grain boundaries in each sample prior to deformation is inversely proportional to the stable stacking fault energy. We show this relation in figure 3. These results indicate that stacking fault energy plays a significant role in the relaxed grain boundary structure, reflected in the presence or absence of non-planar grain boundary features. We propose that the balance between the

stacking fault energy and the atomic arrangement energy in the grain boundary determines whether the development of non-planar grain boundary structures is energetically favorable.

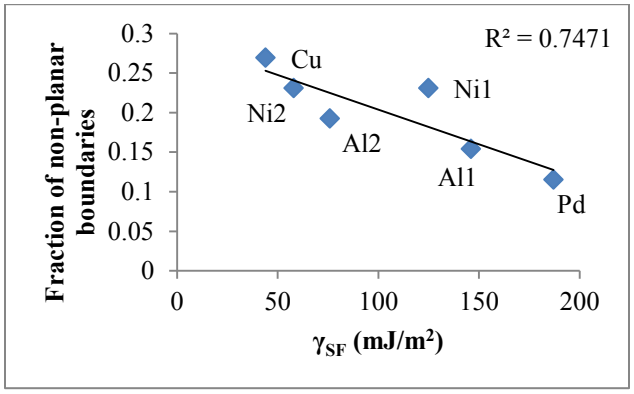

Figure 3: Fraction of non-planar grain boundaries in each sample is inversely proportional to the stacking fault energy.

9.4.2 Grain boundary Energetics

We calculated the overall grain boundary energy in each sample by finding the difference between the total energy of the polycrystalline sample and the total energy of a sample containing the same number of atoms in bulk. We then divided the excess energy of the polycrystalline sample by the cross sectional grain boundary area. The overall grain boundary energies varied from 1552 mJ/m^2 in the Ni1 sample to 293 mJ/m^2 in the Al2 sample. In comparison, Olmstead et al. [12] found an average Ni grain boundary energy of 1088 mJ/m2 using the potential developed by Foiles and Hoyt [36] for Ni. This data point is marked as Ni3 in figure 4 and is qualitatively consistent with the results reported here. In our analysis, we multiplied the C_{44} elastic constant by the lattice parameter, similar to the procedure used in Holm et al. [10] in order to compare quantities with the same units. We found a strong correlation of the grain boundary energy to the cohesive energy. Additionally, the overall grain boundary energy in each sample is also strongly correlated to the a_0C_{44} of each potential.

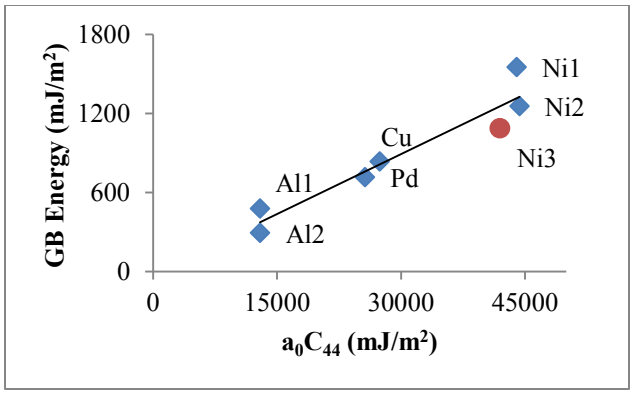

Figure 4: Grain boundary energy is strongly correlated to a_0C_{44}. Ni3 data marker from Olmstead et al. [12].

For completeness, we also considered the grain boundary energies of individual grain boundaries using the Ni1 potential. To begin, we classified the grain boundaries in the Ni1 sample as random high angle (RHA), random low angle (RLA), or coincident site lattice (CSL) types based on misorientation angle and the Brandon criteria for tolerance [37]. We found that this sample consists of 58% RHA boundaries, 23% RLA boundaries and 19% CSL-type boundaries. We list the misorientation angles and boundary classifications for each grain boundary in table 2, notated by the grains they abut. For example, GB 1-2 indicates the boundary between grains 1 and 2.

Table 2: Grain boundaries with their misorientation angles, grain boundary energies for the Ni1 potential, and grain boundary type.

GB Number	Θ_{mis} (^{o})	E_{gb} (J/m^2)	Type
1-2	80.19	1.09	RHA
1-3	125.42	1.08	Σ11
1-4	88.93	1.56	RHA
1-5	156.51	1.43	RHA
1-8	147.13	1.48	RHA
1-9	149.71	1.66	RHA
2-3	154.39	1.57	RHA
2-4	171.26	1.38	RLA
2-5	103.68	1.28	Σ3
2-7	97.90	1.35	RHA
3-5	77.80	0.88	Σ3
3-6	102.53	1.37	Σ3
3-9	85.57	1.19	RHA
4-6	111.72	1.34	Σ3
4-7	90.00	1.44	RHA
4-8	121.18	1.41	RHA
5-7a	21.34	1.59	RHA
5-7b	25.24	1.40	RHA
5-8	171.07	1.28	RLA
5-9	7.51	1.29	RLA
6-7	158.70	1.44	RHA
6-8	170.63	1.22	RLA
6-9	171.89	1.07	RLA
7-8	149.89	1.55	RHA
7-9	151.15	1.62	RHA
8-9	2.00	0.91	RLA

We then proceeded to calculate the grain boundary energy of each grain boundary following a procedure similar to the one used to calculate the overall grain boundary energy. The main difference between the two procedures is that instead of using the entire sample, only the atoms within 1.5nm of the boundary were included in the calculation. We found that individual grain boundary energies in the Ni1 sample range from 1658 mJ/m^2 to 880 mJ/m^2, listed in table 1. In order to confirm that the grain boundary energies in this sample are reasonable, we compared our

results to symmetrical tilt grain boundary energies in Al in work performed by Lee and Choi [2]. For comparison purposes, we normalized the results using the highest grain boundary energy obtained, and the results are shown in figure 5; grain boundary energies for Ni1 appear as blue squares, while the Al results appear as a red line. There are distinct cusps in the grain boundary energies, shown as dashed lines, at the (111) twin boundary (Σ3 at 70^{o}), the (113) twin boundary (Σ11 at 129^{o}), and at low-angle misorientations. An additional cusp, located at 109^{o}, agrees with the (112) symmetrical tilt Σ3 boundary in Al-LC results. The similar trends shown indicate that random [1 1 0] asymmetrical tilt boundaries show a dependence on misorientation angle that is similar to observed behavior in typical symmetrical tilt boundaries. One notable difference is that cusps in the asymmetric boundaries corresponding to CSL boundaries tend to be less deep. This may be due to the randomly misoriented grain boundary planes not allowing for optimal coincident site lattice matching in the boundary region.

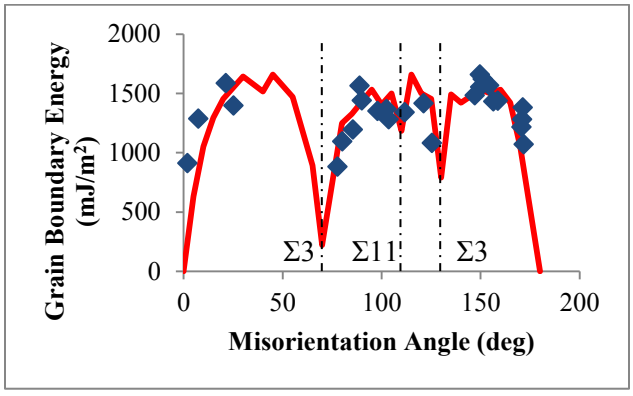

Figure 5: Grain boundary energies as a function of misorientation angle. Ni1 results from asymmetric tilt boundaries shown in blue. Normalized aluminum results [2] from symmetric tilt boundaries shown in red. Results show good agreement between the two samples. Dashed lines indicate cusps in grain boundary energy. Image used with permission from [38].

We also examined how grain boundary energy varies along the boundary plane and at various distances from triple junctions, using the Ni1 potential. We studied five individual grain boundaries, shown in figure 6, by sectioning each of the selected boundaries into three parts in order to determine how grain boundary energy differs along the length of the boundary. We

found that in 4 out of the 5 grain boundaries examined, the middle section of each boundary has the lowest calculated energy. We also found that the energy is generally highest near a triple junction. These results suggest that the energy in randomly misoriented grain boundaries can vary by about 5%. Interior sections generally have lower energies than the regions closer to triple junctions. This may be due to the ability of center sections to restructure their atomic arrangement and achieve a lower energy configuration far from the restricting effect of triple junctions.

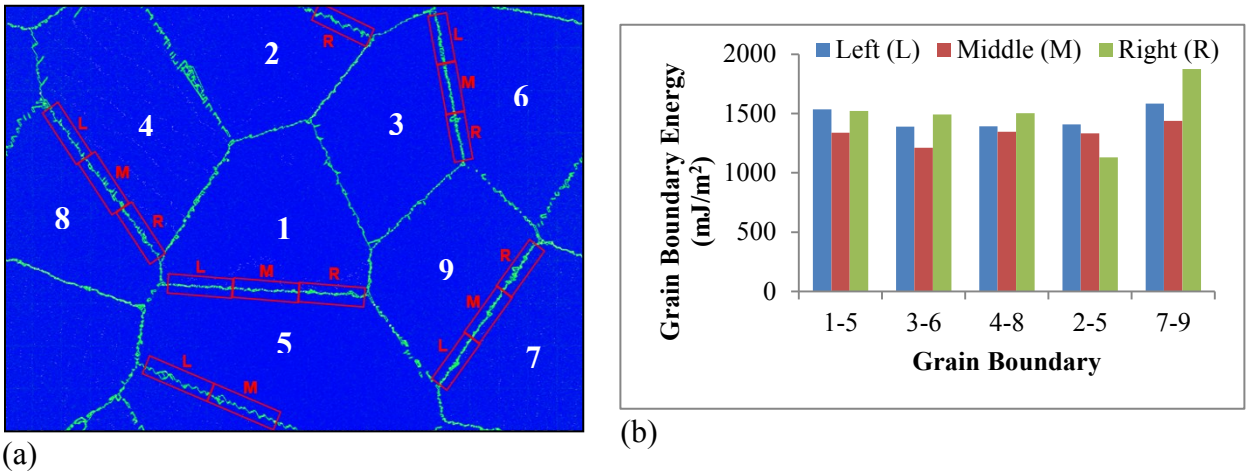

(a) (b)

Figure 6: Variation of grain boundary energy along the boundary in the Ni1 sample. Grain boundary energy increases with proximity to triple junctions in 4 out of 5 grain boundaries studied. Figure 6 (a) used with permission from [38].

9.5 Deformation behavior

9.5.1 Stress-strain behavior

We obtained standard stress-strain curves for each sample from the total stress on the sample calculated during the virtual strain controlled tensile deformation. As shown in figure 7, the macroscopic mechanical behavior produced by each potential varies significantly. We determined the elastic modulus for each potential from the linear portion of its corresponding stress-strain curve between 0 and 0.5% strain. We compared this value to the theoretical elastic

modulus using the equation derived by Hopcroft et al. [39] for a crystal system with [110] texture. We show the observed and predicted values in table 3. There are up to 10% differences between the predicted and the observed values in these results, which may be due to the high percentage of grain boundaries found in nanocrystalline samples, and to differences in relaxed grain boundary structure produced by specific potentials.

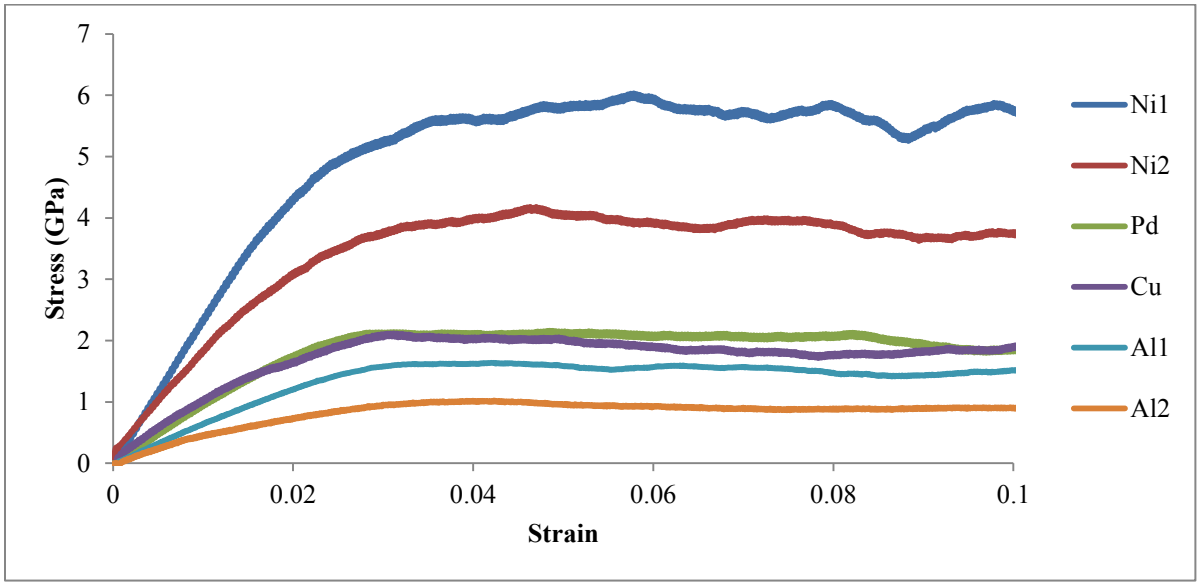

Figure 7: Stress-Strain curves for the samples used in this work. There are significant differences in overall plasticity.

Table 3: Observed and predicted elastic moduli for the studied samples.

Potential	E (predicted) (GPa)	E (calculated) (GPa)	Error (%)
Al1	80.53	67.46	16.23
Al2	75.83	58.84	22.41
Cu	131.44	116.29	11.53
Ni1	232.70	237.51	2.07
Ni2	229.70	234.25	1.98
Pd	144.81	132.57	8.45

We then considered the yield and flow stresses produced by each potential. We used the 0.2% offset yield criteria to determine the yield stress in each sample and considered the flow stress as the total stress at 6% strain. We found that both stresses scale with the unstable stacking fault energy, as shown in figure 8. These results suggest that to simulate accurate yield and flow stress values, the γ_{USF} is the critical parameter. This agrees with the work of Deng and Sansoz [22] dealing with simulations of fcc nanowires.

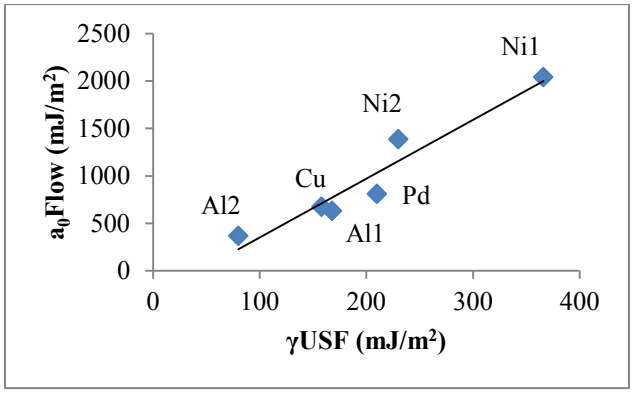

Figure 8: Flow stress measurements scale with the unstable stacking fault energy. We note a similar trend in the behavior of the yield stress.

9.5.2 Dislocation emission as a deformation mechanism

We then proceeded to investigate the details of dislocation emission as a function of grain boundary structure, stable stacking fault energy, and unstable stacking fault energy. Our first step was to investigate the stress at the initial dislocation emission in each sample in three planar boundaries. We chose only boundaries with planar structures in each potential for this comparison, so that we would not compare dislocation emission from different grain boundary structures. We discuss the important effects of grain boundary structure on dislocation emission later in this section. In Figure 9, we plot the average stress for the first dislocation emission event from planar boundaries as a function the unstable stacking fault energy. These results indicate that the unstable stacking fault energy influences the stress necessary to nucleate and emit a

dislocation in planar grain boundaries. This is similar to the work by Jin et al [20, 21] and Deng and Sansoz [22] in fcc nanowires. Deng found that the unstable stacking fault energy was critical to dislocation emission from twin boundaries. Asaro et al. [23] found that the unstable stacking fault energy was also key in the emission of trailing partial dislocations from grain boundaries. In addition, these results show that the stable stacking fault energy is not a factor in dislocation emission when only planar boundaries are considered.

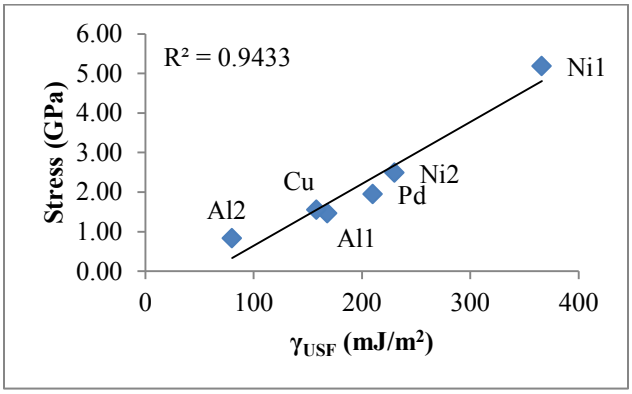

Figure 9: Stress at first dislocation emission scales with unstable stacking fault energy in three planar grain boundaries.

We next examined dislocation emission as a function of stable stacking fault energy, including the changes in grain boundary structure. In order to perform this analysis, we extracted the exact same atoms from each sample at 0, 2, and 5% strain and color coded them based on centro-symmetry. The results shown in figure 10 are in ascending stacking fault energy order. We found that materials with low stacking fault energy, Cu, Ni1, and Ni2, each emitted a dislocation from the grain boundary at low strain. In contrast, the materials with high stacking fault energy, Al1, Al2, and Pd, presented a higher energy barrier to dislocation emission, which delayed dislocation emission in these materials. Further analysis of the Al1, Al2, and Pd samples at 5% strain reveal the beginnings of grain boundary sliding. This nascent sliding could contribute to the lack of sustained dislocation emission in these samples, as local boundary reorganization consumed the available strain energy before dislocation emission could begin.

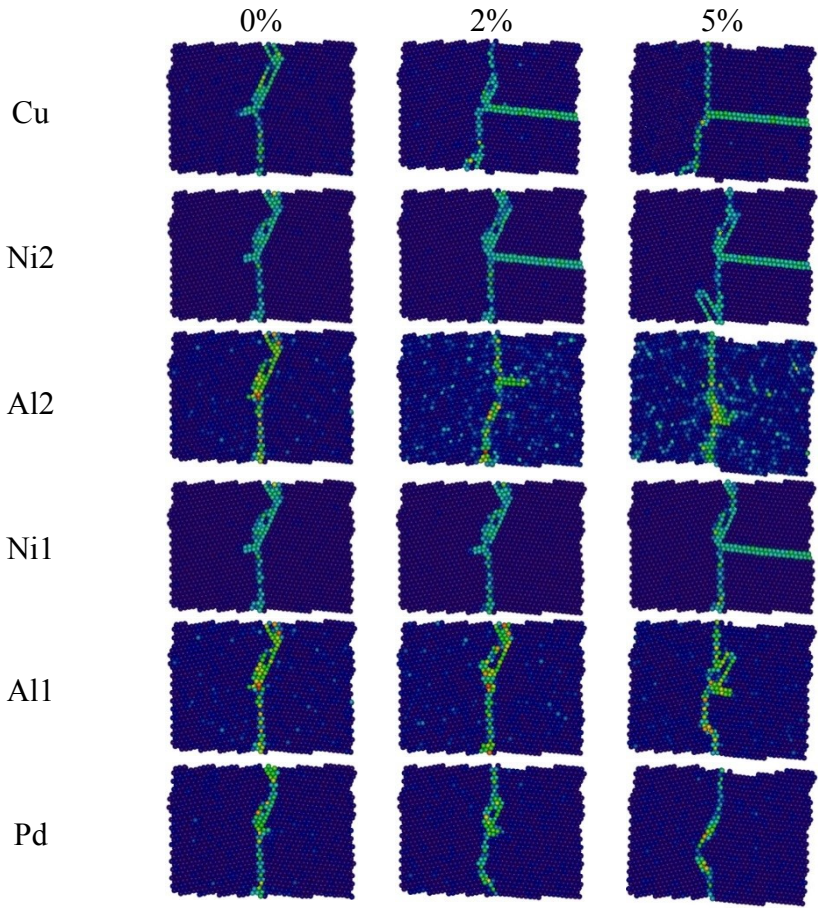

Figure 10: Dislocation behavior for each potential at 0, 2, and 5% strain. Results are displayed in ascending order of stacking fault energy from Cu (44 mJ/m^2) to Pd (187 mJ/m^2). As stacking fault energy rises, fewer dislocations emit from the grain boundary.

Figure 11 shows the results of dislocation emission behavior across the sample. We observed considerable variation in stacking fault debris density in each sample at 5% strain. The images are in order of ascending unstable stacking fault energy. For clarity, we have removed atoms in perfect lattice positions (centro-symmetry<3), with the remaining stacking faults and grain boundaries shown in black. Lower stacking fault energy materials show evidence of dislocation emission activity in the form of dense stacking fault debris in figures 11 (a) and (b). Not surprisingly, higher stacking fault energies tend to show a relative scarcity of stacking fault debris, as in in figures (e) and (f).

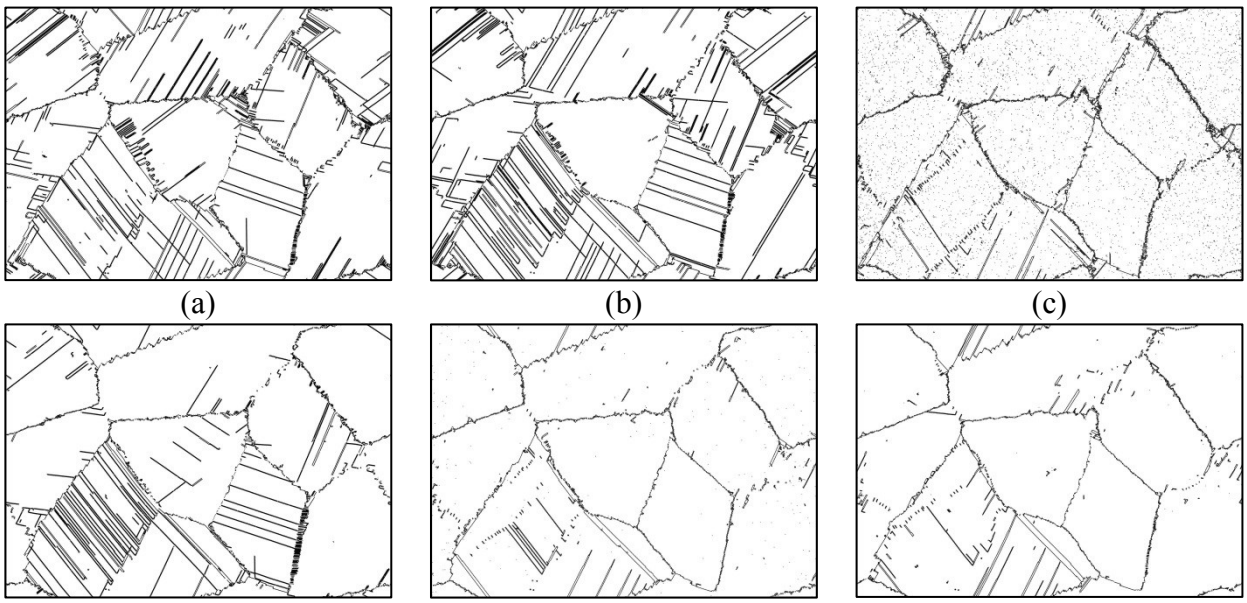

Figure 11: Dislocation emission at 5% strain showing differences in behavior for each potential. Shown in ascending order of stable stacking fault energy. As stacking fault energy rises, fewer stacking faults are observed. (a) Cu – 44 mJ/m^2. (b) Ni2– 58 mJ/m^2 (c) Al2– 76 mJ/m^2 (d) Ni1– 125 mJ/m^2 (e) Al1– 146 mJ/m^2 (f) Pd – 187 mJ/m^2

9.5.3 Grain boundary sliding as a deformation mechanism

We then proceeded to investigate grain boundary sliding behavior , since it is known to be an important deformation in nanocrystalline materials [40]. We investigated grain boundary sliding by isolating a region of each sample containing a grain boundary of interest. We then examined the exact same set of atoms at increasing levels of strain. Grain boundary sliding is revealed as atoms in the two grains are displaced in different directions parallel to the grain boundary plane. This technique also allows quantitative measurement of coupled grain boundary migration [16, 41, 42]. We investigated the extent of grain boundary sliding by measuring the sliding in each boundary at every 1% strain between 0 and 9% in each sample. Again, we chose only planar boundaries for this comparison. We found that grain boundary sliding in planar boundaries decreases with increasing grain boundary energy, shown in figure 12.

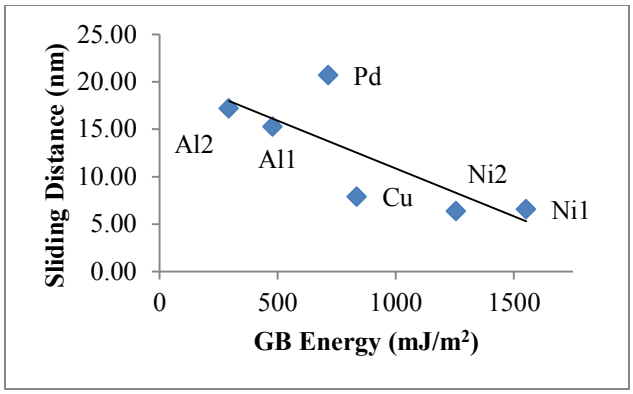

Figure 12: Grain boundary sliding in the studied samples as a function of grain boundary energy. Grain boundary sliding decreases as grain boundary energy increases

We also observed coupled grain boundary migration. In this work, the coupling factor β ranged from 0.81 for Pd to 1.91 for Cu, with an average value of 1.25. β is the ratio of the velocity of the grain boundary motion perpendicular to the grain boundary plane over the velocity of grain boundary motion parallel to the grain boundary plane. Grain boundary sliding and coupled migration has been studied extensively in special grain boundaries [40, 43-45], in polycrystalline networks [42, 46] similar to the one studied in this work, and in networks including triple junctions [47].

We then investigated the effect of grain boundary planarity on grain boundary sliding and found that non-planar grain boundaries simply do not slide. This result implies that the non-planar features found in some grain boundaries raise the energetic barrier to grain boundary sliding so high that sliding is prevented entirely. Since low stacking fault energy produces a higher fraction of non-planar grain boundaries, it follows that low stable stacking fault energy should also lower the contribution of grain boundary sliding to plasticity.

9.5.4 Relative contribution of grain boundary sliding and dislocation emission to overall plasticity

Finally, we considered the relative contributions to plastic deformation from dislocation emission and grain boundary sliding as deformation mechanisms at each percent strain. We quantitatively estimated the contribution of dislocation emission to plasticity from the Burger's vector, the average distance traveled by the dislocations, the number of dislocations observed, and the cosine of the average angle of the active slip systems with respect to the tension axis. Similarly, we quantitatively estimated the contribution from grain boundary sliding to plasticity from the measured average sliding in each grain boundary and the cosine of the average angle of the grain boundary with respect to the tension axis. We estimated the error in this analysis by adding the calculated percentages from each deformation process. We then compared it to the nominal overall strain level, obtaining agreement within an error of 15%. Figure 13 shows results for each potential, ordered by ascending stacking fault energy.

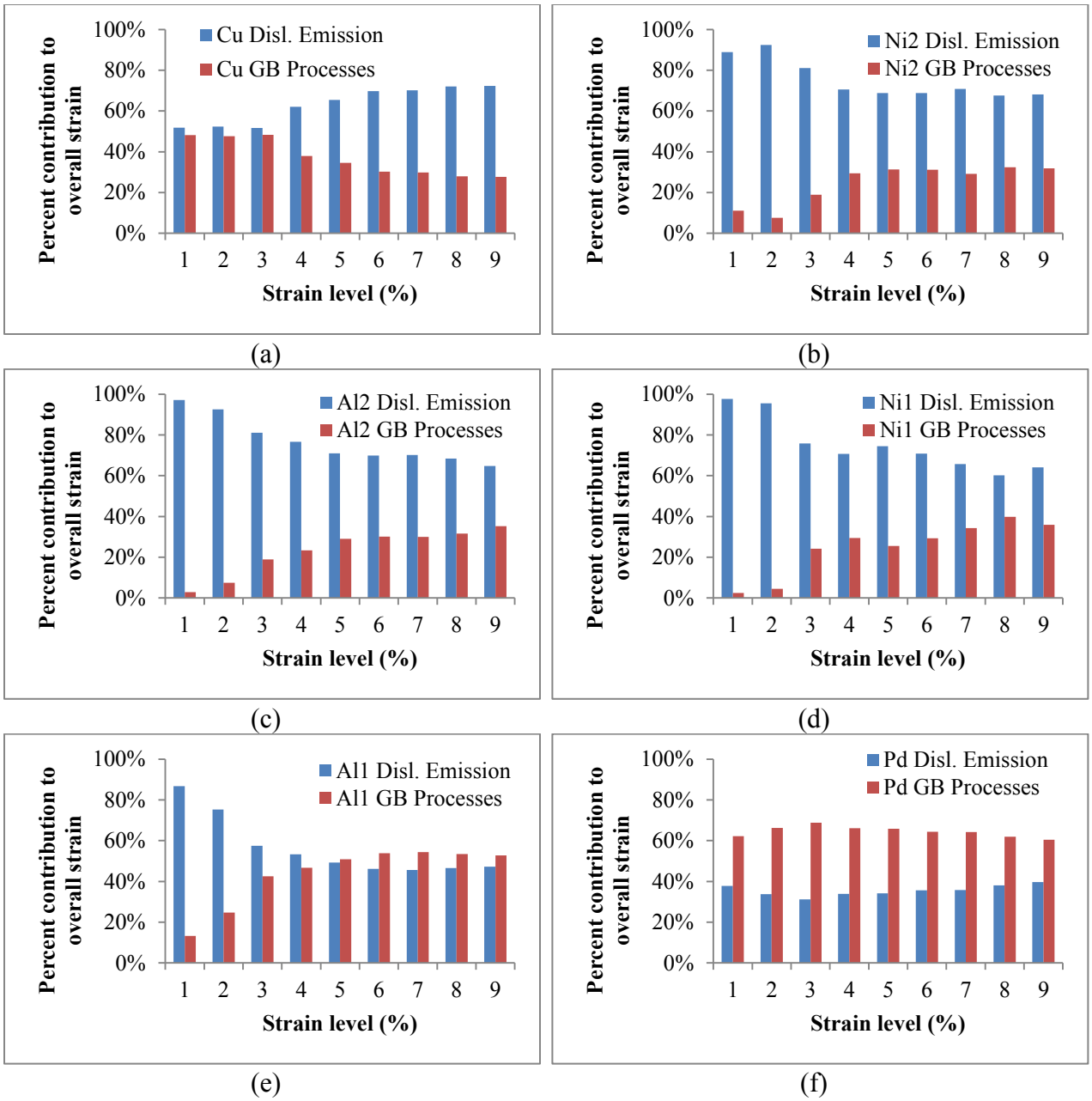

Figure 13: Contributions to strain from dislocation emission and grain boundary sliding for each potential studied in this work.

We found that dislocation emission is the dominant mechanism of plastic deformation in materials with low stacking fault energy at all strain levels. For the Cu potential, dislocation emission and grain boundary sliding initially contribute to the plasticity at a ratio of about 1:1. As strain increases in Cu, dislocation emission takes over as the dominant contributor to plastic

deformation. At 9% strain, dislocation emission contributes to plastic deformation at a ratio of about 4:1. For the Ni1, Ni2, and Al2 potentials, grain boundary sliding becomes a more significant contributor to plasticity as strain levels rise, though dislocation emission remains the dominant mechanism at 9% strain. For the Al1 potential, deformation is initially dominated by dislocation emission. As strain levels increase, grain boundary sliding and other accommodation processes eventually rise to contribute a little more than 50% of the plastic deformation at 9% strain. Finally, in Pd grain boundary sliding processes are consistently dominant regardless of strain level.

We analyzed the relative contributions to plastic deformation as a function of stacking fault energy. We found that the contribution from grain boundary sliding and accommodation processes correlates with the stable stacking fault energy. We show this relationship between deformation from grain boundary sliding and stable stacking fault energy in figure 14. This correlation is mainly driven by the fact that for low stacking fault energy values, the grain boundary structure is more likely to present non-planar features, preventing sliding.

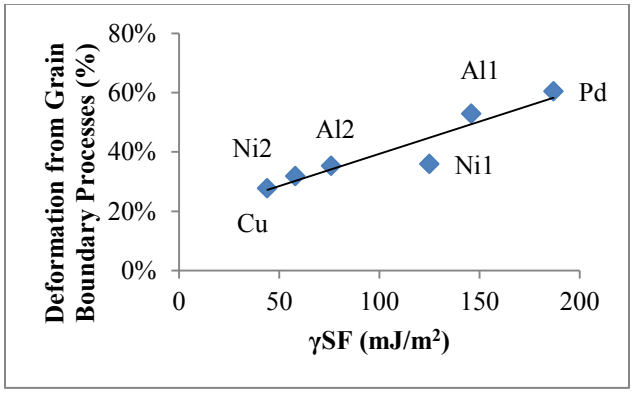

Figure 14: The contribution of deformation from grain boundary accommodation as a function of stable stacking fault energy. This clearly shows a correlation between stable stacking fault energy and grain boundary deformation processes.

9.6 Summary of correlations found

We show a quantitative summary of the resulting correlations in table 4. We linked the quantitative analysis on how observed energetics and deformation to the atomistic parameters of the potentials by using the values of R^2 linear correlation coefficients in each case. The parameters depicting potential characteristics are listed as the column headings in table 4, whereas the resulting observations are listed as row headings. Each value of R^2 was obtained using a linear best-fit procedure for the results obtained for each of the six potentials utilized. In order to ensure an adequate comparison, we adjusted the units of the elastic modulus, the yield and flow stress, and the C_{44} value by the lattice parameter to obtain consistent units of mJ/m^2. Values of R^2 of around 0.9 or higher are indicative on a clear correlation. We summarize the key correlations observed as:

- The grain boundary energy correlates strongly with both the cohesive energy and a_0C_{44}.
- The yield and flow stress in these simulations correlate strongly with the unstable stacking fault energy.
- The relative contributions to plasticity from dislocation emission and grain boundary sliding correlate strongly with the stable stacking fault energy.

Table 4: R^2 values showing correlation between atomistic parameters described by interatomic potentials and mechanical behavior.

	Cohesive Energy (mJ/m^2)	γ_{SF} (mJ/m^2)	γ_{USF} (mJ/m^2)	T_m (K)	a_0C_{44} (mJ/m^2)
Grain Boundary Energy (mJ/m^2)	0.94	0.01	0.83	0.86	0.94
a_0Elastic Modulus (mJ/m^2)	0.90	0.00	0.89	0.96	0.96
a_0Yield Stress (mJ/m^2)	0.83	0.00	0.90	0.89	0.81
a_0Flow Stress (mJ/m^2)	0.82	0.00	0.92	0.89	0.80
% Deformation from GB Process	0.18	0.88	0.00	0.01	0.16
% Deformation from Dislocation Emission	0.18	0.88	0.00	0.01	0.16
Average GB Sliding (nm)	0.59	0.41	0.27	0.37	0.56
Total Dislocation Emission	0.00	0.34	0.14	0.07	0.01

9.7 Discussion and conclusions

We found that the overall grain boundary energies for the samples used in this work scale with the shear modulus. This result is similar to the results found by Holm et al. [10, 11] in their work comparing grain boundary energies in Al, Au, Cu, and Ni. In addition, we found that the grain boundary energies also scale with the cohesive energy given by the potential. These results imply that in order to obtain accurate grain boundary energies in simulated polycrystals, it is important to ensure that the shear modulus and cohesive energies predicted by the potential are accurate. As these two quantities are generally used in the fitting procedure of the potentials, this is generally a requirement satisfied by construction of the potentials.

When we considered the energies of each grain boundary we found that individual grain boundary energies are dependent on the misorientation angle in a way that is similar to the dependence found in symmetrical tilt boundaries [2]. This implies that the special properties of high coincidence boundaries persist even in in randomly selected grain boundary networks. We investigated the variance of grain boundary energy along a boundary and as a function of

distance from triple junctions. In four of the five grain boundaries inspected for internal variability in energy (figure 6), the sections adjacent to triple junctions had a higher energy than those further away. One explanation for this variability is that the triple junctions impose constraints on the grain boundary mobility and structure. Such constraints may limit the ability of the grain boundary to reconfigure into a lower energy structure. In the grain boundaries analyzed for energy variability, the difference between grain boundary energy calculated for the entire boundary and the averaged energy from the sections did not exceed 5%. This indicates that the approximation used in this work to determine the excess grain boundary energy is appropriate. It is important to note that the boundaries studied in this work are straight; there may be somewhat more variation in energy in curved boundaries. These results suggest that variations in grain boundary energy are heavily influenced by both local and overall grain boundary structure. Analysis of the trends in figure 5 between asymmetric and symmetric tilt boundaries suggests that fcc polycrystalline metals behave similarly with regard to the relationship between grain boundary energy and misorientation angle. The cusps observed for the special CSL misorientations are less deep, pointing out the fact that the grain boundary plane can have a significant effect on energy and structure [48-50].

We found that the planarity of relaxed grain boundary structure in the samples studied correlate to the stable stacking fault energy. Low stacking fault energy promotes non-planar grain boundary structures, while higher stacking fault energy encourages a higher fraction of planar grain boundaries in the samples. We propose that e-units, a region of excess free volume in grain boundaries [18, 51, 52], and similar grain boundary structures contribute to the higher energy found. Consequently, the higher stacking fault energy prevents the e-units from collapsing to emit dislocations into neighboring grain structures. A similar correlation was found in the shear

response of a special incoherent twin boundary in various fcc metals [53]. Our results suggest that such dependence is also present for the case of randomly generated tilt boundaries. The local grain boundary structures for low stacking fault energy materials include non-planar features that extend into neighboring grains. We observed these differences in the relaxed grain boundary structure after the exact same equilibration treatment and deformation process. The differences can be clearly linked to the specific interatomic potential used and, in particular the corresponding stacking fault energies. We anticipate that this relationship would persist in grain boundary networks with larger grains and a wider variety of grain boundary structures.

Plastic deformation in nanocrystalline materials, as measured by the yield and flow stress, correlates to the unstable stacking fault energy. This work echoes that of Deng [22] in fcc nanowires. We observed the expected deformation mechanisms of dislocation emission and grain boundary sliding in this work. The non-planar features observed for some boundaries in this work promote dislocation emission and have not been observed in symmetrical tilt boundaries [54]. The presence or absence of non-planar structures in the grain boundary is critical in determining deformation behavior. Because non-planar grain boundary structures resemble nascent stacking faults, they lower the energetic barrier to dislocation emission in grain boundaries. In contrast, these features completely prevented grain boundary sliding and the grain boundaries without non-planar features showed more deformation through grain boundary sliding and coupled migration. Due to the importance of these non-planar features, the atomistic-scale plastic deformation processes (dislocation emission and grain boundary deformation) are closely correlated to the stable stacking fault energy. The relationship between stable stacking fault energy and mechanical behavior has been observed experimentally [55, 56] and in mesoscale simulations [57]. Experimental studies of the effect of stacking fault energy and grain

size in Ni-Co alloys [58, 59] show that low stacking fault energy promotes grain size refinement. With reduced grain size, the authors noted an increase in dislocation emission and density. These experimental results are consistent with our simulation results that low stacking fault energy promotes non-planar grain boundary features that are effective sources of dislocation emission. In our previous work with Cu and Pd, we found that high stacking fault energy is associated with planar grain boundary structures, increased grain boundary sliding, and a decrease in the total number of emitted dislocations. We confirmed that trend in this work when we analyzed all six samples. We also considered the contributions of grain boundary sliding and dislocation emission to the overall plasticity of each sample as functions of the atomistic parameters. We found a clear correlation to the stable stacking fault energy, further confirming our previous work.

Acknowledgments

This work was supported by the Department of Energy, Office of Basic Energy Sciences, under grant DE-FG02-08ER46525 and the National Science Foundation, IRD program. The authors acknowledge Advanced Research Computing at Virginia Tech for providing computational resources and technical support that have contributed to the results reported within this paper. URL: http://www.arc.vt.edu

References

[1] D. V. Bachurin, R. T. Murzaev, and A. A. Nazarov, "Atomistic computer and disclination simulation of 001 tilt boundaries in nickel and copper," *Physics of Metals and Metallography,* vol. 96, pp. 555-561, Dec 2003.

[2] B. J. Lee and S. H. Choi, "Computation of grain boundary energies," *Modelling and*

Simulation in Materials Science and Engineering, vol. 12, pp. 621-632, Jul 2004.

[3] N. Takata, T. Mizuguchi, K. I. Ikeda, and H. Nakashima, "Atomic and electronic structure of < 110 > symmetric tilt boundaries in palladium," *Materials Transactions,* vol. 45, pp. 2099-2105, Jul 2004.

[4] S. M. Allameh, S. A. Dregia, and P. G. Shewmon, "Structure and energy of (110) twist boundaries in the Ag/Ni system," *Acta Metallurgica Et Materialia,* vol. 42, pp. 3569-3576, Oct 1994.

[5] S. Y. Dai, Y. Xiang, and D. J. Srolovitz, "Structure and energy of (111) low-angle twist boundaries in Al, Cu and Ni," *Acta Materialia,* vol. 61, pp. 1327-1337, Feb 2013.

[6] A. J. Patrinos, I. P. Antoniades, and G. L. Bleris, "MONTE-CARLO AND MOLECULAR-DYNAMICS INVESTIGATION OF 001 TWIST BOUNDARIES IN CU3AU AT T=0 K," *Physical Review B,* vol. 52, pp. 9291-9299, Oct 1 1995.

[7] B. Schonfelder, G. Gottstein, and L. S. Shvindlerman, "Comparative study of grain-boundary migration and grain-boundary self-diffusion of 001 twist-grain boundaries in copper by atomistic simulations," *Acta Materialia,* vol. 53, pp. 1597-1609, Apr 2005.

[8] J. M. Zhang, X. M. Wei, and H. Xin, "Calculating the energies for Ag(001) twist boundaries utilizing the modified analytical embedded atom method," *Surface and Interface Analysis,* vol. 36, pp. 1500-1504, Nov 2004.

[9] I. P. Antoniades, A. J. Patrinos, and G. L. Bleris, "Molecular dynamics investigation of the Sigma 5 energy cusp in 001 twist boundaries in Cu3Au at T=0 K," in *Intergranular and Interphase Boundaries in Materials, Pt 2*. vol. 207-, A. C. Ferro, J. P. Conde, and M. A. Fortes, Eds., ed, 1996, pp. 833-836.

[10] E. A. Holm, D. L. Olmsted, and S. M. Foiles, "Comparing grain boundary energies in face-centered cubic metals: Al, Au, Cu and Ni," *Scripta Materialia,* vol. 63, pp. 905-908, Nov 2010.

[11] E. A. Holm, G. S. Rohrer, S. M. Foiles, A. D. Rollett, H. M. Miller, and D. L. Olmsted, "Validating computed grain boundary energies in fcc metals using the grain boundary character distribution," *Acta Materialia,* vol. 59, pp. 5250-5256, Aug 2011.

[12] D. L. Olmsted, S. M. Foiles, and E. A. Holm, "Survey of computed grain boundary properties in face-centered cubic metals: I. Grain boundary energy," *Acta Materialia,* vol. 57, pp. 3694-3703, Aug 2009.

[13] G. S. Rohrer, E. A. Holm, A. D. Rollett, S. M. Foiles, J. Li, and D. L. Olmsted, "Comparing calculated and measured grain boundary energies in nickel," *Acta Materialia,* vol. 58, pp. 5063-5069, Sep 2010.

[14] N. Q. Vo, J. Schafer, R. S. Averback, K. Albe, Y. Ashkenazy, and P. Bellon, "Reaching theoretical strengths in nanocrystalline Cu by grain boundary doping," *Scripta Materialia,* vol. 65, pp. 660-663, Oct 2011.

[15] R. Monzen, M. Futakuchi, K. Kitagawa, and T. Mori, "Measurement of grain-boundary sliding of 011 twist boundaries in copper by electron-microscopy," *Acta Metallurgica Et Materialia,* vol. 41, pp. 1643-1646, Jun 1993.

[16] N. Chandra and S. Namilae, "Multi-scale modeling of nanocrystalline materials," in *Superplasticity in Advanced Materials*. vol. 447-4, R. I. Todd, Ed., ed Stafa-Zurich: Trans Tech Publications Ltd, 2003, pp. 19-25.

[17] M. de Koning, R. J. Kurtz, V. V. Bulatov, C. H. Henager, R. G. Hoagland, W. Cai*, et al.*, "Modeling of dislocation-grain boundary interactions in FCC metals," in *Workshop on Modeling and Experimental Validation*, Les Diableret, Switzerland, 2002, pp. 281-289.

[18] M. A. Tschopp and D. L. McDowell, "Asymmetric tilt grain boundary structure and energy in copper and aluminium," *Philosophical Magazine,* vol. 87, pp. 3871-3892, 2007 2007.

[19] G. J. Tucker, M. A. Tschopp, and D. L. McDowell, "Evolution of structure and free volume in symmetric tilt grain boundaries during dislocation nucleation," *Acta Materialia,* vol. 58, pp. 6464-6473, Nov 2010.

[20] Z. H. Jin, P. Gumbsch, K. Albe, E. Ma, K. Lu, H. Gleiter*, et al.*, "Interactions between non-screw lattice dislocations and coherent twin boundaries in face-centered cubic metals," *Acta Materialia,* vol. 56, pp. 1126-1135, Mar 2008.

[21] Z. H. Jin, P. Gumbsch, E. Ma, K. Albe, K. Lu, H. Hahn*, et al.*, "The interaction mechanism of screw dislocations with coherent twin boundaries in different face-centred cubic metals," *Scripta Materialia,* vol. 54, pp. 1163-1168, Mar 2006.

[22] C. Deng and F. Sansoz, "Fundamental differences in the plasticity of periodically twinned nanowires in Au, Ag, Al, Cu, Pb and Ni," *Acta Materialia,* vol. 57, pp. 6090-6101, Dec 2009.

[23] R. J. Asaro and S. Suresh, "Mechanistic models for the activation volume and rate

sensitivity in metals with nanocrystalline grains and nano-scale twins," *Acta Materialia,* vol. 53, pp. 3369-3382, Jul 2005.

[24] S. M. Foiles and J. J. Hoyt. (2001, Computer Simulation of Bubble Growth in Metals Due to He. *Sandia Report SAND2001-0661*.

[25] Y. Mishin, D. Farkas, M. J. Mehl, and D. A. Papaconstantopoulos, "Interatomic potentials for monoatomic metals from experimental data and ab initio calculations," *Physical Review B,* vol. 59, pp. 3393-3407, Feb 1999.

[26] Y. Mishin, M. J. Mehl, D. A. Papaconstantopoulos, A. F. Voter, and J. D. Kress, "Structural stability and lattice defects in copper: Ab initio, tight-binding, and embedded-atom calculations," *Physical Review B,* vol. 63, Jun 2001.

[27] A. F. a. C. Voter, S. P., "High temperature ordered intermetallic alloys," *Materials Research Society Symposium Proceedings,* vol. 82, p. 175, 1987.

[28] D. Farkas and L. Patrick, "Tensile deformation of fcc Ni as described by an EAM potential," *Philosophical Magazine,* vol. 89, pp. 3435-3450, 2009.

[29] L. Smith and D. Farkas, "Non-planar grain boundary structures in fcc metals and their role in nano-scale deformation mechanisms," *Philosophical Magazine,* vol. 94, pp. 152-173, 2014/01/12 2013.

[30] S. Plimpton, "Fast parallel algorithms for short-range molecular-dynamics," *Journal of Computational Physics,* vol. 117, pp. 1-19, Mar 1995.

[31] M. J. Mehl, J. E. Osburn, D. A. Papaconstantopoulos, and B. M. Klein, "Structural properties of ordered high-melting-temperature intermetallic alloys from 1st-principles total-energy calulations," *Physical Review B,* vol. 41, pp. 10311-10323, May 1990.

[32] C. L. Kelchner, S. J. Plimpton, and J. C. Hamilton, "Dislocation nucleation and defect structure during surface indentation," *Physical Review B,* vol. 58, pp. 11085-11088, Nov 1998.

[33] A. Stukowski, "Visualization and analysis of atomistic simulation data with OVITO-the Open Visualization Tool," *Modelling and Simulation in Materials Science and Engineering,* vol. 18, Jan 2010.

[34] F. Ernst, M. W. Finnis, D. Hofmann, T. Muschik, U. Schonberger, U. Wolf*, et al.*, "Theoretical prediction and direct observation of the 9R structure in Ag," *Physical Review Letters,* vol. 69, pp. 620-623, Jul 1992.

[35] U. Wolf, F. Ernst, T. Muschik, M. W. Finnis, and H. F. Fischmeister, "The influence of grain-boundary inclination on the structure and energy of sigma=3 grain-boundaries in copper," *Philosophical Magazine a-Physics of Condensed Matter Structure Defects and Mechanical Properties,* vol. 66, pp. 991-1016, Dec 1992.

[36] S. M. Foiles and J. J. Hoyt, "Computation of grain boundary stiffness and mobility from boundary fluctuations," *Acta Materialia,* vol. 54, pp. 3351-3357, Jul 2006.

[37] D. Brandon, "Structure of high-angle grain boundaries," *Acta Metallurgica,* vol. 14, 1966.

[38] N. Floyd, "Energetics and deformation response of random grain boundaries in fcc nickel," M.S., Materials Science and Engineering, Virginia Polytechic Institute and State University, Blacksburg, VA, 2010.

[39] M. A. Hopcroft, W. D. Nix, and T. W. Kenny, "What is the young's modulus of silicon?," *Journal of Microelectromechanical Systems,* vol. 19, pp. 229-238, Apr 2010.

[40] J. Weissmueller, J. Markmann, M. Grewer, and R. Birringer, "Kinematics of polycrystal deformation by grain boundary sliding," *Acta Materialia,* vol. 59, pp. 4366-4377, Jun 2011.

[41] D. Caillard, F. Mompiou, and M. Legros, "Grain-boundary shear-migration coupling. II. Geometrical model for general boundaries," *Acta Materialia,* vol. 57, pp. 2390-2402, May 2009.

[42] D. Farkas, A. Froseth, and H. Van Swygenhoven, "Grain boundary migration during room temperature deformation of nanocrystalline Ni," *Scripta Materialia,* vol. 55, pp. 695-698, 2006.

[43] J. W. Cahn and Y. Mishin, "Recrystallization initiated by low-temperature grain boundary motion coupled to stress," *International Journal of Materials Research,* vol. 100, pp. 510-515, Apr 2009.

[44] J. W. Cahn, Y. Mishin, and A. Suzuki, "Duality of dislocation content of grain boundaries," *Philosophical Magazine,* vol. 86, pp. 3965-3980, Sep 1 2006.

[45] J. W. Cahn, Y. Mishin, and A. Suzuki, "Coupling grain boundary motion to shear deformation," *Acta Materialia,* vol. 54, pp. 4953-4975, Nov 2006.

[46] D. Farkas, S. Mohanty, and J. Monk, "Strain-driven grain boundary motion in nanocrystalline materials," *Materials Science and Engineering a-Structural Materials Properties Microstructure and Processing,* vol. 493, pp. 33-40, Oct 15 2008.

[47] M. Velasco, H. Van Swygenhoven, and C. Brandl, "Coupled grain boundary motion in a nanocrystalline grain boundary network," *Scripta Materialia,* vol. 65, pp. 151-154, Jul 2011.

[48] Y. Mishin, M. Asta, and J. Li, "Atomistic modeling of interfaces and their impact on microstructure and properties," *Acta Materialia,* vol. 58, pp. 1117-1151, Feb 2010.

[49] V. Randle, "The role of the grain boundary plane in cubic polycrystals," *Acta Materialia,* vol. 46, pp. 1459-1480, Mar 1998.

[50] D. Wolf, "Structure-energy correlation for grain-boundaries in fcc metals .3. Symmetrical tilt boundaries," *Acta Metallurgica Et Materialia,* vol. 38, pp. 781-790, May 1990.

[51] D. E. Spearot, "Evolution of the E structural unit during uniaxial and constrained tensile deformation," *Mechanics Research Communications,* vol. 35, pp. 81-88, Jan-Mar 2008.

[52] M. A. Tschopp, G. J. Tucker, and D. L. McDowell, "Structure and free volume of < 110 > symmetric tilt grain boundaries with the E structural unit," *Acta Materialia,* vol. 55, pp. 3959-3969, Jun 2007.

[53] J. Wang, A. Misra, and J. P. Hirth, "Shear response of Sigma 3{112} twin boundaries in face-centered-cubic metals," *Physical Review B,* vol. 83, Feb 18 2011.

[54] L. Wan and S. Wang, "Shear response of the Sigma 9 < 110 > {221} symmetric tilt grain boundary in fcc metals studied by atomistic simulation methods," *Physical Review B,* vol. 82, Dec 20 2010.

[55] X. H. An, Q. Y. Lin, S. D. Wu, Z. F. Zhang, R. B. Figueiredo, N. Gao*, et al.*, "Significance of stacking fault energy on microstructural evolution in Cu and Cu-Al alloys processed by high-pressure torsion," *Philosophical Magazine,* vol. 91, pp. 3307-3326, 2011 2011.

[56] Y. Ivanisenko, L. Kurmanaeva, J. Weissmueller, K. Yang, J. Markmann, H. Roesner*, et al.*, "Deformation mechanisms in nanocrystalline palladium at large strains," *Acta Materialia,* vol. 57, pp. 3391-3401, Jun 2009.

[57] A. Hunter, I. J. Beyerlein, T. C. Germann, and M. Koslowski, "Influence of the stacking fault energy surface on partial dislocations in fcc metals with a three-dimensional phase field dislocations dynamics model," *Physical Review B,* vol. 84, Oct 10 2011.

[58] P. L. Sun, Y. H. Zhao, J. C. Cooley, M. E. Kassner, Z. Horita, T. G. Langdon*, et al.*, "Effect of stacking fault energy on strength and ductility of nanostructured alloys: An

evaluation with minimum solution hardening," *Materials Science and Engineering a-Structural Materials Properties Microstructure and Processing,* vol. 525, pp. 83-86, Nov 15 2009.

[59] Z. W. Wang, Y. B. Wang, X. Z. Liao, Y. H. Zhao, E. J. Lavernia, Y. T. Zhu*, et al.*, "Influence of stacking fault energy on deformation mechanism and dislocation storage capacity in ultrafine-grained materials," *Scripta Materialia,* vol. 60, pp. 52-55, Jan 2009.

10 Effect of Temperature on the Deformation Response of Grain Boundary Networks

Laura Smith[1], Diana Farkas[1], Niklas Floyd[1], Josh Kacher[2], and I.M. Robertson[2]

[1]Department of Materials Science and Engineering

Virginia Polytechnic Institute and State University

Blacksburg, VA 24061

[2]Department of Materials Science and Engineering

University of Illinois

1304 West Green Street

Urbana IL 61801

10.1 Abstract

Temperature effects on the deformation response of random grain boundary networks are explored using molecular dynamics atomistic simulations and an embedded atom method interatomic potential. The results from the simulations are compared with those from *in situ* TEM deformation experiments and similarities identified. We find that deformation at higher temperatures promotes dislocation emission, dislocation accommodation in the grain boundary, slip in the grain boundary plane, grain boundary sliding, and slip transmission. Crack nucleation at the grain boundaries occurs at increasingly higher applied loads for increasing temperatures. We have also explored the effects of strain rate at the various temperatures. The activation energies found for the deformation process are consistent with estimates for that of grain boundary diffusion in nanocrystalline Ni.

10.2. Introduction

Deformation of metallic materials is governed by dislocation slip that may involve perfect and partial dislocations or deformation twins [1-4]. These dislocations can be pre-existing or newly generated, from sources such as Frank-Reed sources, grain boundaries and interfaces, precipitates, and surface flaws. Many of these same features also serve as obstacles to dislocation motion, providing strengthening mechanisms. In the case of grain boundaries, there is a dependence of the barrier strength, source effectiveness and slip transfer efficiency on the grain boundary misorientation, structure, strain energy density or defect state, and local stress state [5]. Furthermore, these dependencies can change through processes and interactions that alter the composition and structure of the grain boundary. For example, under bombardment with energetic particles, the defect density accumulated within the grain boundary can increase. The chemical composition can be altered as segregation of elements to and from the boundary is enhanced or induced by the irradiation [6]. The local structure and element segregation can also be affected as more dislocations interact with and are accommodated in the grain boundary. Knowledge of the atomistic processes associated with dislocation accommodation and emission from grain boundaries is key to understanding these effects.

The interaction of dislocations with grain boundaries has been studied using various experimental [7-12] and simulation techniques [13-19]. From the experimental studies at room temperature, it was shown that several dislocations were accommodated in a grain boundary prior to the emission of a dislocation into the adjoining grain. The slip system activated at a grain boundary from an incoming dislocation system is determined by a series of local conditions: the angle between the incident and emerging slip systems in the grain boundary plane should be minimized, the Schmid factor as determined by the local stress state should be maximized, and

the strain energy density within the grain boundary should be minimized [7-11]. For grain boundaries in face-centered cubic systems, the Schmid factor and the strain energy density control the response and are competitive in nature. That is, the system experiencing the maximum resolved shear stress can operate even if it increases the strain energy density in the grain boundary, but only briefly. Conversely, the system that increases the strain energy density the least but experiences no shear stress will not be activated. Although these conditions are deterministic, there is a paucity of information about the atomistic processes occurring within the grain boundary on accommodation and ejection of a dislocation. Furthermore, the role of temperature and hence of the ability of dislocations to climb, on these conditions and the deformation processes that occur at and in the grain boundary are not well understood.

Most atomistic level studies have focused on bicrystals and special boundaries, such as symmetric tilt boundaries [14, 20]. This has also been studied at the meso-scale as well [16, 21]. Neither temperature effects nor systems containing multiple grains with random misorientation distributions have been studied in detail despite the importance of this phenomena in experimental systems. Recently, Sangid and co-workers devised a method to obtain the energy required for dislocation emission from grain boundaries and for slip transmission across them [5]. They found that as the boundaries are characterized by larger values of the reciprocal density of coincident sites, more complex structures are present in experiment and simulations and that slip nucleation and transmission is more difficult for low sigma, low energy boundaries. For the higher coincident site lattice boundaries, the energy associated with the interaction was approximately constant. This investigation provided unique insight as to the dependence of the barrier strength on the grain boundary type.

The present work utilizes computer simulation of deformation behavior of random grain boundary networks, guided by experimental studies, to focus on the effect of temperature on the deformation behavior in polycrystalline systems. Specifically, we study the effects of temperature on dislocation emission from the grain boundaries, grain boundary accommodation of slip and the transfer of slip across boundaries. We also address the issue of intergranular crack nucleation at different temperatures. Comparison of the results with experiments is made with the caveat that each approach imposes vastly different system constraints.

This paper is organized as follows: Section 2 describes the essential experimental observations from *in situ* TEM studies that guided the simulation work. Section 3 reports the simulation techniques used and discusses the limitations intrinsic to these techniques. In Section 4 we report the observed trends in the simulation results as a function of increasing temperature. These are i) increased dislocation emission, ii) increased grain boundary sliding, iii) easier slip transmission across the boundaries and iv) decreased propensity to crack nucleation. We also calculate the strain rate sensitivity, activation volume, and activation energy for the deformation process. In section 5 the implication of these results are then discussed and compared with the experimental observations.

10.3. Experimental observations

In situ TEM deformation experiments have been performed primarily using 304 stainless steel. Straining bars with approximate dimensions of 11.5 mm-long x 2.5 mm-wide and 150 μm-thick were cut from a sheet, annealed for 30 minutes at 1303 K, and thinned to electron transparency using a perchloric acid/methanol electrolyte. The straining was performed using a Gatan displacement-controlled heating/straining stage. This stage does not allow for measurement of

the applied load and sample displacement. The experimental samples were deformed at nominal sample temperatures of 300 and 673 K, compared to the simulated samples deformed at 300 and 60% T_{MP}. Here the temperature is given as the nominal sample temperature as the thermocouple is on the heating element and not on the sample. As the sample is not in intimate contact with the heater the sample temperature is not measured. It has been shown that the sample temperature can differ from that of the heater by as much as -150 K [22]. The stage displacement was activated in an incremental manner with a maximum rate of 1 μm/s. The precise strain rate is not determined, but is considerably lower than that used in MD simulations. The *in situ* TEM experiments were conducted in a JEOL 2010 LaB_6 TEM operated at 200 kV. The dynamics of the interaction between dislocations and grain boundaries were captured using a CCD camera and recorded at a frame rate of 10 fps.

Grain boundaries serve as effective barriers to the motion of dislocations. This is exemplified in the series of micrographs presented in Figure 1, which show the same region as a function of increasing incremental loading during *in situ* straining of 304 stainless steel at room temperature. In the dynamic experiments conducted in the TEM the development of a dislocation pile-up at a grain boundary was readily observed. As shown in the series of images presented in Figure 1, many dislocations can pileup at a grain boundary prior to slip being transferred to the adjoining grain. The dark contrast visible in the adjoining grain in Figures 1a and 1b are evidence of elastic distortions of the lattice and do not indicate that dislocations have been ejected from the grain boundary into the adjoining grain. With increasing strain, the number of dislocations in the pileup increased and eventually dislocations were ejected into the adjoining grain. Interestingly, prior to the initiation of slip transfer across the grain boundary, dislocations cross-slip out of the pileup as seen in Figure 1b and 1c.

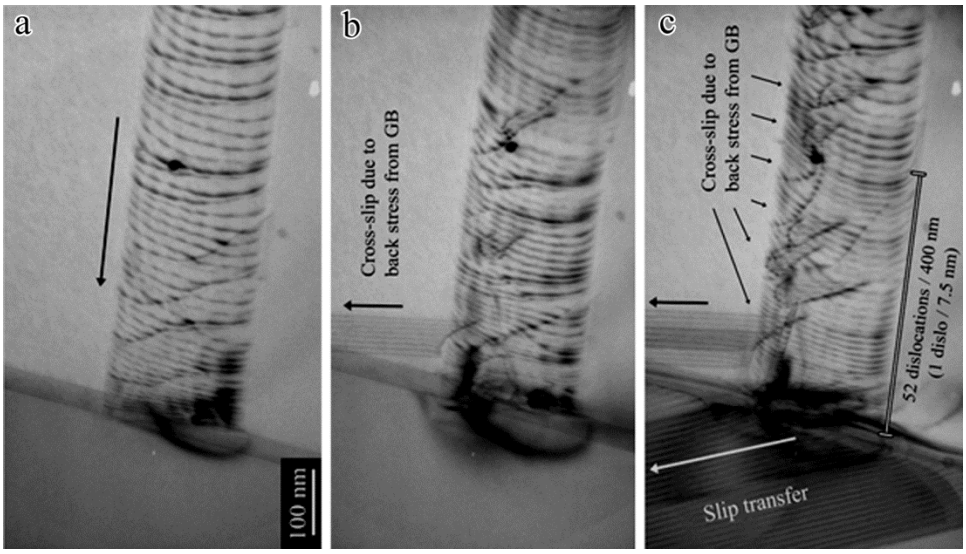

Figure 1. Frames taken from a video showing dislocations interacting with a grain boundary during *in situ* straining at room temperature. Arrows indicate direction of dislocation motion. Note the ejection of dislocations from the pile-up by cross slip. Figure by Kacher.

Grain boundaries, as well as other sites of high stress concentration, are also effective sources for dislocations. The ejected dislocations are generally of the same type although they are not necessarily coplanar. Experimentally it has been found that the source activity is greater at higher temperatures, although local stress conditions cannot be determined to sufficient accuracy for direct comparison between experiments conducted at different temperatures. In other words, variations in local stress conditions are always a significant variable when comparing experiments, making it difficult to isolate the effects of elevated temperature on dislocation/grain boundary interactions. To address this concern the activity at the same grain boundary was observed at two different temperatures. An example of the result of such an experiment is shown in Fig. 2 for dislocations, emitted from a crack tip, interacting with a Σ3 coherent twin boundary. The series of images presented in Figs. 2a-c show partial dislocations interacting with the grain boundary. From this image it is unclear if the fringes trailing the partial dislocations are indicative of a deformation twin or overlapping stacking faults. However, from the observed interaction with the twin boundary it can be surmised that they are partial dislocations bounding

stacking faults and not twinning partial dislocations. The interaction resulted in the creation of a dislocation pile-up against the boundary, accommodation of these dislocations into the grain boundary and slip along the grain boundary plane rather than emission from it into the adjoining grain. Evidence for slip along the grain boundary can be seen in the form of contrast fluctuations along the grain boundary, Fig. 2a. For the dislocations to become glissile on the grain boundary, the leading and trailing partial dislocations must first constrict to form a perfect dislocation or the accommodation of the leading partial dislocation in the boundary must be accompanied by the formation of twinning partial dislocations that would result in a thickening or thinning of the twin. Further support for these partial dislocations bounding stacking faults and not twins is the interaction itself. For these to be twinning dislocations strain accommodation, as noted by Mahajan *et al*., would require the emission of two systems out of the boundary in addition to the system gliding in the boundary [23, 24].

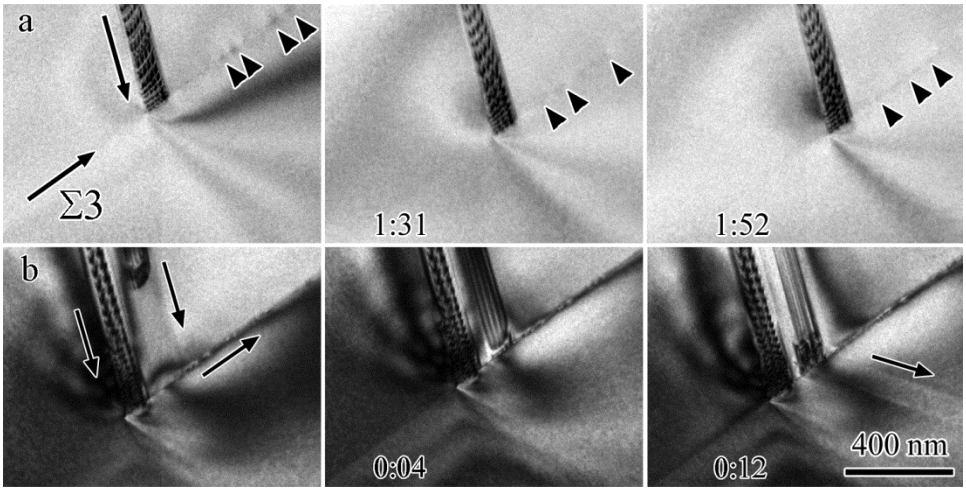

Fig. 2. Frames taken from a video showing dislocations interacting with a coherent twin boundary during in situ straining. Arrows indicate direction of dislocation motion. Elapsed time is given in each image. a) Room temperature interaction of dislocations with boundary. Arrowheads indicate location of dislocations in the boundary. b) Dislocations interacting with same boundary as a) but at a nominal temperature of 673 K. Figure modified and used with permission from [25].

Before the sample temperature was increased to a nominal temperature of 673K, the stage displacement was driven backwards to remove but not reverse the load, and then reloaded after the temperature had stabilized. On reloading at elevated temperature, another set of dislocations was released from the same source but on a parallel slip plane. As shown in the series of micrographs presented as Figs. 2b, these dislocations intersected and entered the grain boundary and were glissile along it. However, notably different from the room temperature interaction was the density of dislocations in the pileup at the twin boundary was significantly lower at the higher temperature. Also, dislocations were periodically emitted from the boundary into the adjoining grain, a process not observed during deformation at the lower temperature. These results suggest that the twin boundary posed a weaker barrier to dislocation accommodation and transmission at elevated temperature.

Another difference noted at higher temperature was that the deformation processes and dislocation activity tended to be more complex with more sources being activated. The complexity of the processes is illustrated in Figures 3-4 which show dislocations impinging on another coherent Σ3 twin boundary. The dislocation source in this case was the Σ3 coherent twin boundary shown in Figure 2. Two separate dislocation slip systems impinge on the boundary as shown in the bright-field images acquired with different diffraction vectors and presented in Figure 3. These systems are referred to as system 1, the system visible in Figure 3a, and system 2, the system visible in Figure 3b.

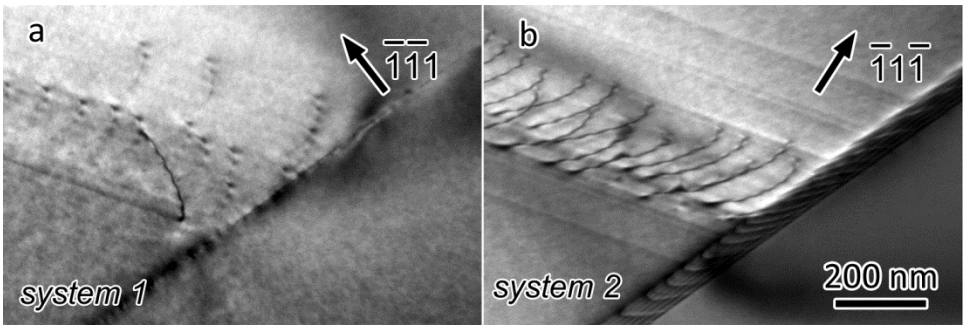

Figure 3. Two images of a grain boundary/dislocation interaction taken using different diffraction conditions to show the two types of dislocations present. The dynamics of the interactions are shown in Figure 4. The diffraction vector used is given for each image and system labeling is given for reference in the text. Figure modified from [25].

Following the interaction in real time allows for detailed analysis of the dislocation absorption and transmission process at the grain boundary including the interaction sequence. The series of images presented in Fig. 4 show mobile dislocations travelling along a ∑3 twin boundary in both directions. As this interaction occurred during an *in situ* TEM straining experiment it was observed that system 2 dislocations, which impacted the boundary to the right of the main interaction point, cross-slipped onto the boundary and travelled in direction labeled 1, Fig 4a. Conversely, system 2 dislocations that impacted the boundary to the left of the main interaction point travelled in the opposite direction, labeled 2 in Fig. 4b. It was also noted that dislocation emission into the neighboring grain coincided with a system 1 dislocation being absorbed at the main interaction point (Fig. 4c). Surprisingly, all three interactions, propagation along the boundary in directions 1 and 2 as well as slip transmission followed a one-to-one correspondence with the incoming dislocations. That is, each incoming dislocation triggered an event.

The twin plane, identified by tilting the boundary such that the plane normal was perpendicular to the electron beam direction was $(\bar{1}\,\bar{1}\,1)$. Analysis of the dislocations, using the $|\mathbf{g}\bullet\mathbf{b}|$ invisibility condition, showed that the Burgers vector of system 1 dislocations is $\mathbf{b} = \pm a/2[110]$ and for system 2 is $\mathbf{b} = \pm a/2[101]$. Analysis of the diffraction patterns yields that the dislocations

from the two systems must reside on either (111) or $(1\bar{1}\,\bar{1})$ plane. Dislocations with the observed Burgers vectors are not glissile on (111), leaving $(1\bar{1}\,\bar{1})$ as the slip plane. As [101] is common to both $(1\bar{1}\,\bar{1})$ and $(\bar{1}\,\bar{1}\,1)$, the lattice dislocations with this Burgers vector can cross-slip onto the twin plane, which is consistent with the observations. The dislocations from system 1, however, cannot cross-slip onto the twin plane, suggesting that emission into the neighboring grain is linked with the impingement of it on the grain boundary. Again, this is consistent with the observed dislocation activity.

There is no available slip plane in the lower grain that allows direct transfer of the system 1 dislocations across this grain boundary. Accordingly, dislocation absorption and transmission must be accompanied by an increase in strain energy density in the boundary [5]. The stored strain energy may create a barrier to dislocation propagation along the boundary, explaining the observed dislocation glide in both directions along the boundary. However, the atomistic mechanisms responsible for these dislocation interactions are not currently available for experimental observation, encouraging further investigation by simulation techniques.

Grain boundary disintegration has also been observed during *in situ* TEM straining at high temperatures. An example of this disintegration is shown in Figure 5 [22]. These images compare the microstructure before and after straining an Al-4Mg-0.3Sc sample at a nominal temperature of 733K [22]. Several grain boundaries can be identified in these images, and each is numbered for ease of reference. Grain boundary 1 has started to disintegrate and is no longer connected to the grain boundary on the opposite side; this detachment is not seen in the presented images. In the increment of strain shown in Figure 5, this disintegration continues by the emission and release of dislocations in the direction shown. Similarly, grain boundary 2 disintegrates and these dislocations are incorporated in boundary 3; the slip traces on the sample

surface due to the motion of the dislocations can be seen in Figure 5b. A small grain, labelled x, is stable under this increment of loading. Close inspection of grain boundary 3 and 4 show that changes in the form of cusped regions, arrowed segments along boundary 3, which are consistent with the grain boundary having moved.

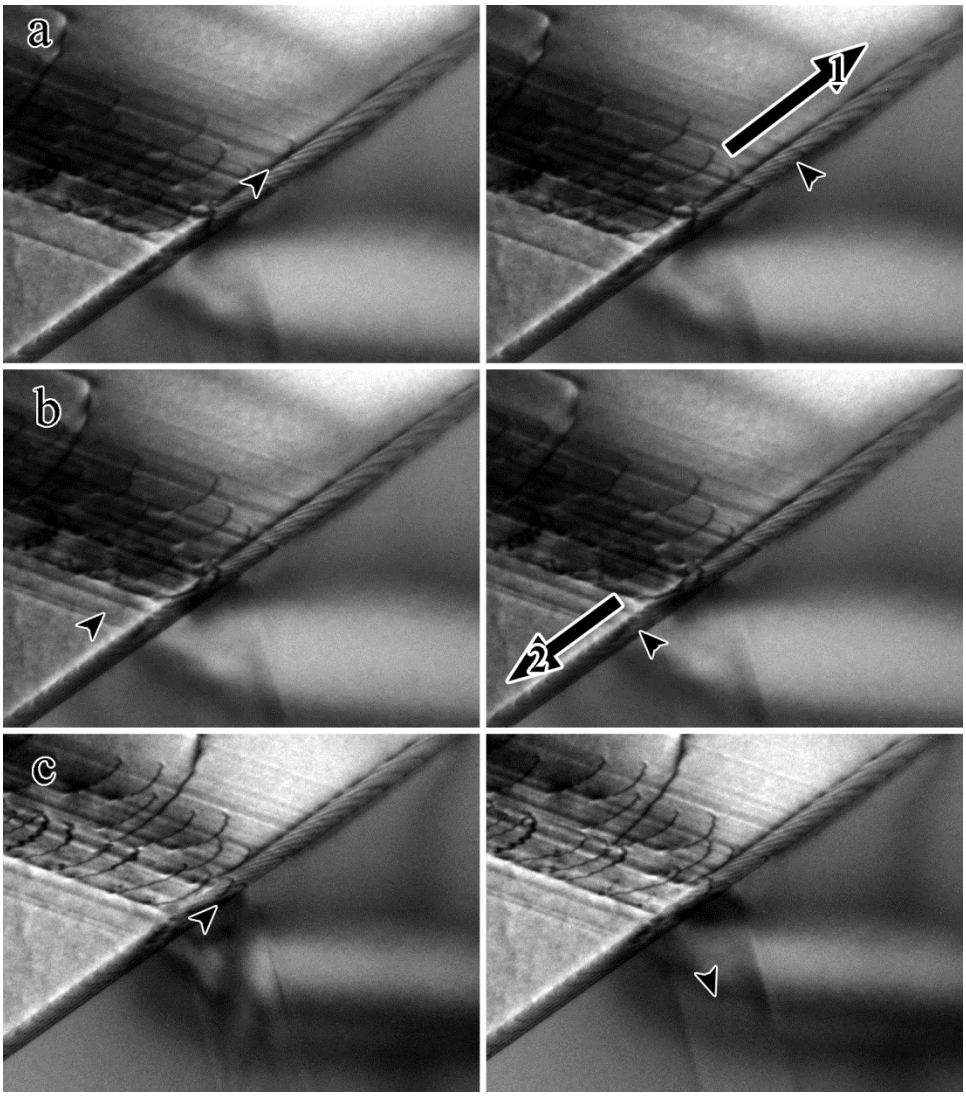

Figure 4. Frames taken from a video showing dislocations being incorporated into a grain boundary during *in situ* straining. The pairs of images are taken 0.1 s apart from each other. The dislocation being absorbed and its subsequent location in the grain boundary is indicated in the image. a) Dislocation being incorporated to the right of the main interaction zone; b) Dislocation being incorporated to the left of the main interaction zone; and c) Dislocation being incorporated at the main interaction zone, resulting in the emission of a dislocation into the neighboring grain. Note that the dislocation in (c) is in a g●b = 0 condition. Arrows show direction of dislocation motion in the boundary and are labeled for reference in the text. Figure modified from [25].

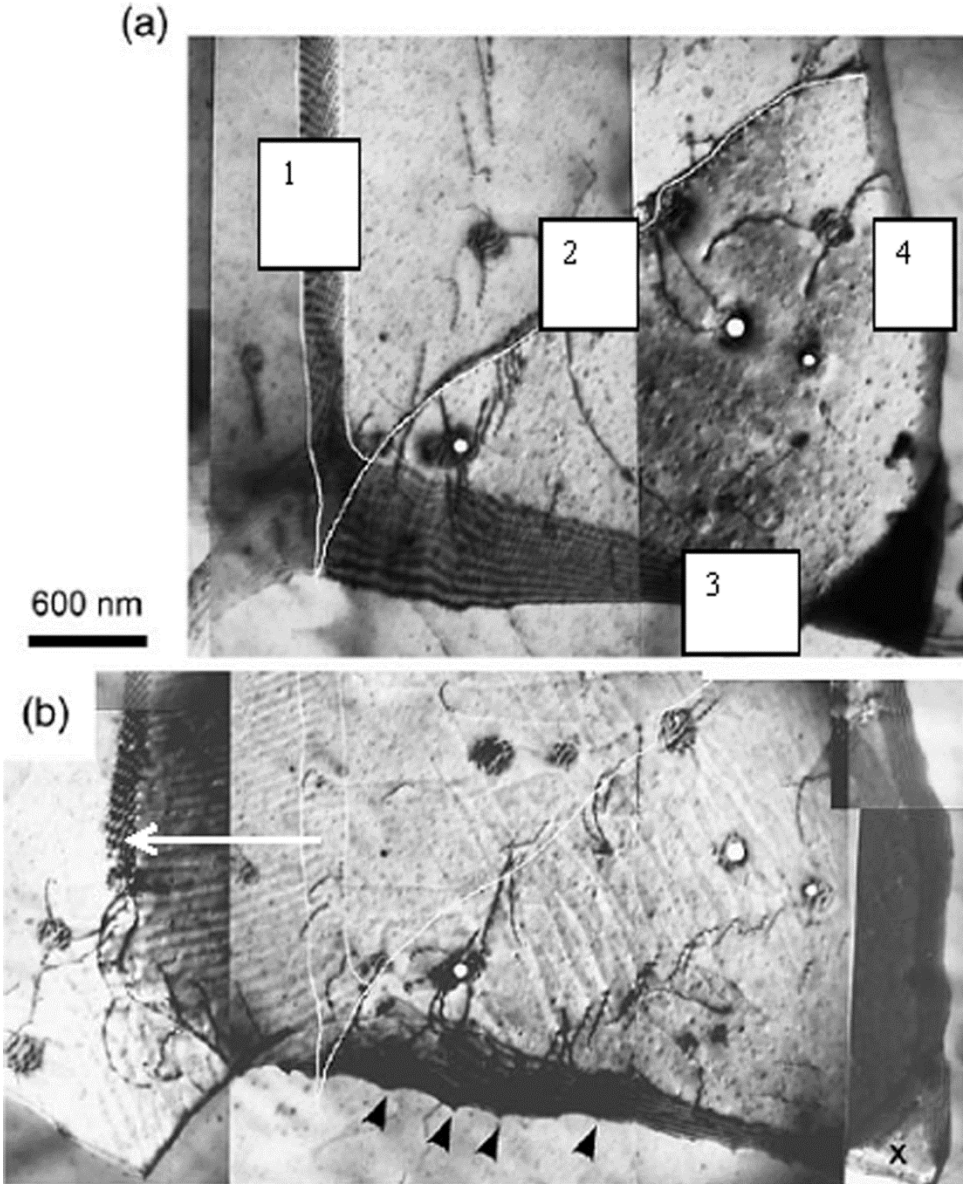

Fig 5. Images taken before (a) and after (b) straining Al-4Mg-0.3Sc *in situ* at a nominal temperature of 733 K showing the disintegration of a sub-grain boundary. Labeling is for reference in the text. Reprinted from [22] with permission from Elsevier.

10.4 Simulation procedure

Two sample geometry types, periodic and thin film, are used in this work with average grain sizes of approximately 40nm. The periodic samples shown in Figure 6 (a, b) have columnar grains randomly tilted around a <110> axis and periodic boundary conditions in three dimensions to eliminate surface effects [26]. Two different periodic samples were generated and

used in this work. The thin film samples have periodic boundaries in the x and y directions and free surfaces in the z direction. Four types of thin-film samples were considered in this work, though only one is shown in Figure 6(c). The samples were constructed using a Voronoi construction technique, similar to our previous work [19, 27, 28]. It is important to note that the periodic samples have a quasi-2D nature, seen in Figure 6 (a) and (b), in which only straight-line dislocations are possible. While the 40nm grain size is much smaller than the experimental grains, it is large enough to avoid most of the nano-scale effects observed for grain sizes below 20 nm [29]. The 40nm grain size used also precludes the possibility of dislocation generation or multiplication through Frank-Read sources.

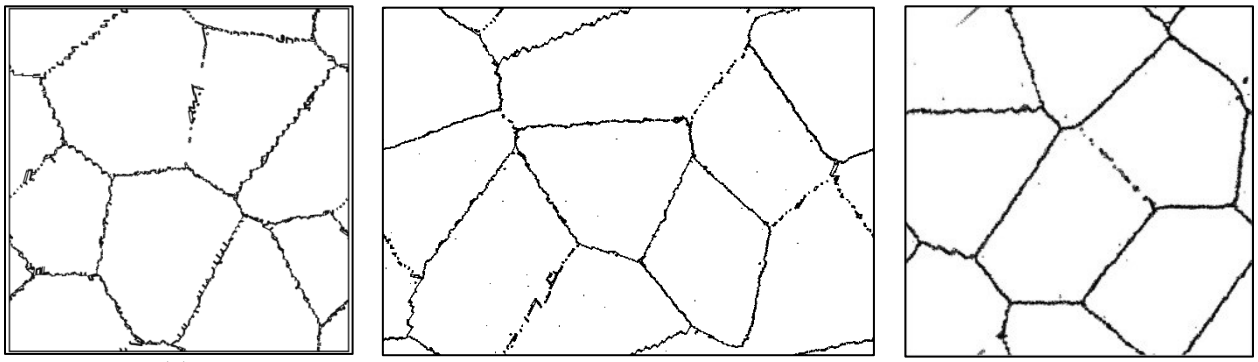

(a) (b) (c)

Figure 6: Simulation sample morphologies used in this work. (a) and (b) are fully periodic samples. (c) is a thin-film sample. Figure by author.

We selected the embedded atom method potential developed to represent nickel by Mishin et al. [30] The melting temperature produced by the potential used in this work was determined by equilibrating the sample at intervals of 10% of the experimental melting temperature until a spike in the potential energy was observed. The melting temperature was determined to be 2160K (125% of experimental). The critical parameters for the potentials used in this work are summarized in Table 1.

Table 1: Critical parameters for the nickel potential used in this work.

Cohesive Energy (eV)	Lattice Constant (Å)	C_{11} (GPa)	C_{12} (GPa)	C_{44} (GPa)	Stable SFE (mJ/m^2)	Unstable SFE (mJ/m^2)	Potential Tm (K)
-4.45	3.52	247	148	125	125[30]	366[30]	2160

The molecular dynamics implementation in LAMMPS [31] was used to perform the sample relaxation and virtual mechanical testing reported, with a Nosé-Hoover thermostat and barostat. To achieve relaxed and equilibrated grain boundary structures, the temperature of the sample was raised from 300K to 1200K, and then cooled to 300K over 60ps.

Deformation simulations were performed at temperatures ranging from 300 to 1300K, that is, up to 60% of the melting temperature for the potential used. Both sample configurations were deformed in tension in the horizontal (x) direction with a constant strain rates ranging from $3.3x10^6$ s^{-1} to $3.3x10^9$ s^{-1}at the various temperatures. We maintained the pressure at zero bars in the directions perpendicular to the tension axis during deformation.

For both sample geometries, data for individual atoms, including atomic positions, centro-symmetry [15], and stress state, were recorded every 1% strain. To examine the deformation behavior after each strain increment, heterogeneous displacement maps were created. These were obtained by calculating the difference between the individual atomic positions to those that would result from the homogeneous deformation of the sample to the same strain level. This comparison revealed regions of strain localization with the magnitude of the difference color coded for visualization purposes. This analysis indicates differences in the local distribution of the overall strain among the different grains, revealing localization within the grains or the grain boundary vicinity. This technique also allowed visualization of dislocation activity for full dislocations that traverse a grain, since the effect on the local strain can be seen clearly. Partial

dislocations are easily identified by the presence of the corresponding stacking fault. The visualization software OVITO [32] was used to color code the atoms by the centro-symmetry parameter. This allowed the easy identification of microstructural changes in the samples.

10.5. Simulation Results

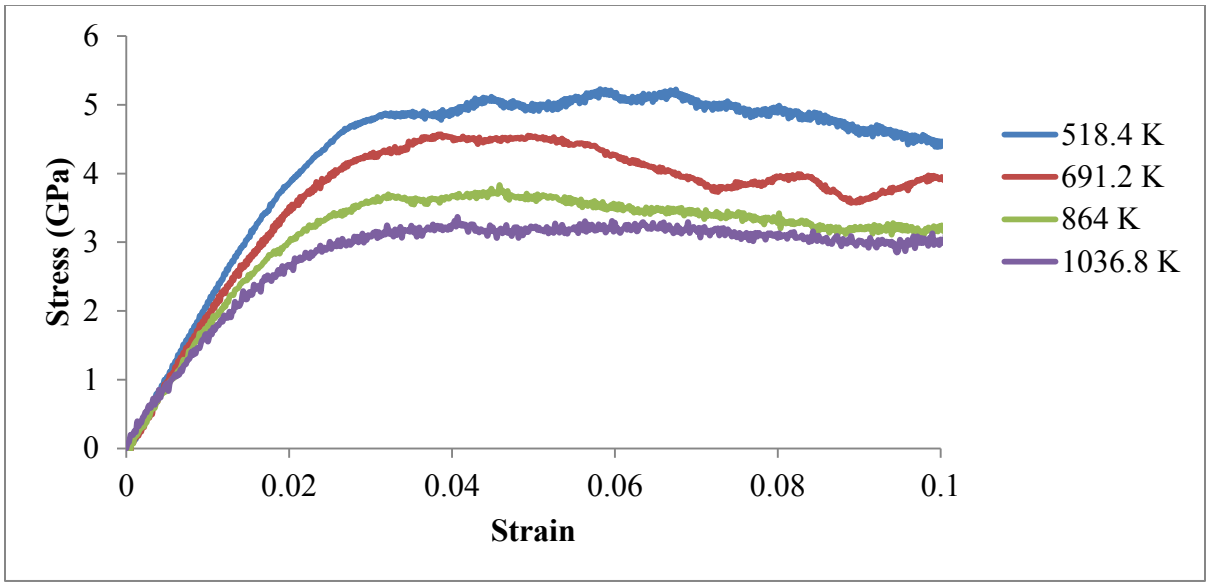

Figure 7: Stress-strain curves for the sample shown in Figure 6(b) at several temperatures. The flow stresses from these stress-strain curves were used to construct the Arrhenius behavior plot shown in Figure 8. Figure by author.

10.5.1 Stress-strain behavior as a function of temperature

The stress-strain behavior was obtained for various temperatures. In Figure 7, we show the results of virtual tensile testing at a strain rate of $3x10^{8}$ s^{-1} and the sample periodic depicted in Figure 6b. The sample softens as the temperature is increased. Both the yield and the flow stresses observed to decrease as the temperature is increased. This is indicative that thermal processes are important, even at the very high strain rates of molecular dynamics virtual mechanical testing. Figure 8 shows an Arrhenius plot of the flow stresses observed at various temperatures. The slope obtained from this Arrhenius plot can be used to obtain an estimate of

the activation energy for the overall deformation process, and we report this estimate in the following section.

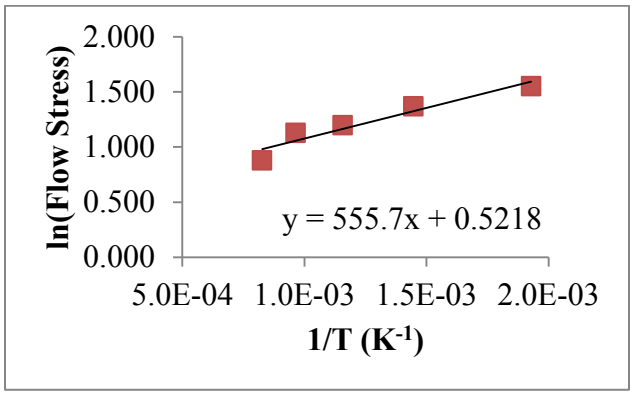

Figure 8: Arrhenius behavior for the sample shown in Figure 6(b). The slope of this line was used to calculate the strain rate sensitivity exponents determined in this work. Figure by author.

10.5.2 Strain rate sensitivity and activation energy

In Figure 9, we show the stress-strain curves obtained for the periodic sample at a temperature of 300K and different strain rates. These results show that the flow stresses increase significantly with strain rate. This is also consistent with thermally activated processes paying an increasing role in slower strain rates that imply longer simulation times.

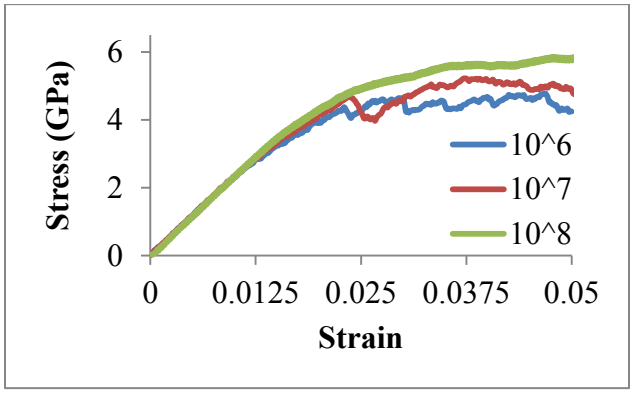

Figure 9: Stress-strain curves for the sample shown in Figure 6(b) at three strain rates ranging from $3x10^6$ s^{-1} to $3x10^8$ s^{-1}. Figure by author.

From these results, strain rate sensitivity exponents (*m*) were calculated for the periodic sample used in this work at different temperatures. Figure 10 shows the plot of the flow stress as a

function of strain rate in a log/log scale, for the lowest temperature of 300K and the highest temperature of 1300K. The strain rate sensitivities are the slopes of the lines shown. The value of *m* was found to be m = 0.03 at 300k. 1300K, *m* was found to have increased to a value of m = 0.16. This agrees well with experimental work by Luo, Pico, and Romhanji [33-35] which found that *m* increases with temperature in Al and Ti alloys at temperatures from 123 to150K for the Al alloys at 1093 to 1303K for the Ti. The strain rates studied in their work range from $6.4x10^{-4}$ s^{-1} to $1x10^{1}$ s^{-1}. From these results we also calculated the value of the activation volume according to

$$V = \frac{\sqrt{3}kT}{m\sigma} \qquad 5.1$$

Where V is the activation volume, k is the Boltzman constant, T is the temperature in Kelvin, m is the strain rate sensitivity constant, and σ is the uniaxial flow stress [36, 37]. We obtained activation volumes that range from 0.04 nm3 at 300K to 0.09 nm3 at 1300K. This is consistent with the work of Deng and Sansoz [36] for Au nanowires that also report activation volumes that increase with temperature. These values represent a range of 3 to 6 b3, using the value of the Burgers vector of a full dislocation. (0.245 nm)

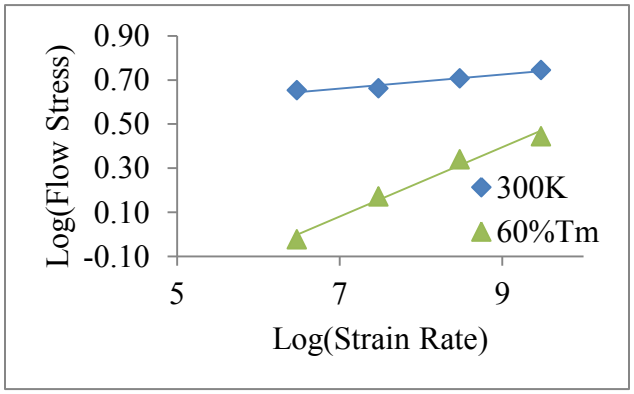

Figure 10: Strain rate sensitivity plots showing differences in slope for the periodic sample shown in Figure 6(b) at two different temperatures. Figure by author.

Having the slopes of the Arrhenius plots in Figure 8 and the strain rate sensitivities, we can estimate the activation energy for the deformation process, according to:

$$\ln \sigma = \frac{-E_a}{R}\frac{1}{T} + \ln A \qquad 5.2$$

Where σ is the flow stress, Ea is the activation energy, R is the gas constant, T is the temperature in Kelvin and A is a pre-exponential factor. The activation energy calculated from an Arrhenius plot of the flow stress as a function of temperature, and a median value of 0.09 for the strain rate was determined to be 0.53 eV/atom. This agrees well with the 0.46 determined for nano-crystalline nickel by Bokstein et al. [38].

The values of activation volumes and activation energies obtained are consistent with the deformation process in our virtual tensile test being controlled by atomic process involving a few atoms in the grain boundary region.

10.5.3 Effect of temperature on the individual deformation mechanisms

In order to study the details of the processes occurring at the grain boundaries, we created heterogeneous deformation maps, as described in Section 3. These heterogeneous displacement maps at 3, 4, and 5% strains for the sample depicted in Figure 6(a) at 300K and 700K are compared in Figure 11. The strain rate is $3x10^8$ s^{-1}. Sharp gradients in the color indicate that a complete dislocation has passed through the grain and resulted in slip. Black symbols in each figure indicate atoms in the grain boundaries, dislocation cores and stacking faults, as identified by higher centro-symmetry parameters. The overall analysis of the sample reveals increased dislocation activity as well as activation of additional slip systems at the higher temperature. To highlight the differences between the two deformation temperatures, four regions, labeled *a-d*, are indicated in Figure 11e and 11f.

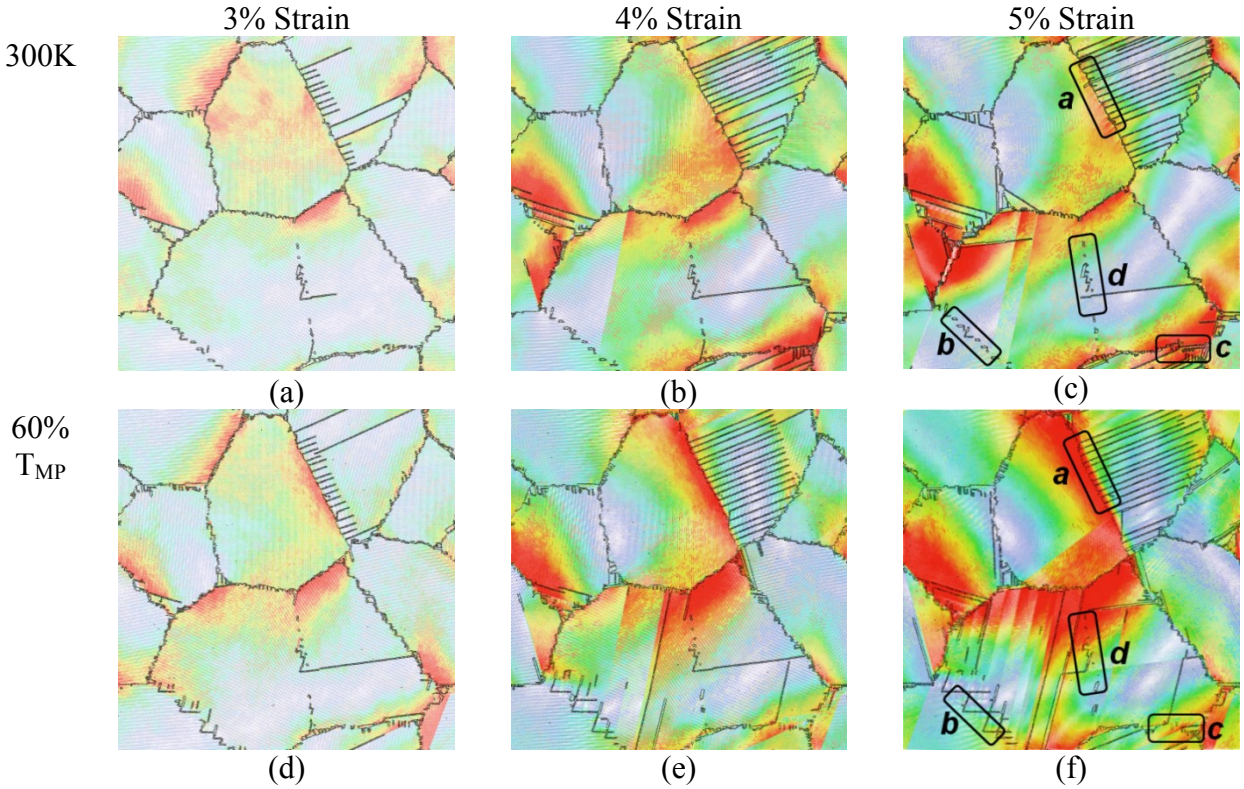

Figure 11: Heterogeneous deformation maps for a thin film sample. Strain levels of 3, 4, and 5% in the X-direction are shown. (a), (c), and (e) show the sample deformed at 300K, while (b), (d), and (f) show the sample deformed at 60% T_{MP}. Overall analysis shows that the sample deformed at the higher temperature had an increased level of dislocation emission and activation of multiple slip systems. The color map used is from blue to red where red indicates heterogeneous displacements up to 0.25 in (a) and (d), 0.55 in (b) and (e), and 0.8 nm in (c) and (f). Atoms with centrosymmetry parameter greater than 3 are in black. Areas of interest outlined and labeled in black. Figure by author.

Grain boundary migration driven by strain was observed in area *a* at the higher temperature simulation. This grain boundary emits a large number of partial dislocations. Greater detail of the process occuring in a segment in the area marked *a* in Figure 11 is shown in Figure 12 as a function of strain and of temperature. These examples show that in the simulations, as in the experiments, greater dislocation emission from grain boundary sources occurred at the higher temperature. This also is apparent in the area labeled *b* in Figure 11, which shows that the grain boundary emits many more dislocations at 700K than at 300K. That is, for the same loading condition, grain boundary dislocation sources are more active at higher temperature suggesting a

thermally activated component to dislocation emission. Similarly, area *c* in Figure 11 also contains a boundary with a misorientation angle of 16.9^{o} that presents additional active slip systems at the higher temperature.

Figure 12 shows a detailed segment of the grain boundary indicated in area *a*. This area is shown for exactly the same group of atoms for deformation at two different strain levels at two different temperatures. The relaxed structure of the grain boundary is similar with non-planar features that are located in the same points in the boundary, irrespective of temperature. The dislocation emission behavior differs under deformation at each temperature. At a strain level of 2% this short segment has emitted five dislocations in the simulation at 300K and 8 dislocations at 60% T_{MP}, clearly illustrating that dislocation emission is easier at the higher temperature. This occurs through the activation of additional source points at the higher temperature that are not activated for the lower deformation temperature. In addition, at a deformation level of 5% migration, of the boundary is observed at high temperature but not at 300K. This can be seen by comparing the position of the grain boundaries at the two temperatures at 5% strain. In this example, the boundary has migrated 1.5 nm at 5% deformation. The fast rate of strain and limited time scales in our molecular dynamics simulations are not long enough to observe thermal migration of the boundary at 700K. It is the combination of temparature and stress that drives this migration. This is consistent with the experimental observation of grain boundary migration driven by a combination of strain and temperature that was shown in Figure 5.

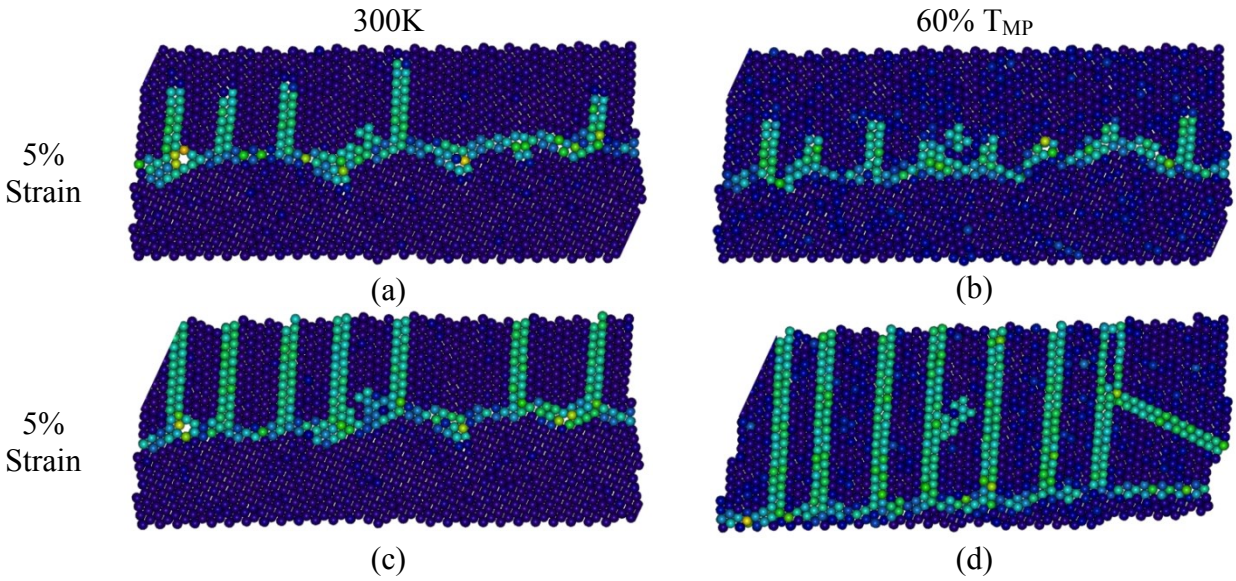

Figure 12: Detail of area a at 2% and 5% strain illustrating strain driven GB migration. Atoms colored with the centrosymmetry parameter from 0 (blue) to 12 (yellow). Images a-b show the sample at 300K. (a) at 2% and (b) at 5%. Images c-d show the same boundary at 60% T_{MP}. By 5% strain, the grain boundary has clearly migrated by 1.5nm in the sample deformed T 60% T_{MP} while the sample deformed at 300K shows similar dislocation emission from the boundary, but little to no grain boundary migration. Figure by author.

10.5.4 Effect of temperature on dislocation emission and grain boundary sliding

A detailed examination of area *c* in Figure 11 is shown in Figure 13. This detail shows a dislocation that is emitted from the boundary into the top grain (grain 7) only at high temperature. In addition this particular boundary emits mostly leading partial dislocations at low temperature, as evidenced by the stacking faults present in this grain (grain 3). At high temperature both the leading and the trailing partial have been emitted from this boundary into the lower grain, as evidenced by the lack of stacking faults and the changes in the heterogeneous displacement color map that can be seen in the lower grain. Figure 8 also shows that the strain is more homogenously distributed for deformation at 700K than at 300K. The emission of the trailing partials into grain 3 at high temperature can be attributed to the fact that the higher activation barrier necessary for the emission of the trailing partial is overcome by the combined effects of stress and temperature. The boundary structures shown in Figure 13 suggest that at

higher temperatures, the structure of the boundary is more easily restored to higher order, lower energy configurations.

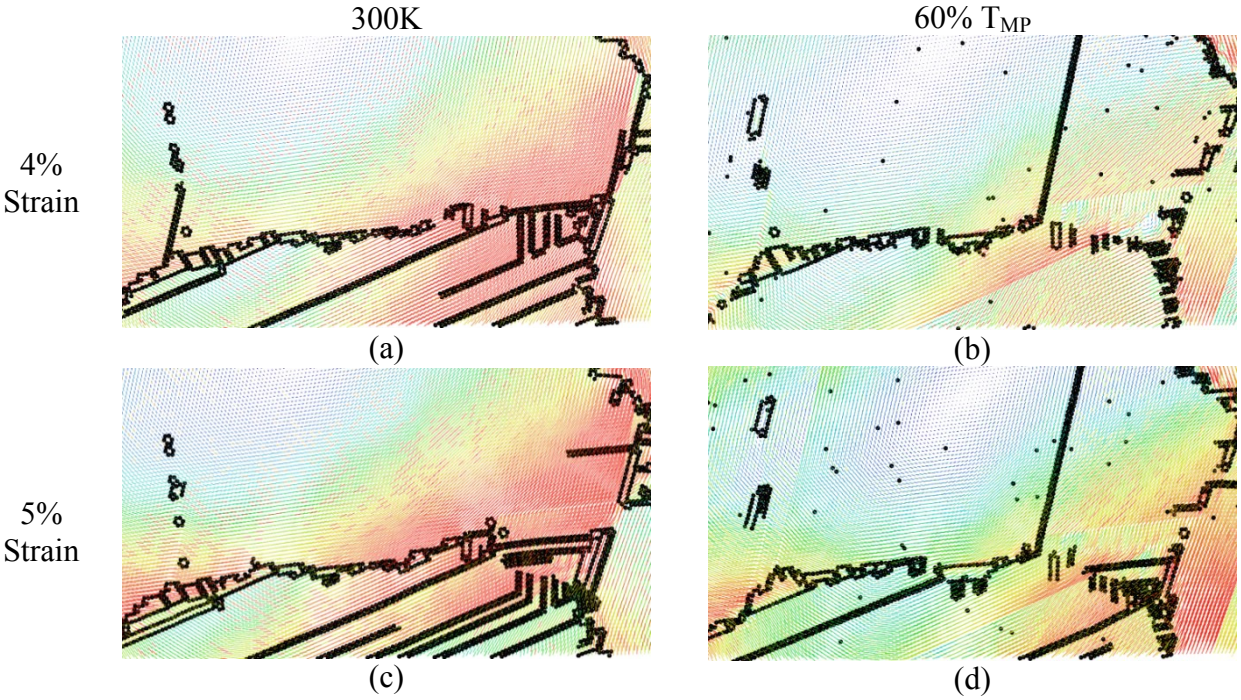

Figure 13. Detail of area c at 4% and 5% strain, denoted by pink box "c" in Fig. 4. (a) shows the 300K sample at 4% strain. (b) shows the same section at 4% strain at 60% T_{MP}. The color map used is from blue to red where red indicates heterogeneous displacements up to 0.55 nm. Figure by author.

Another interesting phenomenon is observed in area *d* of figure 11 , where a sub-grain boundary disintegrates through dislocation emission at 700K, while it remains intact at 300K. This loss of a grain boundary coincides with the migration of a neighboring boundary, which results in the annihilation of a short segment of grain boundary that effectively converts two triple junctions to one. This disintegration is similar to what was seen experimentally during the deformation of the aluminum alloy at elevated temperature (Figure 5).

In order to further study the effect of temperature on the overall deformation behavior of the columnar sample shown in figure 6 (b), a quantitative evaluation of the dislocation emission process was performed by counting the total number of partial dislocations emitted from grain

boundaries in the sample as the strain was increased at 300K and 1300K. Figure 14(a) shows the cumulative number of dislocations emitted from 0 to 9% strain. The total number of dislocations rises by a factor of 2 at the higher temperature, as shown in Figure 14(a). These results imply that an increase in temperature lowers the barrier to dislocation emission from grain boundaries. As the temperature is increased, an increase in grain boundary sliding is also observed, as shown in Figure 14(b). This is again consistent with both deformation mechanisms being driven by a combination of strain and temperature.

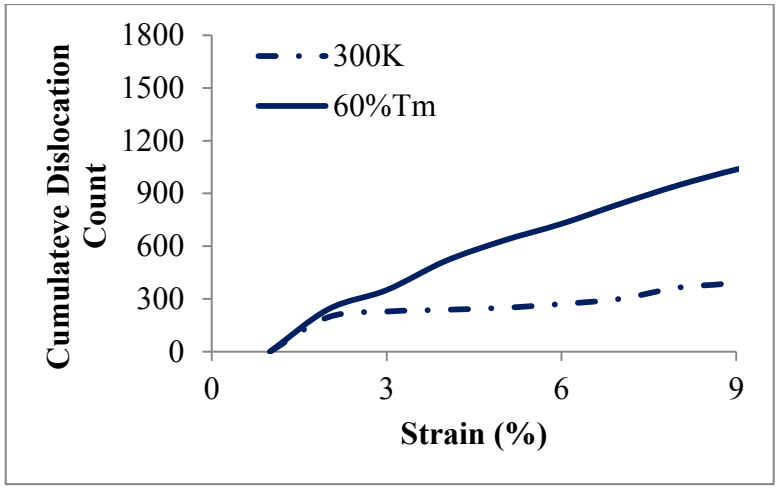

(a)

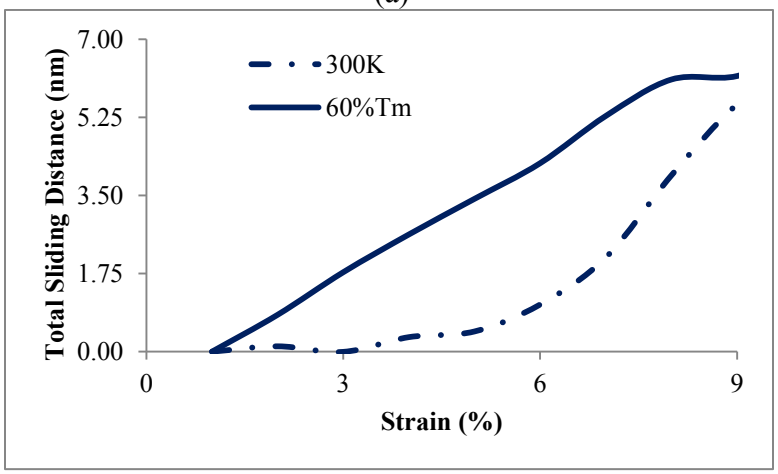

(b)

Figure 14: Deformation mechanisms dependence on temperature. a) Number of dislocations emitted as a function of strain for two different temperatures. b) Average sliding distance observed in representative grain boundaries as a function of strain for two different temperatures. Figure by author.

10.5.5 Effect of temperature on slip transfer and grain boundary migration/relaxation.

Slip transmission across grain boundaries was also enhanced with increasing temperature. In the simulations, dislocation transfer across grain boundaries occurred in the columnar grain sample at 60% T_{MP} and across a boundary that is close to a Σ=3 misorientation, as shown in Figure 15. At 3% strain, the red arrow shows the path of the partial dislocation through grain 3 before it arrives at the boundary. The blue arrow shows the displacement of the boundary as a result of an incoming Shockley partial dislocation. At 5% strain, a trailing partial dislocation follows along the same path and transfers across the boundary into the other grain. The incoming dislocation is of edge character and glides along a {111} type plane in the left grain. The dislocation emitted into the right grain is also of edge character and is glissile along a {111} type plane in that grain. The two directions are almost parallel in this particular misorientation, as indicated in Figure 15. The residual Burgers vector left in the boundary is very small. This dislocation transfer mechanism is not seen at 300K. The mechanism of dislocation transmission across the boundary in this example involves a change in the grain boundary structure that occurs when the leading partial dislocation first arrives at the boundary. Upon the arrival of the trailing partial dislocation, a leading partial dislocation is emitted into the adjoining grain. In the example of Figure 15 it can be seen that the atomistic grain boundary structure has changed due to the interaction of dislocations and grain boundaries with a restructuring of the affected region of the boundary.

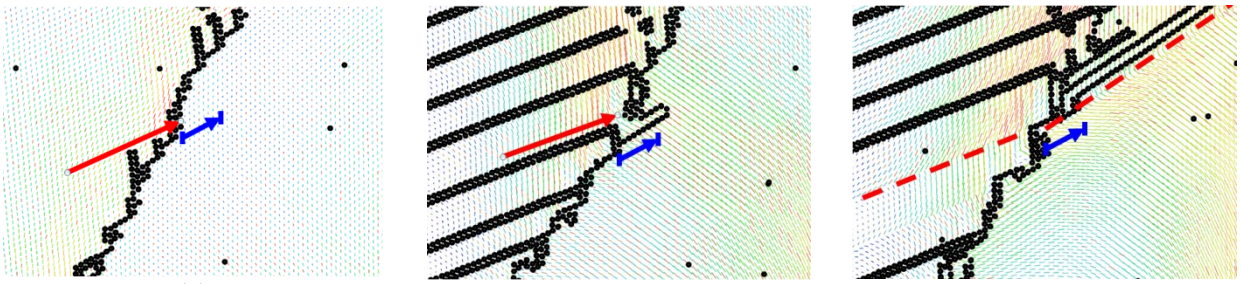

(a) (b) (c)

Figure 15: Detail of a grain boundary in the sample shown in the Figure 6(a) sample at 3, 4, and 5% strain deformed at 60% T_{MP}. Dislocation transfer shown across a near Σ=3 boundary. The color map used is from blue to red where red indicates heterogeneous displacements up to 0.25, 0.55, and 0.8 nm. Atoms with centrosymmetry parameter greater than 3 are in black. Red arrows represent movement of partial dislocation, blue arrows serve as a reference for boundary displacement, and the red dotted line is the result of a full dislocation slip. Figure by author.

Figure 16 shows the evolution of the microstructure as the sample of Figure 6b is being deformed to 3% using the slowest strain rate considered, of $3x10^{6}$ s^{-1}. In this sequence, significant grain boundary relaxation and migration is found during the deformation process at the high temperature, but not at 300K. This is additional evidence that these processes are driven by combinations of strain and temperature.

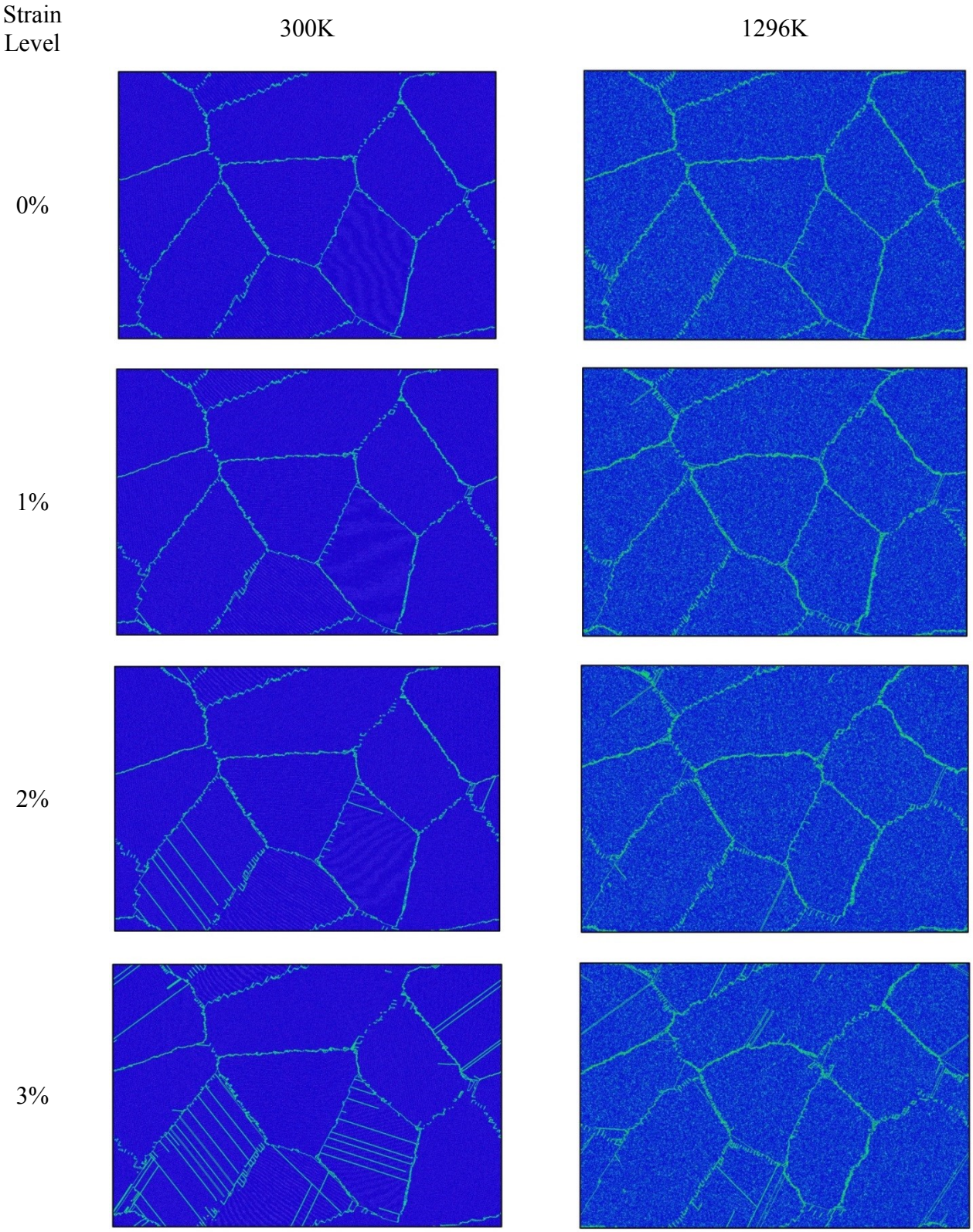

Figure 16: Deformation at 300 and 1296K of the periodic sample shown in Figure 6(b). Note the differences in microstructure evolution under applied strain between the two samples, in particular the higher grain mobility shown at 1296K. Figure by author.

10.5.6 Effect of temperature on crack nucleation

In the simulations, intergranular crack nucleation was observed to be more difficult at higher temperature. In Figure 17 (a-b), the stress-strain curves are marked with black crosses to reveal the stress and strain level required for crack nucleation. Figure 18 is an example of the heterogeneous deformation maps created and shows that for one of the thin film samples grain samples deformed at 300K, cracks nucleated at 5% deformation. No cracks were nucleated during deformation at 700 up to 10% deformation. The sample geometry is also important, with cracks nucleating earlier in the samples that have a thin film configuration. The differences can be related to the lower level of dislocation activity necessary to relieve stress at the grain boundary.

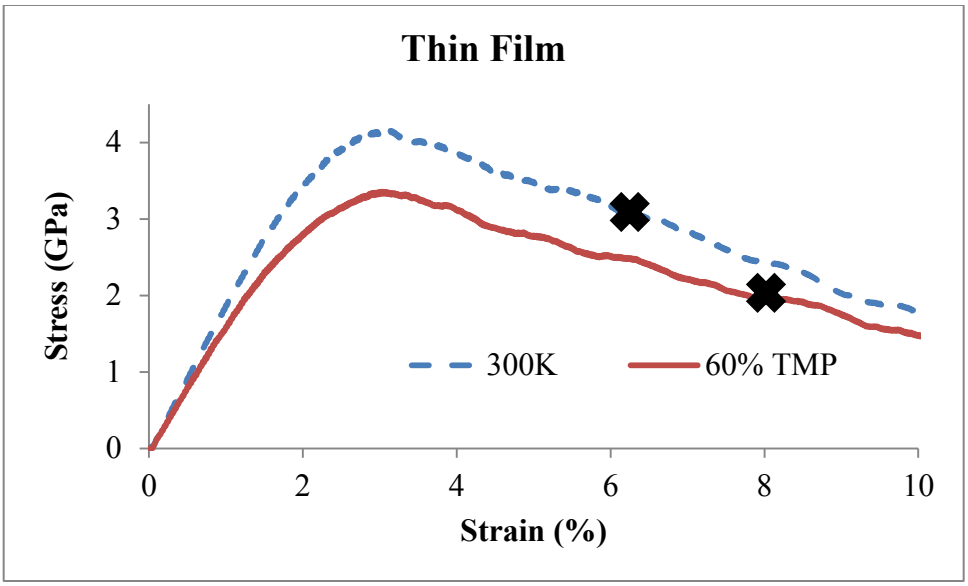

(a)

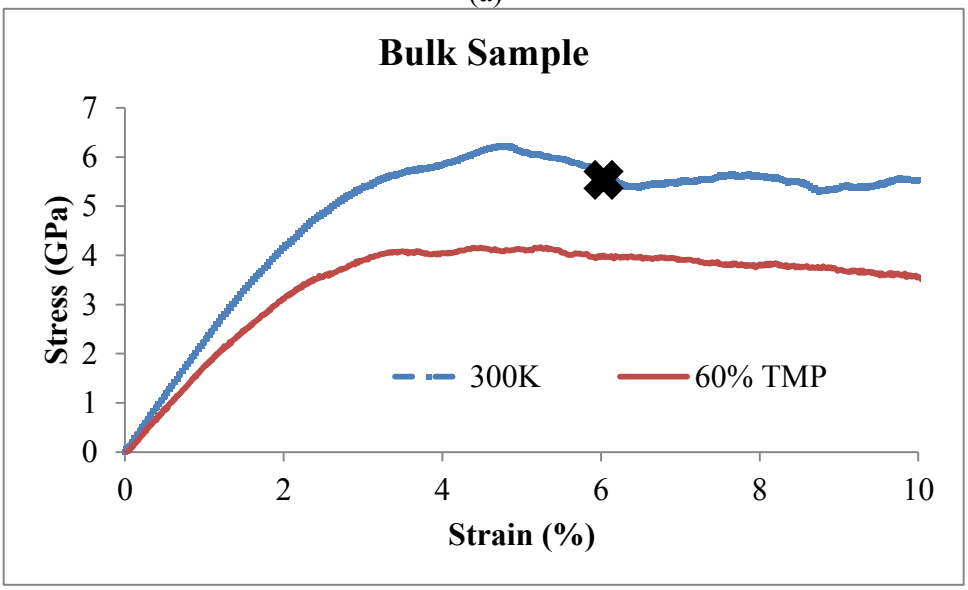

(b)

Figure 17: Stress-strain curves for the two types of samples in this work. Note that in both cases, deformation at the higher temperature delayed or prevented crack nucleation. Figure by author.

The activation of additional grain boundary sources at higher temperatures suggests a reduction in the stress experienced by the grain boundary and to a lower strain energy density. As seen in Figure 18 the strain localized in the boundary region is higher for deformation at lower temperature. The additional possibilities of transmission of dislocations across grain boundaries

at higher temperatures also contributes to the grain boundaries being subject to overall lower stresses and strain energy densities, resulting in cracks not nucleating until higher levels of strain.

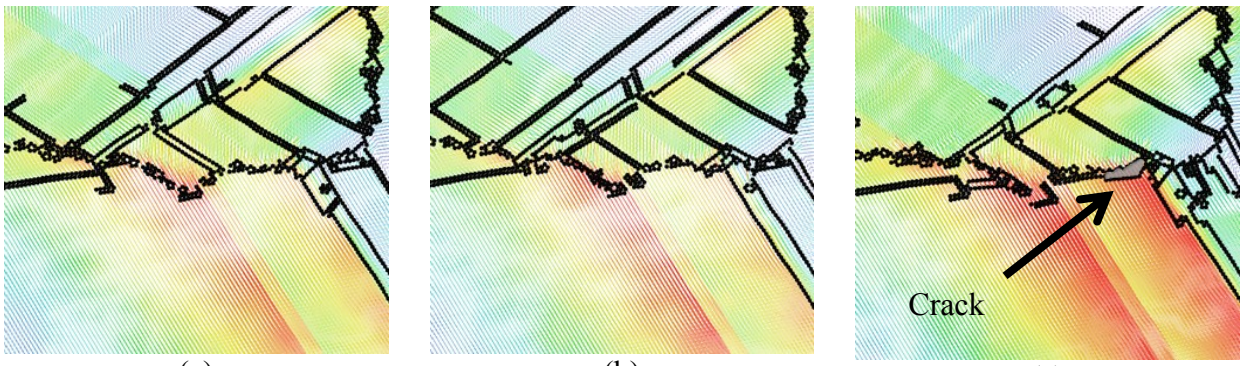

(a) (b) (c)

Figure 18: Detail of the columnar grain sample at 3, 4, and 5% strain deformed at 300K. Crack nucleation shown in a random high angle boundary. The color map used is from blue to red where red indicates heterogeneous displacements up to 0.25, 0.55, and 0.8 nm. Atoms with centrosymmetry parameter greater than 3 are in black. Figure by author.

Further detail of the effect of temperature on crack initiation is shown in Figure 19, where the increased dislocation emission at higher temperatures in Figure 19b appears to prevent the formation of the crack.

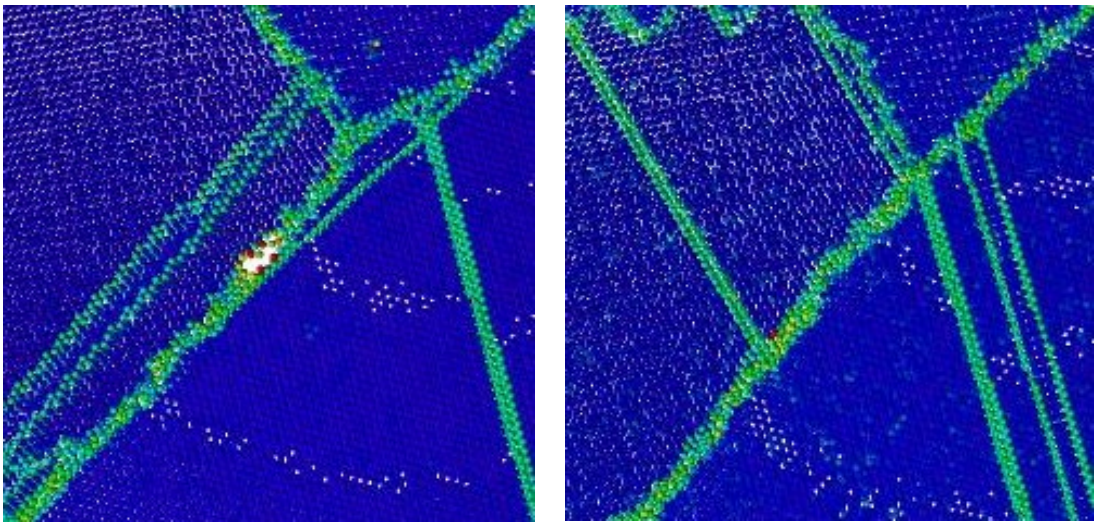

(a) (b)

Figure 19: Grain boundary response as a function of temperature and strain for a thin film sample at 9% strain at (a) 300K and (b) 60% TMP. Crack nucleation occurs only at the lower 300K temperature. Figure by author.

10.6. Discussion and Conclusions

The results presented in this study highlight the benefits of combining experimental observations with computer simulations in understanding complex interactions associated with material deformation. Computational simulations allow experiments to be repeated with variation of only a single variable; in this case temperature. This allows the effects of that variable to be isolated and removes ambiguity inherent to repeating experiments as not all variables can be reproduced exactly. The simulations also provide dynamic observations of material behavior at the atomic level during deformation at known stress and strain levels. However, the extreme strain rates associated with MD simulations necessitate experimental results for verification. Additionally, experimental observations can be made over time-length scales not yet available to atomistic simulations and can provide observations not readily apparent in the simulations. Thus, the two combined, computational simulations and experiment, can act as complementary techniques with each addressing shortcomings found in the other.

In this study, the combined application of experiment and simulation has helped clarify factors responsible for increased ductility and softening of metals during deformation at elevated temperatures. Both the experimental results and computer simulations showed that at elevated temperatures, dislocation systems nucleate at, are accommodated in, and are transmitted across grain boundaries at lower levels of stress than what would be required at lower temperatures. This was directly evident in the MD simulations where the exact load was known and could be inferred from the lower pileup density preceding slip transfer seen during *in situ* TEM deformation experiments. The atomistic simulations presented here help clarify this response by demonstrating the enhanced ability of grain boundaries to restructure to more ordered configurations at elevated temperatures (see the example of Figure 11), facilitating the process of

slip transfer across the boundary as well as enabling the emission of both leading and trailing partial dislocations as opposed to the emission of only the lead partial dislocation seen at room temperature (Figure 11). Additionally, while computational simulations demonstrate the activation of additional deformation mechanisms at elevated temperature such as grain boundary glide and disintegration, the high strain rates used in the simulations require experimental verification. This verification is provided by the observations made during deformation of an aluminum alloy at elevated temperature (Figure 5).

The activation of additional dislocation sources at grain boundaries and lower barrier to slip transfer at elevated temperature enhances the ability of the boundaries to accommodate and distribute elastic strain. This in turn reduces the magnitude of local stress buildups which act as damage nucleation sites; consequentially delaying the onset of cracking and increasing the ductility of materials under deformation.

Using a combined approach of MD simulations and guided by *in situ* deformation in the TEM, the mechanisms responsible for increased ductility and material softening during elevated temperature deformation have been investigated and identified. It was shown that increased dislocation activity at grain boundaries and a lower barrier to dislocation transfer across grain boundaries during elevated temperature deformation reduces the stress felt by the boundaries, delaying crack nucleation and material failure. It was also shown that additional deformation mechanisms such as grain boundary migration activate at elevated temperature, further increasing the material's ability to accommodate plastic deformation.

Acknowledgements:

The simulation work was supported by the Department of Energy, Office of Basic Energy Sciences, under grant DE-FG02-08ER46525. The electron microscopy work of JK was supported by Department of Energy, Office of Basic Energy Sciences, under grant *DEFG-02-07ER46443.* Dr. Y. Matsukawa is acknowledged for providing Figure 1. DF and IMR acknowledge the support of the NSF, IRD program.

References

[1] E. Arzt, "Size effects in materials due to microstructural and dimensional constraints: a comparative review," *Acta Materialia,* vol. 46, pp. 5611-26, 1998.

[2] E. Ma, "Eight routes to improve the tensile ductility of bulk nanostructured metals and alloys," *Jom,* vol. 58, pp. 49-53, Apr 2006.

[3] N. A. Mara, D. Bhattacharyya, R. G. Hoagland, and A. Misra, "Tensile behavior of 40 nm Cu/Nb nanoscale multilayers," *Scripta Materialia,* vol. 58, pp. 874-877, 2008.

[4] I. J. Beyerlein, N. A. Mara, D. Bhattacharyya, D. J. Alexander, and C. T. Necker, "Texture evolution via combined slip and deformation twinning in rolled silver-copper cast eutectic nanocomposite," *International Journal of Plasticity,* vol. 27, pp. 121-146, Jan 2011.

[5] M. D. Sangid, T. Ezaz, H. Sehitoglu, and I. M. Robertson, "Energy of slip transmission and nucleation at grain boundaries," *Acta Materialia,* vol. 59, pp. 283-296, Jan 2011.

[6] G. S. Was and J. T. Busby, "Role of irradiated microstructure and microchemistry in irradiation-assisted stress corrosion cracking," *Philosophical Magazine,* vol. 85, pp. 443-465, Feb-Mar 2005.

[7] T. C. Lee, I. M. Robertson, and H. K. Birnbaum, "Prediction of slip transfer mechanisms across grain boundaries," *Scripta Metallurgica,* vol. 23, pp. 799-803, 1989.

[8] T. C. Lee, I. M. Robertson, and H. K. Birnbaum, "TEM in situ deformation study of the interaction of lattice dislocations with grain boundaries in metals," *Philosophical*

Magazine A (Physics of Condensed Matter, Defects and Mechanical Properties), vol. 62, pp. 131-53, 1990.

[9] T. C. Lee, I. M. Robertson, and H. K. Birnbaum, "In situ transmission electron microscope deformation study of the slip transfer mechanisms in metals," *Metallurgical Transactions A (Physical Metallurgy and Materials Science),* vol. 21A, pp. 2437-2447, 1990.

[10] W. A. T. Clark, R. H. Wagoner, Z. Y. Shen, T. C. Lee, I. M. Robertson, and H. K. Birnbaum, "On the criteria for slip transmission across interfaces in polycrystals," *Scripta Metallurgica et Materialia,* vol. 26, pp. 203-6, 1992.

[11] S. Suri, G. B. Viswanathan, T. Neeraj, D. H. Hou, and M. J. Mills, "Room temperature deformation and mechanisms of slip transmission in oriented single-colony crystals of an α/β titanium alloy," *Acta Materialia,* vol. 47, pp. 1019-1034, 1999.

[12] D. J. Dingley and R. C. Pond, "Interaction of crystal dislocations with grain-boundaries," *Acta Metallurgica,* vol. 27, pp. 667-682, 1979.

[13] M. de Koning, R. Miller, V. V. Bulatov, and F. F. Abraham, "Modelling grain-boundary resistance in intergranular dislocation slip transmission," *Philosophical Magazine a-Physics of Condensed Matter Structure Defects and Mechanical Properties,* vol. 82, pp. 2511-2527, Sep 2002.

[14] Z. H. Jin, P. Gumbsch, K. Albe, E. Ma, K. Lu, H. Gleiter*, et al.*, "Interactions between non-screw lattice dislocations and coherent twin boundaries in face-centered cubic metals," *Acta Materialia,* vol. 56, pp. 1126-1135, Mar 2008.

[15] C. L. Kelchner, S. J. Plimpton, and J. C. Hamilton, "Dislocation nucleation and defect structure during surface indentation," *Physical Review B,* vol. 58, pp. 11085-11088, Nov 1998.

[16] R. Kumar, F. Szekely, and E. Van der Giessen, "Modelling dislocation transmission across tilt grain boundaries in 2D," *Computational Materials Science,* vol. 49, pp. 46-54, Jun 2010.

[17] S. L and F. D, "Non-planar grain boundary structures in fcc metals and their role in nano-scale deformation mechanisms," *Philosophical Magazine,* vol. In Press, 2013.

[18] L. Smith and D. Farkas, "Non-planar grain boundary structures in fcc metals and their role in nano-scale deformation mechanisms," *Philosophical Magazine,* vol. 94, pp. 152-

173, 2014/01/12 2014.

[19] L. Smith, J. A. Zimmerman, L. M. Hale, and D. Farkas, "Molecular dynamics study of deformation and fracture in a tantalum nano-crystalline thin film.," *MSMSE,* vol. Accepted, 2014.

[20] D. E. Spearot and D. L. McDowell, "Atomistic Modeling of Grain Boundaries and Dislocation Processes in Metallic Polycrystalline Materials," *Journal of Engineering Materials and Technology-Transactions of the Asme,* vol. 131, Oct 2009.

[21] T. R. Bieler, P. Eisenlohr, F. Roters, D. Kumar, D. E. Mason, M. A. Crimp*, et al.*, "The role of heterogeneous deformation on damage nucleation at grain boundaries in single phase metals," *International Journal of Plasticity,* vol. 25, pp. 1655-1683, Sep 2009.

[22] L. M. Dougherty, I. M. Robertson, and J. S. Vetrano, "Direct observation of the behavior of grain boundaries during continuous dynamic recrystallization in an Al-4Mg-0.3Sc alloy," *Acta Materialia,* vol. 51, pp. 4367-4378, Sep 2003.

[23] S. Mahajan, D. E. Barry, and B. L. Eyre, "A thin twin and its interaction with a coherent twin boundary in copper," *Philosophical Magazine,* vol. 21, pp. 43-52, 1970/01/01 1970.

[24] S. Mahajan and G. Y. Chin, "Twin-slip, twin-twin and slip-twin interactoins in Co-8 wt. % Fe alloy single crystals," *Acta Metallurgica,* vol. 21, pp. 173-179, 1973.

[25] J. Kacher and I. M. Robertson, "Quasi-four-dimensional analysis of dislocation interactions with grain boundaries in 304 stainless steel," *Acta Materialia,* vol. 60, pp. 6657-6672, Nov 2012.

[26] D. Farkas and W. A. Curtin, "Plastic deformation mechanisms in nanocrystalline columnar grain structures," *Materials Science and Engineering a-Structural Materials Properties Microstructure and Processing,* vol. 412, pp. 316-322, Dec 2005.

[27] D. Farkas and L. Patrick, "Tensile deformation of fcc Ni as described by an EAM potential," *Philosophical Magazine,* vol. 89, pp. 3435-3450, 2009.

[28] L. Smith and D. Farkas, "Non-planar grain boundary structures in fcc metals and their role in nano-scale deformation mechanisms," *Philosophical Magazine,* vol. 94, pp. 152-173, 2014/01/12 2013.

[29] H. Van Swygenhoven, M. Spaczer, A. Caro, and D. Farkas, "Competing plastic deformation mechanisms in nanophase metals," *Physical Review B,* vol. 60, pp. 22-25, 1999.

[30] Y. Mishin, D. Farkas, M. J. Mehl, and D. A. Papaconstantopoulos, "Interatomic potentials for monoatomic metals from experimental data and ab initio calculations," *Physical Review B,* vol. 59, pp. 3393-3407, Feb 1999.

[31] S. Plimpton, "Fast parallel algorithms for short-range molecular-dynamics," *Journal of Computational Physics,* vol. 117, pp. 1-19, Mar 1995.

[32] A. Stukowski, "Visualization and analysis of atomistic simulation data with OVITO-the Open Visualization Tool," *Modelling and Simulation in Materials Science and Engineering,* vol. 18, Jan 2010.

[33] J. Luo, M. Q. Li, W. X. Yu, and H. Li, "The variation of strain rate sensitivity exponent and strain hardening exponent in isothermal compression of Ti-6Al-4V alloy," *Materials & Design,* vol. 31, pp. 741-748, Feb 2010.

[34] R. C. Picu, G. Vincze, F. Ozturk, J. J. Gracio, F. Barlat, and A. M. Maniatty, "Strain rate sensitivity of the commercial aluminum alloy AA5182-O," *Materials Science and Engineering a-Structural Materials Properties Microstructure and Processing,* vol. 390, pp. 334-343, Jan 2005.

[35] E. Romhanji, A. Dudukovska, and D. Glisic, "The effect of temperature on strain-rate sensitivity in high strength Al-Mg alloy sheet," *Journal of Materials Processing Technology,* vol. 125, pp. 193-198, Sep 2002.

[36] C. Deng and F. Sansoz, "Effects of twin and surface facet on strain-rate sensitivity of gold nanowires at different temperatures," *Physical Review B,* vol. 81, p. 7, Apr 2010.

[37] J. Monk and D. Farkas, "Strain-induced grain growth and rotation in nickel nanowires," *Physical Review B,* vol. 75, p. 5, Jan 2007.

[38] B. S. Bokstein, H. D. Brose, L. I. Trusov, and T. P. Khvostantseva, "Diffusion in nanocrystalline nickel," *Nanostructured Materials,* vol. 6, pp. 873-876, 1995.

11 Conclusions

This work used computer simulations of polycrystalline materials at the atomistic scale. Virtual mechanical testing was conducted using molecular dynamics techniques and empirical interatomic force laws. Several connections between atomic level structure and processes with overall mechanical response were uncovered. This work successfully met the specific goals outlined in the introduction in the following ways:

- A large-scale simulation study was performed with simulated samples that ranged in size from approximately 500K to 5M atoms at strain rates ranging from 10^5 to 10^9 s^{-1}.
- Stacking fault energy significantly affects grain boundary structure. Low stacking fault energy promotes non-planar grain boundary features; high stacking fault energy promotes planar grain boundary features.
- The resulting planar or non-planar grain boundary features have distinct effects on subsequent deformation mechanisms.
    - Non-planar grain boundary structures tend to encourage dislocation emission from grain boundaries. They also raise the energetic barrier to grain boundary sliding such that sliding can be completely prevented.
    - Planar grain boundary features promote grain boundary sliding as a deformation mechanism.
- Quantitative estimations of dislocation emission and grain boundary sliding as a function of stacking fault energy reveals:
    - The low stacking fault energy materials Cu emitted twice as many dislocations as the high stacking fault energy material Pd.

    - The grain boundaries in the high stacking fault energy material Pd slid about three times farther than in the low stacking fault energy material Cu.
- Quantitative estimations of dislocation emission and grain boundary sliding as a function of strain rate reveals:
    - Deformation in nanocrystalline Ta at lower strain rates from 10^5 to 10^7 s^{-1} is a competitive process between dislocation emission and twin formation.
    - At higher strain rates of 10^8 and 10^9 s^{-1}, deformation is dominated by twin formation, at ratios of 3:1 and 4:1, respectively.
- Quantitative estimations of dislocation emission and grain boundary sliding as a function of temperature reveals:
    - Dislocation emission and grain boundary sliding both increase at higher temperatures.
        - About 3 times as many dislocations are emitted at high temperature as at lower temperatures.
        - Grain boundary sliding occurs more consistently at higher temperatures, although the totally amount of sliding is similar at 9% strain.

Expanded conclusions regarding the simulation setup, sample preparation, and from each chapter are detailed below:

The present work was successful in creating virtual realistic polycrystalline samples of one bcc material, Ta, and four fcc materials, Al, Cu, Ni, and Pd. Two types of samples were constructed using a Voronoi construction. One set of samples had a thin-film structure with periodic

boundary conditions in the x and y directions. The other set of samples were fully periodic, with a quasi-2D nature. All samples had columnar grains and an approximate grain size of about 40nm. The grain boundaries in the periodic samples were randomly misoriented around the [110] axis, lending a [110] texture to the entire sample. The samples were all deformed using standard molecular dynamics along the horizontal axis using a strain-controlled process. Several strain rates were used, from $10^5 s^{-1}$ to $10^9 s^{-1}$, with most of the work conducted at $10^8 s^{-1}$. The majority of the simulations were performed at 300K with the pressure maintained at zero in the directions perpendicular to the tensile axis.

The following step undertaken was to compare the results from the simulation to experimental results with a focus on crack initiation. The experimental work was performed by our collaborators at the University of Michigan, where samples were made from sheets of Fe-13Cr-15Ni austenitic stainless steel with a grain size of about 50 microns. The steel samples were irradiated with 2MeV protons to a dose of 5dpa. The samples were then strained under tension in 288°C simulated boiling water reactor conditions. The simulated samples were created from orientation imaging microscopy scans of experimental samples in order to more accurately compare results and were run with a nickel potential [1] at 300K with a $3x10^8 s^{-1}$ strain rate. The results from the experiments and the simulations were compared and similar trends were observed. The results in both the simulations and the experiments showed that key factors in crack initiation were the angle of the boundary with respect to the tension axis and the type of boundary. Random high angle boundaries were found to crack more often than coincident site lattice or low angle boundaries. Boundaries where slip transfer was observed are less likely to crack than boundaries that do not show this method of strain accommodation. The experimental samples were also examined for areas of strain localization, where the local strain is in excess of

the homogenous strain imposed upon the sample. This was achieved through the adherence and imaging of gold nanoparticles to the surface of the experimental sample prior to straining. After deformation, the sample was again imaged and areas of excess strain were identified through the gold speckle pattern. Similar regions of excess local strain were found in both the simulation and experimental samples. Additionally, similar types of dislocation-grain boundary interactions were observed in both sample sets, including slip transmission and discontinuous slip.

The conclusion of the comparison was that there is agreement in the trends between the simulations and the experimental methods indicating that the model is accurately representing deformation mechanisms that activate at the macroscale despite the considerable difference in grain size.

The next effort was to examine the relationship between deformation mechanisms and grain boundaries in the fully periodic [110] textured samples. The simulations were run using the same Ni potential and conditions that were used in the previous work, at 300K deformation temperature and $10^8 s^{-1}$ strain rate. It was found that the local structure of a grain boundary is a very important factor in how the boundary responds to applied strain. The critical resolved shear stress for different boundaries varies, as shown in table 6.2. Each grain boundary emits dislocations at different values of critical resolved shear stress ranging from 0.63 to 2.5 GPa. It was also found that the grain boundary structure undergoes significant change as a result of dislocation emission with low-angle grain boundaries found to nearly disappear as deformation progresses.

The structure of equilibrated individual grain boundaries was examined in depth using the periodic samples and potentials developed to represent Cu [2] and Pd [3]. These simulations were performed at 300K and at the $3x10^8 s^{-1}$ strain rate. The potentials were selected due to their

significantly different stable stacking fault values: Cu at 44mJ/m^2 and Pd at 187mJ/m^2. Relaxed grain boundary structures were found to be significantly non-planar in the Cu sample, resembling nascent stacking faults extending from the boundary into the surrounding grain structure. These non-planar features encouraged dislocation emission in the Cu sample and tended to inhibit grain boundary sliding. At 9% strain, the Cu sample was found to have emitted nearly twice as many dislocations as the Pd sample. In comparison, the Pd sample was found to have more planar boundaries containing the E structural unit. The planar grain boundaries were found to exhibit considerably more sliding. At 9% strain the Pd sample was found have three times as much sliding as the Cu sample. The conclusion is that local grain boundary structure is critical and needs to be considered in plasticity models.

Deformation behavior in bcc materials was also investigated, using a potential developed to represent tantalum [4]. Two thin-film bcc samples were created, one with about 500K atoms and three grains with an approximate grain size of about 30nm to facilitate study at the strain rate of $10^5 s^{-1}$, and one an order of magnitude larger with 4.6M atoms and 30 grains. Both samples were deformed at 300K at strain rates increasing in orders of magnitude from $10^6 s^{-1}$ to $10^9 s^{-1}$. It was found at strain rates slower than $10^8 s^{-1}$, emission of perfect a/2 |<111>| dislocation is the initial deformation mechanism observed, though the strain at which each dislocation emits varies with strain rate. Crystallographic slip in the tantalum systems was found in the {112}/<111> slip system. This is consistent with previous tantalum simulations using other tantalum potentials. Twin formation begins at higher strain levels than the dislocation emission up to $10^8 s^{-1}$. Analysis of the amount of dislocation emission and twinning at the lower strain rates show that there is competition between the two mechanisms, with plastic strain carried approximately equally. At $10^8 s^{-1}$, the initial and predominant deformation mechanism changes to

twinning, with plastic strain carried by twinning at a rate of at least 3:1. These results indicate that strain rate effects on deformation become more pronounced at $10^8 s^{-1}$ and faster. The agreement between the results from the two samples also indicate that very small systems can accurately represent mechanical behavior of larger systems and can facilitate molecular dynamics studies at strain rates below $10^6 s^{-1}$.

The study was then expanded to six different fcc potentials in order to establish the relationship between specific atomistic parameters, grain boundary energetics and deformation behavior. These potentials included 2 separate potentials for Ni [1, 5], two separate potentials for Al [1, 5], and the Cu [2] and Pd [3] potentials mentioned above. It was found that the grain boundary energy scales with the shear modulus. This agrees with the work done by Holm et al. [6]. It was also found that the grain boundary energy in asymmetric tilt boundaries varies along the boundary and increases with proximity to triple junctions. Strong correlations were found between the unstable stacking fault energy and the yield and flow stress. Relaxed grain boundary structures correlate with the stable stacking fault energy, with high stacking fault energy corresponding to planar grain boundary structures. Correspondingly, the fraction of non-planar boundaries in the samples scales inversely with the stable stacking energy. The overall stress in the sample at the initial dislocation emission from three planar boundaries in each sample was investigated, and determined to scale with the unstable stacking fault energy. These results show that atomistic parameters, grain boundary energetics, and mechanical behavior are heavily interdependent, making it difficult to establish a causal relationship between a specific deformation mechanism and the atomistic parameter that governs it.

Finally, the effect of temperature on deformation was examined in both periodic and thin-film samples. The simulations were performed at 300K and at 60% of the melting temperature

predicted by the nickel potential [1] used. Increased temperature leads to both increased dislocation emission and grain boundary sliding in all samples. This improved the ability of the grain boundaries to accommodate the applied strain and delayed crack initiation by an average of 2% strain. Grain boundary migration was also observed at the elevated temperature. Temperature is shown to affect the strain rate sensitivity, which is found to increase with temperature. The Activation energy for the process was estimated to be 0.53 eV/atom. This agrees well with the experimental value of 0.46 eV/atom found by Bokstein et al. [7].

References

[1] Y. Mishin, D. Farkas, M. J. Mehl, and D. A. Papaconstantopoulos, "Interatomic potentials for monoatomic metals from experimental data and ab initio calculations," *Physical Review B,* vol. 59, pp. 3393-3407, Feb 1999.

[2] Y. Mishin, M. J. Mehl, D. A. Papaconstantopoulos, A. F. Voter, and J. D. Kress, "Structural stability and lattice defects in copper: Ab initio, tight-binding, and embedded-atom calculations," *Physical Review B,* vol. 63, Jun 2001.

[3] S. M. Foiles and J. J. Hoyt. (2001, Computer Simulation of Bubble Growth in Metals Due to He. *Sandia Report SAND2001-0661*.

[4] Y. H. Li, D. J. Siegel, J. B. Adams, and X. Y. Liu, "Embedded-atom-method tantalum potential developed by the force-matching method," *Physical Review B,* vol. 67, p. 8, Mar 2003.

[5] A. F. a. C. Voter, S. P., "High temperature ordered intermetallic alloys," *Materials Research Society Symposium Proceedings,* vol. 82, p. 175, 1987.

[6] E. A. Holm, D. L. Olmsted, and S. M. Foiles, "Comparing grain boundary energies in face-centered cubic metals: Al, Au, Cu and Ni," *Scripta Materialia,* vol. 63, pp. 905-908, Nov 2010.

[7] B. S. Bokstein, H. D. Brose, L. I. Trusov, and T. P. Khvostantseva, "Diffusion in nanocrystalline nickel," *Nanostructured Materials,* vol. 6, pp. 873-876, 1995.